Title
Resonance Electronic Raman Scattering in Rare Earth Crystals

Author
Williams, G.M.

Publication Date
1988-12-01

Lawrence Berkeley Laboratory

UNIVERSITY OF CALIFORNIA

Materials & Chemical Sciences Division

Resonance Electronic Raman Scattering in Rare Earth Crystals

G.M. Williams
(Ph.D. Thesis)

November 1988

Prepared for the U.S. Department of Energy under Contract Number DE-AC03-76SF00098.

DISCLAIMER

LBL-26344

Resonance Electronic Raman Scattering in Rare Earth Crystals

Ph.D. Dissertation

November 10, 1988

Glen Munroe Williams

Department of Physics
University of California
and
Materials and Chemical Sciences Division
Lawrence Berkeley Laboratory
1 Cyclotron Road
Berkeley, California 94720

Resonance Electronic Raman Scattering in Rare Earth Crystals

By

Glen Munroe Williams

November 10, 1988

Abstract

The intensities of Raman scattering transitions between electronic energy levels of trivalent rare earth ions doped into transparent crystals were measured and compared to theory. A particular emphasis was placed on the examination of the effect of intermediate state resonances on the Raman scattering intensities. Two specific systems were studied: $Ce^{3+}(4f^1)$ in single crystals of $LuPO_4$ and $Er^{3+}(4f^{11})$ in single crystals of $ErPO_4$.

In Ce^{3+}:$LuPO_4$ the relative Raman scattering intensities were measured for transitions from the Ce^{3+} ground state to the crystal field levels of the $^2F_{5/2}$ and $^2F_{7/2}$ multiplets. The Raman scattering was excited by the 514.5 nm line of an argon ion laser. The measured intensities were found to be very different than the values predicted by the standard theory. The calculation for the Raman scattering intensities involved a sum over virtual intermediate states. For electronic Raman scattering from rare earth

ions in transparent crystals, the virtual intermediate states are usually assumed to be states belonging to the excited electronic configurations of the rare earth ion. In the standard theory approximations are made regarding the detailed energy level structure of these excited configurations. A second calculation of the relative electronic Raman scattering intensities from Ce^{3+}:$LuPO_4$ was made by explicitly evaluating the sum over virtual intermediate states using the measured values of the energies of the states belonging to the first excited configuration ($5d^1$) of Ce^{3+} in $LuPO_4$. This calculation agreed well with the measured values.

Electronic Raman scattering from Ce^{3+}:$LuPO_4$ was also excited by the frequency-tripled output of a Nd^{3+}:YAG laser at 355 nm. This excitation is in near resonance with the ground-to-first excited configuration transitions ($4f^1 \rightarrow 5d^1$) of Ce^{3+} in $LuPO_4$. The electronic Raman scattering intensities were found to be on the order of 100 times greater for excitation at 355 nm relative to excitation at 514.5 nm These enhancements were accurately predicted by the explicit calculation.

In addition to the measurement of relative electronic Raman scattering intensities, values for the absolute electronic Raman scattering cross-sections were obtained through a calibration of the collection efficiency of the detection system using standards with known scattering cross-sections. The measured absolute cross-sections were compared to values calculated from Hartree-Fock estimates of the radial overlap integral between the ground and first excited configurations of Ce^{3+}. It was found that the measured cross-sections were smaller than the calculated cross-sections by factors ranging from approximately 5 to 10. This observation was consistent with the small values observed for the $4f^1 \rightarrow 5d^1$ transition oscillator strengths for Ce^{3+}: $LuPO_4$.

An intra-configurational ($4f^{11} \rightarrow 4f^{11}$) formally parity-forbidden resonance of electronic Raman scattering was studied in $ErPO_4$. Electronic Raman scattering was observed for transitions between the ground state and excited crystal field states of the ground $^4I_{15/2}$ multiplet of Er^{3+}. The exciting laser light was selected to be in or near resonance with the transition between the ground state and the crystal field states of the $^4F_{7/2}$ multiplet. Excitation profiles for the electronic Raman scattering were obtained by measuring the scattering intensities as the laser frequency was scanned through the

resonance associated with a transition between the ground state and one particular crystal field state of the $^4F_{7/2}$ multiplet. Large enhancements of the scattering intensities of the order of 100 were observed. The shapes and magnitudes of the excitation profiles are accurately modelled using information obtained from the one-photon absorption spectrum of $ErPO_4$. Suggestions were given for determining the circumstances under which large intra-configurational resonances of electronic Raman scattering should be observable.

Contents

List of Figures

List of Tables

Acknowledgements

There are a great number of people that I would like to thank for their support and assistance during the course of my graduate career. This dissertation would not exist were it not for these people.

First I would like to thank my research supervisor, Norman Edelstein, for his patience and support and for allowing me to play softball every now and then. Me and Norm (whoops!, Norm and I) had our disagreements but I will admit now that he was right at least 50% of the time. I would like to thank my research advisor, Sumner Davis, for contributing greatly to my education as a physicist. I will never forget our weekly group meetings and Sumner's uncanny ability to always ask the question you hadn't expected.

Many people from other institutions contributed in some way to this work. Foremost of these is Arnold Koningstein (Dr. Electronic Raman) who got us started in the electronic Raman business. Marvin Abraham and Lynn Boatner supplied us with our lifeblood, "the crystals", and critically reviewed all our work. I would like to thank Brian Judd for his suggestions that resulted in the last half of Chapter 3 and a publication. Rick Leavitt, in his two month visit to our laboratory, added the most to my understanding of atomic theory. I also acknowledge Rufus Cone, Michael Reid, and Gerhardt Shaack for some very useful discussions.

A large number of people at LBL deserve to be thanked. I start by acknowledging Rick "The Capo" Russo because I figure someday he's going to be the head of DOE. Seriously Rick, thanks for getting Phil and I going and showing me the meaning of enthusiasm. John Conway and George Shalimoff taught me a lot about spectroscopy. Barbara Moriguchi always greeted my arrival at the lab with a smile and a "good morning". I would like to thank Jerry Bucher for being so wily with the computers and equipment

and for generally being such a nice guy. I know it's customary at this point to make some joke regarding Jerry's office, but really no words can describe it. Thanks goes to my officemate, David Piehler, for liking Clint Eastwood movies and talking physics with me (in that order). Sharon Beshouri and Isabelle Poirot are the best of friends and are always willing to help around the lab. Sharon, I'm sorry about the Oakland A's. Remember, there is always next year.

There are a large number of people who I did not work with directly, but who supported me through their friendship. I would like to thank, my ex-roomie Petie "whippit" Davis, my lifting buddy Adlai SMITH, my volleyball buddy Kevin Derby, my Kentucky buddy Frank "The Giant Frank" Gerner, my French buddy Philippe "Arnie" Arnaudon, my double-date buddies Bruce (Drolen) Hunt and Melany (Hunt) Drolen, my softball buddies Rob Rosen and Steve Stults, my Hunter S. Thompson buddy Joe Weiner, my LA Laker buddy Wing Kot, my misery loves company buddy Lou "LOJO" Terminello, and my Shirley-group buddies (Jane Medhurst, Laisheng and Liquiong Wang , to name a few).

Phil Becker deserves special recognition for the dual distinction of being my closest friend and closest scientific collaborator. You only have to look at the number of citations of his dissertation to understand how important he was to this work. Thanks for everything Phil.

Finally, I would like to offer a special thanks to the people closest to me. My family, especially my mom and dad, Joan and Howard, and my sister Teri, have always supported me through their love in everything I have attempted. My friend and soulmate Jacki has been my inspiration for finishing this dissertation. Without your love Jacki I wouldn't have made it. I love all of you.

Chapter 1

Introduction

Transparent crystals containing trivalent rare earth ions form a unique and interesting class of optical materials. These crystals' optical properties are characterized by absorption spectra which exhibit sharp lines, more reminiscent of gaseous rather than solid state spectra. The sharpness of the spectral lines is a consequence of the electronic structure of the trivalent rare earth ions. The trivalent rare earth ions have electronic configurations consisting of a filled xenon core and a partially filled 4f shell. The optical spectra of the rare earth crystals results from transitions between states of the partially filled 4f shell. This unfilled shell lies inside the filled 5s and 5p shells of the xenon core. The 4f electrons are thus shielded from the influences of the other elements of the crystal. This shielding and the consequent small interaction with the crystal results in the observed sharp line absorption spectra.

It is the unique structure and resulting optical properties that have generated interest in the study of transparent rare earth crystals. For the solid state physicist, these crystals offer a situation in which solid state interactions are small, and may be calculated using perturbative techniques. For technological applications, transparent rare earth crystals have optical properties that can be found in no other solid state system. They have already been used extensively as phosphors (*ie* the red in most color televisions), and as the active medium in solid-state lasers (most notably the Nd^{3+}:YAG laser). Their potential future applications include use as amplifiers in optical communcation networks, optical frequency converters, and optical memory devices. It is with this background of interest that this thesis was undertaken.

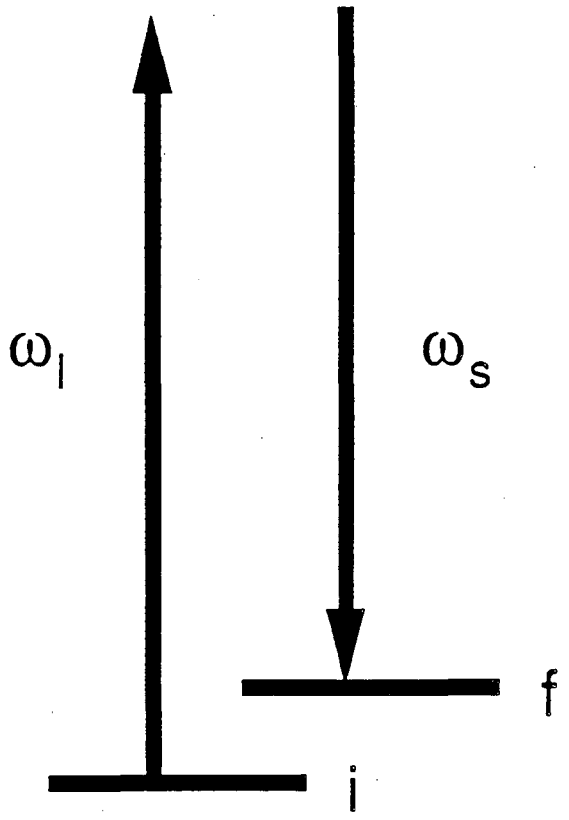

Figure 1.1: Raman scattering process.

This thesis describes the results of experiments on Raman scattering transitions between the electronic states of the [Xe]$4f^N$ configuration of trivalent rare earth ions in transparent crystals. Raman scattering is a process involving the inelastic scattering of light by a material system. Figure 1.1 shows schematically a Raman process. A photon of energy $\hbar\omega_l$ is incident upon the material system and a scattered photon of lesser energy (we are specifically discussing Stokes scattering here) $\hbar\omega_s$ is emitted. The material system, initially in an state i, ends up in an excited state f. Energy is conserved in the process because the difference in the incident and scattered photon energies ($\hbar(\omega_l - \omega_s)$) is equivalent to the change in the energy of the material system ($E_f - E_i$). Most often the excitation is a vibrational mode of the material system. For this work, however, the excitation involves a change in the electronic state of a trivalent rare earth ion.

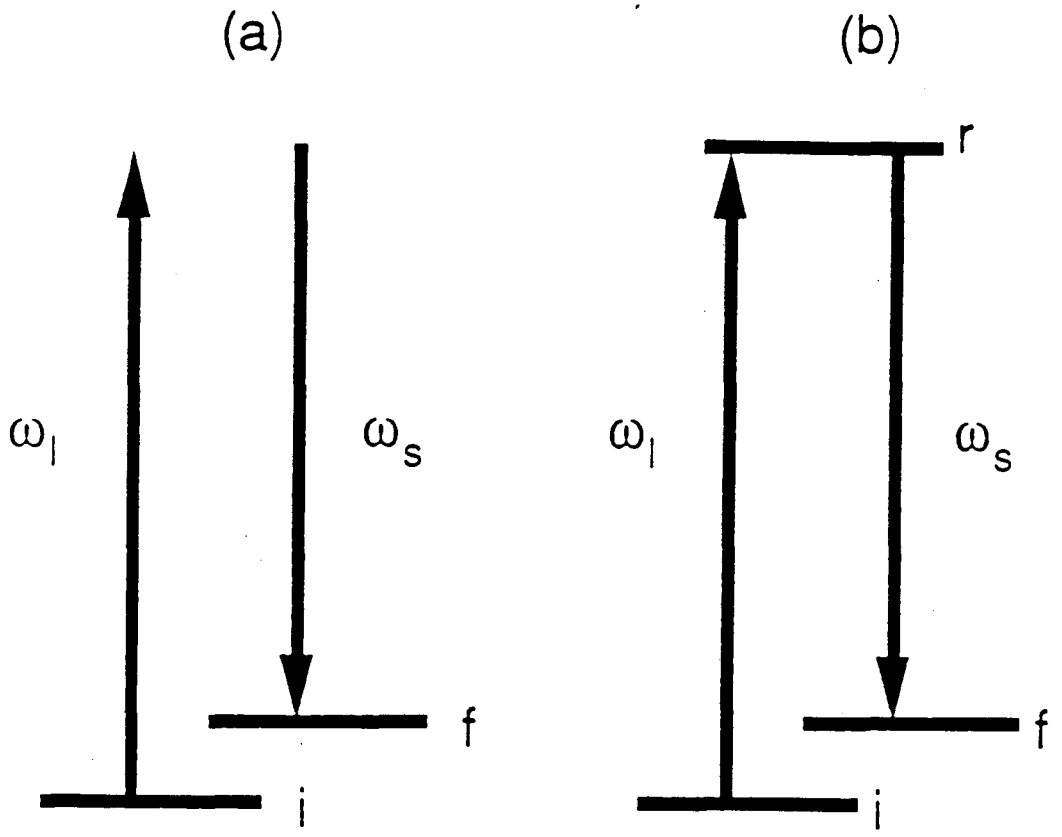

Figure 1.2: (a) Non-resonant Raman scattering. (b) Resonant Raman scattering.

Raman spectroscopy has proven to be a very useful tool for the characterization of materials. In this thesis we use electronic Raman scattering to locate low lying energy levels of the rare earth ions. However, we are most interested in the intensity of the Raman scattered light; how it depends on the nature of the initial and final electronic states, and particularly how it changes as a function of the energy of the incident photon. As the energy of the incident photon approaches the energy difference between states of the material system the Raman scattering intensities are expected to increase. The increased scattering is commonly referred to as resonant Raman scattering. Figure 1.2 contrasts a non-resonant and resonant Raman scattering process.

The study of resonant electronic Raman scattering in transparent rare earth crystals is important in that it lends insight into; (a) the understanding of the intensities of non-

resonant scattering, and (b) the possibilites of resonance enhancement of multiphoton processes in transparent rare earth crystals. This latter point has important implications for the certain device applications in which non-linear optical effects are either desired or need to be avoided.

This thesis has four chapters with the first chapter being this brief introduction. Chapter 2 includes details of the all the experimental work performed for the thesis. Chapters 3 and 4 describe the results of electronic Raman scattering experiments in two different crystal systems, Ce^{3+} in cystal of $LuPO_4$ and Er^{3+} in crystals of $ErPO_4$. These two chapters are self contained and may be read independently of any other part of the thesis with the exception of the experimental chapter.

In Chapter 3 the intensities of electronic Raman scattering from Ce^{3+} ($[Xe]4f^1$) in $LuPO_4$ for both non-resonant and resonant excitation are compared to the values expected by theory. Ce^{3+} was selected for study because its energy level structure; (a) makes for a severe test of the standard theory, and (b) allows for the possibility of a large parity allowed resonance. Chapter 3 includes Appendix B which was added after the completion of this chapter. This appendix includes additional analysis of the Raman and absorption spectra of Ce^{3+}:$LuPO_4$.

In Chapter 4 a formally parity forbidden resonance of electronic Raman scattering in Er^{3+} ($[Xe]4f^{11}$) in $ErPO_4$ is studied. The resonance is interesting in that it is the type most often encountered in transparent rare earth crystals and is an order of magnitude bigger than anything observed previously. A model explains the large resonance and establishes the conditions under which such large resonances may be observed.

Chapter 2

Experimental Aspects

In this chapter we lay out the details of the experimental work supporting this thesis. Overall a number of experimental techniques and setups were employed. The chapter will be organized in much the same way as the thesis, with a section devoted to the experiments involving Ce^{3+} and a section for the Er^{3+} experiments. In addition, there is a section describing the computer data acquisition system common to both sets of experiments. The chapter starts with a general discussion on the crystals used in the experiments.

2.1 The Crystals

2.1.1 Structure

In the course of this work experiments were performed on two systems; Ce^{3+} doped into crystals of $LuPO_4$ and $ErPO_4$ crystals ($ErPO_4$ may be thought of as $LuPO_4$ with 100% doping of Er^{3+}). The crystals were grown by L.A. Boatner and M.M. Abraham [1,2] at Oak Ridge National Laboratory using a flux method [3,4,5]. Details of the crystal structures of $LuPO_4$, $ErPO_4$, and similar crystals may be found in References [5,6,7,8]. We offer here just a brief review of the aspects relevant to our work.

$LuPO_4$ is an insulating crystal with a band gap of approximately 70,000 cm^{-1} [9]. It is uniaxial with a tetragonal zircon type structure (space group D_{4h}^{19}). The unit cell contains four formula units, although a primitive cell may be defined which contains only two formula units. In the doped compounds the rare earth ions substitute for the lutetium. All the Lu^{3+} sites are equivalent. The Lu^{3+} site symmetry is D_{2d}. It

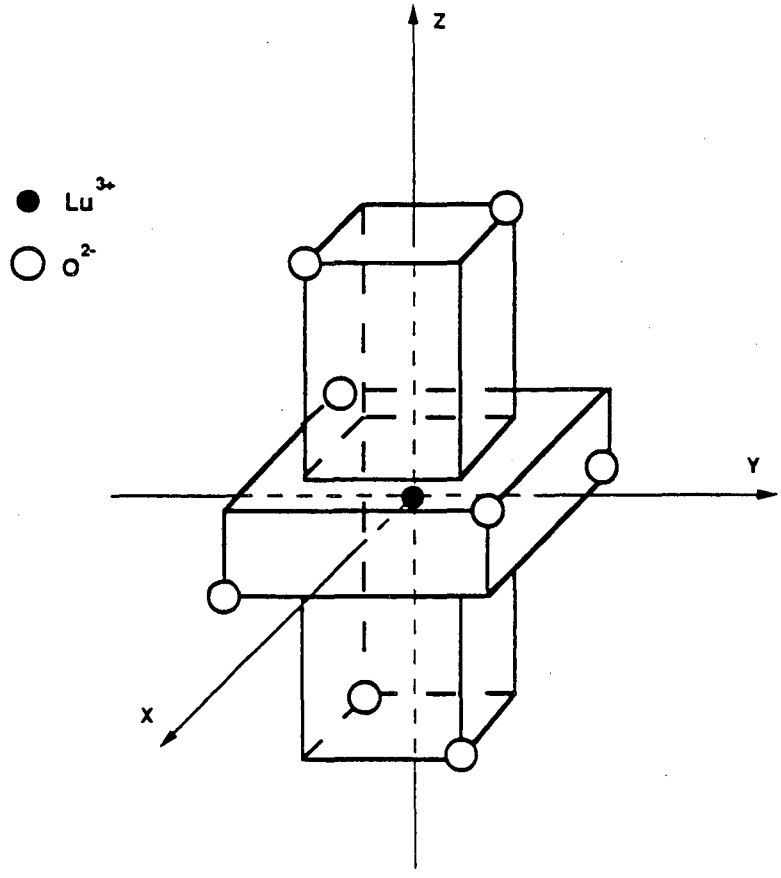

Figure 2.1: Local environment of Lu^{3+} in $LuPO_4$.

is important to note that the reference axes for the crystal symmetry operations are different from the reference axes for the D_{2d} operations. Throughout this thesis, the crystal axes are labelled by upper case x,y,z ($\hat{\mathbf{X}}, \hat{\mathbf{Y}}, \hat{\mathbf{Z}}$) while the D_{2d} axes are labelled by lower case x,y,z ($\hat{\mathbf{x}}, \hat{\mathbf{y}}, \hat{\mathbf{z}}$). $\hat{\mathbf{Z}}$ is the optical axis of the crystal while $\hat{\mathbf{X}}$ and $\hat{\mathbf{Y}}$ are the two equivalent axes. The D_{2d} axes are related to the crystal axes by a rotation of $\pi/4$ about the $\hat{\mathbf{Z}}$ axis. The lutetium ions have eight nearest neighbor oxygen ions. They are arranged in two slightly different size tetrahedras about the lutetium ion. Figure 2.1 from Reference [8] shows this arrangement. The approximate Lu^{3+}-O^{2-} distances are 2.3Å, 2.3Å, 2.3Å, 2.3Å, 2.35 Å, 2.35Å, 2.35Å, and 2.35Å. The next nearest Lu^{3+} ions are at a distance of approximately 3.4Å.

In order to maximize the electronic Raman signals crystals were grown with the

maximum allowable doping levels of rare earth ions. For the later part of the rare earth series (Tb,Ho,Er,Tm,and Yb) the sizes of the trivalent rare earth ions are close enough to the Lu^{3+} size so that substitution may occur without changes to the crystal structure. Doping levels up to 100% are possible. Thus, crystals with 100% doping of Er^{3+} ($ErPO_4$ were used.

However, the size of the trivalent rare earth ions increases as the atomic number decreases. The ions below Tb^{3+} are large enough such that substitution for Lu^{3+} is difficult and crystals with high doping levels can not be grown without a change in the crystal structure. This is particularly true for Ce^{3+}, the largest of the ions. For cerium it was discovered for cerium that if the molar ratio of cerium to lutetium in the starting materials of crystal growth was much greater than 0.20 no tetragonal crystals were grown. Crystals were grown with 1%, 10%, and 20% mole percent of cerium relative to lutetium in the starting materials. X-ray fluorescence analyses [10] showed that the true Ce^{3+} concentrations in the final crystals were much lower, 0.06%, 0.3%, and 0.638%, respectively. This fractional substitution is not expected to occur for the heavy rare earths, such as erbium, for which the there is no significant size mismatch with lutetium.

The crystals that were selected for spectroscopy were all of good optical quality. They had typical dimensions 15 mm × 4 mm × 1 mm. Figure 2.2 shows the shape of a typical crystal along with the crystal axes and the D_{2d} axes. Note that the surfaces defined by the planes $\hat{\mathbf{X}}\hat{\mathbf{Z}}$ and $\hat{\mathbf{Y}}\hat{\mathbf{Z}}$ are smooth while the surfaces defined by the $\hat{\mathbf{X}}\hat{\mathbf{Y}}$ are rough and jagged. It is as result of this that no optical experiments were performed with light incident or scattered along the $\hat{\mathbf{Z}}$ axis.

Some additional important numbers for the $LuPO_4$ (and $ErPO_4$) crystal system are given below in Table 2.1.

2.1.2 Vibrational Spectra

In the Raman experiments scattering to both electronic excitations of the rare earth ions and vibrational excitations of the crystal are observed. Thus, knowledge of the crystal vibrations is of crucial importance since they form the background for our experiments. In addition, the vibrational Raman peaks are used for intensity normalization and to

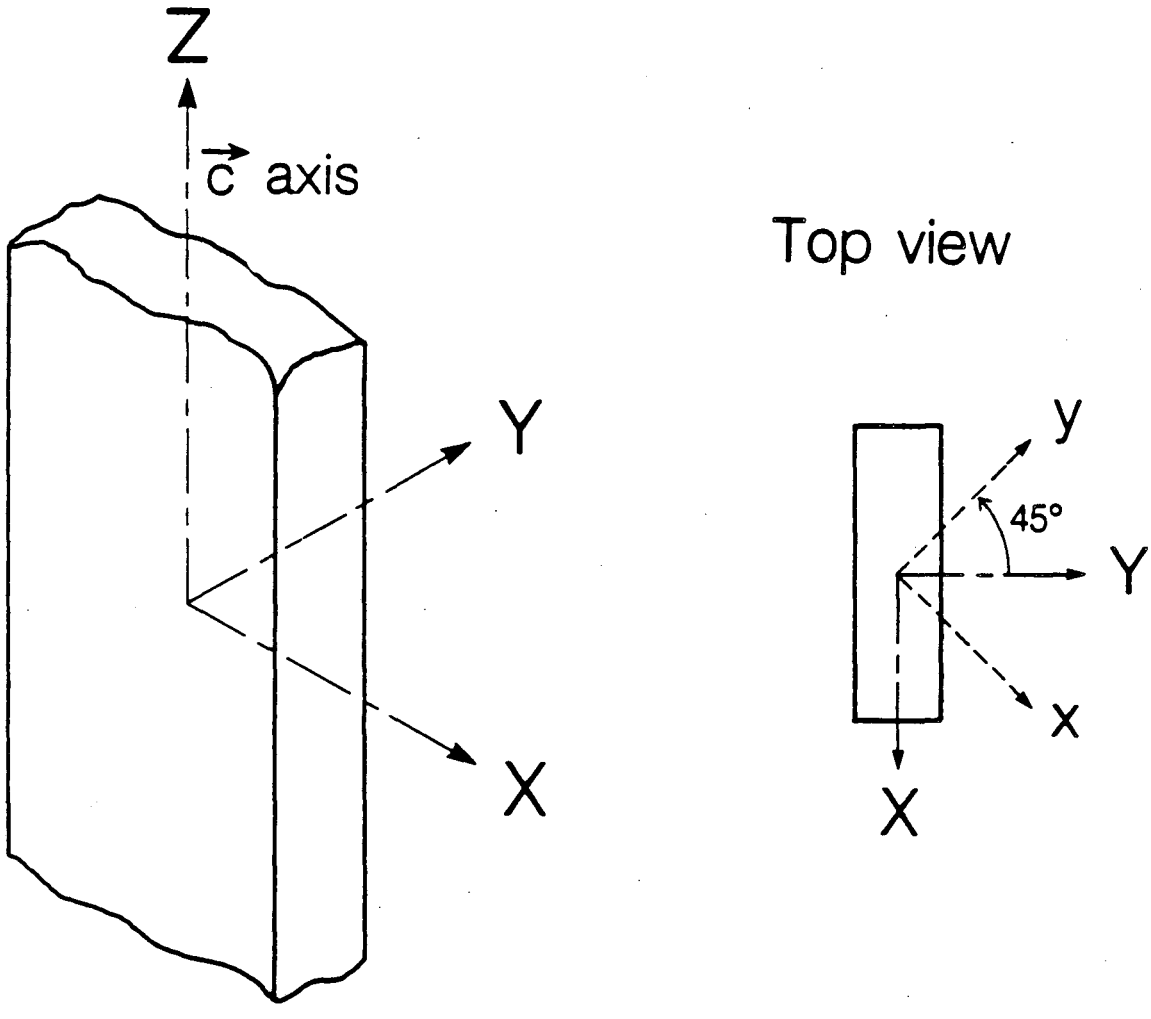

Figure 2.2: Typical sample crystal showing crystal and D_{2d} axes.

	$LuPO_4$	$ErPO_4$
number density of RE^{3+}, cm^{-3}	1.456×10^{22}	1.415×10^{22}
refractive index $n_{X=Y}$	1.728 at 520.8 nm	-
refractive index n_Z	1.694 at 520.8 nm	-

Table 2.1: Some properties of $LuPO_4$ and $ErPO_4$ crystals.

check the integrity of the light polarizations.

For $LuPO_4$ and $ErPO_4$ the primitive cell contains 12 atoms so that there are $3 \times 12 = 36$ vibrational modes, 3 acoustic and 33 optical. Raman processes occur only for symmetric optical modes with $\vec{k} = 0$.The $\vec{k} = 0$ optical modes are classified by the irreducible representations of the factor group of D_{4h}^{19}, D_{4h}. The 33 modes are $2A_{1g} + A_{2g} + 4B_{1g} + B_{2g} + 5E_g + A_{1u} + 3A_{2u} + B_{1u} + 2B_{2u} + 4E_u$. Only twelve of these modes are symmetric and thus Raman active, $2A_{1g} + 4B_{1g} + B_{2g} + 5E_g$. The Raman polarization selection rules for scattering to these modes are given by the scattering tensors shown in Table 2.2 from Reference [11].

The vibrational Raman spectra of the tetragonal phosphate crystals, YPO_4, $HoPO_4$, $ErPO_4$, $TmPO_4$, $YbPO_4$, and $LuPO_4$, have been thoroughly studied by Becker [11]. The energies observed by Becker for the Raman spectra of $ErPO_4$ and $LuPO_4$ are given in Table 2.3. [12] We observe that the vibrational Raman spectrum of Ce^{3+} doped into $LuPO_4$ is no different than the spectrum of pure $LuPO_4$. This probably a result of the low doping levels of Ce^{3+}.

More detailed discussions of the nature of the crystal vibrations are given in Reference [13]. Here we note that the vibrational Raman spectra of these crystals do not change significantly as a function of temperature. Both the line center energies and the linewidths are nearly independent of temperature.

$$A_{1g}: \begin{pmatrix} a & 0 & 0 \\ 0 & a & 0 \\ 0 & 0 & b \end{pmatrix}$$

$$B_{1g}: \begin{pmatrix} c & 0 & 0 \\ 0 & -c & 0 \\ 0 & 0 & 0 \end{pmatrix}$$

$$B_{2g}: \begin{pmatrix} 0 & d & 0 \\ d & 0 & 0 \\ 0 & 0 & 0 \end{pmatrix}$$

$$E_g: \begin{pmatrix} 0 & 0 & e \\ 0 & 0 & 0 \\ e & 0 & 0 \end{pmatrix} \quad \text{or} \quad \begin{pmatrix} 0 & 0 & 0 \\ 0 & 0 & f \\ 0 & f & 0 \end{pmatrix}$$

Table 2.2: Phonon Raman scattering tensors for D_{4h}. Entry ij corresponds scattered light polarized along the i axis and incident light polarized along the j axis. E_g has two tensors because it is a doubly degenerate mode.

	E_g^1	B_{1g}^1	E_g^2	B_{1g}^2	E_g^3	B_{2g}^1	A_{1g}^1	E_g^4	B_{1g}^3	A_{1g}^2	E_g^5	B_{1g}^4
$ErPO_4$	133	140	186	a	303	329	487	579	659	1004	1026	1064
$LuPO_4$	133	140	187	a	307	329	490	583	666	1013	1034	1072

Table 2.3: Energies of the vibrational Raman peaks for crystals of $LuPO_4$ and $ErPO_4$. The B_{1g}^2 phonon is not observed. Its energy is approximated from the Raman spectrum of the isostructural crystal YVO_4 (Reference [12]). All energies are in cm^{-1}.

2.2 Cooling the Crystals

The work in this thesis concerns spectral details associated with the electronic states of rare earth ions in insulating crystals. Much of this detail can be obscured through interaction of the rare earth ion electrons with phonons of the crystal. Cooling of the crystal reduces phonon populations and removes to a large extent the possibility of such interactions. Thus, for most of the experiments performed in the course of this work the sample crystals were cooled to low temperatures (usually near 10K).

The crystal samples were glued to oxygen free copper plates using silver epoxy. The plates were then mounted by screws to the coldfinger of a Janis Supertran cyrostat operated using liquid helium. The intent of this mounting scheme was to maximize thermal contact between the crystals and the cyrostat coldfinger.

The cyrostat has four supersil quartz windows at 90° from each other. The temperature is monitored by a calibrated Si-diode mounted at the base of the coldfinger. The fact that the sensor is not located directly on the sample creates uncertainty as to the actual temperature of the sample. Becker [11] has estimated from the ratio of anti-Stokes to Stokes scattering from a particular Raman transition that an indicated temperature of 4.2K corresponds to a true sample temperature of 5-12K (50 mW of laser power on the crystal). In this work excited state absorption measurements (see Section 4.2.3) show that for near liquid helium temperature the sample temperature is 3 ± 1K higher than the indicated temperature.

The temperature of the sample may be varied by use of a heater coil wrapped around the coldfinger. The current through the coil was controlled by a commercial unit (Lakeshore DRC-80C) which used feedback from the diode temperature sensor. This feature was employed in the excited state absorption experiments of Section 4.2.3.

2.3 Cerium Experiments

2.3.1 Near Ultra-Violet Absorption

Absorption spectra of the $4f^1 \longrightarrow 5d^1$ transitions of Ce^{3+} in $LuPO_4$ were measured. These transitions lie in the approximate energy range of 30,000 cm^{-1} ($\approx$ 333 nm) to 51,000

cm^{-1} ($\approx$ 196 nm). Fortunately, the upper energy is just below the lower limit of the vacuum ultraviolet. The absorption spectra were taken using two experimental setups, depending on the spectral resolution required.

Low resolution spectra were taken using a Cary 17H commercial spectrophotometer. All data were digitized and stored on floppy disks using a LSI-11/2 microcomputer. The slit width of the instrument was usually set such that the spectral resolution was on the order of 100 cm^{-1} ($\approx$ 1 nm). The spectrophotometer was continuously purged with dry N_2 gas to allow observation at energies higher than the O_2 absorption at roughly 50,500 cm^{-1} ($\approx$ 198 nm). The crystal samples were selected for their optical clarity and thiness. The strength of the 4f$\longrightarrow$5d transitions in combination with the high densities of solid state materials make the measured absorptions very large. Absorbances of 100 cm^{-1} or larger were typical. Thus, to keep the transmitted light at measurable levels, crystals were selected with thicknesses well below 1 mm. The crystals were mounted and masked such that any light reaching the detector had passed through the crystal. This is an important consideration when measuring absolute values of absorbance. The Cary 17H is a double beam instrument with the absorption signal being determined by a comparison between the two beams; one passing through the sample crystal and one passing through a reference of the experimenter's choice. For most of our spectra only an aperture that approximated the cross-sectional dimensions of the sample crystal was placed in the reference beam. The only exceptions to this were polarization spectra. Polarized spectra were taken using polarizer sheets which transmitted up to approximately 40,000 cm^{-1} ($\approx$ 250 nm). The polarizer sheets were placed in both the sample beam and the reference beam. Low temperature spectra ($\approx$ 10 K and 77 K) were taken using a Janis Super-Trans coldfinger cyrostat. Details of this cyrostat will be given in the following sections. The smallness and limited accessibility of the Cary's sample area made alignment of the sample when in the cyrostat extremely difficult. As a result of this problem and the limitations on the resolution of the Cary 17H, another experimental setup was used for high resolution spectra.

The high resolution experimental setup duplicates most aspects of the Cary spectrophotometer with improvements in the frequency dispersion component and the ac-

cessibility of the sample. Figures 2.3 and 2.4 show two slightly different versions of the high resolution setup. The two versions cover two separate energy ranges.

Both setups employ a 30 watt D_2 lamp as a light source. The D_2 lamp emits a broad molecular continuum of light in the near ultraviolet peaking in the region of 43,500 cm^{-1} ($\approx$ 230 nm). In addition, there are some strong sharp atomic deuterium lines in the blue and red. All the lenses shown in Figures 2.3 and 2.4 are made of near ultraviolet transmitting supersil quartz. L_1, focal length 5 cm, is used to form a magnification one image of the D_2 lamp on the sample. The sample is mounted on the coldfinger of the Janis-Supertrans cyrostat. The cyrostat has supersil quartz windows. All high resolution spectra were taken at liquid helium temperature. After passing through the sample the light was collected and focussed at infinity by L_2, focal length 5 cm. A Glan-Thompson linear polarization analyzer selected the polarization of interest. The light was then focussed onto the slit of the monochromator by L_3 (focal length 25 cm) which nearly matches the f-number of the monochromator. A polarization scrambler was used to remove the polarization response of the monochromator. The monochromator used was a Spex 1403 double with 1800 groove/mm gratings blazed in the green. The entrance, exit, and two intermediate slits of the monochromator were all set at 200μ.

The problem with this monochromator is that it cannot be operated above 30,000 cm^{-1} due to a limit on the rotation angle of the gratings. Thus, for ultraviolet work it was necessary to operate the monochromator in second-order. However, the first-order spectrum of the deuterium atomic lines appears in the same region as the ultraviolet second-order spectrum. An element was needed which passes ultraviolet light but blocks red and blue light. This is the source of difference in the experimental setups shown in Figures 2.3 and 2.4.

For the low end of the energy range (Figure 2.3) a Hoya 7-54 colored glass filter was used. It passes bands in the near ultraviolet and infrared regions of the spectrum. The ultraviolet band cuts off on the low energy end at approximately 25,600 cm^{-1} ($\approx$ 390 nm), and on the high energy end the transmission begins to roll off steeply at approximately 37,000 cm^{-1} ($\approx$ 270 nm). The infra-red band is low enough in energy not to admit the deuterium red line.

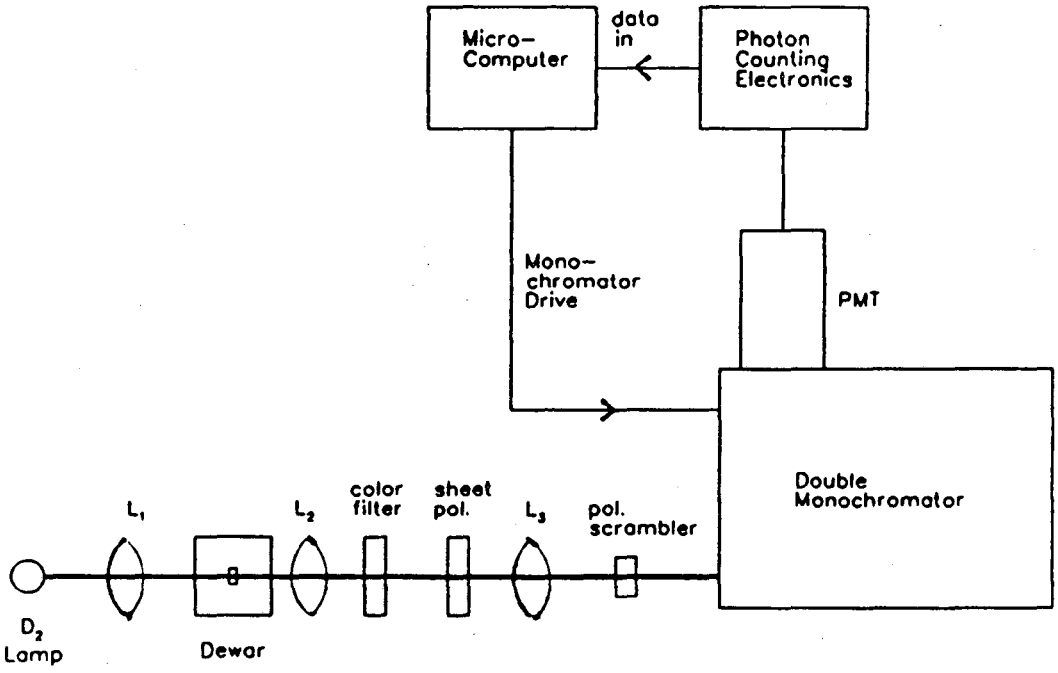

Figure 2.3: Setup for high resolution ultra-violet absorption experiment, range 28,000-37,000 cm^{-1}.

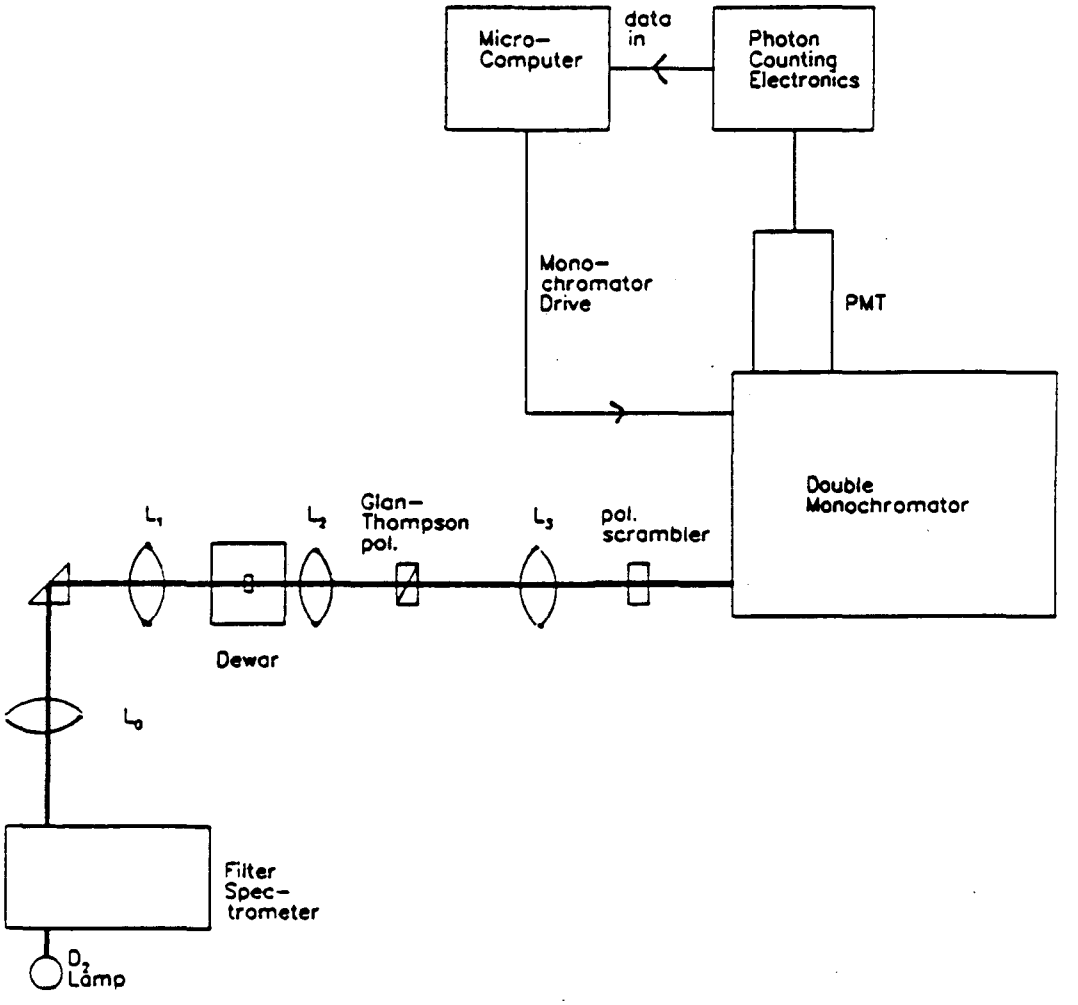

Figure 2.4: Setup for high resolution ultra-violet absorption experiment, range 36,000-44,000 cm^{-1}.

For energies higher than 37,000 cm^{-1} it was necessary to filter the light using a 0.25 m Jarrel-Ash Ebert (Figure 2.4) monochromator. The grating is blazed at 300 nm. The entrance and exit slits are removed to allow a large bandwidth of light to pass. L_0 (focal length 20 cm) keeps the output of the 0.25 m Ebert from diverging too rapidly.

After the light was spectrally dispersed by the SPEX 1403 monochromator it was detected by an RCA C31034 photomultiplier tube. The resulting signal was then quantified by the SPEX DPC-2 photon counting system. A *Digital* LSI-11/2 microcomputer was used to digitize and store the data and scan the SPEX monochromator. Normalization was performed on the computer by dividing all spectra by corresponding spectra taken with the sample removed from the optical path. The spectral resolution of this "high resolution" setup was approximately 1 cm^{-1}.

2.3.2 Electronic Raman Scattering with the CW Laser

The non-resonant electronic Raman scattering experiments reported in Chapter 3 were performed using a continuous wave (CW) argon ion laser as an excitation source. A complete and thorough description of the CW Raman setup can be found in Becker's thesis [11]. Here we will just briefly describe some important aspects of the setup.

The major difficulty in the experiment is detecting the very small electronic Raman scattering signal in the background of potentially a great deal of laser light. The Raman signal and the laser are at different frequencies, but the differences are in general small. Collection of the Raman signal at 90° from the direction of the incident laser beam keeps most of the laser light from entering the detection system, however, a portion significant compared to the Raman signal may be introduced by specular scattering of the beam by imperfections in the crystal surface or bulk. The whole game is increasing the Raman signal while maintaining or reducing the scattered laser light. This is accomplished through:

- Proper preparation of the laser beam through spatial filtering and good focussing on the crystal sample.
- Selection of a sample crystal of good overall optical quality and then interactive selection (during the course of the experiment) of a particular path through the

crystal yielding a high signal-to-noise ratio.

- Use of a double monochromator to discriminate spectrally the Raman signal. The double monochromator has the advantage of a very large stray light rejection ratio. Even if stray laser light enters the monochromator very little of it will reach the detector.

Figure 2.5 from Becker's thesis [11] shows schematically the CW Raman setup. The excitation source used was a *Coherent* CR-8 (8 watts all lines) argon ion laser. The laser was operated in single line mode with spectra being taken at various times using the 514.5 nm (19,429.7 cm^{-1}), 488 nm (20,486.7 cm^{-1}), and 457.9 nm (21,831 cm^{-1}) lines. The non-lasing emission from the argon ion discharge (plasma lines) was filtered from the laser output by passing the beam through a narrow pass interference filter. The laser power was adjusted such that approximately 50 mW of power was incident on the sample. The beam was spatially filtered (creating a *clean* intensity profile) and expanded using the combination of the spatial filter (*Newport Research Corp.* model 900 with .5 cm focal length microscope objective and 25μ pinhole) and lens L_1 (achromatic doublet with a focal length of 14.5 cm). The final beam diameter was approximately 2 cm. This prepared beam was focused onto the sample (mounted in the cyrostat) using lens L_2 which is identical to L_1. In the diffraction limit a focussed beam diameter of approximately 1μ with a depth of field of approximately 10μ (distance over which the beam expands by a factor of 2) is expected. However, Becker [11] found from measurement that true focussed beam diameter was approximately 116μ (in air) while the depth of field was approximately 1000μ (in air).

The scattered light was collected at 90° from the path of the laser by a *Canon* FD 50 mm camera lens, L_3. The sample was located at approximately the focus of the lens. The camera lens is used because (a) it is fast (f/1.3), collecting a large solid angle of the scattered light, and (b) it is achromatic. The collected light leaves the camera lens as a beam of collimated rays approximately 4 cm across. The lens L_4 (achromatic doublet focal length 33 cm) focuses the collected light onto the slit of the monochromator. The lens' focal length was selected so that the monochromator gratings were filled. The

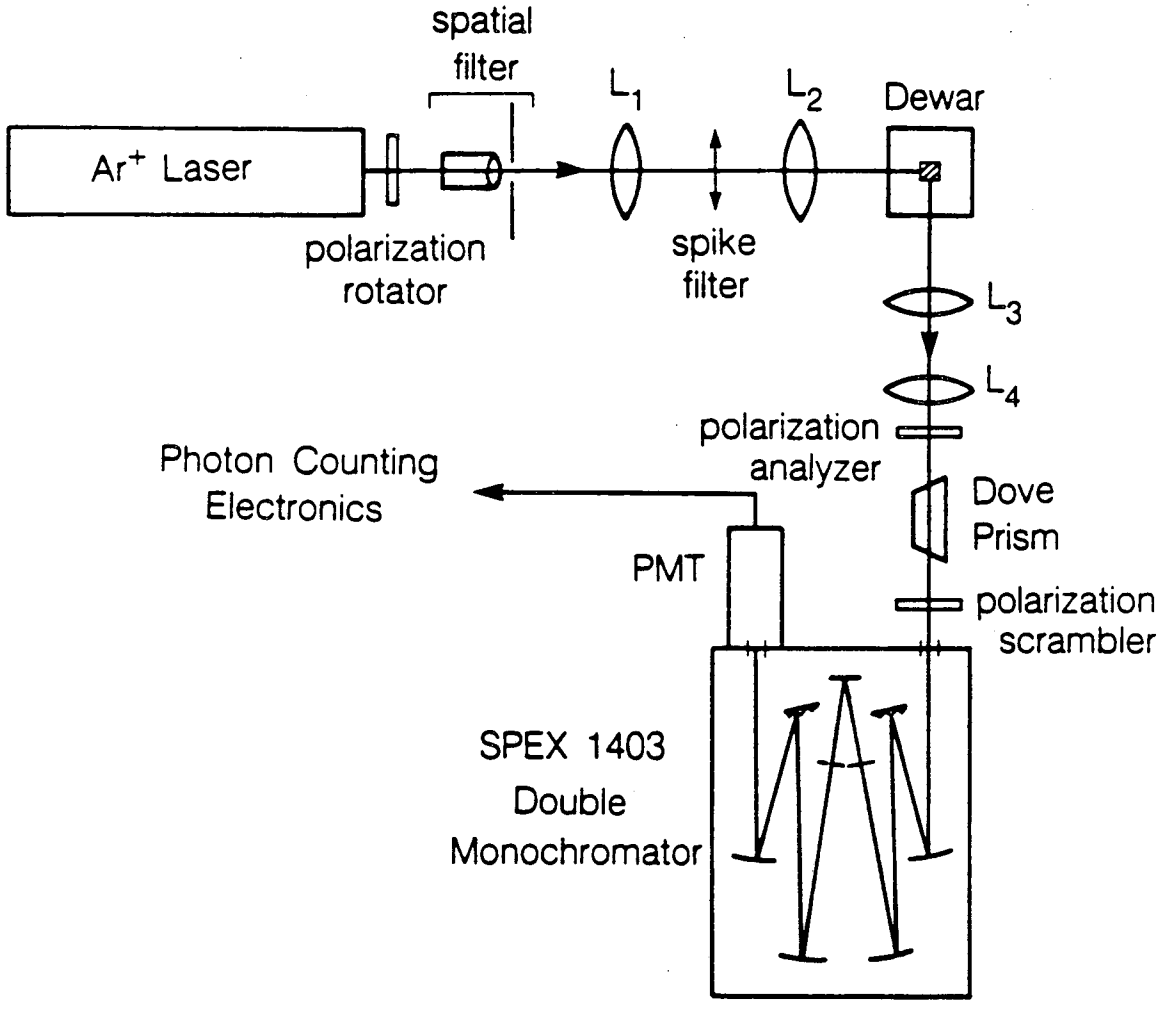

Figure 2.5: CW Raman experimental setup.

collection f-number of the monochromator is 7.8 while the f-number associated with L_4 is $\frac{33\text{ cm}}{4\text{ cm}} = 8.2$, a fairly good match. The overall magnification of the light collection optics (L_3 and L_4) is 6.6.

Before entering the monochromator the light passed through a sheet polaroid (the polarization analyzer), a dove prism, and finally a polarization scrambler. The dove prism rotated the image by 90° so that the long axis of the image of the irradiated region in the crystal was parallel to the slits of the monochromator. The polarization scrambler was used to depolarize the light entering the monochromator eliminating the need to correct for the polarization response of the instrument.

The monochromator used was a SPEX 1403 double monochromator operated with 1800 groove/mm holographic gratings blazed for green light. For most experiments the entrance, exit, and two intermediate slits were set to be 200μ wide. These settings result in a spectral resolution of approximately 2 cm^{-1} for radiation in the visible region of the spectrum. The choice of slit settings is a trade off between spectral resolution and the amount of signal light entering the monochromator. Since the irradiated region in the crystal has a width of approximately 100μ and the magnification of the collection optics is 6.6, we see that a slit width on the order of 600μ would be necessary to admit all the signal light into the monochromator. However, such a slit width is unacceptable in terms of spectral resolution. it was found empirically that the slit width of 200μ resulted in the best spectra.

After being spectrally dispersed by the monochromator the collected light was detected by an RCA C31034 photomultiplier tube biased at 1500 V and cooled to approximately -25° C by a *Products for Research* TE-104 PMT housing. The C31034 PMT offers, high gain (10^6, low dark count (20-30 counts per second), and enhanced red sensitivity. The low dark count is extremely desirable when looking for the inherently small Raman signals. The PMT output signal is quantified SPEX photon counting system. The PMT pulses are converted to digital pulses by a preamp/discriminator and then counted by the SPEX DPC2 (Digital Photon Counter). Raman spectra were recorded in one of two ways. In one procedure the monochromator was scanned continuously by the SPEX Compu-Drive system with output from the DPC2 being recorded on a chart

recorder. In the other method the monochromator was stepped by commands from a *Digital* LSI-11/2 mini-computer to the SPEX Compu-Drive. At each scan point photon counting was performed for a specified length of time by the DPC2 with the results being sent to the LSI-11/2 for storage on a floppy disk. Further details of the computer system are given in Section 2.5.

2.3.3 Electronic Raman Scattering with the Pulsed Laser

Section 3.5 of this thesis describes the resonance enhancement of electronic Raman scattering in Ce^{3+}:$LuPO_4$ as a result of tuning the frequency of the exciting laser radiation closer to the energy of the transitions to states associated with the $5d^1$ configuration of Ce^{3+}. Enhancements were observed when the exciting radiation was changed from the argon ion blue-green lines ($\approx$ 20000 cm^{-1}) to the frequency tripled output of a Nd^{3+}:YAG laser. The energy of the frequency tripled Nd^{3+}:YAG is at 3×9397.17 $cm^{-1} \approx$ 28191.5 cm^{-1}. This excitation energy is close enough to the energies of the transitions $^2F_{5/2}(4f^1) \rightarrow 5d^1(\approx 30000$ $cm^{-1})$ to create significant enhancements of the electronic Raman scattering but still far enough removed to avoid excitation of fluorescence from the $5d^1$ levels. (This actually is only true at cryogenic temperatures. At elevated temperatures the $5d^1$ states are populated through the simultaneous absorption of single 355 nm photons and multiple phonons resulting in strong $5d^1 \rightarrow 4f^1$ fluorescence).

Figure 2.6 shows the setup for the experiment. The laser used was a *Quanta-Ray* DCR-1 Q-switched Nd^{3+}:YAG laser. The laser was operated at a repetition rate of 10 Hz. The temporal width of each pulse is approximately 10 ns. The 1064 nm output of the Nd^{3+}:YAG is passed through a KD*P (deuterated potassium di-phosphate, $KD_2(PO_4)$) converting a certain portion of the beam into radiation at the second harmonic wavelength 532 nm. The 532 nm output and the remaining 1064 nm radiation are then passed through a second KD*P crystal generating the sum frequency, the desired third harmonic of the 1064 nm radiation, at approximately 355 nm (28,191.5 cm^{-1}). Both KD*P crystals are mounted in the *Quanta-Ray* SHG unit which is equipped with a provision for fine tuning of the attitude of the crystals. This adjustment is necessary for optimization of the phase-matching between the input and generated waves. The third

harmonic output is linearly polarized. It has a donut shaped cross-section (characteristic of the 1064 nm output) with a diameter of approximately 1 cm.

The output beam is passed through the *Quanta-Ray* PHS (prism harmonic separator) unit which separates spatially the 355 nm radiation from the remaining unconverted 1064 nm and 532 nm radiation. As the name of the unit implies this is accomplished through the use of a number of prisms including a dispersive Pellin-Broca. The PHS also contains an easily insertable $\frac{\lambda}{2}$ plate for the 355 nm radiation. This was used to rotate the polarization of the 355 nm light when desired.

The 355 nm light was focused onto the sample (mounted in the cyrostat) by lens L_1, a 15 cm focal length lens made of near ultraviolet transmitting supersil quartz. At high intensities of the focused light the crystal sample was visibly damaged (see Section 3.5). The damage threshold was observed to be approximately 0.3 milli-joules per pulse in conjunction with the tightest focusing possible from lens L_1. Raman spectra were always taken with excitation below this damage threshold.

The elements of the scattered light collection system are very similar to those used in the CW experiments but with the necessary replacement of the glass optics with optics made of materials with improved ultraviolet transmission. Lens L_2 and L_3 are made of supersil quartz and have focal lengths of 5 cm and 30 cm, respectively. The sheet polaroid polarization analyzer of the CW experiment is replaced by a Glan-Thompson prism polarizer made of calcite. The polarization scrambler is the same as used in the CW experiment.

The collected light was spectrally dispersed by the SPEX 1403 monochromator equipped with the same gratings as used in the CW experiments. The efficiency of each of these gratings drops from approximately 65% for green light to approximately 40% for violet-ultraviolet light. The dispersed light is detected by the RCA C31034 PMT which operates as efficiently in the violet-ultraviolet region as in the green with the replacement of the standard glass input window with one made of supersil quartz. Care was taken to insure that the scattered light intensities on the PMT were not so great as to saturate its response. A linearity check was made between the energy per pulse of the exciting radiation and the resulting Raman pulse intensities.

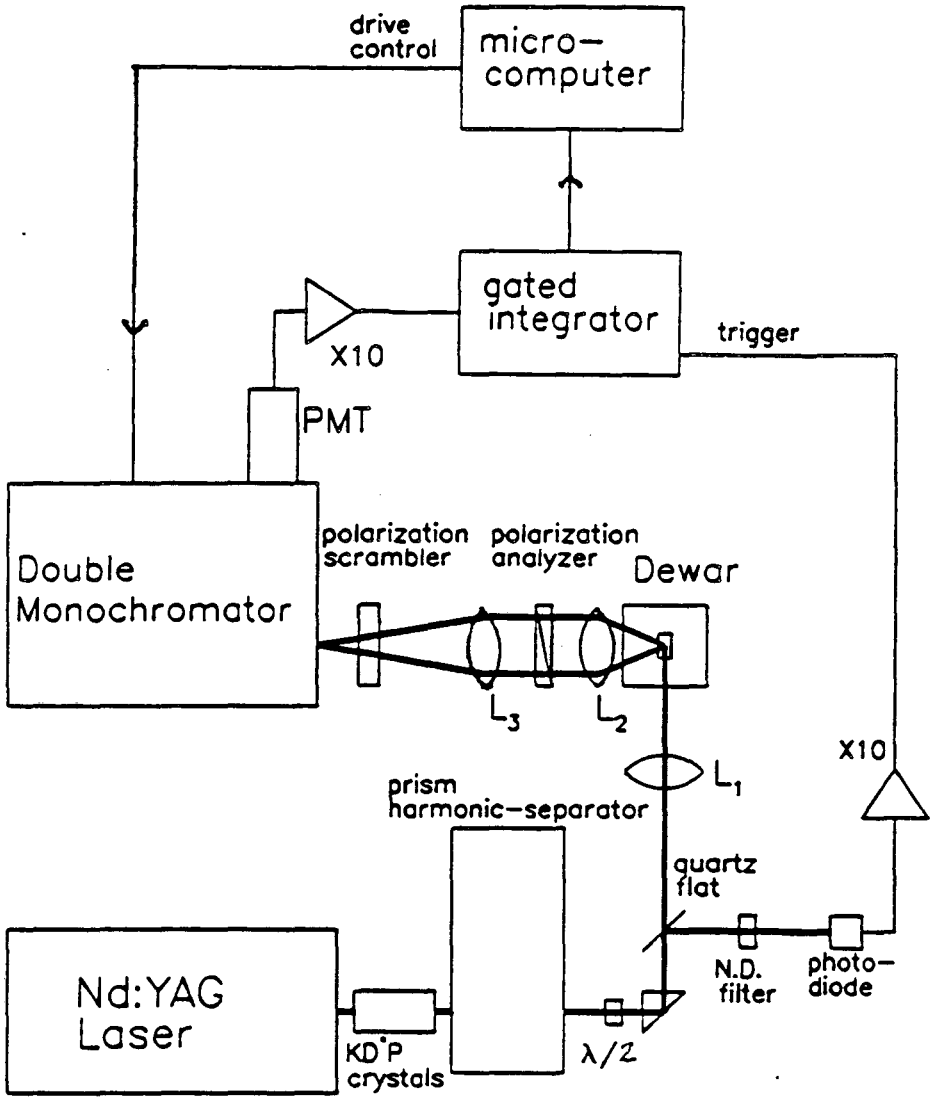

Figure 2.6: Experimental setup for taking pulsed Raman spectra. Laser excitation frequency is approximately 28,191.5 cm^{-1}.

The signal from the PMT is a series of current pulses at a repetition rate of 10 Hz, each with a temporal duration of approximately 20 ns. The Raman intensity associated with a given shot is proportional to the area under the associated signal pulse. For quantification of such a signal the photon counting system used in the CW experiments is no longer viable since all the Raman photons arrive in near temporal coincidence every tenth of a second. Such a signal is ideally suited for quantification using a gated integrator (boxcar). When triggered the boxcar samples the signal for a time window or gate selected by the operator. During this time window the device integrates the signal and stores the information in something akin to an RC network. Different time constants for the storage RC network may be selected changing the number of successive signal pulses accumulated in the RC network. In effect this allows the experimenter to average the signal over a pre-determined number of laser shots. During the course of this experiment two different boxcars were used. The devices were different enough in capability that they were operated in slightly different ways.

The earlier experiments were carried out using a E G& G *Princeton Applied Research* (PAR) Model 162 boxcar averager with a Model 165 gated integrator. The signal was obtained from the PMT and immediately passed through a *LeCroy* $\times 10$ fast current amplifier. The current amplifier helped prevent temporal spreading of the signal pulse as it passed through the approximately 3 meters of coaxial cable to the boxcar input. The input of the boxcar was terminated in a resistance of 50Ω to roughly match the impedances of all previous components in the electronics (PMT, amplifier, and cable). The boxcar was triggered externally by the variable synchronization output of the Nd^{3+}:YAG laser. This synchronization output is useful in that it may be set by the experimenter to fire at anytime during the 500 ns before or 100 ns after the firing of the laser Q-switch. The PAR boxcar requires a 75 ns "wake up" time after triggering, so it was necessary to employ the pre-triggering capability of the variable synchronization output. The boxcar was typically set to sample the signal for a time window of 10 ns. The position of the 10 ns window was selected by controls on the boxcar to maximize the boxcar output. The RC time constant was set to average over anywhere from 10 to 100 laser shots depending on the noisiness of the data. Actual spectra were taken by scanning the monochromator

to a given frequency (using the LSI-11/2 microcomputer), waiting the appropriate time for averaging (*i.e.* 10 sec for 100 shots), passing the analog output of the boxcar to the LSI-11/2 for digitization and storage on floppy disk, and then repeating. Details of the computer interface may be found in Section 2.5.

In later experiments a *Stanford Research Systems* (SRS) SR250 gated integrator with accompanying SR235 analog processor and SR280 powers supply and display module were used. The signal was passed from the PMT to the boxcar in the manner described previously. The SRS boxcar has a shorter "wake up" time, 25 ns. This simplified the triggering allowing triggering off the laser light pulse itself (without the use of long delay lines for the PMT signal). This was beneficial in that Nd^{3+}:YAG variable synchronization output although in general stable occasionally became very sporadic (for still unknown reasons). The light triggering was accomplished by positioning a EG&G SGD-100A fast silicon photodiode biased at -90 V such that some of the 532 nm light from the harmonic generation process was incident upon it. The resulting signal was used to trigger the boxcar. Again typically a 10 ns sampling window was used on the boxcar. However, the signal was not averaged over a number of shots using the boxcar. The SRS boxcar was used more like a *sample and hold* device in which the signal from one shot at a time was stored and then passed to the LSI-11/2 microcomputer for digitization. Averaging of the data over successive shots was then performed on the computer and stored on floppy disk. Such a arrangement was much easier to setup on the SRS than the PAR and yielded results with significantly better signal to noise. Again details of the computer interface can be found in Section 2.5.

2.4 Erbium Experiments

2.4.1 Visible Absorption

In Section 4.2.3 oscillator strengths and line-widths for transitions between crystal field levels of the $^4I_{15/2}$ and $^4F_{7/2}$ multiplets of Er^{3+} in $ErPO_4$ and YPO_4 are given. These quantities were determined from absorption spectra taken using a pulsed dye laser as a light source. Figure 2.7 shows the experimental setup used.

The light source was the *Quanta-Ray* PDL-1 pulsed dye laser operated with *Exciton*

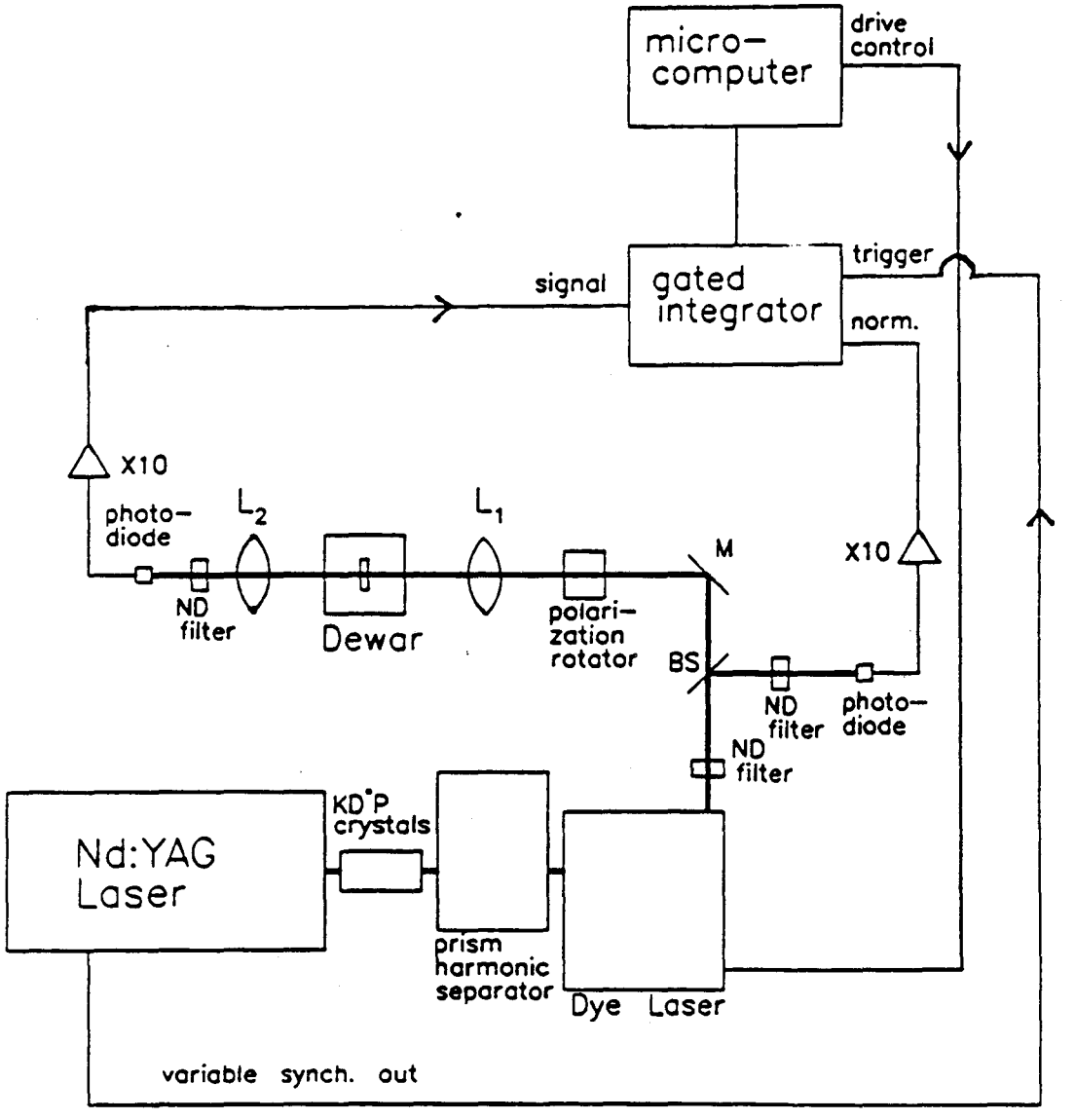

Figure 2.7: Experimental setup for taking the absorption spectra of Er^{3+} in $ErPO_4$ and YPO_4.

Coumarin 500 (tuning range 470 nm - 580 nm, peak response 500 nm) laser dye. The PDL-1 was pumped by the frequency tripled output of the *Quanta-Ray* Nd^{3+}:YAG laser. The PDL-1 consists of three stages; an oscillator, a pre-amplifier, and a amplifier. The oscillator is basically a Hänsch type. It consists of a side-pumped flowing dye cell inside a cavity with a partially transmitting output mirror and a telescope expander illuminating a grating acting as the back reflector. The grating serves as the frequency selective element. The line-width of the output beam is nominally between .25 cm^{-1} and .5 cm^{-1}. The dye cell is oriented at a Brewster angle (along with the pre-amp. and amp. dye cells) so that the output beam is linearly polarized. The pre-amplifier and amplifier stages are both side-pumped flowing dye cells down beam from the oscillator. They are not in laser cavities and serve as single pass amplification devices for the output of the oscillator. The system may be operated either with or without the pre-amp. The amplifiers increase power greatly but also introduce a great deal of *amplified spontaneous emission* (ASE). ASE results generally from false laser cavities in the optical path and appears as a broadband output across the entire gain curve of the particular dye in use. For the absorption experiments large output power was not needed so the PDL-1 was operated with the pre-amp. removed.

Indeed care was taken in the absorption experiments to insure that the laser power on the crystal was small enough to avoid undue heating of the sample or saturation of the absorptions. When operated at powers too close to threshold the PDL-1 output is very noisy so that most of the power reduction was accomplished through the use of neutral density filters (ND).

The appropriately attenuated laser beam passed first through a double rhomb polarization rotator which allowed continuous control over the polarization. The beam then passed through the crystal (mounted on the cold-finger of the *Janis* cyrostat) with the amount of transmitted light being measured by a EG&G SGD-100A fast silicon photodiode. Lens L_1 and L_2 were both achromats with 15 cm focal lengths. L_1 was used to insure the entire laser beam passes through the crystal. The focus of L_1 was intentionally placed outside the crystal to avoid high intensities which could lead to saturation. L_2 re-focused the beam so that it could be measured by the photodiode. The neutral density

filter (ND) in front of the photodiode prevents saturation of the photodiode response.

Before the laser beam passed through the crystal a a small portion (4%) was picked off by a "wedged" glass slide (BS) and detected by another SGD-100A photodiode. The signal was used for normalization. The "wedged" slide was important to prevent etalon effects resulting from interference between reflections off the two surfaces.

Both the transmitted light signal and the normalization light signal were amplified by *LeCroy* 101B ×10 fast current amplifiers and passed to two separate PAR Model 165 gated integrators mounted inside a PAR 162 boxcar averager. Gates were set typically at 10 ns and averaging was done over 10-100 laser shots. The integrators were triggered by the variable synchronization output of the Nd^{3+}:YAG. The *Digital* LSI-11/2 microcomputer was used to digitize and store the transmission and normalization channel data and tune the PDL-1 dye laser (through the *Quanta-Ray* MCI-1 interface). All normalization and mathematical manipulation was then performed on the computer at a later time. Details of the computer system are given in Section 2.5.

2.4.2 Electronic Raman Scattering with the Pulsed Dye Laser

The subject of Chapter 4 of this thesis is resonance enhancement of electronic Raman scattering in $ErPO_4$. Figure 2.8 shows schematically the experimental setup for measuring the intensity of electronic Raman scattering as a function of excitation frequency. Basically the setup can be divided into sections or components that have been described previously in this Chapter. The excitation source was the *Quanta-Ray* PDL-1 pulsed dye laser operated with Coumarin 500 laser dye, just as with the absorption experiments described in the previous Section. The optics used to focus the laser light onto the sample (lens L_1) and the scattered light collection optics are the same as were used for the CW Raman experiments, described in Section 2.3.2. The monochromator, PMT, and gated detection electronics are the same as used in the pulsed Raman experiments, described in Section 2.3.3. The additional element of this setup not described previously is the ASE filter shown in Figure 2.8. ASE is the broadband output (across the dye gain curve) of the pulsed dye laser and presents the major experimental problem for these measurements.

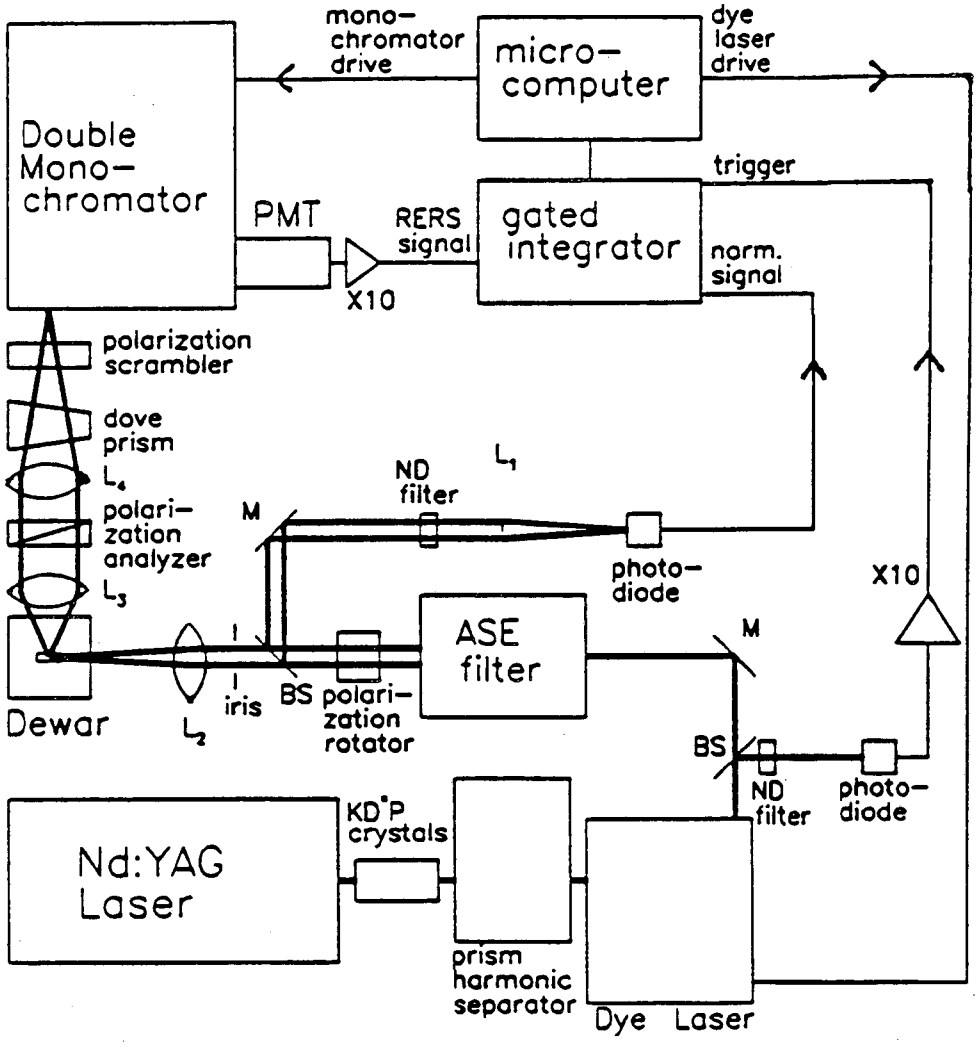

Figure 2.8: Experimental setup for resonance Raman scattering in $ErPO_4$.

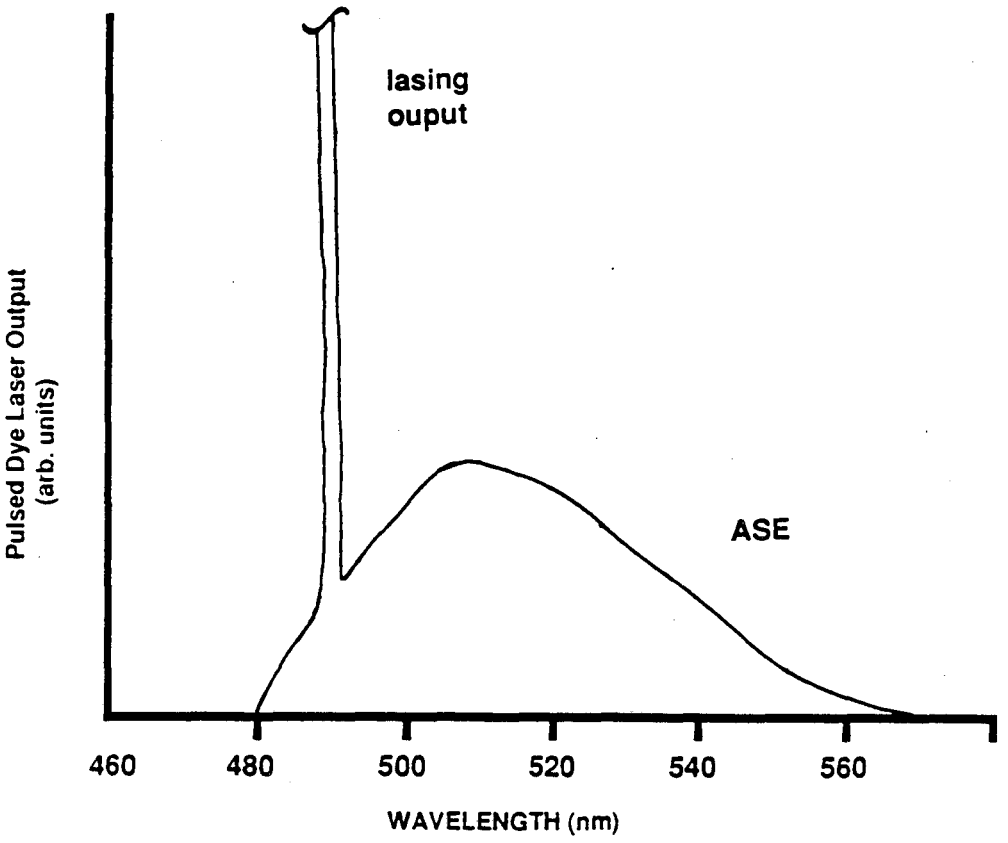

Figure 2.9: Typical output for the PDL-1 pulsed dye laser operated with Coumarin 500 laser dye.

Figure 2.9 shows the spectral output for Coumarin 500 in the PDL-1 pulsed dye laser with an intensity spike at the lasing frequency selected by the grating back reflector ($\approx$488 nm in this case) and the broad ASE background across the entire Coumarin-500 gain curve. Typically the total integrated intensity of the ASE is only about 1-5% of the intensity of the laser peak (for a properly adjusted laser). However, the ASE still presents a major problem in our measurements for the following reason. ASE is present in the output of the pulsed dye laser and is passed down the optics of the experimental setup. When the ASE is incident on the sample, and a small portion is scattered by crystal imperfections into the Raman collection optics. We are looking for a small electronic Raman scattering signals shifted only 33 and 53 cm^{-1} from the laser frequency. Clearly the ASE is present in the frequency region of interest and even though small (especially considering we only look at a small bandwidth of light with the monochromator) is still large enough to swamp the extremely small electronic Raman signals. Thus, removal of the ASE is a requirement for the success of the experiment.

The following steps were taken to drastically reduce the ASE.

- Alignment of the pulsed dye laser components can greatly effect the amount of ASE outputted. A most crucial adjustment is the overlap of the optically pumped regions in the amplifier and pre-amplifier dye cells and the optical path of the laser output from the oscillator. Proper alignment was accomplished interactively by observing simultaneously the ASE output and the lasing frequency output. The two components were spectrally separated using a 0.25 m J-Y monochromator.

- Spatial filtering of the output beam helps to eliminate a portion of the ASE. However, diffraction limited spatial filtering of the pulsed dye laser beam is difficult because of; (a) the poor optical quality of the laser beam (divergent and with a poor radial intensity profile) and (b) the high peak powers involved. Thus, the spatial filtering employed consisted of simply an iris adjusted to allow the central portion of the laser beam through but blocking the light spray outside. This yielded only limited reduction in the ASE.

- The crucial element in removing the ASE is the so-called ASE filter (see Figure 2.8). The ASE filter consists of a 0.25 m J-Y monochromator with accompanying optics. Figure 2.10 shows the optical elements of the ASE filter in detail. The combination of lens L_1 (-2.5 cm focal length concave lens) and L_2 (25 cm focal length) act as inverse telescope to expand the laser beam by a factor of 10 to a diameter of approximately 3 cm. The purpose of this is to fill the grating of the 0.25 m monochromator, improving spectral resolution and preventing damage to the optical elements of the monochromator. Lens L_3 (focal length 20 cm) focuses the expanded beam onto the monochromator entrance slit. The monochromator is a J-Y H-20 0.25 m. It has a holographic grating with 1200 grooves/mm. The linear dispersion of the grating is 4 nm/mm ($\approx$160 cm^{-1}/mm at 500 nm). The entrance and exit slits were .5 mm wide resulting in a bandpass of 80 cm^{-1} (40 cm^{-1} on each side of the central frequency). The monochromator was tuned to a frequency just slightly higher than the laser frequency, still allowing a large portion of the laser light through but decreasing the band pass on the low frequency side

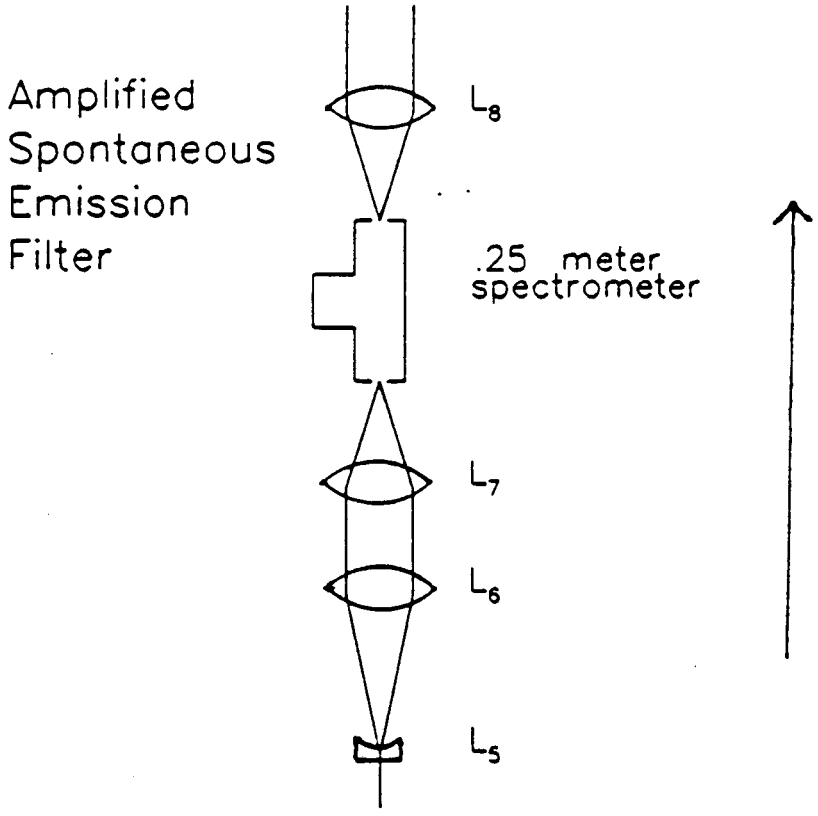

Figure 2.10: Amplified spontaneous emission (ASE) filter.

of the laser from 40 cm^{-1} to approximately 15-20 cm^{-1}. This allowed for ASE free observation of both the 33 and 53 cm^{-1} lines. Lens L_4 (focal length 20 cm) is used to recollimate the light emerging from the 0.25 m monochromator. The major drawback with this system was that it was fairly lossy. With 20 milli-joules/pulse of laser energy emerging from the dye laser at 488 nm only about 2-3 milli-joules/pulse were finally incident on the sample.

There were basically two different ways by which electronic Raman intensity vs. excitation frequency data were obtained. The most straight-forward but also most time-consuming method involved the following steps. The dye laser was tuned manually to some excitation frequency. The 0.25 m monochromator was adjusted in the manner described above. The consistency of this adjustment was checked by examining how cleanly the beam passed through an iris located approximately 3 meters down line from the 0.25 m monochromator. Once all these adjustments were made the SPEX 1403 was scanned yielding a complete Raman spectrum for that particular excitation frequency. The intensities could be measured directly from the spectrum. Then the dye laser was tuned to a new excitation frequency and the entire procedure was repeated.

The other method used was much quicker to perform but had the problems of added complexity and greater uncertainty in the results. The dye laser was adjusted to some excitation frequency. The 0.25 m monochromator was adjusted as described above. The SPEX 1403 was set to either the (laser frequency - 33 cm^{-1}) or (laser frequency - 53 cm^{-1}). Then both the dye laser and the SPEX 1403 were scanned simultaneously at the same rate (controlled by computer) with the resulting signal (electronic Raman intensity vs. excitation frequency) being recorded. The 0.25 m monochromator tuning remained fixed. Both the laser and the SPEX 1403 were scanned to lower frequencies so that the ASE at (laser frequency - 33 cm^{-1}) and (laser frequency - 53 cm^{-1}) was always blocked by the 0.25 m monochromator. Typically the scanning was done over a range of 10 cm^{-1} and then the system was reset to another excitation frequency and the procedure was repeated. During the course of a 10 cm^{-1} scan the power incident on the sample typically dipped by about 30% as the laser frequency moved farther away from the tuned frequency of the 0.25 m monochromator. To account for this reduction in incident power

a fraction of the beam exiting the 0.25 m monochromator was split off and detected by a EG&G SGD-100A photodiode. The resulting signal was used to normalize the electronic Raman results. The other problem with this method was whether the optical alignment of the laser beam on the sample changed sufficiently during the scanning procedure to affect the results. We believe that the results are not affected by the scanning for the following reasons. The alignments of the beam, as monitored by passage through an iris 3 m down line from the 0.25 monochromator, does not change. Excitation profiles for processes that are expected to have flat responses (*ie* phonon Raman) did indeed yield flat responses using this method. The excitation profiles obtained using this method agreed with data obtained by taking complete Raman spectra one at a time for each excitation frequency.

2.4.3 Lifetime Measurements

Lifetime measurements were taken by using pulsed excitation (from the PDL-1 pulsed dye laser) and monitoring the signal from the sample as a function of the boxcar gate's temporal position. The PAR boxcar was used for all lifetime measurements. The gate position of the PAR was easily controlled by application of voltages between 0-10 V. These voltages were applied through computer control.

Figure 2.11 shows the temporal response of the pulsed detection system excited by the nominally 7 ns PDL-1 output. The pulsed detection system includes the RCA C31034 PMT and the *LeCroy* 101B fast current amplifiers both of which have rise and fall times on the order of 2-4 ns. The BNC RG-58U coaxial cable used to transfer the signal to the boxcar also contributed to the final pulse shape.

2.5 Computer System

Most of the experiments described in the earlier sections of this chapter have relied on a computer for data acquisition, data storage, and control of the experimental apparatus. The used was the *Digital Equipment Corp.* (DEC) LSI-11/2 (RT-11 operating system). The LSI-11/2 communicated with the experimental apparatus through a number of different interface boards. The interface software was written in Fortran IV and the

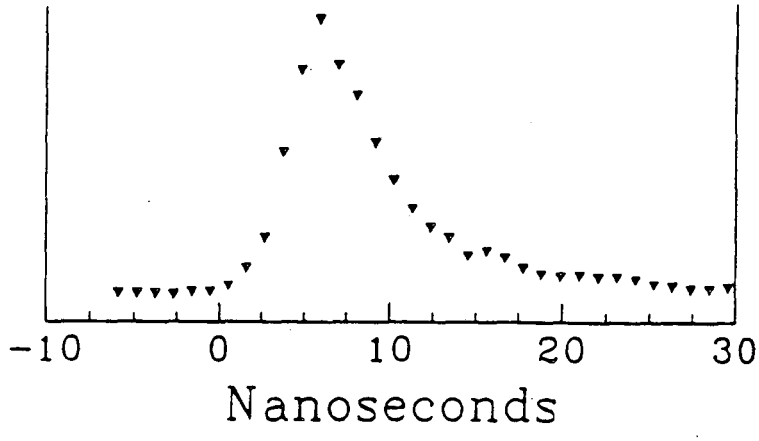

Figure 2.11: Temporal response of the pulsed detection system after excitation by a PDL-1 pulsed dye laser.

LSI-11/2 (RT-11) assembly language, MACRO II. The Fortran routines were used for operator input of the experimental parameters and writing acquired data to storage devices while the assembly language routines were used for communicating with the interface boards. All acquired data was stored on 512K byte floppy disks and then later transferred to one of LBL's DEC VAX 11/780 computers for analysis and plotting.

In the following subsections we give brief descriptions of the computer control of the different experiments.

2.5.1 CW Experiments, Absorption and Raman

Figure 2.12 shows the configuration of the computer system used in the near ultraviolet high resolution absorption (Section 2.3.1) and CW Raman (Section 2.3.2) experiments. For these experiments the computer system does basically two things; tunes the SPEX 1403 monochromator and records the data from the SPEX DPC-2 photon counter. This is accomplished very simply. An ADAC 1604/POC pulse output controller is directed

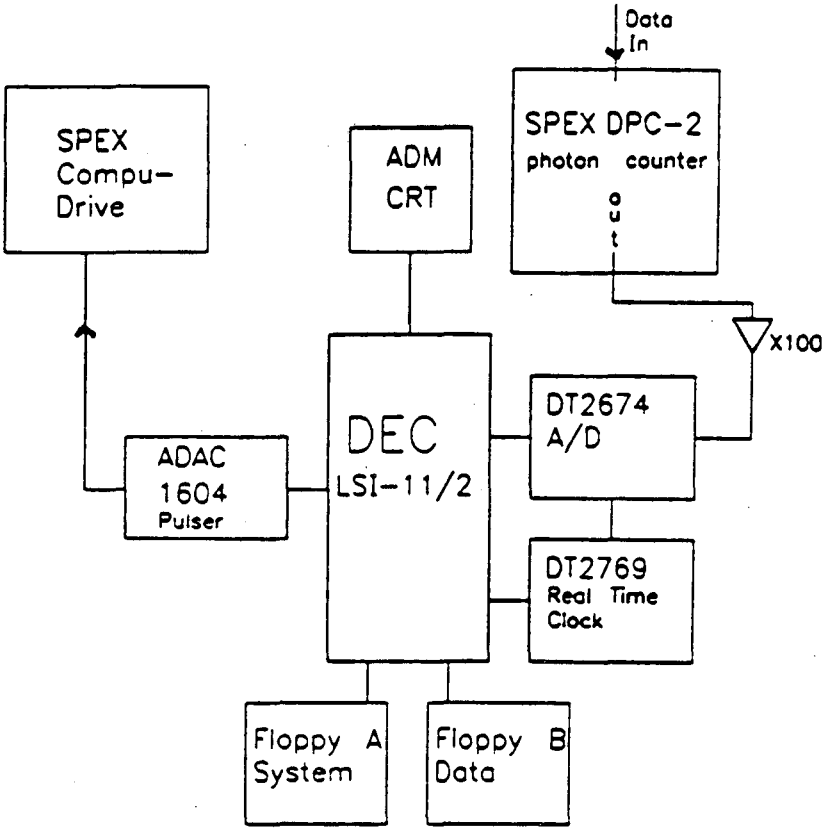

Figure 2.12: Computer configuration for near ultraviolet high resolution absorption and CW Raman experiments.

by program control to send the appropriate number of pulses to the external oscillator input of the SPEX Compu-Drive in order to tune the SPEX 1403 monochromator the operator selected step size. The ADAC 1604/POC is hardware configured to deliver a pulse train readable by the SPEX Compu-Drive (< 5 Vdc, < 500 Hz rep.rate, and > 10 μs individual pulse length). Once the pulse steps are completed, a *Data Translation* DT-2769 programmable real time clock (RTC) is directed to count down an operator selected amount of time allowing enough time for the SPEX 1403 to finish its scan and for the DPC-2 photon counter to perform averaging over the appropriate time. When the RTC counter has run down it triggers a *Data Translation* DT-2674 analog-to-digital converter (A/D) to convert the chart recorder output of the DPC-2. The chart recorder output, between 0-100 mV, is amplified by a factor of approximately 100 before conversion to take full advantage of the dynamic range of the DT-2674 (0-10 V). Once converted the signal is stored in memory and then written to a floppy disk. In addition, the data are immediately displayed on an ADM CRT terminal for viewing by the operator. The

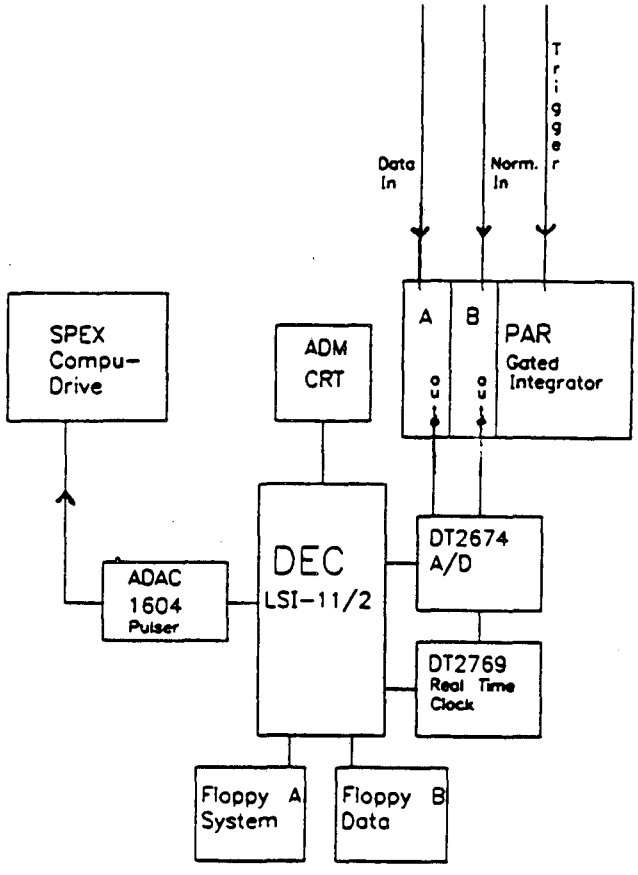

Figure 2.13: Computer configuration for taking pulsed Raman spectra using the PAR boxcar averager.

whole procedure is then repeated starting with the tuning of the monochromator.

2.5.2 Pulsed Raman Spectra

As discussed previously pulsed Raman spectra (Sections 2.3.3 and 2.4.2) were taken over the course of this work using two different types of boxcar averagers. The corresponding setups employed slightly different computer configurations for data aquisition.

Figure 2.13 shows the computer configuration used with the PAR boxcar. The tuning of the monochromator is done as described previously. After tuning the DT-2769 RTC counts down allowing the PAR boxcar to average over the boxcar RC time constant selected by the operator. After the RTC has counted down the DT-2674 A/D is flagged for conversion of the boxcar output; first the data channel and then the normalization channel. The results are written to memory and displayed on the ADM terminal. The whole procedure is then repeated.

Figure 2.14 shows the computer configuration used with the SRS boxcar averager.

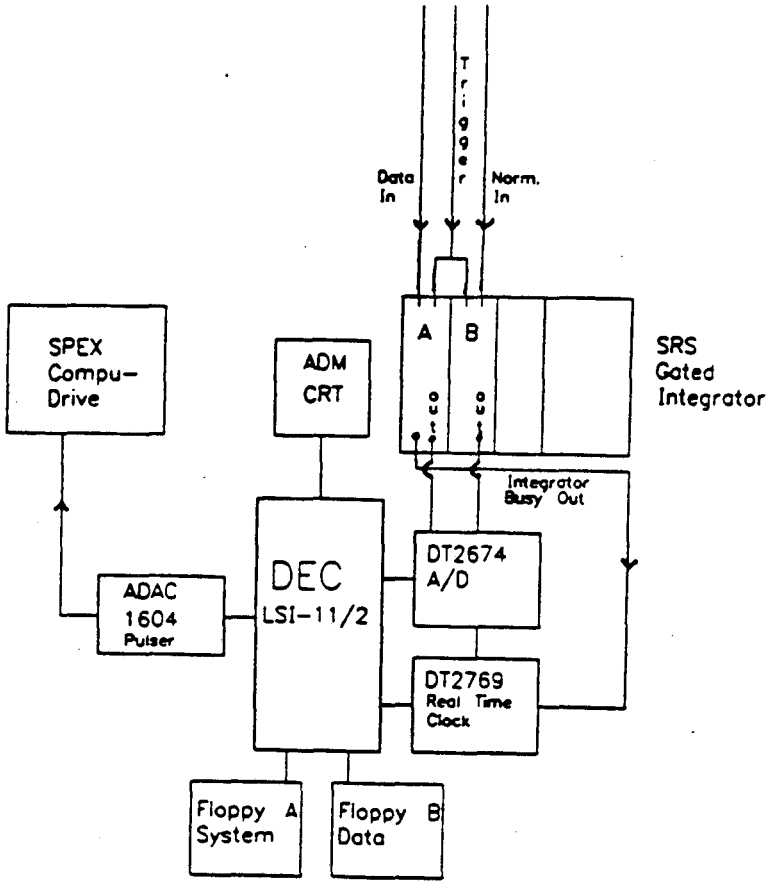

Figure 2.14: Computer configuration for taking pulsed Raman spectra using the SRS boxcar averager.

The configuration is the same as used with the PAR boxcar with the exceptions that the RTC is triggered not by program control but by the SRS boxcar itself and that the averaging is done by the computer not the boxcar. Both of the SRS boxcar channels (data and normalization) are set to sample or average over one shot at a time. Once the one shot has been integrated the boxcar sends out a ready signal on its integrator busy out line. This signal is used to trigger the RTC which then immediately flags the A/D converter which converts and stores the signal form the data and then normalization channels. This procedure is repeated an operator selected number of times. The results are then averaged with the averages being written to a floppy and displayed on the ADM terminal.

2.5.3 Pulsed Raman Excitation Profiles

Figure 2.15 shows the computer configuration for pulsed Raman excitation profile experiments (Section 2.4.2). In these experiments the SPEX 1403 monochromator and the

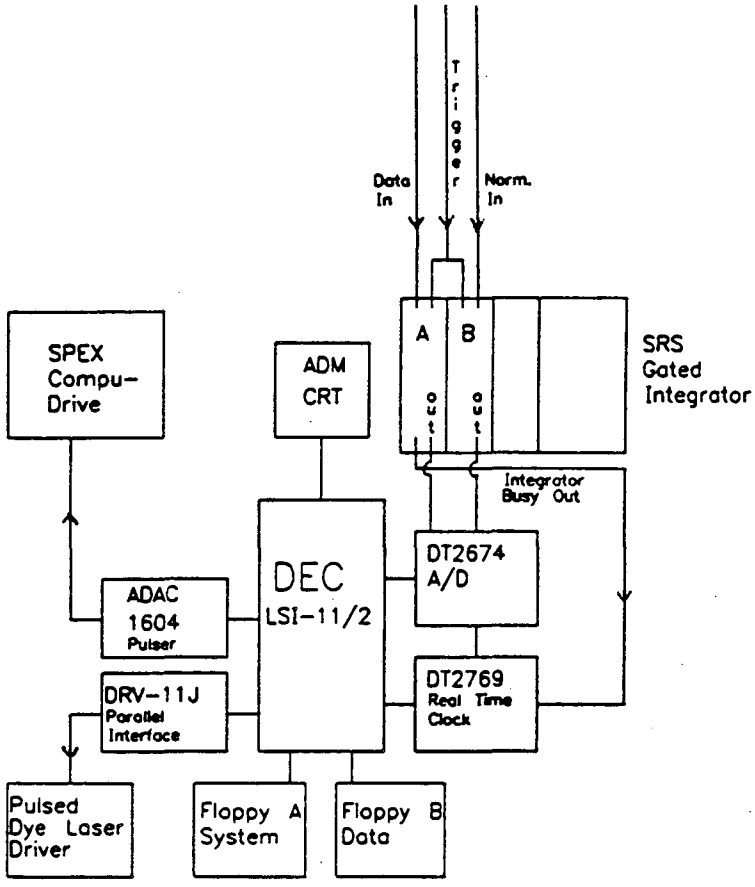

Figure 2.15: Computer configuration for taking Raman excitation profiles.

Quanta-Ray PDL-1 pulsed dye laser are tuned together maintaining a constant frequency shift between the two. As one can see the computer configuration is very similar to the one described in the previous Section. The only difference is the addition of the DEC DRV-11J parallel interface. The DRV-11J parallel interface is used to scan the PDL-1 pulsed dye laser through the *Quanta-Ray* MCI motor control interface.

2.5.4 Lifetime Measurements

Figure 2.16 shows the computer configuration for taking lifetime measurements (Section 2.4.3). Again, this is very similar to the previously described setups. The additional element is the *Data Translations* DT-2766 digital-to-analog converter (D/A). The D/A is used to apply a analog voltage (0-10 V) to the external delay control input of the data channel. The value of this voltage determines the temporal position of the integration window relative to the trigger. Thus, by sweeping the applied voltage we can obtain the data signal as a function of time delay after trigger.

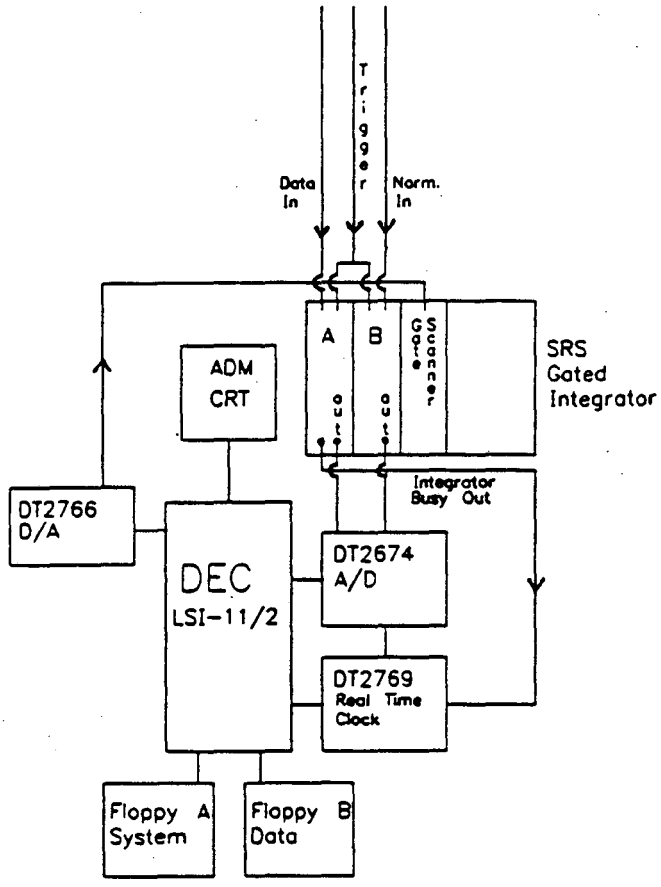

Figure 2.16: Computer configuration for lifetime measurements.

Chapter 3

Electronic Raman Scattering in Ce^{3+}:$LuPO_4$: Non-Resonant and Resonant Excitation

3.1 Introduction

This chapter describes the results of electronic Raman scattering experiments on Ce^{3+} diluted into single crystals of $LuPO_4$. Electronic Raman scattering is used as a spectroscopic tool to locate the crystal field levels of the $4f^1$ configuration of the cerium ion and, more importantly, as a means to test the validity of existing theories and notions regarding optical processes in transparent rare earth solids.

Electronic Raman scattering is a two-photon process in which one photon is provided by the laser field and the second is generated from the vacuum. It is formally equivalent to two photon absorption, in which both photons originate from the laser field, and spontaneous two photon emission, in which both photons are generated spontaneously from the vacuum. The standard second-order theory of the intensities of $4f^N$-$4f^N$ two-photon processes was developed by Axe [14]. The calculation follows the derivation of the intensities of one photon "*forced electric dipole*" transitions in rare earth solids developed by Judd [15] and Ofelt [16]. The only difference between the two calculations being the replacement of the odd-parity crystal field operators (for the one photon calculation) by an electric dipole operator (for the two-photon calculation). Both calculations involve a sum over virtual intermediate states belonging to configurations with parities opposite that of the $4f^N$ configuration. In both instances, the sum may be greatly reduced by

closure techniques if a simplifying approximation is made regarding the virtual intermediate states. It is assumed that one average value may be assigned to the differences between the energies of states in a given excited configuration and the energy of the incident light. In both cases, the result of this approximation is a solution that may be factored into two parts. One term contains matrix elements between the angular parts of the initial and final state wave functions. The angular parts of these wave functions are generally known, so that this term is easily evaluated. The second term involves the radial parts of the initial, the final, and the intermediate state wave functions. Since little is known about the radial parts of the wave functions (particularly the intermediate state wave functions), this term is usually treated as a parameter (or parameters) to be fit to the observed intensities.

In the case of "*forced electric dipole*" one photon processes, at least three independent parameters are needed to describe all the intensities in a given crystal. Applications of the one photon theory has been, in general, quite successful. In the case of two-photon processes at most only one parameter is needed to describe all the relative intensities in a crystal. It may be argued that the reduced number of adjustable parameters makes the prediction of the intensities of two-photon processes a more severe test of the Judd-Ofelt approximation. Indeed, several recent experiments demonstrate that the theory has failings when applied to two-photon processes.

It is with this background that the electronic Raman scattering experiments on Ce^{3+} diluted into $LuPO_4$ are undertaken. The question might be asked, why electronic Raman experiments using Ce^{3+}? Out of the twelve optically active trivalent rare earth ions, Ce^{3+} has an electronic structure which makes it a unique choice for a test of the theory of intensities.

- Ce^{3+} has only one optically active electron. The ground configuration of Ce^{3+} is $[Xe]4f^1$. This results in a relatively small and tractable number of quantum states and, in general, lends simplicity to all calculations.

- Ce^{3+} has a first excited configuration, $[Xe]5d^1$ that is low in energy. When diluted into $LuPO_4$ the states of the $5d^1$ configuration range in energy from approximately

30,000 cm^{-1} to 50,000 cm^{-1}.

The second item has a number of consequences. First, it makes for an especially stringent test of the approximation used in the standard theory. States of the $5d^1$ configuration have parity opposite to states of the ground state configuration, and thus may serve as the intermediate states discussed previously. With an incident laser energy of 20,000 cm^{-1}, the difference $E_{5d} - E_{laser}$ varies by a factor of three across the breadth of the $5d^1$ configuration. It is hoped that this stringent test accentuates and better defines the weaknesses in the intensity theory.

A second advantage of the low energy of the first excited configuration is that it allows for direct spectroscopic examination of the states in that configuration. This, in conjunction with the small number of quantum states in the first excited configuration, allows for a direct computation of the angular parts of the wave functions (based on a phenomenological Hamiltonian model) and then, an explicit evaluation of the sum in the calculation of the electronic Raman scattering intensities. The results of this more direct method of calculation may then be compared to the results of the standard theory.

A final consequence of the low energy of the first excited configuration is that it allows for resonant, or at least near-resonant, excitation of the electronic Raman spectra. Changing the excitation energy from the green-blue lines of an argon ion laser (all at about 20,000 cm^{-1}) to the frequency tripled output of a Nd^{3+}:YAG laser (at approximately 28,191.5 cm^{-1} which is only 2,000 cm^{-1} below the onset of the $5d^1$ levels) significantly enhances the intensities of the electronic Raman scattering transitions.

In the literature, there are few reports of resonance enhancement of optical processes in transparent rare earth solids. Furthermore, the large majority of this work concerns enhancements due to resonances with $4f^N$ configuration levels, which are more accessible by laser light sources. Resonances of this type, which will be discussed in detail in the following chapter are inherently weak because they are formally parity forbidden. However, the 4f-5d resonance discussed in this chapter is parity allowed and thus quite strong.

Beyond the qualitative observation of the strong enhancement, a more quantitative study yields additional insight on the intensity theory.

The chapter now begins with a complete description of the electronic structure of the first two excited configurations of Ce^{3+} diluted into $LuPO_4$. Knowledge of this is essential for an understanding of the optical processes that take place in the crystal.

3.2 Ground Configuration, $4f^1$

Over the past thirty years, there has been a vast amount of work done on the energy level structure of the ground $4f^N$ configuration of trivalent rare earth ions in insulating crystals. A semi-empirical theory has been developed that explains this structure quite well. However, an examination of the literature shows that a disproportionally small amount of work has been done on the ground configuration of trivalent cerium ion. At first this seems surprising because trivalent cerium, with only one 4f electron, has the simplest ground configuration of all the rare earth ions (with the exception of Yb^{3+}). However, a closer look at the $4f^1$ configuration's energy level structure and the semi-empirical Hamiltonian used to model this structure reveals the inherent difficulties in working with trivalent cerium. Following is a general account of the interactions affecting the single 4f electron. In the actual treatment of the problem, all interactions are treated simultaneously. However, for ease of explanation, they are presented here in a step-wise fashion from largest to smallest in magnitude.

In the spherically symmetric potential generated by the nucleus and the electrons of the closed shell orbitals, the $4f^1$ configuration has one fourteen-fold degenerate level. The largest interaction that acts to lift this degeneracy is the interaction of the electron's spin with the magnetic moment associated with its orbital angular momentum. States in which the orbital angular momentum is parallel to the spin angular momentum have a higher energy than states where the two are anti-parallel. This spin-orbit coupling breaks the spherical symmetry; one direction for the ion's orbital angular momentum has a different energy than another direction. However, one can see that if both orbital angular momentum and spin angular momentum are rotated together, there is no change in the energy of the system. The important quantum number is the one associated with the operator that corresponds to rotations in both spin and real space. This operator is the total angular momentum, $\vec{j}$, the vector sum of $\vec{l}$ and $\vec{s}$.

For the cerium ion $4f^1$ configuration, with $\mathbf{l} = 3$ and $\mathbf{s} = \frac{1}{2}$, there are two possible values of $\mathbf{j}$, 5/2 and 7/2. The $\mathbf{j} = 5/2$ level is six-fold degenerate and lower in energy, because it corresponds to the spin being anti-parallel to the orbital angular mometnum. The $\mathbf{j} = 7/2$ level is eight-fold degenerate and higher in energy, because it corresponds to the spin being parallel to orbital angular momentum.

The magnitude of the splitting between these two levels is given by a Hamiltonian of the form

$$H_{spin-orbit} = \zeta_{4f}(\vec{\mathbf{l}} \cdot \vec{\mathbf{s}}) \tag{3.1}$$

where ζ_{4f} is dependent on the radial part of the 4f electron's wavefunction. If the radial wavefunction is known ζ_{4f} can be computed directly. However, it is not possible to analytically solve the radial part of the Schrödinger equation for a many electron system. Self-consistent iterative techniques such as Hartree-Fock may be used to give approximate solutions; however, ζ_{4f} is usually treated as a parameter which is fitted to the observed energy levels. In the Ce^{3+} free ion, the energy separation between $\mathbf{j}$=5/2 and $\mathbf{j}$=7/2 is 2,253 cm^{-1} corresponding to a value of $\zeta_{4f} = 643.7cm^{-1}$[17].

When the cerium ion is placed into a crystal lattice, its surroundings are no longer isotropic. Even the spherical symmetry associated with rotations in both real and spin space no longer exists. The Stark or crystal field of the surrounding ligand ions acts to split the levels of the cerium ion. The number of split levels depends on the remaining degree of symmetry. The symmetry of the ion's surroundings is most easily described using the formalism of group theory. The set of geometric operations which keep the ion's surroundings unchanged as seen by the ion is referred to as the point group of the cerium site. The good quantum numbers are now the irreducible representations of the double group of the point group. However, $\mathbf{j}$ is still an approximately good quantum number because in most cases, the crystal field interaction is smaller than the $\mathbf{j}$ defining spin-orbit interaction. In fact, one can picture each j multiplet maintaining its own identity but being split into various components by the crystal field. For point group symmetries lower than cubic, the $\mathbf{j} = 7/2$ level is split into four components, and the $\mathbf{j} = 5/2$ level is split into three components. Each of these levels is two-fold degenerate. This remaining degeneracy, known as Kramer degeneracy, is a result of time reversal

symmetry as associated with half-integer spin systems.

In order to physically model the actual strength of the crystal field interaction, it is necessary to write down a Hamiltonian. If one assumes that the charge distribution of the 4f electron is removed from the charge distribution of the ligands (possibly a good assumption for shielded 4f orbitals), it is conceivable to treat their interaction as purely electrostatic in nature. The 4f electron located at position $\vec{r}(r,\theta,\phi)$ is affected by the ligand charge $g_j e$ at point $\vec{\rho}_j(\rho_j,\alpha_j,\beta_j)$ by

$$\begin{aligned} H_{crystal-field} &= \frac{-eg_je}{|\vec{r}-\vec{\rho}_j|} \\ &= -g_je^2\sum_k \frac{r^k P_k(cos\omega)}{\rho_j^{k+1}} \end{aligned} \tag{3.2}$$

where ω is the angle between $\vec{r}$ and $\vec{\rho_j}$ and P_k is a Legendre polynomial. Using the spherical harmonic addition theorem and summing over all the ligand charges yields,

$$\begin{aligned} H_{crystal-field} &= \sum_{k,q}\left[\left(\frac{4\pi}{2k+1}\right)^{\frac{1}{2}}\sum_j\left(\frac{g_je^2}{\rho_j^{k+1}}Y_q^{*k}(\alpha_j,\beta_j)\right)r^k\right] \\ &\times(\frac{4\pi}{2k+1})^{\frac{1}{2}}Y_q^k(\theta,\phi) \end{aligned} \tag{3.3}$$

Defining the term in brackets as B_q^k and $C_q^k = (\frac{4\pi}{2k+1})^{\frac{1}{2}}Y_q^k$ results in

$$H_{crystal-field} = \sum_{k,q} B_q^k C_q^k \tag{3.4}$$

It is possible to calculate the B_q^k's if one knows the locations of the ligand charges and the radial extent of the 4f electron. In general however, the results of such *ab initio* calculations do not match well with values of the B_q^k's obtained by fitting experimental data. In fact, the B_q^k's are commonly treated solely as parameters. The fits obtained using this parameterization are usually quite adequate. The inability to calculate the B_q^k's *ab initio* seems to indicate that the success of expression 3.4 is not so much the result of the physical interpretation that the interaction is electrostatic, but the fact that it is a parameterization scheme which reflects the symmetry of the situation accurately. The number of crystal field parameters depends on the remaining degree of symmetry, and is, in general, on the order of ten. For instance, for f electrons in cubic symmetry, there are two independent parameters while for a low symmetry such as C_2, there are fourteen parameters.

In conclusion, the general structure of the $4f^1$ configuration may be described quite simply. There are two multiplets separated by 2,000-2,400 cm^{-1} by the spin-orbit interaction. These multiplets are split further by the crystal field of the host lattice. The magnitude of these effects may be modelled by a parameterized Hamiltonian, with the number of parameters depending on the symmetry of the crystal field. With this background, one can now understand the difficulties in working with the trivalent cerium ion.

The first stumbling block is the use of the parameterized Hamiltonian. For the other trivalent rare earth ions, with the exception of ytterbium, there are a large number of observable $4f^N$ levels. The number of observed levels usually greatly exceeds the number of adjustable parameters. Clearly this is not the case with Ce^{3+}, where the maximum number of levels is seven. A model where the number of free parameters exceeds the number of observables obviously has no physical significance. The second difficulty with Ce^{3+} has to do with the energy separation of the levels and the experimental difficulties associated with measuring these separations.

3.2.1 Spectroscopy of the $4f^1$ Configuration

Most of the rare earth ions have many $4f^N$ energy levels which correspond to electronic transitions in the visible. The cerium ion has $4f^1$ levels exclusively in the range of 0-3,000 cm^{-1}. This corresponds to transitions in the infra-red, a difficult region to work in experimentally. Absorption or fluorescence experiments are not as straightforward as in the case of the other rare earth ions. However, there are two other experimental techniques that are useful in locating the $4f^1$ levels.

Electronic Raman scattering is the technique used in this work. The advantage of this technique is that it may be arranged so that both the incident and scattered light are in the visible. The difficulty with electronic Raman scattering is that the signal levels are usually quite low. Thus, the experiment is considerably more difficult to perform than the usual optical absorption experiment.

Another experiment useful in studying the cerium ion involves optical transitions between the first excited configuration, $5d^1$ and the ground configuration, $4f^1$. Elec-

tric dipole transitions between states of the $4f^1$ configuration and the $5d^1$ configuration are parity allowed. Thus, the oscillator strengths of such transitions are quite strong compared to those of formally parity forbidden 4f-4f transitions. Unfortunately, the inter-configurational 4f-5d transitions for most of the trivalent rare earth ions correspond to energies in the vacuum ultra-violet (VUV) region of the spectrum, a difficult region experimentally. However, for Ce^{3+} in most crystals, the entire $5d^1$ configuration lies in the near ultra-violet region of the spectrum. In Ce^{3+}:$LuPO_4$, the configuration spans the region 30,000-50,000 cm^{-1}. The lowest level at approximately 30,000 cm^{-1} is the primary source of luminescence even if a higher level in the configuration is excited. This is because the stronger coupling between the radially extended 5d electron and the lattice vibrations of the crystal facilitates fast non-radiative decay from upper levels to lower levels. Therefore, all of the luminescence is in the region 30,000 cm^{-1} to 28,000 cm^{-1}, corresponding to the transitions $5d^1_{lowest} \rightarrow {}^2F_{5/2}$ and $5d^1_{lowest} \rightarrow {}^2F_{7/2}$, respectively. These energies are quite simple to observe.

Unfortunately, it is a difficult task to assign electronic energy levels from the observed luminescence. This difficulty is a result of the complicated structure of the $5d^1$-$4f^1$ spectrum. As mentioned previously, an electron in a radially extended 5d orbital is much more strongly coupled to the lattice than when in a 4f orbital. As a result, the $5d^1$-$4f^1$ luminescence is very broad ($\approx 1{,}000$ cm^{-1}) with a great deal of *vibronic* structure. Figure 3.1 is a configurational coordinate diagram [18] for what one might expect for a transition between a state of the $5d^1$ configuration and a state of the $4f^1$ configuration. The difference in coupling with the lattice is manifested in the different shapes of the two potential curves and the difference in the equilibrium position of the ligands, Q_0 and Q'_0. Shown in the figure are both the luminescence and absorption spectra.

From Figure 3.1, it appears as though the pure electronic-electronic (also known as zero-phonon and 0-0) transition is easily identified as the sharp feature on the low energy side of the luminescence. The difficulty arises when a second $4f^1$ level is involved. Luminescence to an excited crystal field level, at for instance 500 cm^{-1} would be hidden in the broad background of the ground state luminescence. The way around this is to compare the low temperature $4f^1$-$5d^1$ absorption spectra to the luminescence spectrum.

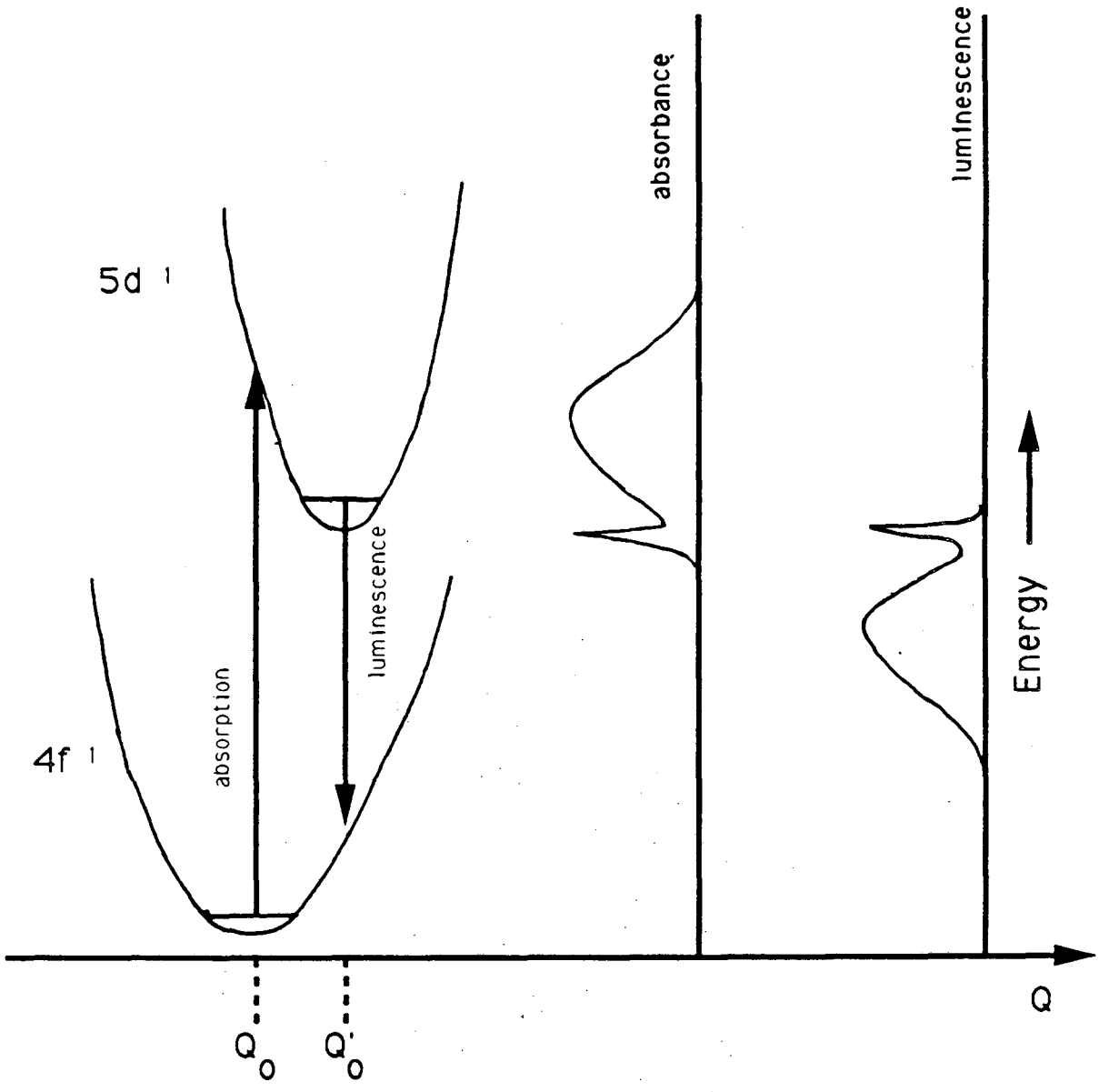

Figure 3.1: Configurational coordinate diagram for transition between a state of the $5d^1$ configuration and a state of the $4f^1$ configuration.

The low temperature absorption spectrum should show features associated with the ground state alone. Additional sharp features that appear in the luminescence spectrum are identified as terminating on excited levels.

3.2.2 $4f^1$ Configuration in Ce^{3+}:$LuPO_4$, Early Studies

The first work on the energy level structure of the $4f^1$ configuration of Ce^{3+}:$LuPO_4$ was done by Hoshina and Kubinowa [19]. They had powders of nominally .1% Ce^{3+} doped into $LuPO_4$. The levels were identified by the aforementioned technique of comparing the $5d^1$-$4f^1$ luminescence spectrum to the $4f^1$-$5d^1$ excitation (equivalent to absorption) spectrum. The point group of the cerium ion site was known to be D_{2d}. Therefore, the quantum states of the cerium ion should be labelled by the irreducible representations of the double group of D_{2d}, Γ_6 and Γ_7. Furthermore it is known that, under the perturbation of the crystal field with D_{2d} symmetry, the $^2F_{5/2}$ multiplet splits into three components, two Γ_6 levels and a Γ_7 level, and the $^2F_{7/2}$ multiplet splits into four components, two Γ_6 levels and two Γ_7 levels. However, Hoshina and Kuboniwa were only able to identify two levels associated with the $^2F_{5/2}$ multiplet and three levels associated with the $^2F_{7/2}$ multiplet. The levels they observed were at 444 cm^{-1}, 2180 cm^{-1}, 2231 cm^{-1}, and 2620 cm^{-1}. These results are tabulated in Table 3.1. In order to explain the missing levels, it was hypothesized that the crystal field was approximately cubic. The tetragonal distortion which results in the D_{2d} point group was assumed to be quite small. In the higher symmetry cubic field, the number of splittings is expected to be smaller, with the $^2F_{5/2}$ split into two levels and the $^2F_{7/2}$ split into three levels. Figure 3.2 shows schematically the splittings in a cubic field and the additional splittings due to the introduction of a tetragonal distortion.

Nakazawa and Shinoya [20] performed the same experiment on single crystals of .1% of Ce^{3+} doped into $LuPO_4$. Again, only the same five levels could be identified in the $4f^1$ configuration. However, with single crystals it was possible to do polarization studies. In a cubic field, the directions $\hat{\mathbf{X}}$,$\hat{\mathbf{Y}}$, and $\hat{\mathbf{Z}}$ are equivalent, and there should be no polarization in the spectra. In a tetragonal field $\hat{\mathbf{Z}}$ becomes inequivalent to $\hat{\mathbf{X}}$ and $\hat{\mathbf{Y}}$, and the π (parallel to $\mathbf{Z}$) polarized spectra should be different than the σ (perpendicular

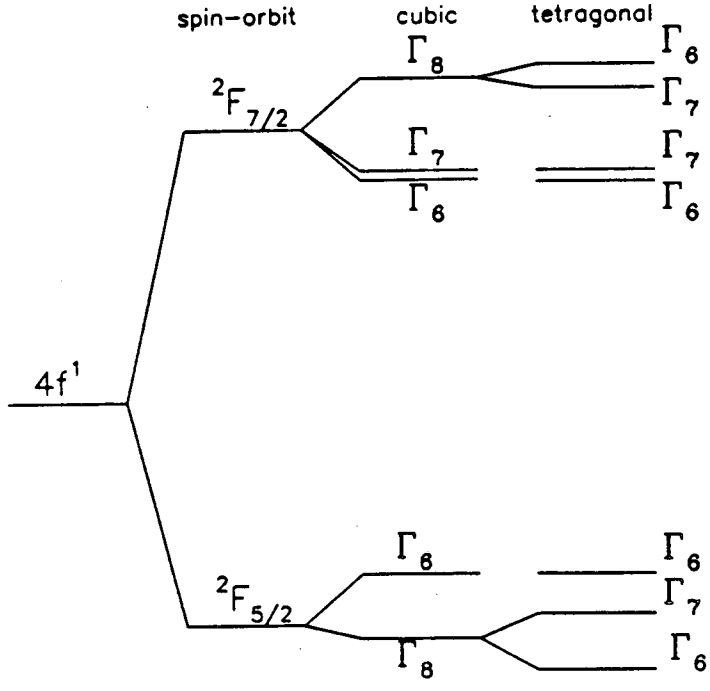

Figure 3.2: Crystal field splittings for $4f^1$ in cubic field (O_h) and a tetragonal field (D_{2d}).

to $\hat{\mathbf{Z}}$) spectra. The electric dipole selection rules are

$$\sigma = \hat{\mathbf{X}}, \hat{\mathbf{Y}} \begin{cases} \Gamma_6 \longrightarrow \Gamma_6 \text{ or } \Gamma_7 \\ \Gamma_7 \longrightarrow \Gamma_6 \text{ or } \Gamma_7 \end{cases}$$

$$\pi = \hat{\mathbf{Z}} \begin{cases} \Gamma_6 \longrightarrow \Gamma_7 \\ \Gamma_7 \longrightarrow \Gamma_6 \end{cases}$$

Nakazawa and Shinoya observed strongly polarized spectra in the crystals. Their conclusion was that the tetragonal distortion seen by a $4f^1$ electron is indeed small, resulting in only five levels, while the tetragonal distortion seen by a $5d^1$ electron is much larger, resulting in the observed polarized spectra. From the polarized spectra, they identified the symmetry of the two observed levels in the $^2F_{5/2}$ multiplet. Their results are also listed in Table 3.1.

3.2.3 Electronic Raman Spectroscopy of Ce^{3+}:$LuPO_4$

In this work, Raman scattering was observed between crystal field levels of single crystals of Ce^{3+}:$LuPO_4$. The relative amounts of Ce^{3+} and Lu^{3+} used in the starting materials

for the crystal growth were 0.20 and 0.80, respectively. Thus, through the remainder of this chapter this crystal will be referred to as $Ce_{.20}Lu_{.80}PO_4$. A discussion of the true relative concentrations of Ce^{3+} and Lu^{3+} will be given in Appendix B.

Scattering was observed from the ground state to the six other crystal field levels. The levels not seen in the earlier experiments are observed at 240 cm^{-1} and 2676 cm^{-1}. The incident laser light was linearly polarized, and the polarization of the scattered light was analyzed. Because of experimental difficulties described in Section 2.1.2, only the polarization combinations $\hat{X}\hat{Z}$,$\hat{Z}\hat{Y}$,$\hat{X}\hat{Y}$ and $\hat{Z}\hat{Z}$ were checked. However, based on these observed polarizations, symmetry assignments of the levels could be made using the electronic Raman scattering selection rules . The electronic Raman scattering selection rules for the double group of D_{2d} are:

$$\hat{X}\hat{Z},\hat{Z}\hat{Y},\hat{X}\hat{Y}\begin{cases}\Gamma_6 \longrightarrow \Gamma_6 \text{ or } \Gamma_7\\ \Gamma_7 \longrightarrow \Gamma_6 \text{ or } \Gamma_7\end{cases}$$

$$\hat{Z}\hat{Z}\begin{cases}\Gamma_6 \longrightarrow \Gamma_6\\ \Gamma_7 \longrightarrow \Gamma_7\end{cases}$$

More concisely, the rule to remember is that in $\hat{Z}\hat{Z}$ polarization the initial state and final state must have the same symmetry.

Figure 3.3 shows some typical polarized electronic Raman spectra. The transitions shown are from the ground state to the states at 2179 cm^{-1} and 2221 cm^{-1}. Because the transition to the level at 2221 cm^{-1} disappears in $\hat{Z}\hat{Z}$ polarization, and the transition to the level at 2179 cm^{-1} does not, they are assigned opposite symmetries with the 2179 cm^{-1} level having the same symmetry as the ground state. A complete list of the observed levels and their assigned symmetries is given in Table 3.1.

There is some question as to the symmetry of the 2620 cm^{-1} and 2676 cm^{-1} levels. As stated previously, it is known that the $^2F_{7/2}$ multiplet splits into two Γ_6 and two Γ_7 levels. The 2179 cm^{-1} level and the 2221 cm^{-1} level are assigned to Γ_6 and Γ_7 respectively, meaning that the levels at 2620 cm^{-1} and 2676 cm^{-1} should have opposite symmetry. It would be a simple matter to assign these levels if one of them disappeared in $\hat{Z}\hat{Z}$ polarization. Unfortunately, neither level is observed in $\hat{Z}\hat{Z}$ polarization. The level

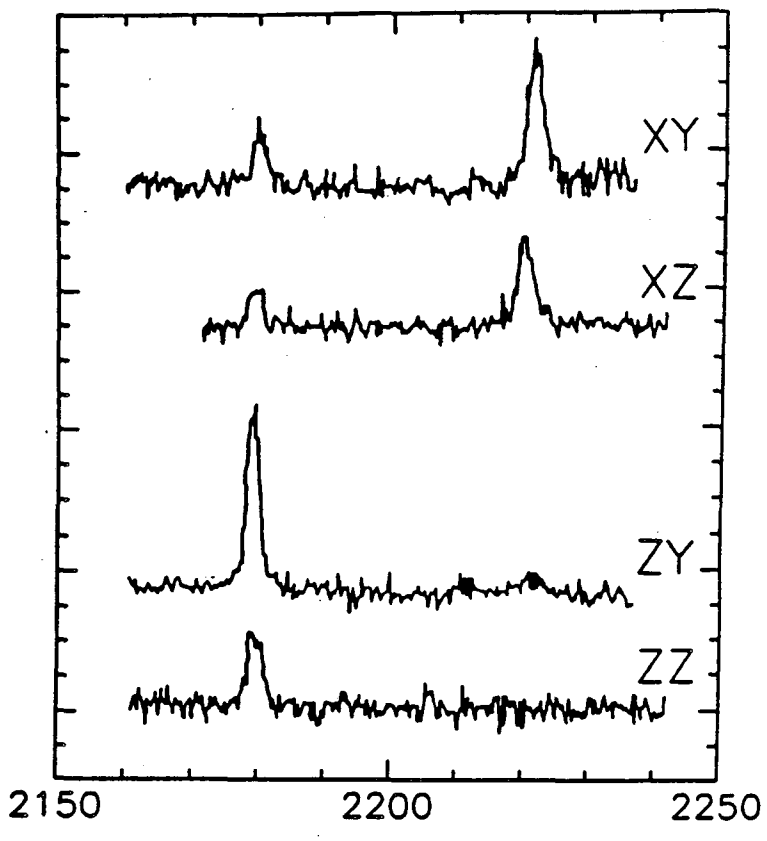

Figure 3.3: Polarized electronic Raman scattering spectra in the region $\Delta 2150$ cm^{-1} to $\Delta 2250$ cm^{-1} for $Ce_{.20}Lu_{.80}PO_4$.

Reference [19]	Reference [20]		This Work	
Energy,cm^{-1}	Energy,cm^{-1}	Symmetry	Energy,cm^{-1}	Symmetry
0	0	Γ_8	0	Γ_6
-	-	-	240	Γ_7
444	433	Γ_6	429	Γ_6
2196	2179	-	2179	Γ_6
2231	2221	-	2221	Γ_7
2620	2620	-	2620	Γ_7
	-	-	2676	Γ_6

Table 3.1: $4f^1$ energy levels observed in Ce^{3+}:$LuPO_4$. The symmetry assignments for Reference [20] are for cubic symmetry while the assignments for this work are for D_{2d} symmetry.

at 2676 cm^{-1} is assigned to be Γ_6, meaning it should be observed in $\hat{Z}\hat{Z}$ polarization. The rationale for this is that the observed intensities for transitions to the 2676 cm^{-1} level for all polarizations are comparatively small. It seems reasonable to assume that the $\hat{Z}\hat{Z}$ transition is formally allowed but not observed because of a small intensity. The choice of symmetry is further supported by the values of the fitted crystal field parameters. This will be discussed in a Section 3.2.4.

It should also be mentioned that there is some uncertainty regarding the identification of the spectral feature at 240 cm^{-1} as being the result of electronic Raman scattering. There is a possibility that it is the result of vibrational Raman scattering. There is expected to be a B_{1g} phonon with an energy somewhere in the neighborhood of 200 cm^{-1} to 350 cm^{-1}. This phonon, as discussed in Section 2.2 of Chapter 2, has not been observed in either $LuPO_4$ or YPO_4 [11]. The expected value of the phonon energy is estimated from the observed energy in YVO_4 of 265 cm^{-1} [12]. In addition to the approximate energy range, the other suggestive observation is that the 240 cm^{-1} spectral feature only appears in $\hat{X}\hat{Y}$ polarization. Although Raman scattering to B_{1g} phonons is only allowed in $\hat{X}\hat{X}$ and $\hat{Y}\hat{Y}$ polarizations, they consistently show leakage into $\hat{X}\hat{Y}$ polarizations. There are two arguments which suggest that the peak is electronic in nature. Most importantly, the peak is not observable at room temperature, only at 10K. Even when the crystal is rotated about the $\hat{Z}$ axis in order to observe $\hat{X}\hat{X}$ or $\hat{Y}\hat{Y}$ polarization, in which case scattering to all B_{1g} phonons is allowed, the peak at 240 cm^{-1} is not observed at room temperature. In general, phonon peak widths do not change significantly with temperature as opposed to electronic peaks which may broaden greatly as the temperature increases. A phonon peak should be just as observable at room temperature as at liquid helium temperature; the suggestion being that the spectral feature is electronic, not vibrational. Secondly, extrapolation from the YVO_4 spectra places the expected B_{1g} phonon energy closer to 300 cm^{-1} than 240 cm^{-1}.

Finally, the question arises why the levels at 240 cm^{-1} and 2676 cm^{-1} were not observed in the luminescence experiments. The proposed explanation is that the intensity for both of these transitions is small. The transition intensities confirming this proposition will be calculated later. It is first necessary to find accurate wavefunctions for the

$4f^1$ levels and the lowest $5d^1$ level.

3.2.4 Crystal Field Fit, Ce^{3+}:$LuPO_4$

As described previously, the splitting of the $4f^1$ configuration may be described by a parameterized Hamiltonian. The parameters may be varied to achieve the minimum root-mean-square difference between the eigenvalues of the Hamiltonian matrix and the observed energy values. The Hamiltonian matrix may then be diagonalized, yielding the eigenstate wavefunctions. These wavefunctions are essential for the calculation of the electronic Raman scattering intensities in Section 3.4.2.

In detail, the Hamiltonian for Ce^{3+} in D_{2d} symmetry is

$$\begin{aligned} H &= H_{spin-orbit} + H_{crystal-field} \\ H_{spin-orbit} &= \zeta_{4f}(\vec{l}\cdot\vec{s}) \\ H_{crystal-field} &= B_0^2C_0^2 + B_0^4C_0^4 + B_4^4(C_4^4 + C_{-4}^4) + B_0^6C_0^6 \\ &\quad + B_4^6(C_4^6 + C_{-4}^6) \end{aligned} \tag{3.5}$$

where ζ_{4f} is the spin-orbit coupling parameter, and the B_q^k's are the parameters describing the crystal field. There are only five crystal field parameters for a 4f electron in D_{2d} symmetry, giving a total of six parameters. Beacause there are seven levels it is possible to perform a fit. However, the validity of a fit with seven levels and six parameters could be in doubt. This is especially true in light of the fact that the symmetry of two of the levels at 2620 cm^{-1} and 2676 cm^{-1} are not certain. To confirm the validity of the symmetry assignments and the subsequent fit, other criteria besides accurate prediction of the energy level structure are used.

The first check is the comparison of the predicted values of the ground state magnetic g-values to the experimental values. The two g values, one perpendicular to the $\hat{Z}$ axis and one parallel to the $\hat{Z}$ axis, are easily calculated from the ground state wavefunction. The calculated g-values for fits corresponding to the two different symmetry assignments for the lines at 2620 cm^{-1} and 2676 cm^{-1} are listed in Table 3.2. The experimental g-values have been measured by Abraham and Boatner [21] in an electron paramagnetic resonance experiment. In their experiment, g-values were measured for less than 1% Ce^{3+} doped into single crystals of $LuPO_4$, YPO_4, and $ScPO_4$. In all cases, the value for

	g-parallel	g-perpendicular
$Ce_{.20}Lu_{.80}PO_4$ calculated 2,620 $cm^{-1}=\Gamma_7$	0.53	1.79
$Ce_{.20}Lu_{.80}PO_4$ calculated 2,620 $cm^{-1}=\Gamma_6$	0.25	1.83
$Ce_{.01}Lu_{.99}PO_4$ measured	0.2(2)	1.656(1)
$Ce_{.01}Y_{.99}PO_4$ measured	0.63(2)	1.713(1)
$Ce_{.01}Sc_{.99}PO_4$ measured	0.44(2)	1.476(1)

Table 3.2: Measured and calculated magnetic g-values for Ce^{3+}:MPO_4, M= Lu, Sc, or Y. Experimental errors are in parenthesis.

g-parallel has a relatively large error. This is because the spectral line width increases as the direction of the applied magnetic field is rotated from perpendicular to $\hat{\mathbf{Z}}$ to parallel to $\hat{\mathbf{Z}}$. The actual value of g-parallel was extrapolated from a plot of the resonance magnetic field versus $\cos^2\theta$. As can be seen from Table 3.2, both fits yield reasonable g-values. The differences that do exist between experimental and calculated g-values may be, in part, the result of true differences between g-values in $Ce_{.20}Lu_{.80}PO_4$ and $Ce_{.01}L_{.99}PO_4$. At first this may not seem plausible, knowing that the nearest neighbor cerium ions are far removed from the cerium ion under question and thus have little effect on the crystal field. For example, the energy level structure of a rare earth ion doped in $LuPO_4$ is almost identical to that of the same ion doped into YPO_4[22,23]. However, the effect on g-values of such a change appears to be much more significant. This may be seen from the experimental values for Ce^{3+} in $LuPO_4$, YPO_4 and $ScPO_4$ in Table 3.2.

The second check is an examination of how close the values of the fitted parameters are to what might be expected from a physical point of view. The parameters for both crystal field fits for Ce^{3+} in $LuPO_4$ (2620 cm^{-1} = Γ_7 and 2620 cm^{-1} = Γ_6) and crystal field fits for other rare earth ions diluted into $LuPO_4$ are listed in Table 3.3.

RE^{3+}	x	$4f^n$	Crystal Field Parameters					Spin-orbit	Reference
			B_0^2	B_0^4	B_4^4	B_0^6	B_4^6	ζ	
Ce[a]	0.20	1	26	263	−1247	−1270	148	615	this work
Ce[b]	0.20	1	−48	392	−1243	−758	460	618	this work
Pr	[c]	2	21	280	−808	−1658	291	744	[22]
Nd	[c]	3	178	209	−922	−1256	−147	878	[22]
Eu	0.05	6	151	430	−820	−1263	272	1330	[24]
Er	[c]	11	146	69	−760	−643	−89	2367	[25]
Tm	[c]	12	203	117	−673	−705	16	2629	[23]
Yb	[c]	13	256	14	−608	−705[d]	16[d]	2903	[23]

[a] 2,620 $cm^{-1}=\Gamma_7$ and 2,676 $cm^{-1}=\Gamma_6$
[b] 2,620 $cm^{-1}=\Gamma_6$ and 2,676 $cm^{-1}=\Gamma_7$
[c] Approximately 0.01.
[d] Fixed at Tm^{3+} values.

Table 3.3: Fitted parameters for $RE_x^{3+}Lu_{1-x}PO_4$.

It should be first noted that both fits have spin-orbit coupling parameters on the order of 615 cm^{-1}. This value is only slightly smaller than the observed free ion value. The near equivalence is exactly what is expected, because **j** is still a fairly good quantum number for the atomic-like 4f orbital.

The choice between the two symmetry assignments is based on the values of the fitted crystal field parameters. It is difficult to draw conclusions concerning the trends of the crystal field parameters for different rare earth ions in a particular host crystal. This is, no doubt, a result of the fact that the physical significance of the crystal field parameters is not well understood. However, as shown in Table 3.3, trends do exist and the symmetry assignment with 2,620 $cm^{-1}=\Gamma_7$ and 2,676 $cm^{-1}=\Gamma_6$ seems to comply with these trends. The wavefunctions for this symmetry assignment are listed in Table 3.4.

3.3 First Excited Configuration, $5d^1$

The first excited configuration of Ce^{3+} consists of a full xenon core and one 5d electron, $[Xe]5d^1$. In contrast to the relatively small amount of work done on states of the ground configuration of Ce^{3+} in crystals, the first excited configuration of Ce^{3+} is the most thoroughly studied of all the rare earths [26,27,28,29,30,31,32,33,34,35,36,37]. This is most certainly the result of the experimental ease of observing the states of this low lying configuration. Of all the rare earths, only Ce^{3+}, Tb^{3+}, and Pr^{3+} have first excited

Calculated Energy (cm^{-1})	Observed Energy (cm^{-1})	Symmetry	Wavefunction $\sum_{J,J_z} a(J,J_z)^{2S+1}L\|J,J_z\rangle$
0.0	0.0	Γ_6	$.749^2\mathrm{F}\|\frac{5}{2},-\frac{3}{2}\rangle + .658^2\mathrm{F}\|\frac{5}{2},\frac{5}{2}\rangle$
240.0	240.0	Γ_7	$.991^2\mathrm{F}\|\frac{5}{2},-\frac{1}{2}\rangle + -.103^2\mathrm{F}\|\frac{7}{2},-\frac{1}{2}\rangle$
429.0	429.0	Γ_6	$-.749^2\mathrm{F}\|\frac{5}{2},\frac{5}{2}\rangle + .651^2\mathrm{F}\|\frac{5}{2},-\frac{3}{2}\rangle$ $+.113^2\mathrm{F}\|\frac{7}{2},-\frac{3}{2}\rangle$
2179.0	2179.0	Γ_6	$-.867^2\mathrm{F}\|\frac{7}{2},\frac{5}{2}\rangle + -.484^2\mathrm{F}\|\frac{7}{2},-\frac{3}{2}\rangle$ $+.117^2\mathrm{F}\|\frac{5}{2},-\frac{3}{2}\rangle$
2221.0	2221.0	Γ_7	$.756^2\mathrm{F}\|\frac{7}{2},-\frac{1}{2}\rangle + .653^2\mathrm{F}\|\frac{7}{2}\frac{7}{2}\rangle$
2620.0	2620.0	Γ_7	$.753^2\mathrm{F}\|\frac{7}{2},\frac{7}{2}\rangle + -.645^2\mathrm{F}\|\frac{7}{2},-\frac{1}{2}\rangle$ $+ - .131^2\mathrm{F}\|\frac{5}{2},-\frac{1}{2}\rangle$
2676.0	2676.0	Γ_6	$-.868^2\mathrm{F}\|\frac{7}{2},-\frac{3}{2}\rangle + .491^2\mathrm{F}\|\frac{7}{2},\frac{5}{2}\rangle$

Table 3.4: $Ce_{.20}Lu_{.80}PO_4$ $4f^1$ wavefunctions.

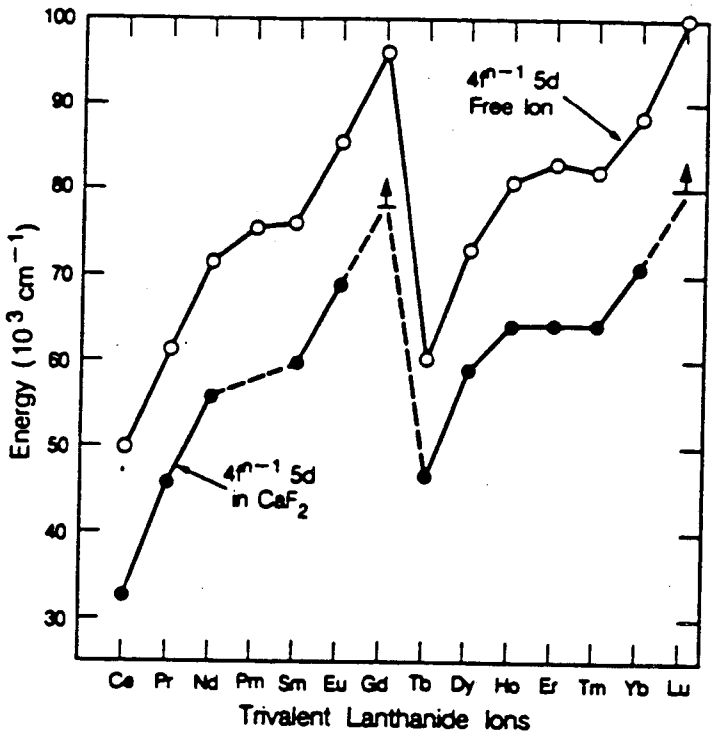

Figure 3.4: Energies of the lowest states of the first excited configurations of free trivalent rare earth ions and trivalent rare earth ions in CaF_2.

configuration states in insulating crystals below the vacuum ultra-violet cutoff of 50,000 cm^{-1}. Figure 3.4[38,39] shows the energy of the lowest $4f^{N-1}5d$ configuration state for the trivalent rare earth ions in the gas phase and in a crystal of CaF_2.

The $5d^1$ configuration is of primary interest in this work because the states of this configuration are expected to serve as the dominant virtual intermediate states in the electronic Raman scattering between states of the ground configuration. However, a study of the configuration in and of itself is of interest. The interaction between a 5d electron and the crystal lattice is the next step up in strength from the small crystal field seen by the electrons in 4f orbitals. It is clear from spectra resulting from transitions either to or from states with 5d electrons, that the radially extended 5d orbitals are not nearly as atomic-like as the 4f orbitals. As discussed in Section 3.2.1, this is manifested in such things as broad spectral peaks ($\approx$1,000 cm^{-1}) and Stokes shifts between luminescence and absorption. In fact, there is some question as to whether it is correct to treat the levels associated with the $5d^1$ configuration in the same way as the levels of the

$4f^1$ configuration. The belief that the states are localized states of the cerium ion (thus the labelling $5d^1$ configuration) perturbed by the ligands may lose much of its validity as the degree of overlap between the cerium ion orbitals and the ligand orbitals increases. However, as the simplest of starting points, this view is adopted. It will be tested first by how accurately it explains the observed spectra. Later it will be seen whether the electronic Raman scattering intensities can also be explained in the context of this view.

In the Ce^{3+} free ion, the difference between the mean energies of the $4f^1$ and $5d^1$ configurations is approximately 50,000 cm^{-1}. Placing the ion in a crystal has a dramatic effect on the $5d^1$ configuration. The crystal field is the dominant interaction, being as large as 10,000 cm^{-1}, and the spin-orbit interaction remains approximately as it is for the 4f orbital at $\approx$ 1,000 cm^{-1}. The crystal field not only splits the configuration into a number of levels, but also lowers the mean energy of the entire configuration through the so-called "*nephelauxetic effect*" [26] For example, in the case of Ce^{3+}:$LuPO_4$, the mean energy is lowered to approximately 40,000 cm^{-1} above the $4f^1$ ground state. Furthermore, due to the large crystal field, **j** is no longer an approximately valid quantum number as it was for the $4f^1$ wavefunctions. As will be seen in Section 3.3.4, the $5d^1$ wavefunctions are heavily j-mixed.

3.3.1 The $5d^1$ Configuration in D_{2d} Symmetry

If the relatively small spin-orbit coupling is neglected, the $5d^1$ configuration in D_{2d} symmetry is split into four levels labelled by irreducible representations of the group, D_{2d} . There are three singlets, Γ_1, Γ_3, and Γ_4 and one doubly degenerate Γ_5 level. The degeneracy of each of these levels is doubled when the electronic spin is considered. With the introduction of the spin-orbit interaction, the doublet Γ_5 level is split into two levels. This splitting may or may not be observable depending on the degree of splitting relative to the widths of the lines. The five levels should now be labelled by the irreducible representations of the double group. There are three Γ_7 levels and two Γ_6 levels. Each of these levels are Kramer doublets. Figure 3.5 shows schematically the splittings for the $5d^1$ configuration.

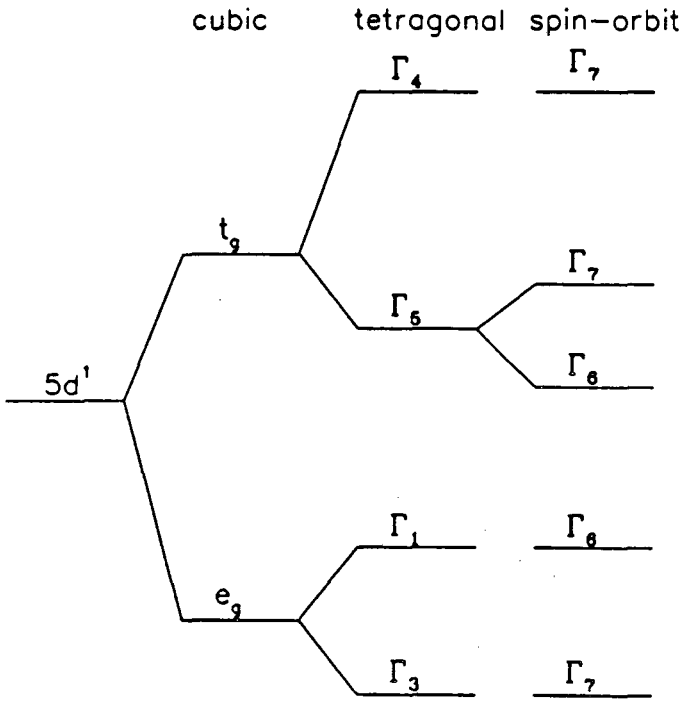

Figure 3.5: Splittings for the $5d^1$ configuration in a cubic field (T_d) and then with the addition of a tetragonal distortion (D_{2d}).

3.3.2 The $5d^1$ Configuration in Tetragonal Phosphate Crystals, Early Work

The only studies of the $5d^1$ configuration of Ce^{3+} diluted into $LuPO_4$ are the two $5d^1_{lowest}$-$4f^1$ luminescence experiments discussed in Section 3.2.4. However, there has been a great deal of work done on the $5d^1$ configuration of Ce^{3+} diluted into a crystal which is isostructural and overall very similar to $LuPO_4$, YPO_4. The only difference between the two crystals is that lutetium ion is replaced by yttrium ion. These ions have the same valence and roughly the same ionic size. Earlier experiments[22,23] have shown that the two crystals have nearly identical crystal fields ,as seen by the $4f^N$ configuration electrons. Even though the 5d electrons have a greater radial extension resulting in larger crystal fields and possibly enhancing the effect of next nearest neighbor ligands, it is expected that the strong similarities between the crystal fields in $LuPO_4$ and YPO_4 should still hold. Given this a review of the work on Ce^{3+}:YPO_4 should be helpful in this study of Ce^{3+}:$LuPO_4$. However, in the body of work on Ce^{3+}:YPO_4 there exist a good deal of disagreement regarding the location and symmetry assignment of levels. Following

is an overview of earlier work. The results of this work are compiled in Table 3.5 and Table 3.6 at the end of this section.

In the earlier work several different experimental techniques were employed. An understanding of the advantages and disadvantages of each of these techniques is important in reconciling the different observations of the previous workers. The most commonly used experimental techniques were excitation and absorption (usually derived from diffuse reflectance) spectra. Excitation and absorption are very similar techniques and may be viewed as two different ways of measuring the amount of absorbed light. However, differences arise if there are two distinct absorbers present in the sample, such as the cerium ion and an impurity. An absorption experiment will not differentiate between the two absorbers. However, if there is no energy transfer between absorbers, an excitation experiment will yield the spectrum of each absorber independently, depending upon which luminescence is monitored.

Luminescence is another experimental technique employed in earlier work. As stated in Section 3.2.1, almost all of the luminescence from the $5d^1$ configuration originates from the lowest energy level, as upper level excitations relax through non-radiative decay to the lowest level. However, through the use of a strong excitation source and careful detection upper level luminescence may be detected. The luminescence spectrum will be absorber specific so long as the excitation energy of the source is selected so as not to overlap an impurity absorption. The two main points regarding luminescence spectra are that it is more complicated than absorption/excitation spectra and also Stokes shifted relative to absorption/excitation spectra. The added complication arises from the fact that luminescence may occur to excited states. The Stokes shift was explained in Section 3.2.1. In fact, neither the peaks of the absorption/excitation spectra nor the peak of the luminescence gives the true location of the electronic transition. However, this will be treated as a minor concern until Section 3.3.4.

The first work on the first excited configuration of Ce^{3+} in YPO_4 was done by Blasse and Bril [27]. They used diffuse reflectance spectra and excitation of the $5d^1_{lowest}$-$4f^1$ luminescence in 1-2% Ce^{3+} in YPO_4 to locate three out of the expected four levels (assuming the spin-orbit splitting is not observable). The three levels were at 32,800

cm^{-1}, 36,900 cm^{-1}, and 41,500 cm^{-1}. However, no spectra were taken beyond 220 nm ($\approx$45,500 cm^{-1}). Ropp [40] in a study of rare earth phosphate phosphors located five levels in 5 % Ce^{3+} in YPO_4 at 203 nm ($\approx$ 49,261 cm^{-1}), 227 nm ($\approx$ 44,529 cm^{-1}), 239 nm ($\approx$ 41,841 cm^{-1}), 252 nm ($\approx$ 39,683 cm^{-1}), and 325 nm ($\approx$ 30,769 cm^{-1}). These levels were located using the excitation spectra of the $5d^1_{lowest}$-$4f^1$ luminescence.

Briffault and Denis [41] were the first to assign symmetries to all the observable levels, even though their method of assignment was somewhat indirect. They used diffuse reflectance spectra in powders of 5 % Ce^{3+} doped into YPO_4 to identify three $5d^1$ levels at 30,970 cm^{-1}, 35,870 cm^{-1}, and 39,514 cm^{-1}. A fourth level at 50,000 cm^{-1} was identified from the excitation spectra of the $5d^1_{lowest}$-$4f^1$ luminescence. It was assumed that the spin-orbit splitting was too small to be observable. Symmetry assignments were made by choosing the set of assignments that resulted in fitted crystal field parameters that were consistent with those calculated from an electrostatic model using the entire PO_4^{3-} complexes as point charges. The assignments they made were the level at 39,514 cm^{-1} is of Γ_4 symmetry, the level at 35,870 cm^{-1} is of Γ_3 symmetry, and the lowest level at 30,970 cm^{-1} is the doublet Γ_5. The last assignment is consistent with their observation that the lowest level had the largest absorption cross-section. The final fitted crystal field parameters they obtained were B_0^2= 5,688 cm^{-1}, B_0^4= 38,352 cm^{-1} , and B_4^4= 4,550 cm^{-1}.

Balasubramian and Newman [42] made new symmetry assignments for the levels observed by Briffault and Denis based on crystal field models where the eight nearest neighbor O^{2-} ions were treated as the point charges. Based on their calculated values for the crystal field parameters they assigned the 30,970 cm^{-1} level as the Γ_5 doublet, the 35,870 cm^{-1} level as Γ_1, and the level at 39,514 cm^{-1} as a Γ_3. Using these assignments the crystal field parameters were recalculated this time in a fit. The resulting values for the parameters were B_0^2= 3,516 cm^{-1}, B_0^4= 7,288 cm^{-1}, and B_4^4= 18,869 cm^{-1}. The fourth level, identified by Briffault and Denis as the spectral feature in the excitation spectra at 50,000 cm^{-1} , was calculated to be at 21,733 cm^{-1}, outside the range of observation of Briffault and Denis.

Most recently, Naik and Karanjikar [43] have reported the X-ray excited lumines-

Reference [27] Energy,cm^{-1}	Reference [40] Energy,cm^{-1}	Reference [41] Energy,cm^{-1}	Reference [43] Energy,cm^{-1}	This Work Energy,cm^{-1}
32,800	30,769	30,970	30,760	30,468
36,900	-	35,870	-	-
-	39,683	39,514	39,670	39,931
41,500	41,841	-	41,828	41,622
-	44,529	-	44,039	44,038
-	49,261	50,000	49,245	50,290

Table 3.5: Observed $5d^1$ energy levels for Ce^{3+} tetragonal phosphate crystals. For References [27,40,41] the crystal is YPO_4. For this work the crystal is $LuPO_4$.

Reference [41]		Reference [42]		This Work	
Energy,cm^{-1}	Symmetry	Energy,cm^{-1}	Symmetry	Energy,cm^{-1}	Symmetry
-	-	21,733[a]	$\Gamma_4 \rightarrow \Gamma_7$	-	-
30,970	$\Gamma_5 \rightarrow \Gamma_6 \oplus \Gamma_7$	30,970[b]	$\Gamma_5 \rightarrow \Gamma_6 \oplus \Gamma_7$	30,468	Γ_7
35,870	$\Gamma_3 \rightarrow \Gamma_7$	35,870[b]	$\Gamma_1 \rightarrow \Gamma_6$	-	-
39,514	$\Gamma_4 \rightarrow \Gamma_7$	39,514[b]	$\Gamma_3 \rightarrow \Gamma_7$	39,931	Γ_6
-	-	-	-	41,622	Γ_7
-	-	-	-	44,038	Γ_6
50,000	$\Gamma_1 \rightarrow \Gamma_6$	-	-	50,290	Γ_7

(a) Calculated using modelled values for the crystal field.
(b) Energy values from Reference [41].

Table 3.6: Symmetry assignments for $5d^1$ levels of Ce^{3+} tetragonal corresponding double group representations (spin included).

cence and excitation spectra of powders of 1% Ce^{3+} in YPO_4. Luminescence peaks were observed at 28,240 cm^{-1}, 30,367 cm^{-1}, 36,419 cm^{-1}, 38,494 cm^{-1}, 41,105 cm^{-1}, 43,559 cm^{-1}, and 50,109 cm^{-1}. All of these luminescence peaks except the highest peak at 50,109 cm^{-1} could be assigned to transitions originating from the excitation peaks observed at 30,760 cm^{-1}, 39,670 cm^{-1}, 41,828 cm^{-1}, 44,039 cm^{-1}, and 49,245 cm^{-1} and terminating on the $4f^1$ multiplets, $^2F_{5/2}$ or $^2F_{7/2}$.

3.3.3 The $5d^1$ Configuration in Ce^{3+}:$LuPO_4$, This Work

Shown in Figure 3.6 is the unpolarized absoprtion ($\approx$10K) spectrum of $Ce_{.20}Lu_{.80}PO_4$.

Seven broad feature appear in the spectrum between 30,000 cm^{-1} and 50,000 cm^{-1}

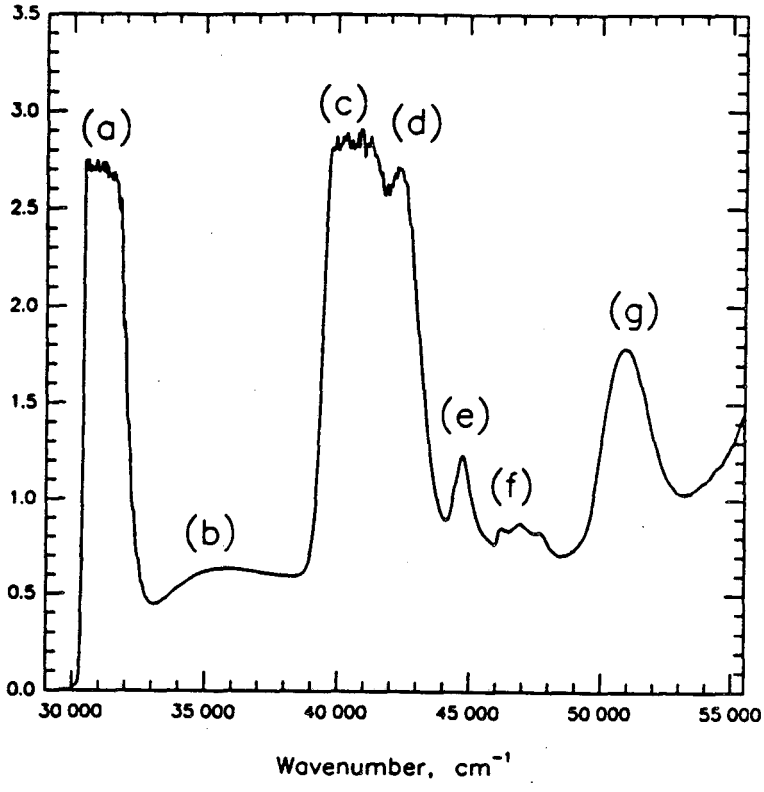

Figure 3.6: Low temperature (10K) absorption spectrum of $Ce_{.20}Lu_{.98}PO_4$. Features a,c,d,e,and g are attributed to Ce^{3+} absorption. Features b and f are attributed to other sources. The resolution of the spectrum is approximately 10 cm^{-1}.

and are labelled (a) through (g). As pointed out previously, there should be only five levels associated with associated with the cerium ion in D_{2d} symmetry. The question is which features are the five associated with absorption by cerium ions and which features are from either the $LuPO_4$ or, more likely, impurities in the $LuPO_4$.

For comparison purposes the absorption spectra of a crystal of pure $LuPO_4$ and crystals of $LuPO_4$ doped with various other rare earth ions were taken. A sampling of these spectra is shown in Figure 3.7. All of the crystals have the absorption feature (f) at approximately 46,500 cm^{-1}. Thus, this feature is attributed to an impurity in the $LuPO_4$ such as possibly Pb^{3+} from the lead flux in which the crystals are grown. Out of the six remaining features (b) and (e) appear to be the most likely impurity candidates. The feature labelled (e) at approximately 44,500 cm^{-1} could possibly be attributed to absorption from Pr^{3+} impurity since the Pr^{3+}:$LuPO_4$ crystal shows a broad absorption in this region. However, the character of this absorption peak in Pr^{3+}:$LuPO_4$ is enough different from the feature (e) in Ce^{3+}:$LuPO_4$ to make this identification unlikely. In the

final analysis the feature labelled (b) at approximately 35,000 cm^{-1} is taken as being the extra feature not attributable to cerium ion. This choice is based on the fact that the absorption spectra of the blank $LuPO_4$ crystal and the other crystals with different rare earth ions, in general displayed broad smooth features similar to feature (b). This choice is confirmed by the earlier work described in the previous section. Even though a feature at approximately 35,000 cm^{-1} was observed in several of the experiments[27,41] this feature was never observed in a selective excitation spectrum. The choice is also confirmed by absorption spectra taken of Ce^{3+}:$LuPO_4$ with varying concentrations of Ce^{3+}. These spectra are given in Appendix B of this chapter. In conclusion, the features (a) ($\approx$31,000 cm^{-1}), (c) ($\approx$40,300 cm^{-1}), (d) ($\approx$42,000 cm^{-1}), (e) ($\approx$44,500 cm^{-1}), and (g) ($\approx$50,500 cm^{-1}) are identified as originating from cerium ion absorption. This is in good agreement with references [40],[43].

Before proceeding further it should be noted that Figure 3.7 shows absorption features for Yb^{3+}:$LuPO_4$ and Eu^{3+}:$LuPO_4$ at approximately 50,000 cm^{-1}. However, from Figure 3.4 it can be seen that Eu^{3+} and Yb^{3+} should have first excited configurations that are much higher in energy than 50,000 cm^{-1}. The observed features are identified as so called *charge transfer* transitions in which a ligand charge is transferred to a rare earth ion 4f orbital. This is supported by the fact that the ions Eu^{3+} with a ground configuration $4f^6$ (one e^- short of a half filled shell) and Yb^{3+} with a ground configuration $4f^{13}$ (one e^- short of a completely filled shell) are expected to have *charge transfer* bands at lower energies than the other rare earth ions [26]. The fact that the *charge transfer* bands are lower in energy than the states associated with the first excited configuration of the rare earth ion may say something to how *molecular* these excited configurations are. However, for Ce^{3+} in $LuPO_4$ the *charge transfer* bands are expected to be much higher in energy than the highest state of the $5d^1$ configuration at 50,000 cm^{-1}.

Of the five levels of the Ce^{3+} ion in D_{2d} symmetry two should be Γ_6 levels, and three should be Γ_7 levels. The ground state of the $4f^1$ configuration is known to be a Γ_6 level. From the electric dipole selection rules in Section 3.3.2 it is known that in $\hat{\mathbf{X}} = \hat{\mathbf{Y}}$ polarization all transitions are allowed, and in $\hat{\mathbf{Z}}$ polarization only transitions in which the symmetry of the states changes are allowed. Therefore, for low temperature (ground

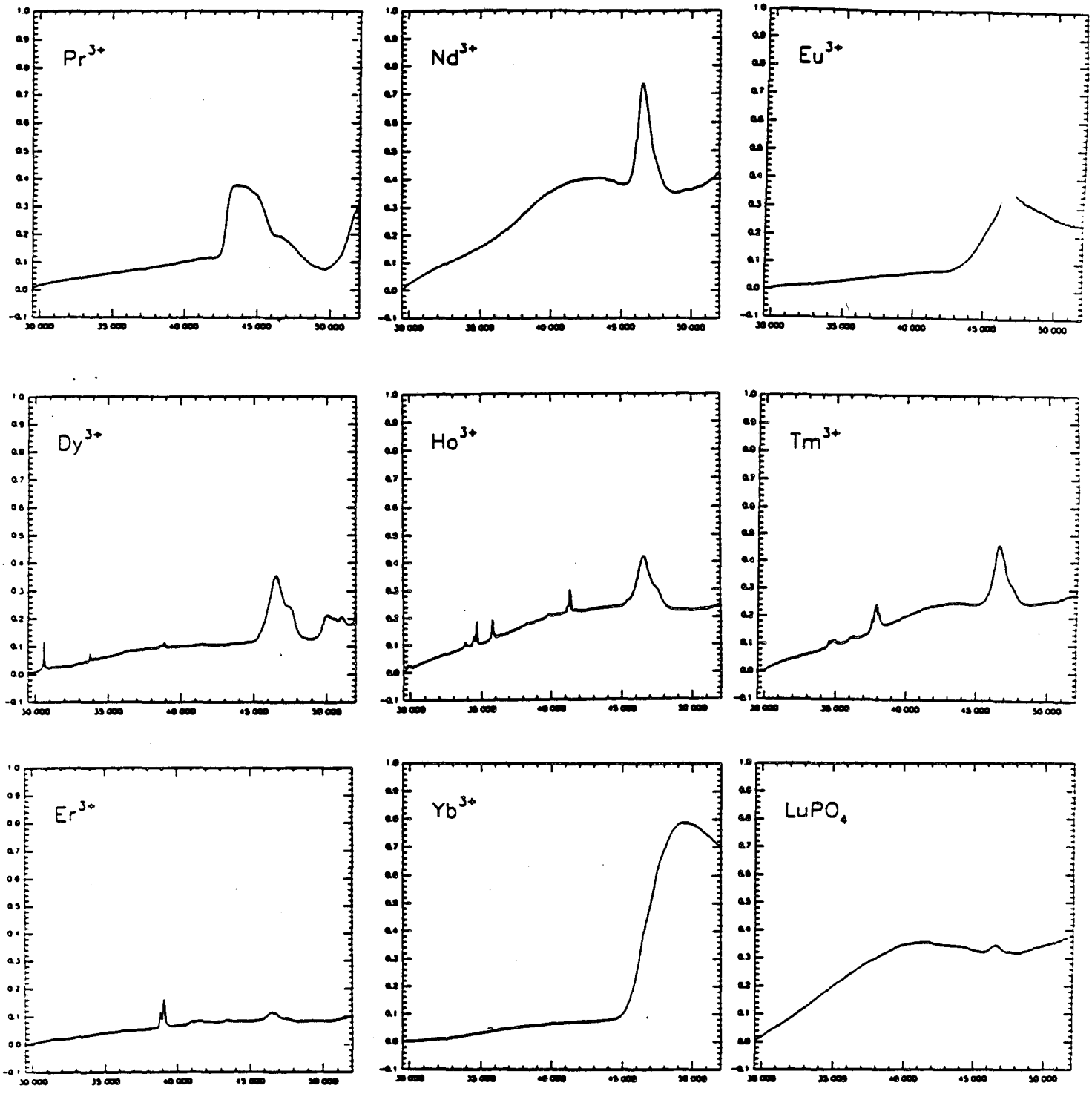

Figure 3.7: Room temperature absorption spectra for $LuPO_4$ and various rare ions doped into $LuPO_4$, RE^{3+}:$LuPO_4$.

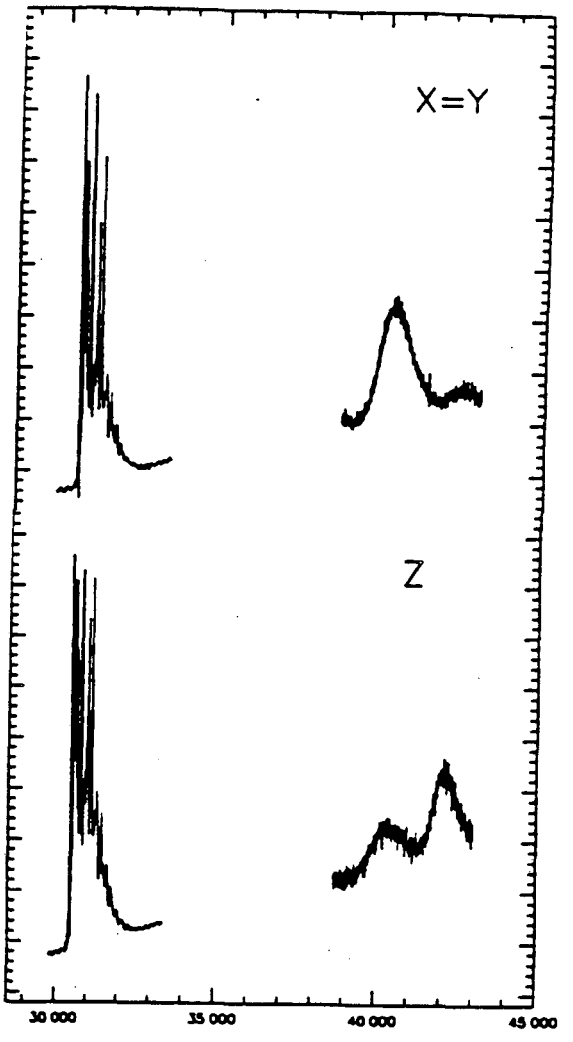

Figure 3.8: Polarized low temperature (≈10K) absorption spectra of $Ce_{.01}Lu_{.99}PO_4$. No data are available above the cutoff energy of the polarizers at 43,000 cm^{-1}.

state populated only) $5d^1$ configuration absorption spectra polarized along the $\hat{\mathbf{Z}}$ axis only the three Γ_7 levels should appear. However, the $5d^1$ absorption spectra show no strong polarization behavior. Polarization spectra were taken using the high resolution absorption experimental setup described in Section 2.3.1. Unfortunately, spectra could only be taken up to the cutoff energy of the polarizers at approximately 43,000 cm^{-1}. In this range the polarization properties of the three lines at 31,000 cm^{-1}, 41,300 cm^{-1}, and 42,000 cm^{-1} could be observed. Figure 3.8 shows the polarized spectra for these lines. As can be seen from the figure there are differences in the two polarizations but no lines disappear in $\hat{\mathbf{Z}}$ polarization as expected.

It is proposed that the lack of strong polarization behavior is a result of the nature of the $5d^1$ peaks. The true nature of the peaks is elucidated by the low temperature high

resolution absorption spectrum of the lowest energy level as shown in Figure 3.9. Under closer inspection the broad absorption line exhibits detail. The sharp peak on the low energy side is identified as the pure electronic-electronic or 0-0 transition from the ground state. This 0-0 peak has either Γ_6 or Γ_7 symmetry. The other features on the broad peak correspond to transitions to states that are couplings between the Ce^{3+} electronic state and one or more optical phonons of the lattice. In fact, given the energy of the pure electronic-electronic transition and the energies of the optical phonons of the crystal it is possible to explicitly assign the individual spectral features to given optical phonons or to combinations of more than one optical phonons. Table 3.7 lists the energy shifts relative to the 0-0 peak of all the individual spectral features in the broad peak. The reader may note the similarities between this table and Table 2.3 which displays the energies of the optical phonons observed in Ce^{3+}:$LuPO_4$ by Raman scattering experiments. However, it should be noted that the Raman experiments only yield the energies of the even (*gerade*) parity optical phonons and not the odd (*ungerade*) parity optical phonons which may also couple to the electronic states. The coupled electron-phonon states have symmetries that are determined by both the symmetry of the electronic state and the symmetry of the optical phonon(s) involved. Therefore, the broad absorption peak is not expected to show any uniform polarization behavior. Only the sharp individual spectral peaks will show definite polarization behavior.

The polarization of an individual feature is dependent on the symmetry of that feature. The symmetry of a coupled electron-phonon state is given by the direct product of Γ_p and Γ_e, where Γ_e is the irreducible representation of D_{2d} labelling the electronic state and Γ_p is the irreducible representation of D_{2d} corresponding to the D_{4h} label for the phonon (see Section 2.1.2). Given the symmetry of the coupled state the polarization behavior is simply given by the electric dipole selection rules for D_{2d} given previously.

Figure 3.10 shows the low temperature high resolution polarization spectra of the lowest energy peak. The first observation to be made is that the 0-0 peak at 30,468 cm^{-1} does not vanish in $\hat{\mathbf{Z}}$ polarization. Given that the $4f^1$ ground state is a Γ_6 state, it follows that the pure electronic state must have Γ_7 symmetry. As far as the polarization behavior of the coupled electron-phonon peaks, the group of peaks marked by the numeral (1) in

Peak Location $Energy_{Peak}$ - $Energy_{0-0}$, cm^{-1}
20
31
111
123*
155
175*
195
224
234
302*
317
332*
427
444*
456
512
536
635
661*
681
786
839
964
994
1070*
1169
1198
1319
1342

Table 3.7: Energy shifts of electron-phonon peaks from the 0-0 peak in the low temperature (10K) absorption spectrum of $Ce_{.01}Lu_{.99}PO_4$. Entries marked with asterisks are features correlated with even parity optical phonons observed from Raman scattering experiments.

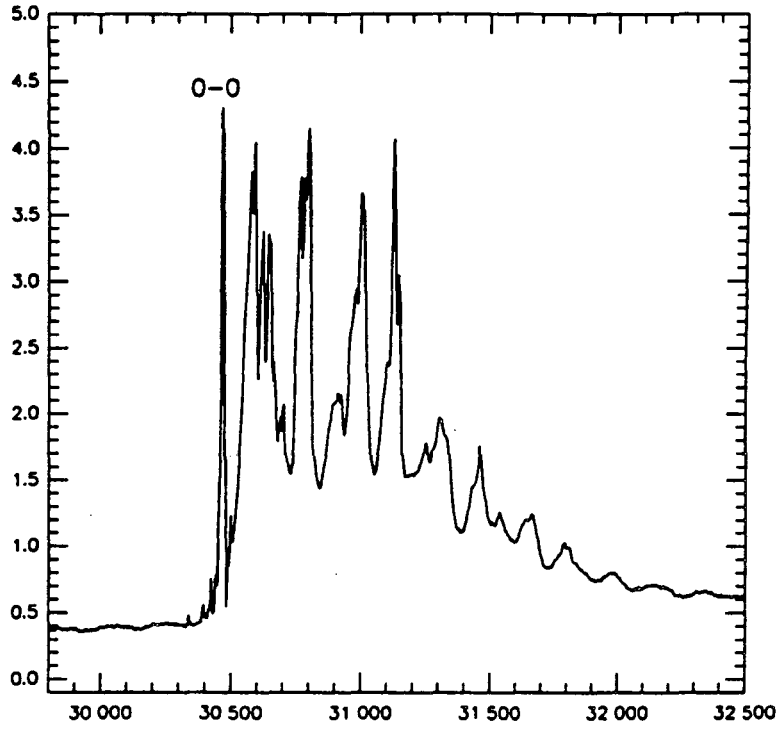

Figure 3.9: Low temperature (10K) absorption spectrum of the lowest energy $5d^1$ level of $Ce_{.01}Lu_{.99}PO_4$. Resolution is approximately 4 cm^{-1}.

(1) in Figure 3.10 serves as a good example. The lowest energy feature is at 302 cm^{-1} and may be assigned to the $D_{4h}(E_g) \longrightarrow D_{2d}(\Gamma_5)$ symmetry phonon at 307 cm^{-1} listed in Table 2.3. The highest energy feature is at 329 cm^{-1} and may be assigned to $D_{4h}(B_{2g}) \longrightarrow D_{2d}(\Gamma_3)$ symmetry phonon at 329 cm^{-1} listed in Table 2.3. Therefore, the symmetry label of the lowest energy feature is given by $\Gamma_7 \otimes \Gamma_5 = \Gamma_6 \oplus \Gamma_7$, while the symmetry label of the highest energy feature is given by $\Gamma_7 \otimes \Gamma_3 = \Gamma_6$ Thus, the electric dipole transition in $\hat{\mathbf{Z}}$ polarization from the Γ_6 ground state is allowed for the lowest energy feature but not for the highest energy feature. Accordingly the polarization spectra shows a marked decrease in the absorption of the highest energy feature in $\hat{\mathbf{Z}}$ polarization.

Clearly, in order to assign symmetries of the other pure electronic states in the $5d^1$ configuration it is necessary to observe the polarization behavior of the respective 0-0 lines. Unfortunately, high resolution spectra of the upper levels do not resolve the 0-0 peaks. It is assumed that non-radiative decay rates are so large for these upper levels that the individual spectral features are lifetime broadened to the point where they are

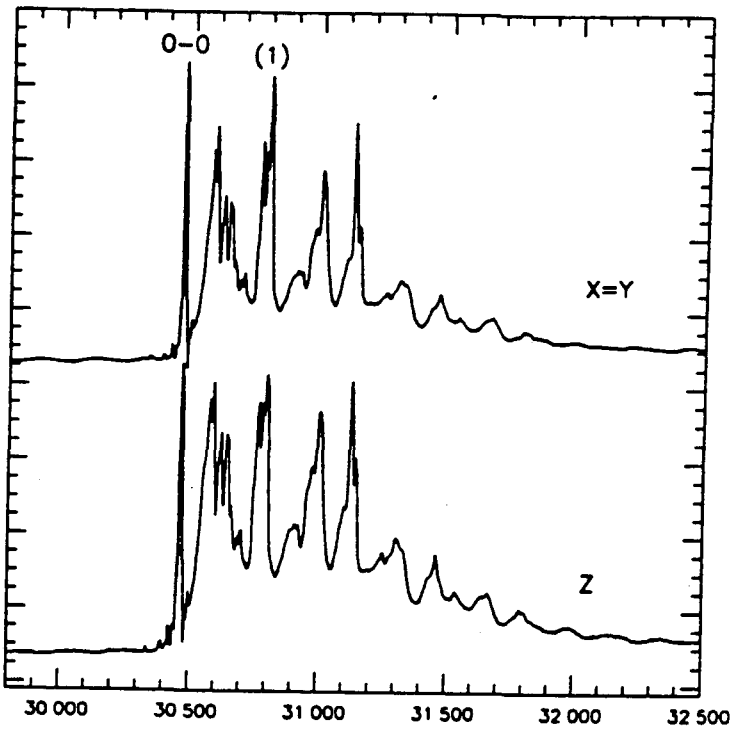

Figure 3.10: Low temperature polarization spectra of $Ce_{.01}Lu_{.99}PO_4$. The 0-0 transition is shown. (1) labels the location of coupled electron-phonon transition displaying polarization behavior. Resolution is 4 cm^{-1}.

symmetries of the remaining four levels.

3.3.4 Crystal Field Fit, $5d^1$ Configuration in Ce^{3+}:$LuPO_4$

The energy level structure of the $5d^1$ configuration may be modelled by a parameterized Hamiltonian similar in form to the one used previously for modelling of the $4f^1$ configuration. As stated in Section 3.3 the validity of using such an approach for the less atomic like $5d^1$ configuration is questionable. However, the approach is the most straightforward, and its validity will be tested by the results obtained.

The parameterized Hamiltonian is of the form

$$\begin{aligned} H &= H_{center-of-gravity} + H_{spin-orbit} + H_{crystal-field} \\ H_{center-of-gravity} &= F_0 \\ H_{spin-orbit} &= \zeta_{5d}(\vec{l}\cdot\vec{s}) \\ H_{crystal-field} &= B_0^2(C_0^2) + B_0^4(C_0^4) + B_4^4(C_4^4 + C_{-4}^4) \end{aligned} \tag{3.6}$$

where F_0 is the parameter fixing the mean energy of the $5d^1$ configuration, ζ_{5d} is the

spin-orbit parameter, and the B_q^k's are the crystal field parameters. For *d* electrons only B_q^k's with $k \leq 4$ have non-zero matrix elements.

In the fit the energy locations of the pure electronic levels should be used. For the four upper levels, for which no sharp 0-0 peak was observed, the location of the pure electronic state is estimated by assuming that the difference in energy between the maximum of the broad absorption peak and the sharp 0-0 peak is the same for all levels and thus can be derived from the observed difference in the lowest level.

As far as the symmetry assignments for the four upper levels , it is known that two are Γ_6 states and two are Γ_7 states. This gives the possibility of six different combinations. The assignment scheme that results in the most *physically* correct values for the Hamiltonian parameters is assumed to be correct. The value of the spin-orbit parameter is expected to be the same or slightly smaller than the free-ion value of 995.6 cm^{-1}[17] The expected values of the crystal-field parameters are derived from the values obtained previously for the $4f^1$ configuration in $LuPO_4$. Following a strict electro-static interpretation of the crystal field and using Equation 3.3 it can be seen that the 4f parameters and the 5d parameters are related by

$$\frac{(B_q^k)_{5d}}{(B_q^k)_{4f}} = \frac{< r^k >_{5d}}{< r^k >_{4f}} \tag{3.7}$$

where $< r^k >$ is the expectation value of the k^{th} power of the radial distance of the electron from the cerium nucleus. Values for $< r^k >_{5d}$ and $< r^k >_{4f}$ in Ce^{3+} have been determined in a Hartree-Fock type calculation [44]. The resulting ratios of $\frac{<r^4>_{5d}}{<r^4>_{4f}} = 13.5$ and $\frac{<r^2>_{5d}}{<r^2>_{4f}} = 4.5$ coupled with the $4f^1$ crystal field parameters listed in Table 3.3 yields expected values for the $5d^1$ crystal field parameters of $B_0^2 = 117$ cm^{-1}, $B_0^4 = 3,550$ cm^{-1}, and $B_4^4 = -16,835$ cm^{-1}.

There is only one assignment scheme that results in fitted crystal field parameters which have the same signs as the expected values. The assignments are listed in Table 3.8 along with the angular parts of the wavefunctions obtained from fitting the observed energies.

As can be seen the fit to the observed energy levels is perfect . Of course this is expected with five parameters and five levels. The more reassuring feature of the

Calculated Energy (cm^{-1})	Observed Energy (cm^{-1})	Symmetry	Wave function $\sum_{J,J_z} a(J,J_z)^{2S+1}L\|J,J_z\rangle$
30,468	30,468	Γ_7	$.702^2\mathrm{D}\|\frac{3}{2},-\frac{3}{2}\rangle + .661^2\mathrm{D}\|\frac{5}{2},\frac{5}{2}\rangle$ $+.266^2\mathrm{D}\|\frac{5}{2},-\frac{3}{2}\rangle$
39,931	39,931	Γ_6	$.953^2\mathrm{D}\|\frac{3}{2},-\frac{1}{2}\rangle + .304^2\mathrm{D}\|\frac{5}{2},-\frac{1}{2}\rangle$
41,622	41,622	Γ_7	$-.888^2\mathrm{D}\|\frac{5}{2},-\frac{3}{2}\rangle + .445^2\mathrm{D}\|\frac{3}{2},-\frac{3}{2}\rangle$ $+ - .117^2\mathrm{D}\|\frac{5}{2},\frac{5}{2}\rangle$
44,038	44,038	Γ_6	$.953^2\mathrm{D}\|\frac{5}{2},-\frac{1}{2}\rangle + -.304^2\mathrm{D}\|\frac{3}{2},-\frac{1}{2}\rangle$
50,290	50,290	Γ_7	$-.742^2\mathrm{D}\|\frac{5}{2},\frac{5}{2}\rangle + .556^2\mathrm{D}\|\frac{3}{2},-\frac{3}{2}\rangle$ $+.376^2\mathrm{D}\|\frac{5}{2},-\frac{3}{2}\rangle$

Table 3.8: Ce^{3+}:$LuPO_4$ $5d^1$ wavefunctions.

	Fitted Value,cm^{-1}	Expected Value,cm^{-1}
ζ_{5d}	1,114	995.6
B_0^2	3,785	117
B_0^4	3,968	3,550
B_4^4	-24,543	-16,835
F_0	41,271	-

Table 3.9: Comparison of expected and fitted values of Hamiltonian parameters for $5d^1$ configuration states of $Ce_{.20}Lu_{.80}PO_4$.

fit is the closeness of the fitted Hamiltonian parameters to those expected from physical arguments. A comparison of the fitted values to expected values is displayed in Table 3.9.

3.4 Intensities of Electronic Raman Scattering in Ce^{3+}:$LuPO_4$

In this section the intensities of electronic Raman scattering transitions observed between crystal field levels of the $4f^1$ configuration of Ce^{3+} in crystals of $LuPO_4$ are compared with the intensities calculated from theory. In the introductory section of this chapter the motivations for doing this particular comparison were briefly described in general terms. Before beginning the analysis of the Ce^{3+} work we offer a more complete description of the large volume of work leading to this study.

3.4.1 Intensities of Optical Processes in Transparent Rare Earth Solids

The first experiments on the optical properties of rare earth ions in the solid state were performed by Becquerel in the early 1900's [45,46,47]. He observed in the spectra of rare earth salts unusually narrow line widths; something not normally associated

with solid state systems. It was later argued that the observed transitions were intra-configurational, being between states of the $4f^N$ configuration of the rare earth ions. The explanation offered was that the 4f orbitals are inside the filled $5s^2 5p^6$ orbitals, which shields them from the host crystal; the result is a gaseous-like narrow line spectra in a solid state environment.

An interesting aspect of this explanation is that transitions between states from the same configuration are not allowed by an electric dipole transition (the first order term in the multi-pole expansion of the Hamiltonian describing the light-ion interaction). States of a given configuration have the same parity and the parity must change during an electric dipole transition. Only the higher order, and much less intense, multi-pole processes such as magnetic dipole and electric quadrupole could facilitate such parity conserving transitions. However, this fit in well with the observation that the transitions observed in the rare earth solids are relatively weak with oscillator strengths on the order of $f \approx 10^{-6}$ (normal electric dipole oscillator strengths are on the order of 1-10^{-2}). Unfortunately, the magnetic dipole and electric quadrupole mechanisms could not explain the large number of lines observed. Angular momentum selection rules for magnetic dipole, $\Delta J \leq 1, \Delta L \leq 1, \Delta S = 0$, and electric quadrupole, $\Delta J \leq 2, \Delta L \leq 2, \Delta S = 0$, restrict the number of allowed transitions. Furthermore, these mechanisms could not explain why the rich rare earth spectra appeared only in solids.

In order to explain this mystery Van Vleck in his classic 1937 paper[48] proposed the mechanism of "*forced electric dipole*". In crystals without inversion symmetry about the rare earth ion site odd parity components of the crystal field can mix into the states of the ground $4f^N$ configuration, states from opposite parity configurations such as $4f^{N-1}$nd and $4f^{N-1}$ng. Electric dipole transitions are formally parity allowed between the zeroth order $4f^N$ part of one wave function and the admixed $4f^{N-1}$nl' part of another wave function. The fact that the admixing is small explains the small observed oscillator strengths. Furthermore, under this mechanism the usual angular momentum selection rules are almost completely relaxed. In a sense the crystal field carries the additional angular momentum necessary in large ΔJ and ΔL transitions.

Much later Judd [15] and Ofelt [16], working concurrently but independently, quan-

tified the mechanism proposed by Van Vleck. In their respective calculations, the initial and final state wave functions are written in the form,

$$|f\rangle = |f^0\rangle + \frac{1}{\hbar}\sum_r \frac{\langle r|V|f^0\rangle}{\omega_r - \omega_{f^0}}|r\rangle \tag{3.8}$$

where $|f^0\rangle$ is the zeroth order wave function including only states from the $4f^N$ configuration. The states $|r\rangle$ are from excited configurations. V is some operator than can mix states from different electronic configurations. Most commonly, V is the crystal field Hamiltonian.

Given this, the electric dipole matrix element between a state $|i\rangle$ and a state $|f\rangle$ is given by

$$\langle f|D|i\rangle \propto \frac{1}{\hbar}\sum_r \left(\frac{\langle f^0|D|r\rangle\langle r|V|i^0\rangle}{\omega_r - \omega_i} + \frac{\langle f^0|V|r\rangle\langle r|D|i^0\rangle}{\omega_r - \omega_f}\right) \tag{3.9}$$

where D is an electric dipole operator. Only the odd parity terms in V are non-zero in the sum. The states $|r\rangle$ are from the excited configurations with parity opposite that of the $4f^N$ configuration.

Equation 3.9 is the real starting point of the calculation. In almost all cases, the number of states in the sum is large and very little is known about their nature. Performing the sum explicitly is not practical, and some simplifying approximation must be made. The essence of the approximation employed by both Judd and Ofelt is the following. If one average value may be assigned to all the energy denominators in Equation 3.9, then the equation may be rewritten in the form

$$\langle f|D|i\rangle \approx \frac{1}{\hbar\Delta\omega_{avg}}\sum_r \left(\langle f^0|D|r\rangle\langle r|V|i^0\rangle + [\langle f^0|V|r\rangle\langle r|D|i^0\rangle\right) \tag{3.10}$$

Because the sum over the states $|r\rangle$ represents the sum over the eigenstates of the Hamiltoninan, a complete set, the closure relation,

$$\sum_r |r\rangle\langle r| = 1 \tag{3.11}$$

holds. The sum may be eliminated so that, there is an expression with a matrix element between the initial and final states only.

$$\langle f|D|i\rangle \approx \frac{1}{\hbar\Delta\omega_{avg}}\langle f^0|DV|i^0\rangle \tag{3.12}$$

However, the approximation that all the eigenstates, $|r\rangle$, may be assigned one energy is rather gross and stronger than the one actually employed by Judd and Ofelt in their respective calculations. Judd and Ofelt assumed that all the states $|r\rangle$ from a given excited configuration could be assigned one average energy, a much more reasonable approximation.

Given this, some form of the closure procedure can be performed piecewise for the states of each excited configuration separately. The closure does not include the radial variable but only the angular variables. As described in the introduction of this chapter, the result is a solution with two parts. One part includes matrix elements between the angular parts of the initial and final state wave functions. These terms are easily evaluated. The second part contains energy denominators, radial integrals, and the radial parts of crystal field operators for the ground and excited configurations. These terms are not easily evaluated and must be treated as parameters. In general, the number of parameters necessary to describe the oscillator strengths between all the crystal field levels depends on the symmetry of the crystal field. However, what are most often measured are integrated multiplet to multiplet oscillator strengths. Low temperatures and greater care are necessary to measure the crystal field to crystal field level strengths. For multiplet to multiplet transitions, assuming equal population of all crystal field levels in a given multiplet, all the oscillator strengths in a crystal are described by only three parameters, known as the Judd-Ofelt parameters $(\Omega_2, \Omega_4, \Omega_6)$. The theory has been tested on many systems and has been very successful in predicting relative oscillator strengths.

Following the publications of Judd's and Ofelt's calculations, Axe [14] realized its applicability to the calculation of the intensities of two-photon processes in rare earth ions. Unlike one photon processes, two-photon transitions between states belonging to the same configuration are formally parity allowed. Examples of two photon processes are two photon absorption, spontaneous two photon emission, and Raman scattering. From the second-order perturbation term of the light-ion interaction (in the electric dipole approximation), the amplitude of a two-photon process may be written in terms

of second-rank tensor, $\boldsymbol{\alpha}$, given by

$$\alpha_{\rho\sigma} = -\frac{1}{\hbar}\sum_{r}\left[\frac{\langle f|D_\rho|r\rangle\langle r|D_\sigma|i\rangle}{\omega_{ri}-\omega_1} + \frac{\langle f|D_\sigma|r\rangle\langle r|D_\rho|i\rangle}{\omega_{rf}-\omega_2}\right] \tag{3.13}$$

The subscripts ρ and σ label the polarizations of the two photons with angular frequencies ω_1 and ω_2, respectively. D_ρ and D_σ are the corresponding components of the electric dipole operator. The states, $|r\rangle$, are excited opposite parity configurations. The terms $\hbar\omega_{ri}$ and $\hbar\omega_{rf}$ represent the the energy differences between the states $|r\rangle$ and $|i\rangle$, and between the states $|r\rangle$ and $|f\rangle$, respectively. The above expression is explicitly for a two-photon absorption process between a state $|i\rangle$ and a state $|f\rangle$. However, the expressions for other two-photon processes are easily obtained by changing the sign(s) of the photon energies. For instance, the amplitude for electronic Raman scattering is given simply by replacing ω_2 by $-\omega_2$.

Equation 3.13 above and Equation 3.9 for "*forced electric dipole*" transitions are almost identical, the only major exception being that the odd parity crystal operators have been replaced by a second electric dipole operator. The closure approximation of Judd and Ofelt can be directly applied to Equation 3.13. The result of the calculation is similar in form to the result obtained for the one photon case, but is simpler because of the elimination of the crystal field operators.

To help elucidate some finer points of the calculation and its result, we rewrite Equation 3.13 in the following form;

$$\begin{aligned}\alpha_{\rho\sigma} &= -\frac{1}{\hbar}\sum_{r}\left\{\frac{1}{2}\left[\frac{1}{\omega_r-\omega_1}+\frac{1}{\omega_r \mp \omega_2}\right]\langle f|D_\rho D_\sigma + D_\sigma D_\rho|i\rangle\right. \\ &+ \left.\frac{1}{2}\left[\frac{1}{\omega_r-\omega_1}-\frac{1}{\omega_r \mp \omega_2}\right]\langle f|D_\rho D_\sigma - D_\sigma D_\rho|i\rangle\right\}\end{aligned} \tag{3.14}$$

where we have made the approximation that $\omega_{ri} \approx \omega_{rf} \approx \omega_r$ and where $\langle f|D_\sigma D_\rho|i\rangle$ symbolizes $\langle f|D_\sigma|r\rangle\langle r|D_\rho|i\rangle$. Included in Equation 3.13 are the signs for both two photon absorption (upper signs) and electronic Raman scattering (lower signs). Performing the Judd-Ofelt closure over the two terms yields the following results. The closure over the first term results in a coupling between electric dipole operators (having angular momentum 1) that yields operators carrying angular momentum 0 and 2. These operators may be conveniently expressed in terms of the spherical unit tensor operators $\mathbf{U^{(0)}}$ and

$\mathbf{U^{(2)}}$. The unit tensor $\mathbf{U^{(0)}}$ is a scalar and can only connect initial and final states that are the same. Thus, this term only contributes to Rayleigh (elastic) scattering and is disregarded here. Closure over the second term in Equation 3.14 results in an operator carrying angular momentum 1 represented by the unit spherical tensor $\mathbf{U^{(1)}}$.

Thus, the final result may be expressed as a sum of two parts each corresponding to one of the terms in Equation 3.14.

$$\alpha_{\rho\sigma} = F_2\langle f|\mathbf{U^{(2)}}|i\rangle + F_1\langle f|\mathbf{U^{(1)}}|i\rangle \tag{3.15}$$

The matrix elements are between the angular parts of the initial and final state wavefunctions, and are easily evaluated once these wavefunctions are known. The terms F_1 and F_2 are dependent on the average energies of the opposite parity configurations and the radial parts of the 4f and excited configuration wavefunctions. In general, very little is known with certainty regarding the excited configuration average energies and the radial wavefunctions. Thus, F_1 and F_2 can not be evaluated explicitly in general, and must be treated as parameters.

Axe [14] pointed out that for two photon absorption from a single laser source ($\omega_1 = \omega_2$), the second term in Equation 3.14, and thus the second term in Equation 3.15 , are identically zero. In this case the expression for the two photon amplitude reduces to

$$\alpha_{\rho\sigma}^{TPA} = F_2\langle f|\mathbf{U^{(2)}}|i\rangle \tag{3.16}$$

In a specific rare earth ion-crystal system, the relative cross-sections for two photon absorption transitions between various $4f^N$ energy levels is given by the relative values of $|\langle r|\mathbf{U^{(2)}}|i\rangle|^2$. This is a useful result in that no parameters are required in the description of the relative cross-sections.

Downer *et al.* [49,50,51], noting this, undertook the study of relative two photon absorption cross-sections in rare earth crystals as a "*new test*" of the Judd-Ofelt closure approximation. Experiments were performed on the $4f^7$ systems, Eu^{2+} and Gd^{3+}, doped into crystals of LaF_3. They found that many transitions formally parity forbidden ($\Delta J > 2$, $\Delta L > 2$, and$\Delta S \neq 0$) by the theory were observed and that these forbidden transitions were sometimes stronger than neighboring allowed transitions. Judd and

Pooler [52] suggested that these anomalous transitions could be explained by expanding the standard second-order theory to third and fourth order in perturbation. These higher order perturbation terms include effects of the crystal field and spin-orbit coupling on the virtual intermediate states. A typical third-order term has the form

$$\alpha^{(3)}_{\rho\sigma} = (\frac{1}{\hbar})^2 \sum_{j,m} \left[\frac{\langle f|D_\rho|j\rangle\langle j|H'|m\rangle\langle m|D_\sigma|i\rangle}{(\omega_{im}-\omega)(\omega_{ij}-\omega)} + \frac{\langle f|D_\sigma|j\rangle\langle j|H'|m\rangle\langle m|D_\rho|i\rangle}{(\omega_{im}+\omega_s)(\omega_{ij}+\omega_s)} \right] \qquad (3.17)$$

where $|j\rangle$ and $|m\rangle$ are states from an excited opposite parity configuration and H' is some interaction Hamiltonian, such as the crystal field or the spin-orbit interaction, that acts on these states. By the addition of such terms, Downer *et al.* were able to expand the two photon absorption selection rules to $\Delta L, \Delta J \leq 6$ and $\Delta S \leq 1$ and adequately account for intensities of the anomalous transitions.

The possibility of Raman scattering transitions between the electronic levels of impurity ions in crystals was first discussed by Elliott and Loudon[53]. Hougen and Singh[54] were the first to observe such scattering using the lines of a mercury discharge lamp to excite electronic Raman scattering transitions between the ground state of Pr^{3+} in crystals of $PrCl_3$ and states of the $^3H_4$ (ground multiplet), $^3H_5$, $^3H_6$, $^3F_2$, $^3F_3$, and $^3F_4$ multiplets. Subsequently a large body of work on electronic Raman scattering in rare earth crystals has been presented by Koningstein and co-workers[55,56,57,58,59,60]. The first study of electronic Raman scattering intensities was carried out by Axe[14] . He calculated the expected values of the relative intensities for the transitions observed by Hougen and Singh[54] in their electronic Raman experiments in $PrCl_3$. To simplify the calculation, Axe assumed that $\omega_r \gg \omega_1$ and $\omega_r \gg \omega_2$, making the second term in Equation 3.14 (and therefore the second term in Equation 3.15) approximately zero. Thus, the relative intensities were given simply by the relative values of $|\langle f|\mathbf{U^{(2)}}|i\rangle|^2$, much as in the case of two photon absorption cross-sections. The comparison between the calculation and the data, although done only qualitatively, was quite satisfactory.

The approximation $\omega_r \gg \omega_1$ and $\omega_r \gg \omega_2$, although simplifying, removes from consideration an interesting aspect of electronic Raman scattering. Returning to Equation 3.14 we see the first term is symmetric with respect to the interchange of the polarization of the two photons, while the second term is anti-symmetric. It is apparent that

if both the first and second terms are non-zero, the resulting scattering intensity (the squared magnitude of the amplitude given in Equation 3.14) will be asymmetric with respect to the interchange of the incident and scattered photon polarizations. Recalling the correspondence between terms in Equations 3.14 and 3.15, we see that the degree of asymmetry will be dependent on how large the term $F_1\langle f|\mathbf{U^{(1)}}|i\rangle$ is compared to the term $F_2\langle f|\mathbf{U^{(2)}}|i\rangle$. The asymmetry is interesting in that it is not usually observed for vibrational Raman scattering. In vibrational Raman scattering transitions the electronic state of the system does not usually change, thus the second term in Equation 3.14 is zero. The possibilty of such an asymmetry in electronic Raman scattering was first discussed by Placzek[61] and later by Koningstein and Mortensen[58,59]. The first observation of scattering asymmetry was made by Kiel *et al.* [62,63] in studying electronic Raman scattering from Ce^{3+} in crystals of $CeCl_3$.

In this laboratory Becker *et al.* [11,64] have recently completed a thorough study of the intensities of electronic Raman scattering between crystal field levels of Er^{3+}, Tm^{3+} and Ho^{3+} in phosphate crystals (these crystals have the same structure as the $Ce_{.20}Lu_{.80}PO_4$ crystals of this work). Becker *et al.* observed no forbidden transitions. However, they did find differences between the observed relative scattering intensities and the values expected from theory.

Becker *et al.* measured the asymmetries of the various electronic Raman scattering transitions. As stated previously, the values of these asymmetries are directly related to the ratios $F_1\langle f|\mathbf{U^{(1)}}|i\rangle/F_2]\langle f|\mathbf{U^{(2)}}|i\rangle$. The matrix elements are easily evaluated, and thus, the measured asymmetries may be used to fit a value for the ratio F_1/F_2 (this value should be the same for all transitions in a given system). It was expected that the dominant contributions in the sum over virtual intermediate states would be from the states of the first excited configuration of the rare earth ion, $4f^{N-1}5d$. Given this assumption and an estimate of the mean energy of the first excite configuration, a value for the ratio F_1/F_2 may be calculated and compared the value obtained by fitting. For all three ions Tm^{3+}, Er^{3+}, and Ho^{3+} under excitation by visible light the expected value is 0.25. However, for Er^{3+} and Tm^{3+} the asymmetries and in fact all the observed relative intensities were best described by a value for F_1/F_2 of approximately 0. For Ho^{3+} the

best fit was given by a value of approximately -0.22.

It was later pointed out by Becker,Edelstein,Judd, Leavitt, and Lister [65] that the anomalous fitted values for the parameter F_1/F_2 could be explained by assuming g orbital type states contributed as virtual intermediate states in the scattering process. The g orbital states are calculated to contribute to the parameter value nearly equal but opposite in sign to that contributed by the d orbital states. The value of 0 for $TmPO_4$ and $ErPO_4$ was explained by assuming equal contribution from d and g orbitals while the value of -0.22 for $HoPO_4$ was explained as being the result of g orbital contributions solely.

This proposition that g orbital states contribute significantly as intermediate channels at first view might seem dubious. In the rare earth trivalent free ions the g orbitals are so high in energy as to make any contribution from them very small as compared to the contribution from d orbitals. However, it is argued that for rare earth ions in a crystal host the situation may be drastically altered. It may no longer be valid to view the intermediate states as atomic-like states of the rare earth ion. It may be more accurate to describe these intermediate states as molecular states of the rare earth ion and the surrounding ligands. *A priori*, such a molecular state is just as likely to have g orbital character as d orbital character. If indeed molecular orbitals were the important virtual intermediate states in a two photon process then a multiplet to multiplet two photon intensity for a given rare earth ion would be dependent on the particular host crystal in which it was imbedded. A recent experiment by Chase and Payne [66] shows that indeed this is the case for Nd^{3+} in crystals of YLF and YAG. The $^4I_{9/2} \longrightarrow {}^4G_{7/2}$ two photon absorption cross-section was an order of magnitude smaller in YLF than in YAG.

In conclusion, the corrections to the standard theory of two-photon processes have been refinements in the description of the virtual intermediate states. The intermediate states lie high in energy, in most cases in the vacuum ultra-violet region of the spectrum; and as a consequence, there is very little known about their nature. In the following sections the comparison of the observed electronic Raman scattering intensities to those calculated from theory is given for Ce^{3+} in $LuPO_4$. In this case there is the opportunity of actually examining at least a portion of the virtual intermediate states spectroscopically.

3.4.2 Calculation of Electronic Raman Scattering, Standard Theory

In this Section the expressions necessary for the calculation of electronic Raman scattering intensities are given in their full detail. At the end of the Section the electronic Raman scattering intensities are calculated for the specific case of Ce^{3+}:$LuPO_4$.

The intensity of light (polarization ρ) scattered from an incident beam (polarization σ) per unit solid angle by an electronic Raman process is given by,

$$\frac{(I_{scattered})_\rho}{\omega_s} = \frac{(I_{incident})_\sigma}{\omega}\omega\omega_s^3\left(\frac{e^4}{\hbar^2c^4}\right)|\alpha_{\rho\sigma}|^2 \tag{3.18}$$

where ω is the angular frequency of the incident light and ω_s is the angular frequency of the scattered light. For most situations $\omega \approx \omega_s$ yielding the ω^4 term discussed in most descriptions of light scattering phenomena. The term $\alpha_{\rho\sigma}$ represents one element in the 3 x 3 scattering tensor discussed in the previous section. Equation 3.13 of that section, written for two-photon absorption, is easily modified to obtain the scattering tensor element for an electronic Raman process between a state $|i\rangle$ and a state $|f\rangle$.

$$(\alpha_{\rho\sigma})_{fi} = -\frac{1}{\hbar}\sum_r\left[\frac{\langle f|D_\rho|r\rangle\langle r|D_\sigma|i\rangle}{\omega_r-\omega} + \frac{\langle f|D_\sigma|r\rangle\langle r|D_\rho|i\rangle}{\omega_r+\omega_s}\right] \tag{3.19}$$

where now ω is the angular frequency of the incident laser light and ω_s is the angular frequency of the Raman scattered light.

The rare earth ion's initial and final state wave functions are written, as discussed in Section 3.2, as linear combinations of Russell-Saunders terms,

$$\Psi_i = \sum_{J,M} a(i:SLJM)|SLJM\rangle. \tag{3.20}$$

The wave functions for Ce^{3+}:$LuPO_4$ are listed in Section 3.2.4.

Using the Judd-Ofelt approximation closure can be performed over the angular variables of the intermediate states. The calculation is facilitated by the use of spherical tensor operators. The result of the calculation is in terms of the spherical scattering tensors α^1 and α^2. They are given by

$$\begin{aligned}(\alpha_Q^K)_{fi} \;=\; & F(K,\omega)\sum_{SLJM}\sum_{S'L'J'M'} a^*(f:S'L'J'M')a(i;SLJM) \\ & \times(-1)^{J'-M}\begin{pmatrix} J' & K & J \\ -M' & Q & M\end{pmatrix} \\ & \times\langle S'L'J'||U^K||SLJ\rangle\end{aligned} \tag{3.21}$$

where K=1 and 2, Q=-K to K. The terms $a(f)$ and $a(i)$ are the coefficients in the expansion of the initial and final state wave functions.

The matrix elements of $\mathbf{U^{(1)}}$ and $\mathbf{U^{(2)}}$ are reduced matrix elements of the unit tensor operators mentioned in the previous section. They are easily evaluated using the tensor algebra relation

$$\begin{aligned}\langle S'L'J'||U^{(K)}||SLJ\rangle &= (-1)^{S'+L'+J+K}(2J+1)^{\frac{1}{2}}(2J'+1)^{\frac{1}{2}} \\ &\quad \left\{ \begin{array}{ccc} J' & K & J \\ L & S & L' \end{array} \right\} \langle L'||U^{(K)}||L\rangle \end{aligned} \tag{3.22}$$

and the following relations that define the unit tensors. The unit tensor for one electron is defined by

$$\langle l'||u^{(K)}||l\rangle = \left\{ \begin{array}{ll} 1 & \text{if } |l'-l| \geq K \leq l'+l \\ 0 & \text{otherwise} \end{array} \right. \tag{3.23}$$

For a system of N electrons

$$\mathbf{U}^{(K)} = \sum_{i=1}^{N} \mathbf{u}_i^{(K)} \tag{3.24}$$

The terms $F(1,\omega)$ (F_1) and $F(2,\omega)$ (F_2), which weight the relative importance of α^1 and α^2, are dependent on the radial parts of the ground and excited configurations and the average energies of the excited configurations. They are given by

$$\begin{aligned} F(K,\omega) &= \frac{1}{\hbar}\sum_{\chi}\left[\frac{1}{\overline{\omega}_{\chi f}-\omega}+(-1)^K\frac{1}{\overline{\omega}_{\chi f}+\omega}\right] \\ &\quad \times\langle l||c^{(1)}||l'\rangle^2\langle nl||r||n'l'\rangle^2 \\ &\quad (2K+1)^{1/2}\left\{ \begin{array}{ccc} 1 & K & 1 \\ l & l' & l \end{array} \right\}(-1)^K \end{aligned} \tag{3.25}$$

The sum over χ is a sum over opposite parity configurations, where $h\overline{\omega}_{\chi f}$ is the average energy of the given configuration. The labels l and l' are the orbital quantum numbers for the ground configuration and excited configurations, respectively.

Clearly to compute $F(1,\omega)$ and $F(2,\omega)$ one needs the radial wave functions and average energies of the ground and opposite parity excited configurations, something not normally known to any accuracy. If relative intensities are calculated the important quantity is the ratio , $F(1,\omega)/F(2,\omega)$. A value for this ratio may be computed if an assumption is made regarding which excited configurations contribute as virtual intermediate channels in the scattering process. For instance, if the lowest energy opposite

parity configuration, $4f^{N-1}5d$, is assumed to serve solely as the intermediate channel then it is easy to show from Equation 3.28 that

$$\frac{F(1,\omega)}{F(2,\omega)} \approx 1.3 \times \frac{\overline{\omega}_{4f^{N-1}5d}}{\omega} \tag{3.26}$$

However,*a priori*, it is possibly more systematic to treat $F(1,\omega)/F(2,\omega)$ as a parameter with a value chosen to best fit the observed intensities. Then from this value conclusions can be drawn regarding the nature of the virtual intermediate states. The most direct way to fit $F(1,\omega)/F(2,\omega)$ is through use of the observed asymmetry of the scattering. As was discussed in the previous section, the value of $F(1,\omega)/F(2,\omega)$ is directly related to this asymmetry. The connection may be seen in another way by looking at the transformation which gives the Cartesian scattering tensor elements in terms of the spherical tensor elements.

$$\begin{aligned}
\alpha_{xx} &= \frac{1}{2}(\alpha_2^{(2)} + \alpha_{-2}^{(2)}) - \frac{1}{\sqrt{6}}\alpha_0^{(2)} \\
\alpha_{yy} &= \frac{-1}{2}(\alpha_2^{(2)} + \alpha_{-2}^{(2)}) - \frac{1}{\sqrt{6}}\alpha_0^{(2)} \\
\alpha_{zz} &= \frac{2}{\sqrt{6}}\alpha_0^{(2)} \\
\alpha_{xy} &= \frac{-i}{\sqrt{2}}\alpha_0^{(1)} + \frac{-i}{2}(\alpha_2^{(2)} - \alpha_{-2}^{(2)}) \\
\alpha_{yx} &= \frac{i}{\sqrt{2}}\alpha_0^{(1)} + \frac{-i}{2}(\alpha_2^{(2)} - \alpha_{-2}^{(2)}) \\
\alpha_{xz} &= \frac{-1}{2}(\alpha_1^{(1)} + \alpha_{-1}^{1}) + \frac{-1}{2}(\alpha_1^{(2)} - \alpha_{-1}^{(2)}) \\
\alpha_{zx} &= \frac{1}{2}(\alpha_1^{(1)} + \alpha_{-1}^{1}) + \frac{-1}{2}(\alpha_1^{(2)} - \alpha_{-1}^{(2)}) \\
\alpha_{yz} &= \frac{i}{2}(\alpha_1^{(1)} - \alpha_{-1}^{1}) + \frac{i}{2}(\alpha_1^{(2)} + \alpha_{-1}^{(2)}) \\
\alpha_{zy} &= \frac{-i}{2}(\alpha_1^{(1)} - \alpha_{-1}^{1}) + \frac{i}{2}(\alpha_1^{(2)} + \alpha_{-1}^{(2)})
\end{aligned} \tag{3.27}$$

Clearly, $\alpha^{(1)}$, whose value is weighted by $F(1,\omega)$, contributes an anti-symmetric part to the Cartesian scattering tensor, while $\alpha^{(2)}$, whose value is weighted by $F(2,\omega)$, contributes a symmetric part. The scattering asymmetry defined as the ratio Intensity$_{\rho\sigma}$/Intensity$\sigma\rho$ is related in a simple manner to $|F(1,\omega)/F(2,\omega)|^2$.

Now that the details of the calculation of electronic Raman scattering intensities are known some explicit numbers for the scattering in Ce^{3+}:$LuPO_4$ may be calculated.

Following is a step-by-step description of that procedure including subtleties which arise for this special case.

Given the initial and final state wave functions from section 3.2.4 it is easy to calculate the α_Q^K's in terms of $F(1,\omega)$ and $F(2,\omega)$ using Equations 3.21 and 3.22. In Appendix A of this chapter the values of the α_Q^K's are listed along with the intermediate result values for $\mathbf{U^{(1)}}$ and $\mathbf{U^{(2)}}$. Once the α_Q^K's are known the Cartesian tensor elements, $\alpha_{\rho\sigma}$ may be computed from the transformation, Equation 3.27.

Becker has pointed out [11] that for tetragonal rare earth phosphate crystals the crystallographic axes, $\hat{\mathbf{X}}$ and $\hat{\mathbf{Y}}$, are rotated 45° about the $\hat{\mathbf{Z}}$ axis from the two C_2 axes, $\hat{\mathbf{x}}$ and $\hat{\mathbf{y}}$, of the D_{2d} point group of the rare earth ion (see Figure 2.2). In the experiment the polarization axes are the crystallographic axes. However, the calculated $\alpha_{\rho\sigma}$'s are for ρ and σ that are the D_{2d} point group axes. Therefore, it is necessary to rotate the calculated scattering tensor by 45° about the $\hat{\mathbf{Z}}$ axis in order to obtain the observed scattering tensor.

$$\alpha_{obs} = \mathbf{R}\alpha_{\mathbf{calc}}\mathbf{R}^{-1} \tag{3.28}$$

where,

$$\mathbf{R} = \begin{pmatrix} \cos 45° & \sin 45° & 0 \\ -\sin 45° & \cos 45° & 0 \\ 0 & 0 & 1 \end{pmatrix} \tag{3.29}$$

A final point to remember is that each of the crystal field levels of Ce^{3+} in $LuPO_4$ is a Kramer doublet. There are four transitions for each observed intensity. The calculated intensity is averaged over the two possible initial states and summed over the two final states. The intensities from the individual transitions are added incoherently.

$$|(\alpha_{\rho\sigma})_{if}|^2 = \left(|(\alpha_{\rho\sigma})_{if}|^2 + |(\alpha_{\rho\sigma})_{\bar{i}f}|^2 + |(\alpha_{\rho\sigma})_{i\bar{f}}|^2 + |(\alpha_{\rho\sigma})_{\bar{i}\bar{f}}|^2\right) \tag{3.30}$$

where an overbar represents a Kramer conjugate state. The Kramer conjugate states may be obtained from the Ce^{3+}:$LuPO_4$ wave functions by use of the relation

$$\overline{\sum_{J,M} a_{J,M}|J,M\rangle} = \sum_{J,M} a^*_{J,M}(-1)^{J-M}|J,-M\rangle \tag{3.31}$$

3.4.3 Comparison of Observed and Calculated Intensities, Standard Theory

Electronic Raman scattering data were taken for all possible transitions between the crystal field levels of the $4f^1$ configuration originating in the ground state. For each transition four different combinations of incident and scattered polarizations were observed, $\hat{X}\hat{Z}$, $\hat{Z}\hat{Y}$, $\hat{Z}\hat{Z}$, and $\hat{X}\hat{Y}$. All the data shown in this section are from experiments in which the incident light was from the 514.5 nm (19,429.7 cm^{-1} in vacuum) line of an argon ion laser. The area under a given electronic Raman peak is proportional to the intensity of the corresponding transition divided by the energy of the scattered photon, $\hbar\omega_s$ (the amplitude of the electronic Raman spectrum is in photon counts per second which is related to intensity by the factor $\hbar\omega_s$). The values of these areas will be compared with the calculated values of $|\alpha|^2$. In order to make this direct comparison the values of the areas are scaled by the appropriate factors of ω_s^3. This normalizes out the frequency factors relating scattering intensity with $|\alpha|^2$ in Equation 3.18.

For comparison of the observed and calculated intensities an appropriate value of the parameter $F(1,\omega)/F(2,\omega)$ is needed. As stated in the previous section a value for $F(1,\omega)/F(2,\omega)$ may be calculated from the observed asymmetries of each transition. Table 3.10 shows a listing for the calculated expressions for the asymmetries of the various transitions in terms of $F(1,\omega)/F(2,\omega)$. Table 3.11 lists the observed asymmetries and the values of $F(1,\omega)/F(2,\omega)$ calculated from using these values an the expressions in Table 3.10. As can be seen there is no single value of $F(1,\omega)/F(2,\omega)$ that is satisfactory for all the transitions. A closer inspection of the expressions in Table 3.10 shows that even allowing for large errors in the observed asymmetries no consistent value of $F(1,\omega)/F(2,\omega)$ can be extracted. The large variation in the fitted values is much worse than observed by Becker *et al.* in $ErPO_4$, $TmPO_4$, and $HoPO_4$ and may well be indicative of the stringent test Ce^{3+} applies to the Judd-Ofelt approximation.

Since no consistent value of $F(1,\omega)/F(2,\omega)$ appears a value was selected under the assumption that the $5d^1$ configuration is the dominant intermediate channel. From Equation 3.26 it can be seen that with $\overline{\omega}_{5d} \approx 40{,}000$ cm^{-1} and $\omega \approx 20{,}000$ cm^{-1} that $F(1,\omega)/F(2,\omega) \approx 0.65$. Figure 3.11 and Figure 3.12 compare the observed rel-

Transition Δcm^{-1}	Asymmetry in Terms of $\beta = \frac{F(1,\omega)}{F(2,\omega)}$
240	-
429	$\left(\frac{.110+.017\beta}{.110-.017\beta}\right)^2 = 4.3$
2,179	$\left(\frac{.017-.033\beta}{.017+.033\beta}\right)^2 = .34$
2,221	$\left(\frac{.0053-.015\beta}{.0053+.015\beta}\right)^2 = 10.9$
2,620	$\left(\frac{-.028-.020\beta}{.028-.020\beta}\right)^2 = 9.5$
2,676	$\left(\frac{.036+.0035\beta}{.036-.0035\beta}\right)^2 \Rightarrow \infty$

Table 3.10: Calculated expressions for the observed asymmetry, $\frac{I_{X=Y,Z}}{I_{Z,X=Y}}$, as a function of the parameter, $\frac{F(1,\omega)}{F(2,\omega)}$. For the scattering to the 240 cm^{-1} level both I_{XZ} and I_{ZY} are not observed.

Transition Δcm^{-1}	Calculated Values $\frac{F(1,\omega)}{F(2,\omega)}$
240	-
429	2.26 or 18.5
2,179	0.14 or 1.95
2,221	-0.19 or -0.66
2,620	0.71 or 2.74
2,676	10.3

Table 3.11: Values of $\frac{F(1,\omega)}{F(2.,\omega)}$ calculated from asymmetry expressions in Table 3.10.

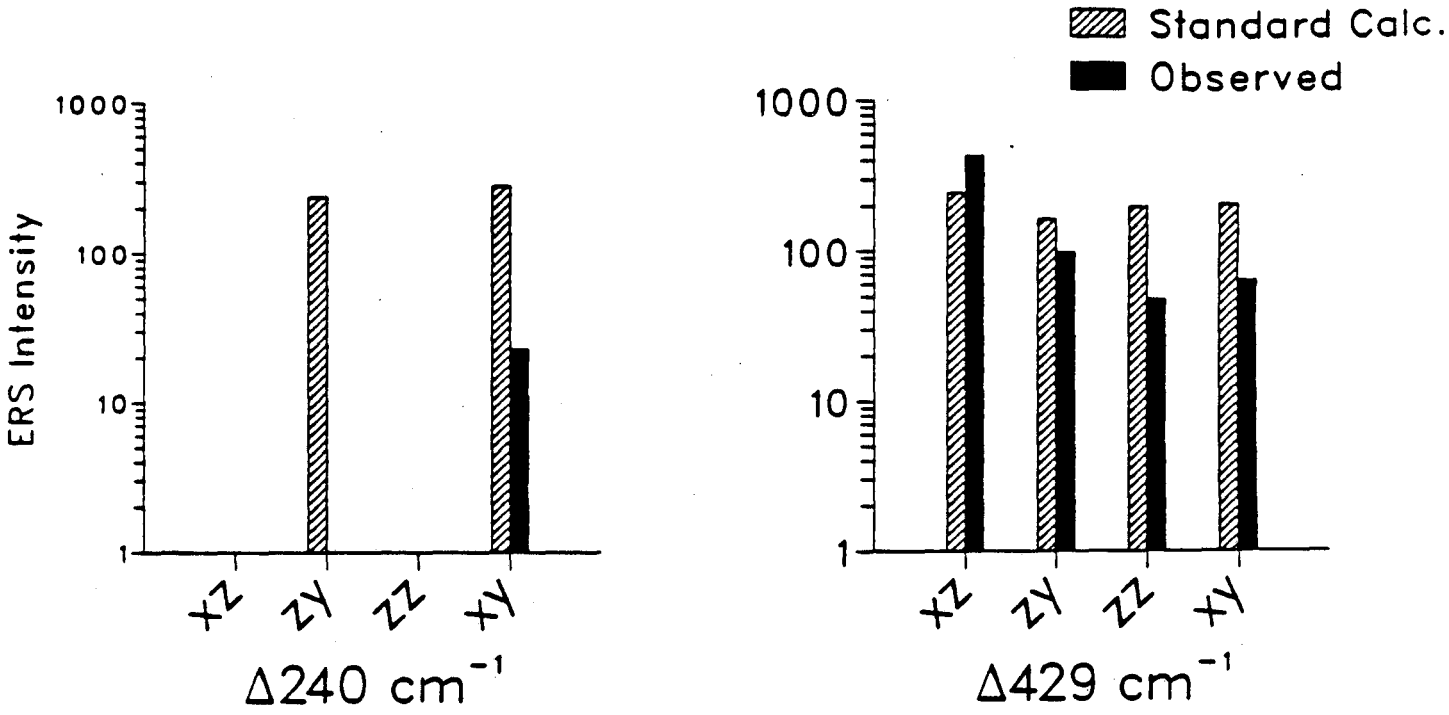

Figure 3.11: Comparison of observed and calculated electronic Raman scattering intensities between crystal field levels of the $^2F_{5/2}$ multiplet using the standard second-order theory with $F(1,\omega)/F(2,\omega) = 0.65$.

ative intensities to those calculated from the second order theory with the parameter $F(1,\omega)/F(2,\omega)$ fixed at the expected value of 0.65. The observed and calculated values were scaled relative to each other by averaging the ratio of observed to calculated for all transitions with non-zero intensity. The agreement is poor but maybe not as bad as one would expect given the approximations used in the calculation. A few specific observations can be made about the results. These observations may help in determining where the standard theory fails and what is needed to correct it.

The largest discrepancies exists for the transitions to the levels at 240 cm^{-1} and 2676 cm^{-1}. However, these two transitions have relatively large linewidths that make measurement of their respective intensities inaccurate. The line widths of the 240 cm^{-1} and 2676 cm^{-1} transitions are on the order of 10 cm^{-1} while, for example, the line widths of the 2179 cm^{-1} and 2221 cm^{-1} transitions are on the order of only 2 cm^{-1}. The larger the linewidth the less accurate the measurement of the intensity. For a given intensity,

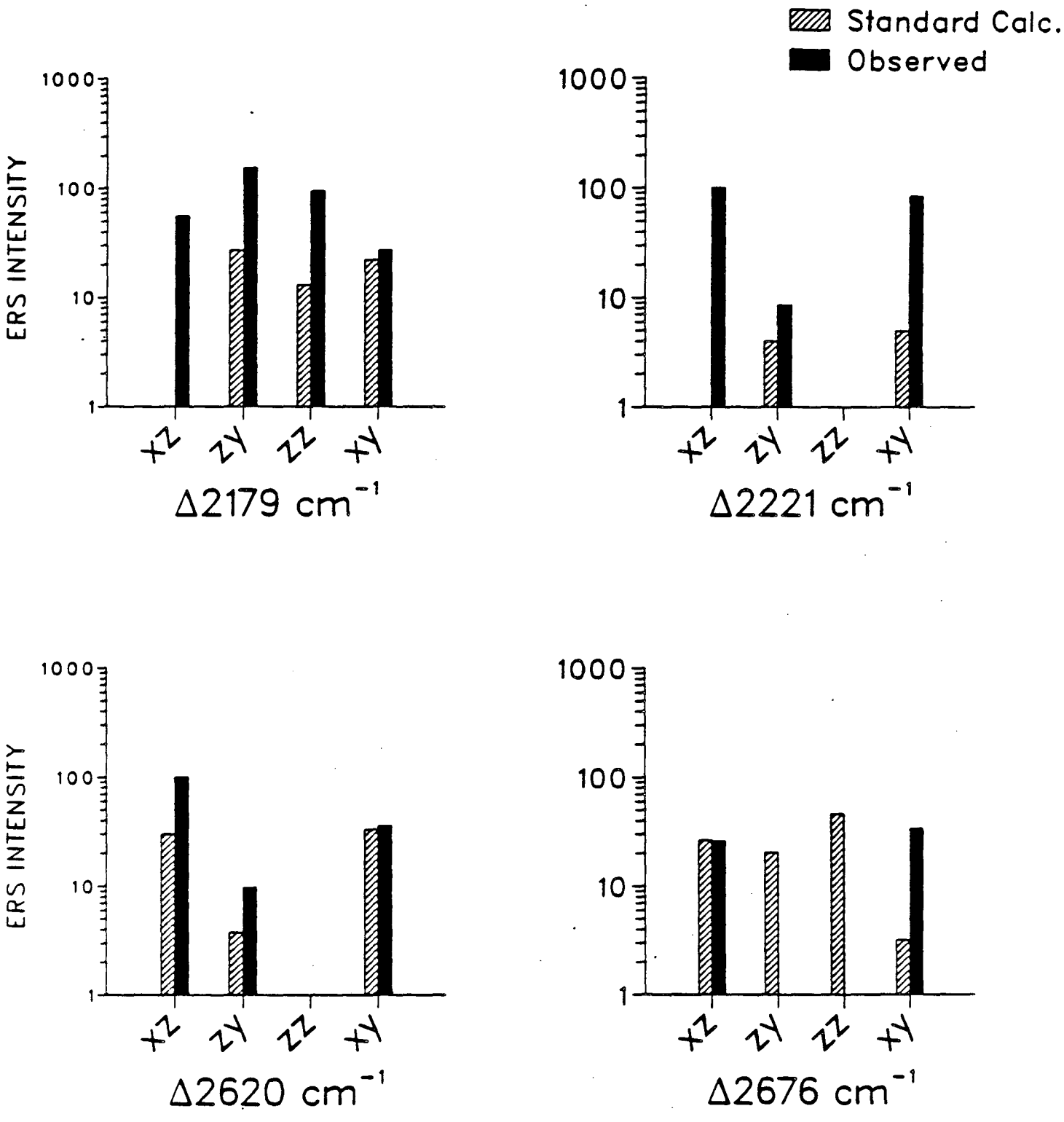

Figure 3.12: Comparison of observed and calculated electronic Raman scattering intensities between crystal field levels of the $^2F_{7/2}$ multiplet using the standard second-order with $F(1,\omega)/F(2,\omega) = 0.65$.

as the linewidth increases the electronic Raman scattering peak becomes buried more and more in the experimental noise. So, on the scale of Figure 3.12, an intensity on the order of 5 maybe observable for the 2179 cm^{-1} transition while an intensity of 20 for the 2676 cm^{-1} transition could be obscured. However, this still does not explain why, for instance, the 240 cm^{-1} transition in ZY polarization, predicted to have intensity 110, is not observed.

Another observation to be made is that the standard theory underestimates the strengths of the transitions to the 2179 cm^{-1}, 2221 cm^{-1}, and 2620 cm^{-1} levels relative to the transition to the 429 cm^{-1} level. This observation may be couched in more general terms by noticing that the 2179 cm^{-1}, 2221 cm^{-1}, and 2620 cm^{-1} levels all belong to the $^2F_{7/2}$ manifold while the 429 cm^{-1} level belongs to the $^2F_{5/2}$ manifold. It is probably reasonable to say that the standard theory underestimates the strength of the $^2F_{5/2} \longrightarrow {}^2F_{7/2}$ scattering relative to the $^2F_{5/2} \longrightarrow {}^2F_{5/2}$. Furthermore, as can be seen by examining the respective values from Appendix A of $\mathbf{U^{(1)}}$ and $\mathbf{U^{(2)}}$ for the transitions $^2F_{5/2} \longrightarrow {}^2F_{5/2}$ and $^2F_{5/2} \longrightarrow {}^2F_{7/2}$, no change in the parameter $F(1,\omega)/F(2,\omega)$ will correct this discrepancy.

The conclusion is that the standard second order theory is insufficient to explain the data. This result is not surprising considering how close the $5d^1$ configuration is to the incident laser energy (10,000 cm^{-1}) compared to the configuration's overall breadth of 20,000 cm^{-1}. The detailed structure of the $5d^1$ configuration should be of importance.

3.4.4 Explicit Evaluation of the Sum Over Virtual Intermediate States

More detail of the $5d^1$ configuration's structure may be added by including in the calculation third-order perturbation terms of the form given in Equation 3.17. A comparison of the expression for the third-order term and the expression for the second-order term shows that the third order term is smaller by a factor of approximately $\frac{H'}{\hbar(\overline{\omega}_{5d}-\omega)}$ where H' is some interaction influencing the structure of the $5d^1$ configuration.

For cerium with one 5d electron the most significant interaction is the crystal field. An order of magnitude estimate of the ratio of the third-order term for the crystal field interaction to the second-order term is given by, $\frac{B^k_{q5d}}{\hbar(\overline{\omega}_{5d}-\omega)}$. For Ce^{3+}:$LuPO_4$, $B^k_{q5d} \approx$

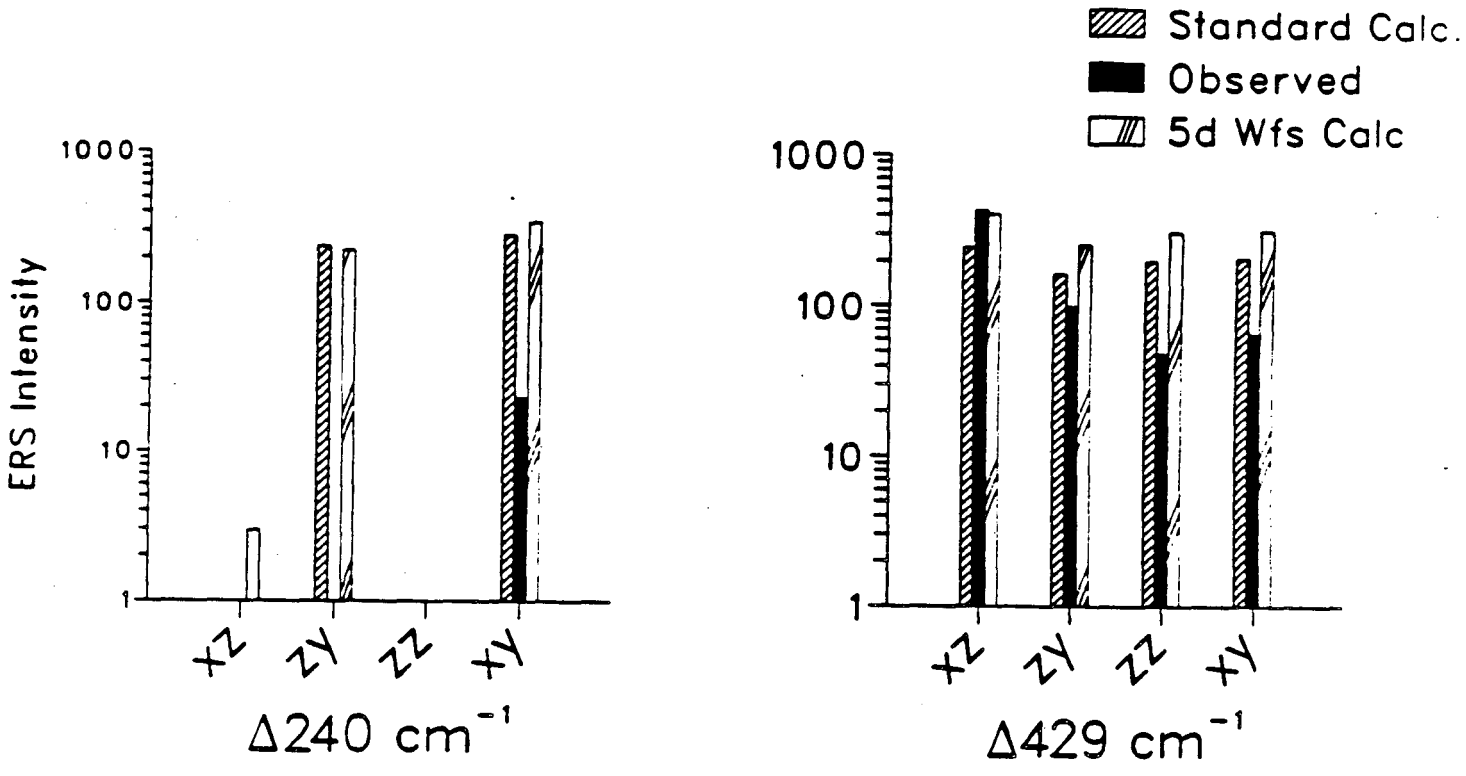

Figure 3.13: Comparison of observed and calculated electronic Raman scattering intensities between crystal field levels of the $^2F_{5/2}$ multiplet. The intensities have been calculated using the standard second-order theory and also by explicitly evaluating the sum over intermediate states.

$20,000\ \text{cm}^{-1}$ and $(\overline{\omega}_{5d}-\omega) \approx 20,000\ \text{cm}^{-1}$ yielding $\frac{B^{k}_{q5d}}{\hbar(\omega_{5d}-\omega)} \approx 1$. An accurate description of the effect of this perturbation would include an expansion to all orders in perturbation theory.

In this work the excited configuration has been observed spectroscopically. A crystal field fit has been performed, and wave functions for the individual states of the configuration are available. There are only five states (actually five Kramer doublets), and it is not difficult to explicitly place the $5d^1$ states along with their respective energies into Equation 3.22 and perform the sum directly. The result of such a calculation as compared to the data is displayed in Figure 3.13 and Figure 3.14. The scaling between the data and the calculated results is done as before for the standard second-order calculation.

The agreement is improved over the results of the calculation using the Judd-Ofelt closure approximation. The prediction of the relative intensities of $^2F_{5/2} \rightarrow ^2F_{5/2}$ transitions to the $^2F_{5/2} \rightarrow ^2F_{7/2}$ transitions has been improved considerably. This improve-

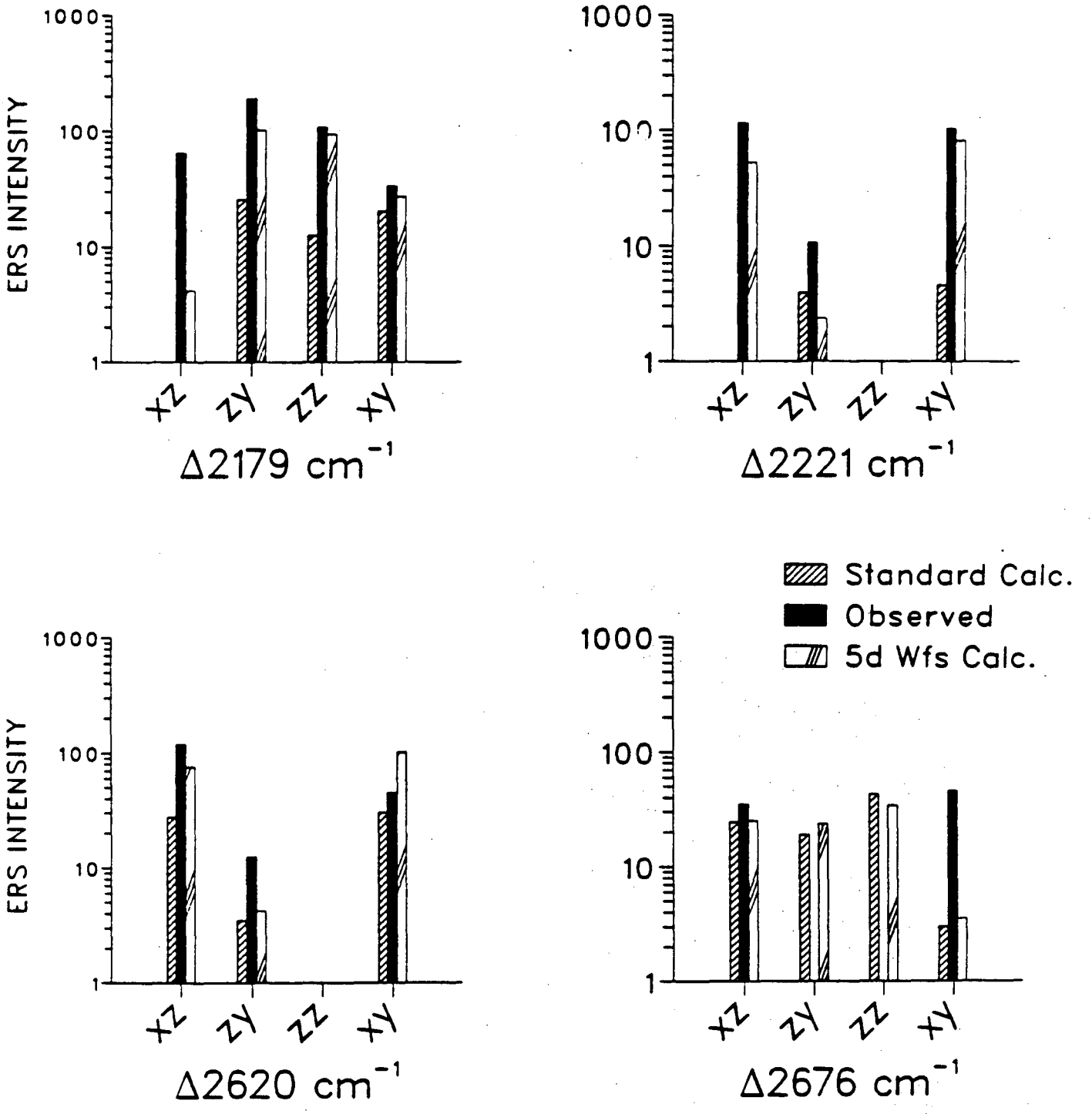

Figure 3.14: Comparison of observed and calculated electronic Raman scattering intensities between crystal field levels of the $^2F_{7/2}$ multiplet. The intensities have been calculated using the standard second-order theory and also by explicitly evaluating the sum over intermediate states.

	Standard Calc.	Measured	Explicit Calc.
$\frac{^2F_{5/2}\rightarrow{}^2F_{5/2}}{^2F_{5/2}\rightarrow{}^2F_{7/2}}$	6.1	0.8	2.9

Table 3.12: Ratios of multiplet to multiplet intensities for electronic Raman scattering in $Ce_{.20}Lu_{.80}PO_4$.

Transition Δcm^{-1}	Standard Calc. Asymmetry	Measured Asymmetry	Explicit Calc. Asymmetry
240	0.0002	-	0.013
429	1.5	4.3	1.6
2179	0.01	0.34	0.04
2221	0.09	10.9	22.2
2620	7.9	9.5	18.0
2676	1.3	large	1.1

Table 3.13: Electronic Raman scattering asymmetries.

ment may be noted from Table 3.12 which displays the measured and calculated values for the ratios of the combined intensities of the $^2F_{5/2} \rightarrow{}^2 F_{5/2}$ transitions to the combined intensities of the $^2F_{5/2} \rightarrow{}^2 F_{7/2}$ transitions. The explicit calculation also offers improvement in predicting the scattering asymmetries. Table 3.13 shows the measured asymmetries along with the values calculated using the Judd-Ofelt closure approximation ($(F(1,\omega)/F(2,\omega)) = 0.65$) and the explicit evaluation of the sum over virtual intermediate states. The most notable improvement is in the prediction of the asymmetry for the $\Delta 2221$ cm^{-1} transition.

Unfortunately, the explicit calculation still fails to accurately predict scattering intensities for the 240 cm^{-1} and 2676 cm^{-1} levels. It is difficult to draw conclusions from this failure. It is not clear whether it is just the result of a poor crystal field fit for the $5d^1$ configuration or actually something more fundamental.

3.5 Electronic Raman Scattering, Resonant Excitation

The form of the expression for the electronic Raman scattering amplitude, Equation 3.19, suggests there should be an enhancement of the scattering intensity as the energy of the incident laser radiation is tuned closer to the electronic states of the rare earth ion.

Usually in rare earth crystals the excited electronic states accessible by lasers belong to the ground $4f^N$ configuration. For such intra-configurational resonances the enhancement of the electronic Raman scattering process is expected to be quite small. This is due to the fact that the $4f^N$-$4f^N$ electric dipole matrix elements determining the strength of the resonance are formally parity forbidden. It is well known that such matrix elements are usually on the order of 1,000 times smaller than a parity allowed inter-configurational electric dipole matrix element. To see any enhancement at all the detuning from the resonance has to be quite small, less than 10 cm^{-1}. At such small detunings linear absorption of the exciting laser by the resonant state begins to proportionally reduce the Raman scattering. Most of the reported enhancements of this type[67,68,69,70,71] have been on the order of only one to five times the non-resonant intensity. The largest reported enhancement of this type has been a factor of approximately fifty seen in a crystal of $ErPO_4$ [72]. An in depth analysis of some of the interesting aspects of this resonance is the subject of the following chapter.

In the cerium ion the first excited configuration is low in energy. As seen earlier, in Ce^{3+}:$LuPO_4$ the $5d^1$ configuration begins at about 30,000 cm^{-1}(≈333 nm). The frequency tripled output of the Nd^{3+}:YAG laser is at 28,191.5 cm^{-1}(≈355 nm). This is still approximately 2,000 cm^{-1} from the bottom of the $5d^1$ configuration, however, the resonance in this case is a parity allowed inter-configurational one. An order of magnitude estimate of the enhancement (excluding the effect of the $\omega\omega_s^3$ scattering dependence) of the electronic Raman scattering intensity excited by the tripled Nd^{3+}:YAG to that excited by the argon ion laser at about 19,429.7 cm^{-1}(≈ 514.5 nm) is given by

$$\frac{I_{355.0}}{I_{514.5}} = \left(\frac{\omega_{5d} - \omega_{514.5}}{\omega_{5d} - \omega_{355.0}}\right)^2 \approx \left(\frac{30,000 - 20,000}{30,000 - 28,000}\right)^2 \approx 25 \qquad (3.32)$$

This calculation presupposes that the bulk of the electronic Raman scattering intensity

is mediated through the states of the $5d^1$ configuration. If, for instance, *g* orbital states contributed significantly to the scattering intensity the observed enhancement factor could be significantly reduced. Presumably the g orbital states would be so far removed in energy so that the change in incident laser energy would have no noticeable effect on the portion of the scattering amplitude they contributed. Comparison of the observed enhancements to the number predicted above should serve as test of the nature of the virtual intermediate states.

Figure 3.15 shows schematically the energy level structure of Ce^{3+}:$LuPO_4$ and the locations of the non-resonant laser energy and the resonant, or more correctly near-resonant, laser energy. The energy of the frequency tripled Nd^{3+}:YAG is actually well suited for this experiment in that it offers the opportunity for significant enhancement of the electronic Raman scattering without the problem of fluorescence.

A common problem in resonance Raman experiments is that the resonant level can be populated and then fluoresce, not only depleting the number of photons in the laser beam available for scattering but also creating a background that can obscure the Raman signal. In this experiment the location of the laser energy, 2,000 cm^{-1} away from the resonant level, almost entirely eliminates this problem. Any absorption process requires the assistance of at least two phonons. At room temperature there is some absorption as evidenced by the observation of broad band fluorescence at 30,000 cm^{-1} from the $5d^1_{lowest} \longrightarrow {}^2F_{5/2}$ transition and at 28,000 cm^{-1} from the $5d^1_{lowest} \longrightarrow {}^2F_{7/2}$ transition. This latter fluorescence would entirely obscure the ${}^2F_{5/2} \longrightarrow {}^2F_{5/2}$ electronic Raman signal from the tripled Nd^{3+}:YAG laser. However, at 10°K the phonons of the crystal are "*frozen*" out and no absorption and subsequent fluorescence is observed. This is true so long as the incident light intensities are kept below a certain threshold. Above the threshold large intensities may be observed even when the crystal is cooled.

3.5.1 Enhancement Measurement

The experiment was carried out in the manner described Section 2.3.3. In order to compare the intensities at 514.5 nm to those at 355 nm some form of normalization must be employed. After all the two experimental setups are different and characteristics such

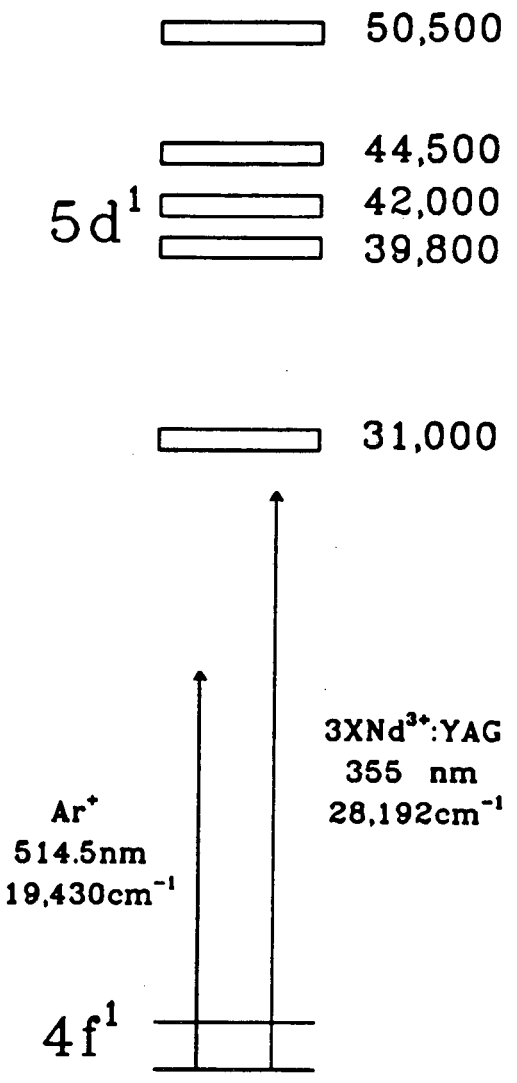

Figure 3.15: Schematic representation of the energies involved in a electronic Raman 4f-5d resonant enhancement experiment in Ce^{3+}:$LuPO_4$.

as collection efficiencies, for example, vary. The vibrational Raman scattering from the phonons of the crystal should be independent of excitation energy beyond the normal $\omega\omega_s^3$ dependence. This is true under the usual assumption that the lattice vibrations of the crystal are not strongly coupled to the electronic states of the rare earth ion. For each experiment the electronic Raman scattering intensities may be normalized by scaling the results relative to the phonon intensities for that experiment.

Figure 3.16 shows the observed electronic Raman scattering intensities for the lines at 429 cm^{-1}, 2179 cm^{-1}, 2221 cm^{-1} ,and 2620 cm^{-1} from excitation at both 514.5 nm and 355 nm. The lines at 240 cm^{-1} and 2676 cm^{-1} were not observed. The data have been normalized using the 1034 cm^{-1} E_g phonon of the crystal and corrected for the $\omega\omega_s^3$ scattering dependence. The enhancement factors are also shown.

For the observed lines the enhancement factors are all of the correct order of magnitude indicating that indeed the $5d^1$ configuration plays a strong role as an intermediate channel. The only unexpected result is that some of the transitions show anomalously large enhancements. For instance the $\hat{Z}\hat{Y}$ polarized transition to the 2221 cm^{-1} level shows an enhancement of approximately 100.

These anomalously large enhancements are suspected to be the result of polarization leakage. This suspicion is supported by looking at the large intensities seen for the forbidden $\hat{Z}\hat{Z}$ transitions to the Γ_7 levels at 2221 cm^{-1} and 2620 cm^{-1}. It is further believed that the leakage is not an artifact of the experimental setup but the result of actual permanent physical changes in the structure of the crystal as a result of the irradiation by the tripled Nd^{3+}:YAG output.

3.5.2 Crystal Damage

Above a certain threshold intensity the crystal is visibly physically damaged. Single pulse energies above approximately 0.3 millijoules (10 nsec in duration) in combination with the tightest focussing possible using a 15 cm lens results in visible pitting of the crystal. In addition, at this threshold intensity the 5d-4f fluorescence, not observable at lower intensities, becomes quite strong and increases non-linearly as a function of the incident intensity. A cursory examination shows that the fluorescence grows roughly as

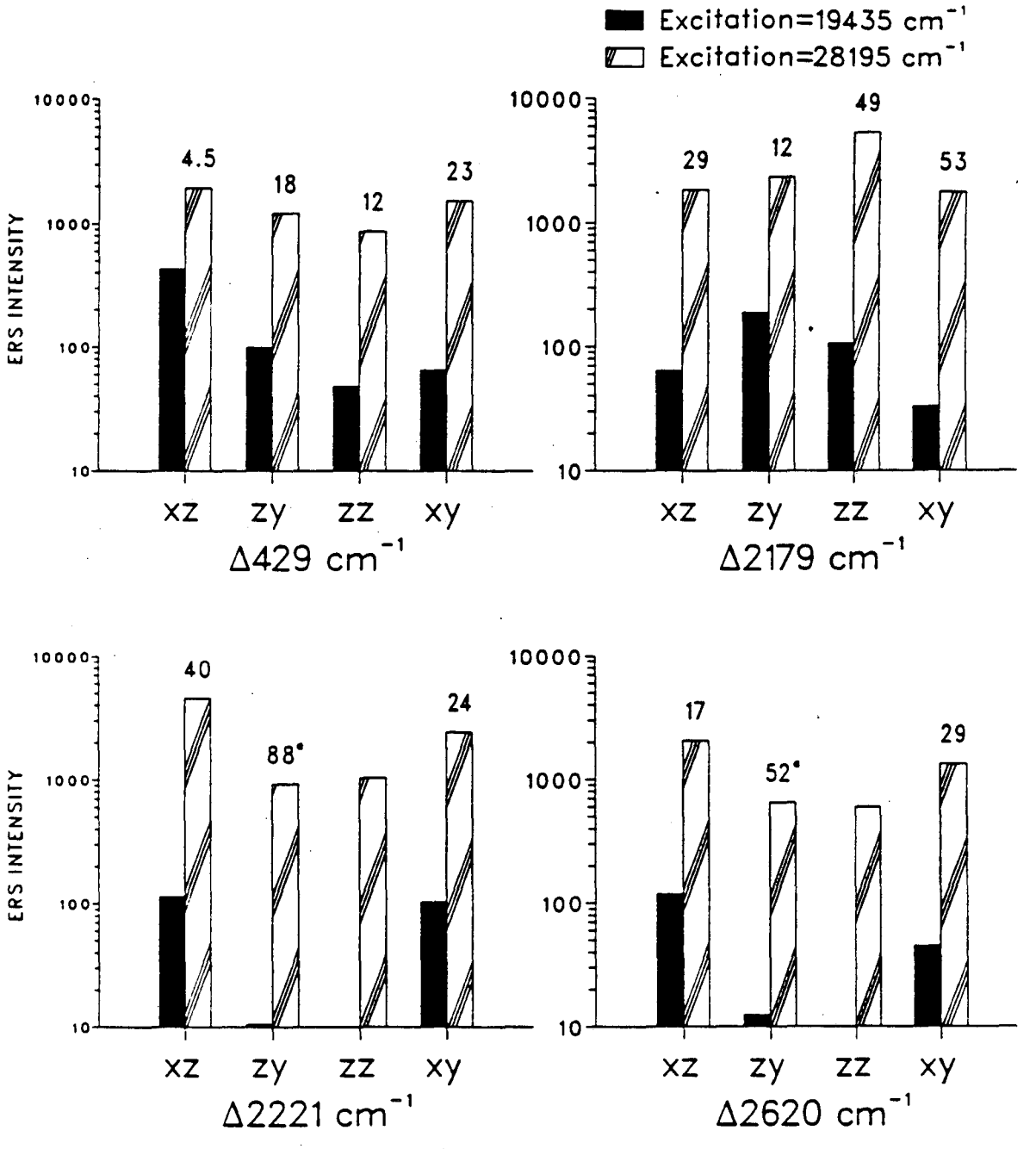

Figure 3.16: The $Ce_{.20}Lu_{.80}PO_4$ electronic Raman scattering intensities for excitation with 514.5 nm radiation and 355 nm radiation. The numbers at the top of the 355 nm intensity bars are the enhancement factors for that particular transition.

the third power of the incident intensity. Furthermore, above the threshold the point at which the incident laser is focussed glows visibly red. A spectral analysis of this glow shows it to be very broad, covering nearly the entire visible spectrum.

Even below the visible damage threshold, anomalies in the polarized phonon Raman spectra are observed. Figure 3.17 compares the $\hat{\mathbf{X}}\hat{\mathbf{Z}}$ spectrum of a $Ce_{.20}Lu_{.80}PO_4$ crystal taken first using excitation at 514.5 nm and subsequently using excitation at 355 nm, with the intensity of the 355 nm radiation kept well below the damage threshold. The A_{1g} phonon at 1013 cm^{-1} should not be seen in this polarization combination; however, it is seen clearly in the 355 nm excited spectrum. In fact, this loss of polarization selection rules is seen for all polarization combinations. Furthermore, once the crystal has been irradiated by the 355 nm light, even a 514.5 nm excited Raman spectrum shows the loss of polarization.

Fortunately, the loss of polarization seems to be stronger in the phonon Raman spectra than in the electronic Raman spectra. The 355 nm excited spectra for the 2179 cm^{-1} and 2221 cm^{-1} transitions are pictured in Figure 3.18. In the electronic Raman scattering spectra the forbidden $\hat{\mathbf{Z}}\hat{\mathbf{Z}}$ transitions are still smaller, in general, than the allowed transitions. This difference might reflect the fact that the phonons tend to be excitations of the whole crystal while the rare earth ion electronic states are more localized in nature, thus making the phonons more sensitive to structural changes.

3.5.3 Calculation of Intensities

Finally, the $5d^1$ wave functions obtained from the crystal field fit are used explicitly to calculate the expected intensities of the electronic Raman scattering. Figures 3.19 and 3.20 show the comparison of the observed intensities from excitation at 355 nm to the calculated values. The calculation is the same as for the non-resonant case except for the change in the energy denominators. The data and calculated values are scaled relative to each other with the same factor used earlier for scaling the non-resonant results. In other words, the scale of Figures 3.19 and 3.20 is equivalent to the scale of Figures 3.13 and 3.14.

The loss of the integrity of the polarizations makes it difficult to compare the results

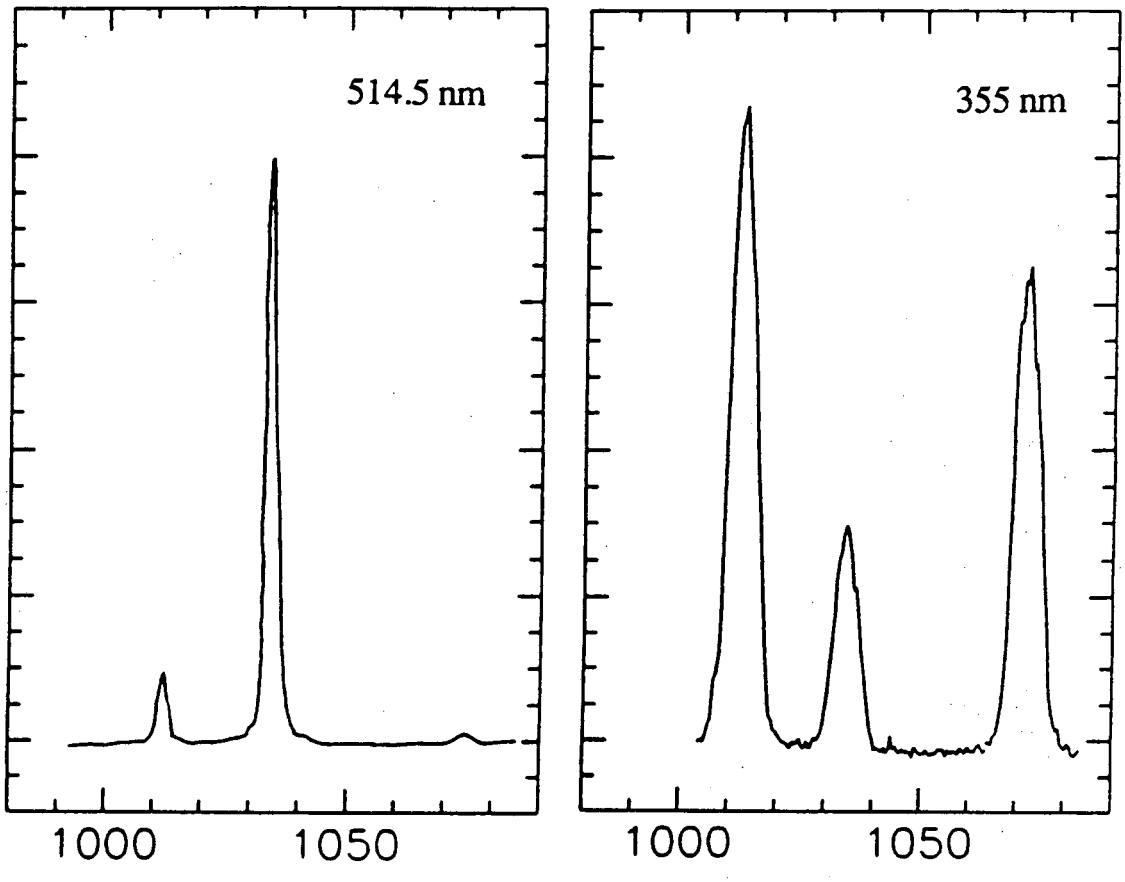

Figure 3.17: Raman spectra of $Ce_{.20}Lu_{.80}PO_4$ in $\hat{\mathbf{X}}\hat{\mathbf{Z}}$ polarization. The left spectrum is from excitation at 514.5 nm and the right spectrum is the result of excitation at 355 nm.

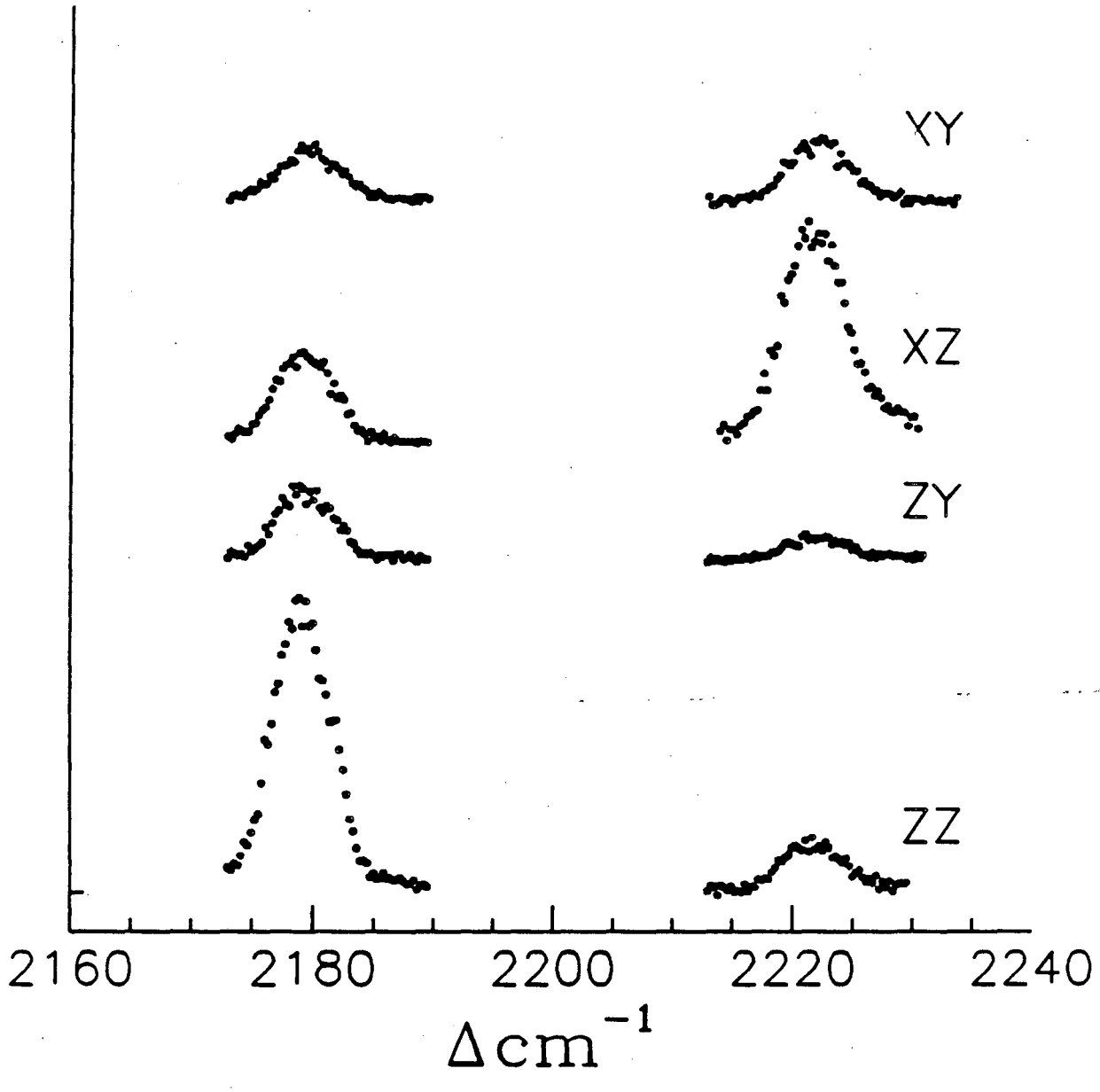

Figure 3.18: $Ce_{.20}Lu_{.80}PO_4$ electronic Raman spectra excited by 355 nm radiation for different polarization combinations.

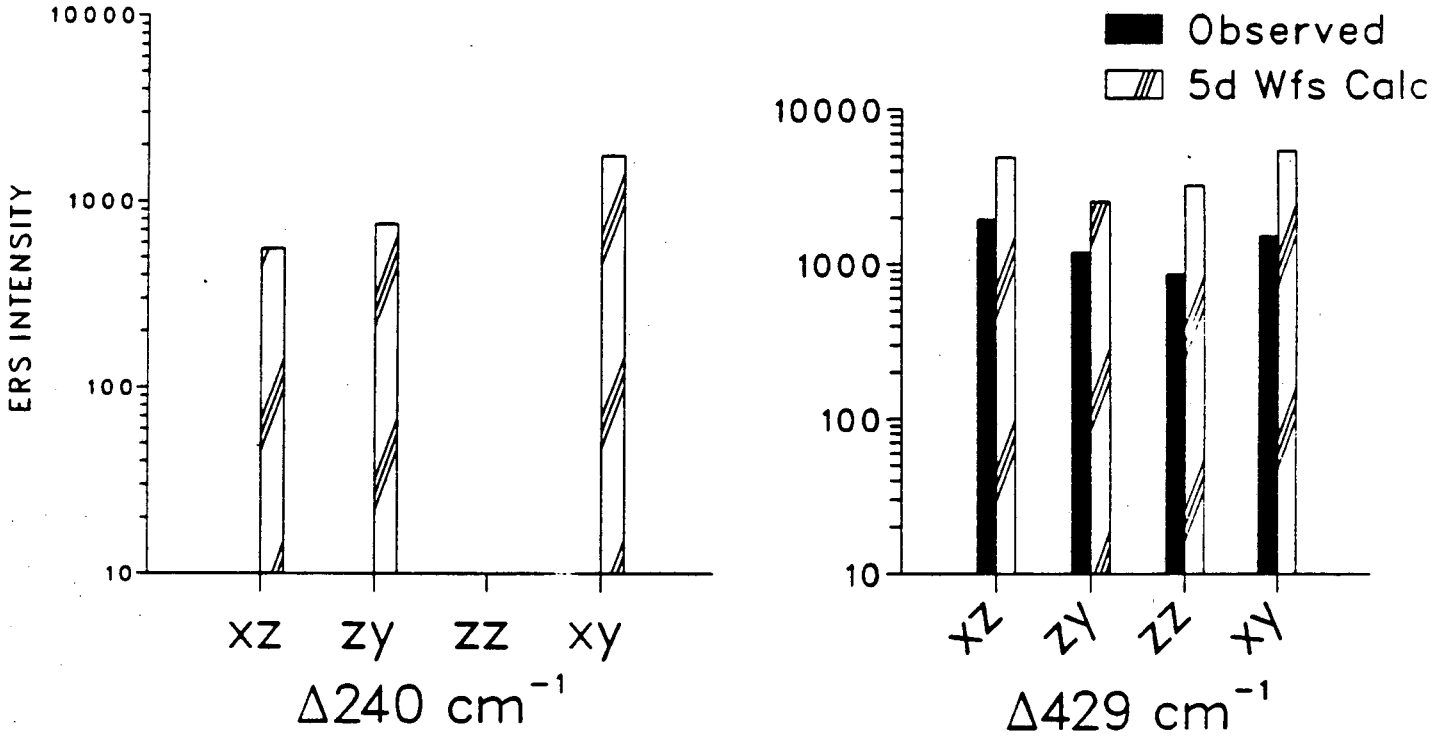

Figure 3.19: Comparison of the observed and calculated electronic Raman scattering intensities between crystal field levels of the $^2F_{5/2}$ multiplet of Ce^{3+} in crystals of $Ce_{.20}Lu_{.80}PO_4$. The intensities are calculated by explicitly evaluating the sum over intermediate states.

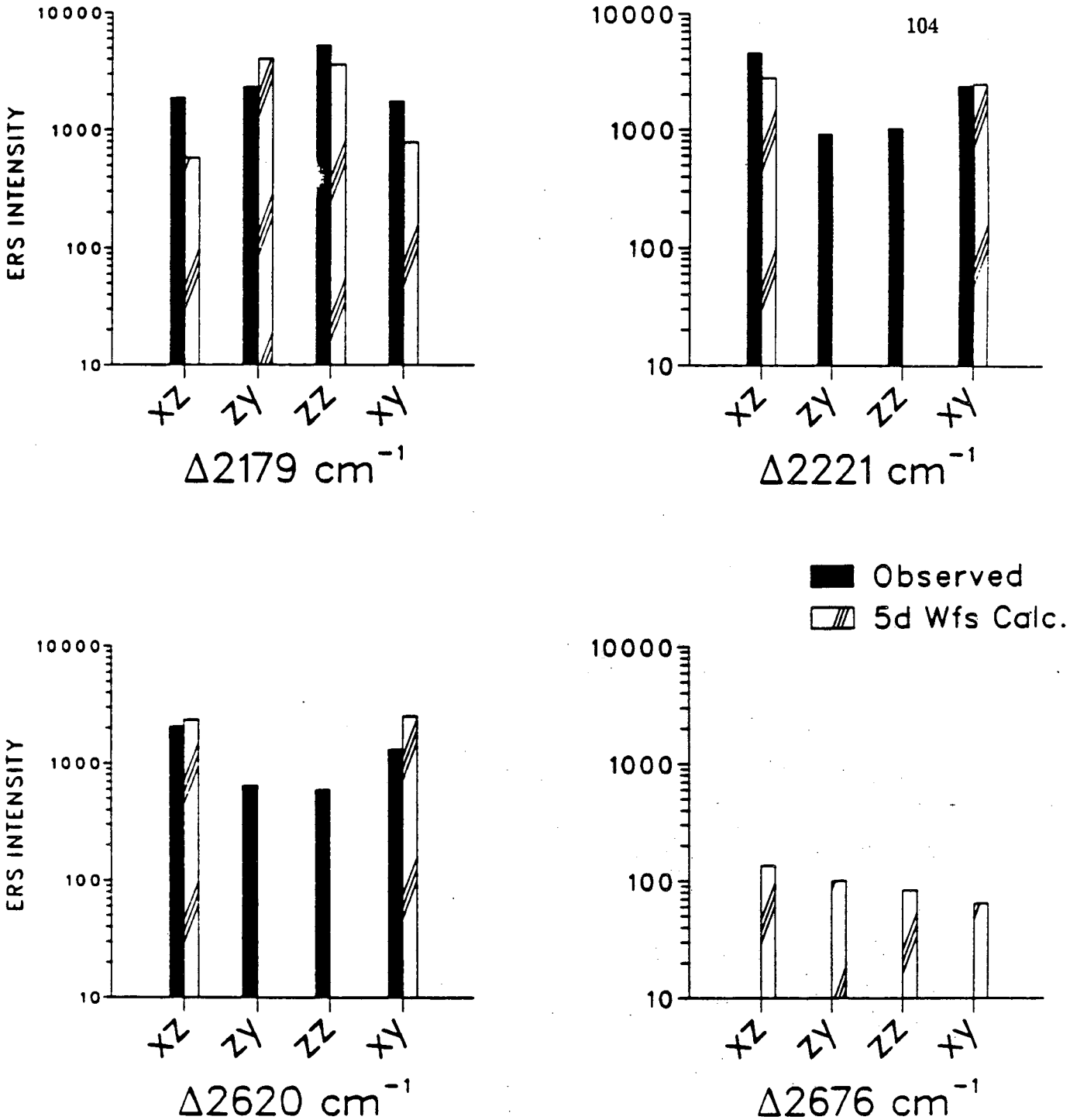

Figure 3.20: Comparison of the observed and calculated electronic Raman scattering intensities between crystal field levels of the $^2F_{7/2}$ multiplet of Ce^{3+} in crystals of $Ce_{.20}Lu_{.80}PO_4$. The intensities are calculated by explicitly evaluating the sum over intermediate states.

Transition Δcm^{-1}	Measured	Calculated
240	-	1543
429	2738	8008
2179	5591	4514
2221	4462	2913
2620	2315	2447
2676	-	193

Table 3.14: Polarization averaged relative intensities for electronic Raman scattering in $Ce_{.20}Lu_{.80}PO_4$.

in a very precise manner. The loss of polarization is apparent in looking at the different polarization combinations for any given transition. While the calculated values sometimes show large differences between different polarizations, the observed values show a smooth variation as if intensity was redistributed from one polarization to another. However, the calculation seems to accurately predict the overall signal level for the observed transitions even if it doesn't predict the relative intensities between different polarization combinations. This is demonstrated in Table 3.14 which shows the calculated and measured polarization averaged relative intensites for the various transitions.

However, again as in the non-resonant case there is difficulty with the transitions to the levels at 240 cm^{-1} and 2676 cm^{-1}. Neither of these levels are observed even with the benefit of resonant enhancement. Before drawing conclusions it should be noted that the detection limit of the 355 nm experiment is approximately 50 times smaller than the detection limit of the 514.5 nm setup. This places the detection limit at approximately 500 on the scale of Figures 3.19 and 3.20. This drop in sensitivity is in large part inherent in the nature of the experimental setups. However, there is still the question, as with the non-resonant case, why the large predicted transitions, such as $\hat{X}\hat{Y}$ 240 cm^{-1}, are not observed.

3.6 Conclusions

Comparison of the non-resonantly excited electronic Raman scattering intensities from Ce^{3+} doped into $LuPO_4$ to those predicted by the standard second-order theory of two

photon processes in rare earth ions showed the theory to be inadequate. This was attributed to the nearness in energy of the states of the first excited configuration in cerium. These states are presumed to serve, at least in part, as the virtual intermediate states in the electronic Raman scattering process.

A second calculation was done by summing explicitly over the crystal field fit wave functions of the $5d^1$ configuration. This calculation described the scattering intensities quite accurately with the exception of the transitions to the level at 2,676 cm^{-1} and to a greater extent the level at 240 cm^{-1}. This result seems to indicate that the states of the $5d^1$ configuration serve as the dominant intermediate channels for the electronic Raman scattering process. Furthermore, it was only necessary to describe these states in terms of an atomic-like Hamiltonian with the addition of a crystal field interaction.

In addition, the electronic Raman spectra exhibited enhancements in intensity on the order of 25 times when the laser excitation was tuned closer to the $5d^1$ configuration. This further supports the stipulation that the $5d^1$ configuration serves as the dominant electronic Raman scattering channel.

Corrections to the theory of two photon processes in rare earth ions doped into crystals ultimately involves refinements in the description of the electronic states involved in the process: either the initial state, final state, or more commonly the virtual intermediate states. The results of this work seem to indicate that by extending the description of the intermediate states by introduction of the crystal field interaction or maybe the spin-orbit interaction (for ions with more than one optically active electron) the theory can be greatly improved. The point being that the excited configurations acting as intermediate channels may still be described in terms of a rare earth ion perturbed by a surrounding crystal.

Unfortunately, all the rare earth ions are different in terms of their respective energy level structures. The cerium ion is especially different in that it has the lowest energy for the first excited configuration.

An extension of the general description of the important electronic Raman scattering intermediate channels for cerium to other rare earth ions will most likely be incorrect. For many of the rare earth ions the free ion value for the energy of the first excited

configuration is near or above the band gap of the host $LuPO_4$ crystal. In these situations a more molecular type description of the intermediate channels is probably necessary. The ligand becomes just as important as the ion.

In Appendix B of this chapter the results of additional work on the Ce^{3+}:$LuPO_4$ system is presented. This work was completed after the writing of this chapter and thus is offered as an appendix.

In the appendix the absolute values (in the chapter only relative values were considered) for both the 4f-5d oscillator strengths and the 4f-4f electronic Raman scattering cross-sections are compared to the values calculated using Hartree-Fock radial wavefunctions. The differences between the measured and calculated values seems to indicate that the atomic description of the 5d wavefunctions is not entirely accurate.

Appendix 3A: Intermediate Result Values

Reduced Unit Tensor Matrix Elements

$\mathbf{U}^K = \langle S', L', J' || U^K || S, L, J \rangle$

$^2F_{5/2} \longrightarrow {}^2F_{5/2}$	$^2F_{5/2} \longrightarrow {}^2F_{7/2}$
$\mathbf{U}^1 = .903$	$\mathbf{U}^1 = .202$
$\mathbf{U}^2 = .857$	$\mathbf{U}^2 = .350$

Spherical Electronic Raman Scattering Tensors $^4F_{5/2} \longrightarrow {}^4F_{5/2}$

$0 \longrightarrow 240\ \mathrm{cm}^{-1}$
$\alpha_1^2 = .116F_2$
$\alpha_1^1 = -.185F_1$

$\overline{0} \longrightarrow 240\ \mathrm{cm}^{-1}$
$\alpha_{-2}^2 = .159F_2$
$\alpha_2^2 = .097F_2$

$0 \longrightarrow \overline{240}\ \mathrm{cm}^{-1}$
$\alpha_{-2}^2 = -.097F_2$
$\alpha_2^2 = -.159F_2$

$\overline{0} \longrightarrow \overline{240}\ \mathrm{cm}^{-1}$
$\alpha_{-1}^2 = -.116F_2$
$\alpha_{-1}^1 = -.185F_1$

$0 \longrightarrow 429\ \mathrm{cm}^{-1}$
$\alpha_0^2 = -.132F_2$
$\alpha_0^1 = -.241F_1$

$\overline{0} \longrightarrow 429\ \mathrm{cm}^{-1}$
$\alpha_1^2 = .220F_2$
$\alpha_1^1 = .034F_1$

$0 \longrightarrow \overline{429}\ \mathrm{cm}^{-1}$
$\alpha_{-1}^2 = .220F_2$
$\alpha_{-1}^1 = -.034F_1$

$\overline{0} \longrightarrow \overline{429}\ \mathrm{cm}^{-1}$
$\alpha_0^2 = -.132F_2$
$\alpha_0^1 = .241F_1$

Spherical Electronic Raman Scattering Tensors $^4F_{5/2} \longrightarrow {}^4F_{7/2}$

$0 \longrightarrow 2{,}179\ \mathrm{cm}^{-1}$
$\alpha_0^2 = -.033F_2$
$\alpha_0^1 = -.075F_1$

$\overline{0} \longrightarrow 2{,}179\ \mathrm{cm}^{-1}$
$\alpha_1^2 = .035F_2$
$\alpha_1^1 = -.067F_1$

$0 \longrightarrow \overline{2{,}179}\ \mathrm{cm}^{-1}$
$\alpha_{-1}^2 = .035F_2$
$\alpha_{-1}^1 = .067F_1$

$\overline{0} \longrightarrow \overline{2{,}179}\ \mathrm{cm}^{-1}$
$\alpha_0^2 = -.033F_2$
$\alpha_0^1 = .075F_1$

$0 \longrightarrow 2{,}221\ \mathrm{cm}^{-1}$
$\alpha_1^2 = -.011F_2$
$\alpha_1^1 = .030F_1$

$\overline{0} \longrightarrow 2{,}221\ \mathrm{cm}^{-1}$
$\alpha_{-2}^2 = .033F_2$
$\alpha_2^2 = -.065F_2$

$0 \longrightarrow \overline{2{,}221}\ \mathrm{cm}^{-1}$
$\alpha_{-2}^2 = .065F_2$
$\alpha_2^2 = -.033F_2$

$\overline{0} \longrightarrow \overline{2{,}221}\ \mathrm{cm}^{-1}$
$\alpha_{-1}^2 = .011F_2$
$\alpha_{-1}^1 = .030F_1$

$0 \longrightarrow 2{,}620\ \mathrm{cm}^{-1}$
$\alpha_1^2 = .055F_2$
$\alpha_1^1 = .040F_1$

$\overline{0} \longrightarrow 2{,}620\ \mathrm{cm}^{-1}$
$\alpha_{-2}^2 = -.046F_2$
$\alpha_2^2 = -.039F_2$

$0 \longrightarrow \overline{2{,}620}\ \mathrm{cm}^{-1}$
$\alpha_{-2}^2 = .039F_2$
$\alpha_2^2 = .046F_2$

$\overline{0} \longrightarrow \overline{2{,}620}\ \mathrm{cm}^{-1}$
$\alpha_{-1}^2 = -.055F_2$
$\alpha_{-1}^1 = .040F_2$

$0 \longrightarrow 2{,}676\ \mathrm{cm}^{-1}$
$\alpha_0^2 = .062F_2$
$\alpha_0^1 = -.029F_1$

$\overline{0} \longrightarrow 2{,}676\ \mathrm{cm}^{-1}$
$\alpha_1^2 = .072F_2$
$\alpha_1^1 = .007F_1$

$0 \longrightarrow \overline{2{,}676}\ \mathrm{cm}^{-1}$
$\alpha_{-1}^2 = .072F_2$
$\alpha_{-1}^1 = -.007F_1$

$\overline{0} \longrightarrow \overline{2{,}676}\ \mathrm{cm}^{-1}$
$\alpha_0^2 = .062F_2$
$\alpha_0^1 = .029F_1$

Cartesian Electronic Raman Scattering Tensors $^2F_{5/2} \longrightarrow {}^2F_{5/2}$

$0\ \text{cm}^{-1} \longrightarrow 240\ \text{cm}^{-1}$

$|\alpha_{XX}|^2 = |\alpha_{YY}|^2 = (.0306F_2)^2$

$|\alpha_{XY}|^2 = |\alpha_{YX}|^2 = (.128F_2)^2$

$|\alpha_{XZ}|^2 = |\alpha_{YZ}|^2 = (.0923F_1 + -.0583F_2)^2$

$|\alpha_{ZX}|^2 = |\alpha_{ZY}|^2 = (.0923F_1 + .0583F_2)^2$

$0\ \text{cm}^{-1} \longrightarrow 429\ \text{cm}^{-1}$

$|\alpha_{XX}|^2 = |\alpha_{YY}|^2 = (.0539F_2)^2$

$|\alpha_{XY}|^2 = |\alpha_{YX}|^2 = (.170F_1)^2$

$|\alpha_{XZ}|^2 = |\alpha_{YZ}|^2 = (.0171F_1 + .110F_2)^2$

$|\alpha_{ZX}|^2 = |\alpha_{ZY}|^2 = (-.0171F_1 + .110F_2)^2$

$|\alpha_{ZZ}|^2 = (.108F_2)^2$

Cartesian Electronic Raman Scattering Tensors $^2F_{5/2} \longrightarrow {}^2F_{7/2}$

$0\ \text{cm}^{-1} \longrightarrow 2{,}179\ \text{cm}^{-1}$
$|\alpha_{XX}|^2 = |\alpha_{YY}|^2 = (.0137F_2)^2$
$|\alpha_{XY}|^2 = |\alpha_{YX}|^2 = (.0528F_1)^2$
$|\alpha_{XZ}|^2 = |\alpha_{YZ}|^2 = (-.0332F_1 + .0174F_2)^2$
$|\alpha_{ZX}|^2 = |\alpha_{ZY}|^2 = (.0332F_1 + .0174F_2)^2$
$|\alpha_{ZZ}|^2 = (.0273F_2)^2$

$0\ \text{cm}^{-1} \longrightarrow 2{,}221\ \text{cm}^{-1}$
$|\alpha_{XX}|^2 = |\alpha_{YY}|^2 = (.0491F_2)^2$
$|\alpha_{XY}|^2 = |\alpha_{YX}|^2 = (.0164F_2)^2$
$|\alpha_{XZ}|^2 = |\alpha_{YZ}|^2 = (-.0150F_1 + .0053F_2)^2$
$|\alpha_{ZX}|^2 = |\alpha_{ZY}|^2 = (.0150F_1 + .0053F_2)^2$

$0\ \text{cm}^{-1} \longrightarrow 2{,}620\ \text{cm}^{-1}$
$|\alpha_{XX}|^2 = |\alpha_{YY}|^2 = (.0035F_2)^2$
$|\alpha_{XY}|^2 = |\alpha_{YX}|^2 = (.0426F_2)^2$
$|\alpha_{XZ}|^2 = |\alpha_{YZ}|^2 = (.0201F_1 + .0276F_2)^2$
$|\alpha_{ZX}|^2 = |\alpha_{ZY}|^2 = (.0201F_1 + -.0276F_2)^2$

$0\ \text{cm}^{-1} \longrightarrow 2{,}676\ \text{cm}^{-1}$
$|\alpha_{XX}|^2 = |\alpha_{YY}|^2 = (.0253F_2)^2$
$|\alpha_{XY}|^2 = |\alpha_{YX}|^2 = (.0205F_1)^2$
$|\alpha_{XZ}|^2 = |\alpha_{YZ}|^2 = (.0035F_1 + .0358F_2)^2$
$|\alpha_{ZX}|^2 = |\alpha_{ZY}|^2 = (-.0035F_1 + .0358F_2)^2$
$|\alpha_{ZZ}|^2 = (.0506F_2)^2$

Appendix 3B: Absolute 4f-5d Oscillator Strengths and 4f-4f Electronic Raman Scattering Cross-Sections

In the main body of this chapter only the relative values of the electronic Raman scattering intensities were given. Inspired by the work of Judd [73] and Chase and Payne[66] we decided to determine the absolute values of the electronic Raman scattering cross-sections and, in addition, the oscillator strengths of the 4f-5d one photon transitions. These were then compared to the expected values calculated using the Hartree-Fock estimates of the 4f and 5d radial wavefunctions. The results of the comparison are very enlightening and add substantially to the conclusions reached in the main body of the chapter. For completeness I wished to include this information in the thesis but did not want to re-write an already completed chapter. The solution was the addition of this appendix. It is presented in the form of an article that is being presented for publication to Physical Review B. I apologize to the reader for the fact that some information given in the main body of the chapter is repeated in this appendix.

Abstract

The oscillator strengths for the $4f^1 \longrightarrow 5d^1$ transitions of Ce^{3+} in $LuPO_4$ are measured from absorption spectra and compared to the values calculated from theory. The measured oscillator strengths are found to be between 2.5 to 20 times smaller than the corresponding calculated values. In addition, absolute cross-sections for electronic Raman scattering between the levels of the $4f^1$ configuration of Ce^{3+} in $LuPO_4$ are measured and found to be significantly smaller than those expected from theory. Both of these discrepancies may be explained by a reduction in the radial integral, $\langle 4f|r|5d\rangle$, for Ce^{3+} in the solid state. Absorption data obtained from the literature for the $4f^1 \longrightarrow 5d^1$ transitions of Ce^{3+} in a number of host crystals are used to establish a correlation between

the cerium ion-ligand distance and the reduction in the $\langle 4f|r|5d\rangle$ integral. The effect on electronic Raman scattering cross-sections for rare earth ions in crystals is discussed.

Introduction

Transparent crystals containing trivalent rare earth ions form a unique and interesting class of optical materials. A great deal of effort has been directed toward establishing a quantitative description of the intensities of optical processes in these crystals. The Judd-Ofelt theory [15,16] for the intensities of the formally parity forbidden one-photon transitions between states of the ground $4f^N$ configuration of the trivalent rare earth ions has proven in general quite successful, with the most notable flaw being the unexpected hypersensitivity [74,75,76] of one of the variable parameters of the theory to changes in the rare earth ion's host crystal.

The similarities between the Judd-Ofelt one-photon theory and the calculation of the intensities of two-photon transitions between states of the $4f^N$ configuration of rare earth ions as developed by Axe [14], have led to studies comparing observed to calculated intensity values for two-photon processes as a new test of the approximations common to both calculations. The two-photon experiments potentially serve as a more stringent and thus more revealing test as a result of the reduced number of free parameters needed to describe the parity allowed two-photon transitions. Comprehensive comparisons between observed and calculated intensities have been carried out by Downer *et al.* [49,50,51,77] using two-photon absorption in crystals of Eu^{2+}:LaF_3 and Gd^{3+}:LaF_3 and by Becker *et al.* [11,64] using electronic Raman scattering in crystals of $ErPO_4$ and $TmPO_4$. The observed discrepancies between experiment and calculation have spurred a number of papers suggesting extensions to the standard second-order theory of two-photon processes. [52,65,78,79,80,81]

Recently Judd [73] has derived a simple expression for the sum of oscillator strengths for transitions of the type $4f^N \longrightarrow 4f^{N-1}5d$. Using this expression, oscillator strength

sums were computed for f$\longrightarrow$d transitions in Ce^{3+}, Tb^{3+}, and Bk^{3+} and compared to the observed values for these ions in aqueous solution [82,83]. It was found that the calculated values exceeded the observed values by factors ranging from 2 to greater than 10. The relevance of this result to the aforementioned intra-$4f^N$ one and two photon transition intensities is immediately realized when one examines the expressions describing these intensities, both of which contain matrix elements of the electric dipole operator between states of the $4f^N$ and $4f^{N-1}5d$ configurations. Thus, if the $4f^N \longrightarrow 4f^{N-1}5d$ oscillator strengths are smaller than expected from calculation this implies that the intensities of the intra-$4f^N$ one and two photon transitions should be smaller than expected.

This proposition is most readily tested by comparing the observed absolute two photon cross-sections to those calculated from theory. It is true that many previous experiments have compared the absolute intra-$4f^N$ one photon cross-sections to those computed using the Judd-Ofelt theory, however, in these cases any reduction in the cross-sections would be manifested in the values of the parameters of the theory. To note any reduction the values of the fitted parameters have to be compared to the values of the parameters expected from physical estimates of such things as the strength of the crystal field, radial overlap integrals between configurations and the average energies of excited configurations. Of course the same is true for the two photon case with the important exception being the reduction in complexity of the parameterization. Most notably the parameters for the two photon processes do not include the strength of the crystal field. The other quantities such as the radial overlap integrals and excited configuration energies may be estimated from Hartree-Fock calculations.

In the two photon work by Downer *et al.* and Becker *et al.* all intensities were calculated to within a factor which was dependent on the radial overlap integrals and excited configuration average energies common for all transitions. In both cases the calculated values were compared to the experimentally observed relative intensities between different transitions thus eliminating the need to know the factor determining the overall scaling for the absolute cross-sections. An experiment which measures absolute two photon cross-sections is in practice difficult to perform because of the problems in estimating the efficiency of the light collection system used in both electronic Raman

scattering and two photon absorption experiments. The small two photon absorption is usually measured by monitoring the fluorescence that results from the absorption making the detection scheme very similar to that needed for electronic Raman scattering. However, Chase and Payne [66] in a carefully executed experiment have succeeded in measuring absolute two photon absorption cross-sections for the $^4I_{9/2} \longrightarrow {}^4G_{7/2}$ transition in Nd^{3+} doped into crystals of YAG and YLF. A comparison with calculated values showed that for the YAG crystal the measured cross-section was as expected, but for the YLF crystal the measured cross-section was smaller than expected by approximately a factor of 10. The first item of note, as pointed out by Chase and Payne, is the remarkable host dependence of the cross-section. In the context of this work it is noted that the small value of the cross-section for the YLF crystal is in accordance with the reduced $4f \longrightarrow 5d$ oscillator strengths noted by Judd [73].

We have recently reported the results of a comparison between the observed and calculated relative electronic Raman scattering intensities from Ce^{3+} in crystals of $LuPO_4$. Ce^{3+}, with a ground state configuration $[Xe]4f^1$, has one optically active electron. A primary motivation for the choice of Ce^{3+} was the relatively low energy of the states of the cerium ion's first excited configuration. This low energy allowed for a direct spectroscopic examination of these states which are believed to serve as the primary virtual intermediate states in the electronic Raman process. Thus data have been obtained on both the electronic Raman scattering intensities and the $4f^1 \longrightarrow 5d^1$ absorption spectra. Through a careful analysis of the absorption data and a calibration of the efficiency of the electronic Raman scattering light collection system absolute values have been obtained for both the electronic Raman scattering cross-sections and the $4f^1 \longrightarrow 5d^1$ oscillator strengths. This affords the opportunity of comparing these linked quantities to their respective calculated values.

Electronic Energy Levels and Wavefunctions

In order to compute the expected values for the 4f⟶5d absorption and the 4f⟶4f electronic Raman scattering cross-sections for Ce^{3+}:$LuPO_4$, expressions for the electronic wavefunctions for states of both the $4f^1$ and $5d^1$ configuration are needed. Figure 3.21 shows schematically the energy level structure of Ce^{3+} in $LuPO_4$. A complete description of this structure has been given including the angular parts of the electronic wavefunctions for the states of both the $4f^1$ and $5d^1$ configurations. The angular wavefunctions associated with the states of a given configuration were obtained through the diagonalization of a parameterized Hamiltonian in which the parameters were varied until a least-squares fit to the observed energy levels was accomplished. Russell-Saunders terms were used as the basis set in the diagonalization so that the derived angular wavefunctions are written as sums of the form

$$|\Psi\rangle = \sum_{J,M_J} a_{J,M_J} |LSJM_J\rangle \tag{3.33}$$

One necessary component for the calculation of absolute cross-sections, is the radial parts of the wavefunctions. They have been estimated numerically using a relativistic Hartree-Fock calculation [84], and the radial integral $\langle 4f|r|5d\rangle$ is found to have a value of $0.441\mathring{A}$ for Ce^{3+}.

4f-5d Absorption

Observed Oscillator Strengths

Absorption spectra of Ce^{3+} in $LuPO_4$ were obtained in the range 29,000-51,000 cm^{-1} using a Cary 17 spectrophotometer purged with dry nitrogen gas. Throughout this paper the absorption spectra are given as the absorbance (α) as a function of wave number ($k = 1/\lambda$). The absorbance is given by the usual definition,

$$\alpha(k) = -\frac{1}{l}\ln\frac{I}{I_o} \tag{3.34}$$

where I_o and I are the intensities of the incident and transmitted light, respectively, and l is the crystal thickness. The oscillator strength, P, for a given transition is proportional

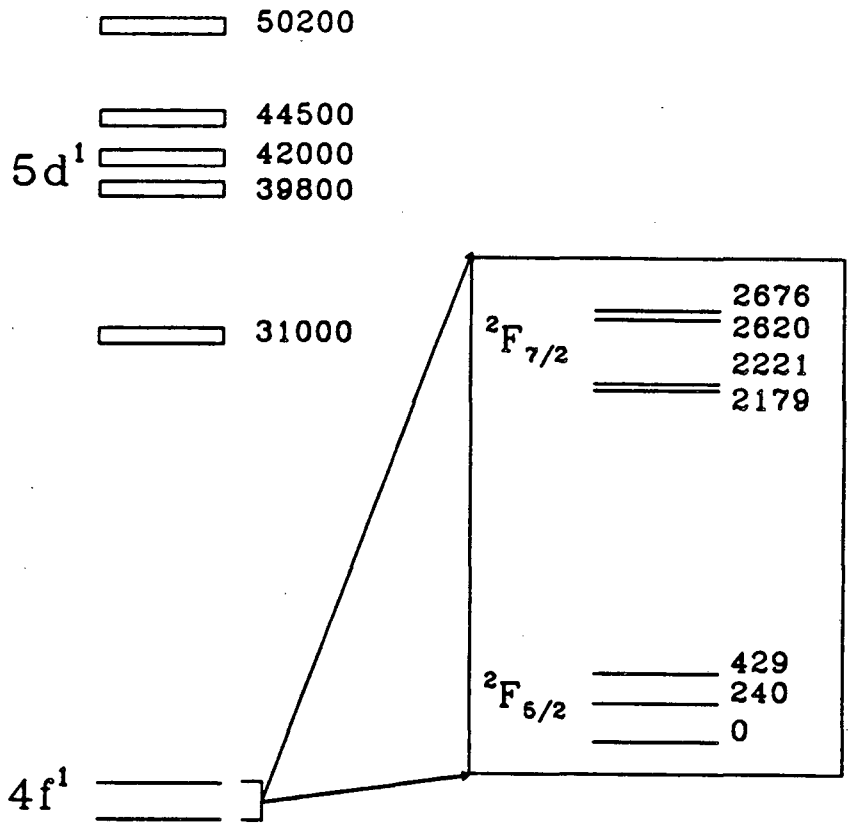

Figure 3.21: Schematical representation of energy level structure of Ce^{3+} in a crystal of $LuPO_4$. All numbers are in cm^{-1}.

to the area under the spectral feature associated with the transition divided by the number density of absorbing ions, n_o.

$$P = \left(\frac{1}{\pi r_o}\right) \frac{1}{n_o} \int_{peak} \alpha(k) dk, \tag{3.35}$$

where $r_o = \frac{e^2}{m_e c^2} \approx 2.813 \times 10^{-13}$cm is the classical radius of the electron.

Crystals with three different doping levels of Ce^{3+} were studied. These crystals had nominally 1%, 10%, and 20% mole ratios of Ce to Lu in the starting materials used for crystal growth. As a more direct measure of the Ce^{3+} concentrations in the final crystals X-ray fluorescence analyses [10] were performed on the nominally 1% and 20% crystals. The analyses showed that the actual mole percents were greatly reduced from the starting proportions to values of 0.0604 mole% and 0.638 mole%, respectively. The number density of Lu^{3+} in $LuPO_4$ [6] is 1.456×10^{22}cm^{-3} so these concentrations correspond to Ce^{3+} number densities of 8.71×10^{18}cm^{-3} and 9.19×10^{19}cm^{-3}. The relatively small values for the final Ce^{3+} concentrations are not surprising because the substitution of Ce^{3+} into Lu^{3+} sites is expected to be diminished as a result of the significantly larger ionic radius of Ce^{3+} compared to that of Lu^{3+}.

Figure 3.22 shows the room temperature absorption spectra for crystals with the three different concentrations of Ce^{3+}. The peaks labelled (a),(b),(c),(d), and (f) have been previously identified as $4f^1 \longrightarrow 5d^1$ transitions of Ce^{3+}. This identification is confirmed by the observation that these peaks increase with increasing Ce^{3+} concentration. For the peak labelled (a) at 31,000 cm^{-1} the integrated absorbances for the nominally 1% and 20% crystals scale roughly as 1 to 10 in agreement with the ratio of the concentrations determined from the X-ray fluorescence analysis. In Ce^{3+}:$LuPO_4$ it is expected that all absorption in the range 30,000 to 50,000 cm^{-1} is solely from the $4f^1 \longrightarrow 5d^1$ transitions of the cerium ions. Pure $LuPO_4$ is transparent up to approximately 70,000 cm^{-1} [9] and transitions associated with charge transfer between the ligands and the cerium ions are expected to occur at a considerably higher energy [1] than 50,000 cm^{-1}. In addition, reflection losses resulting from the refractive index of $LuPO_4$ are not ex-

[1] Charge transfer bands for Ce^{3+} should occur at higher energies than those observed for Yb^{3+} in the same host crystal. In Yb^{3+}:$LuPO_4$ the onset of the first charge transfer band is observed at 48,500 cm^{-1}.

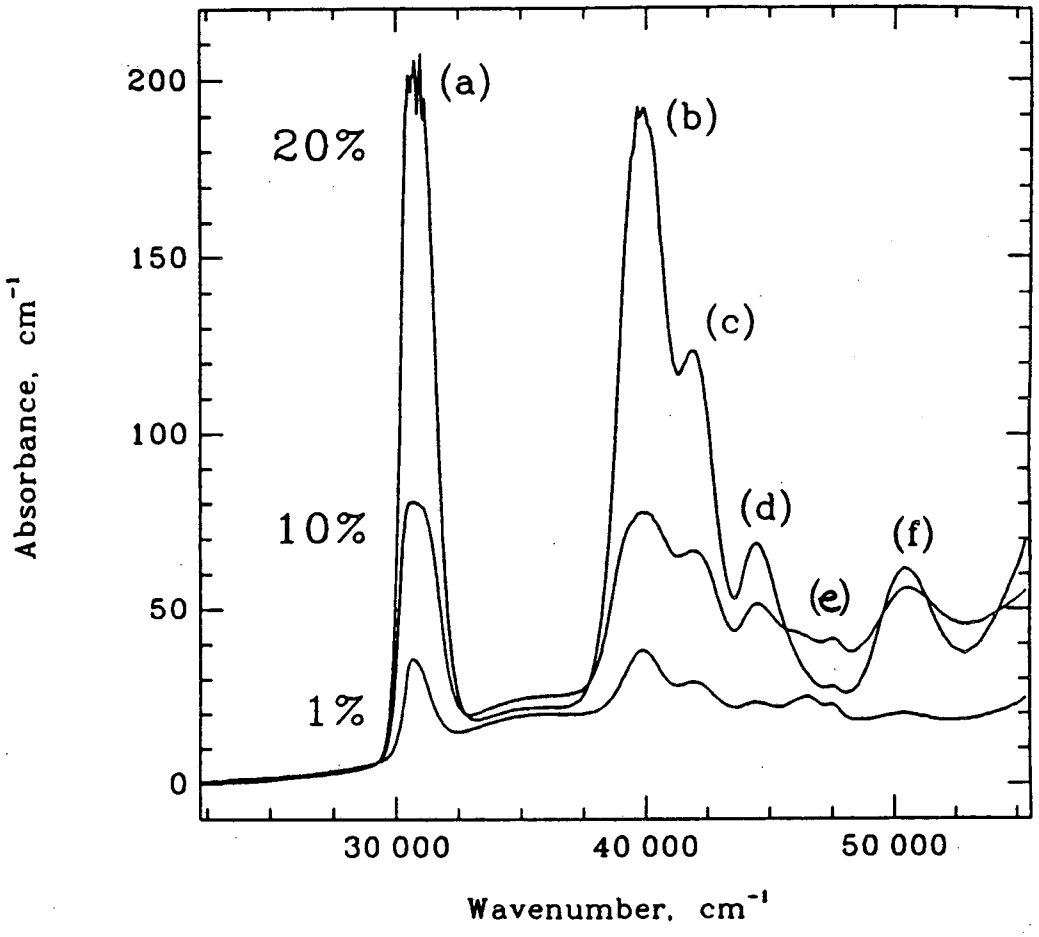

Figure 3.22: Room temperature absorption spectra of Ce^{3+}:$LuPO_4$ for three different concentrations of Ce^{3+}. The peaks labelled (a),(b),(c),(d), and (f) are attributed to absorption in cerium. The peak (e) is due to an impurity.

pected to vary significantly with excitation energy at energies so far removed from the band gap of $LuPO_4$. However, in addition to the labelled peaks there is absorption that is not correlated to the concentration of cerium ions . The absorption is in the form of several well-defined peaks in the range 46,000-47,500 cm^{-1} and a broad background over the entire range of 30,000-50,000 cm^{-1}. A similar structure appears in the absorption spectrum of pure $LuPO_4$. Attempts to remove the background in the Ce^{3+}:$LuPO_4$ spectra by simply subtracting the $LuPO_4$ spectrum did not seem justified due to the observed variations in the background from sample to sample.

The approach taken was to pick for each concentration a smooth background such that after subtraction the remaining spectra scale as the known Ce^{3+} concentrations. The

Absorption Peak cm^{-1}	Integrated Absorbances,$cm^{-1}/10^3$		
	x=.01	x=.10	x=.20
31,000	31.4	120.3	299.9
39,800	40.9	117.5	395.0
42,000	13.3	67.7	150.6
44,500	6.9	28.1	79.7
50,500	3.	32.5	66.1
Sum for all peaks	95.8	366.1	990.4
Sum with Background	529.7	1,215	1,682

Table 3.15: Room temperature integrated absorbances for $Ce_xLu_{1-x}PO_4$ where x represents the proportion of Ce^{3+} in the starting materials.

most obvious choices for the backgrounds seemed to work fairly well in this respect. As an example of the choices of the background, Figure 3.23 shows the corrected spectrum for the nominally 20% crystal, the background that is subtracted, and the spectrum of a $LuPO_4$ crystal for comparison purposes. Table 3.15 lists the integrated absorbances for the Ce^{3+} peaks for the three different concentrations after background subtraction. The areas of the peaks at 31,000 cm^{-1} and 50,500 cm^{-1} were obtained by direct integration of the spectra. The peaks at 39,800 cm^{-1}, 42,000 cm^{-1}, and 44,500 cm^{-1} overlap significantly so that it was necessary to fit each spectrum in this region with three overlapping lines. In order to fit the peaks asymmetric gaussian functions were used. Although there was a certain amount of arbitrariness in these fits the sums of the areas of the three fitted lines accurately represented the integrated absorbances in this region of the spectrum.

Examination of Table 3.15 indicates that with the selected backgrounds the absorbances scale fairly accurately. The highest error appears to occur for the peak at 50,500 cm^{-1}. This is not surprising because the largest background absorption is in this region. The table also includes the sums of the absorbances of the Ce^{3+} peaks after background subtraction and as an upper limit to this sum, the integrated absorbances from

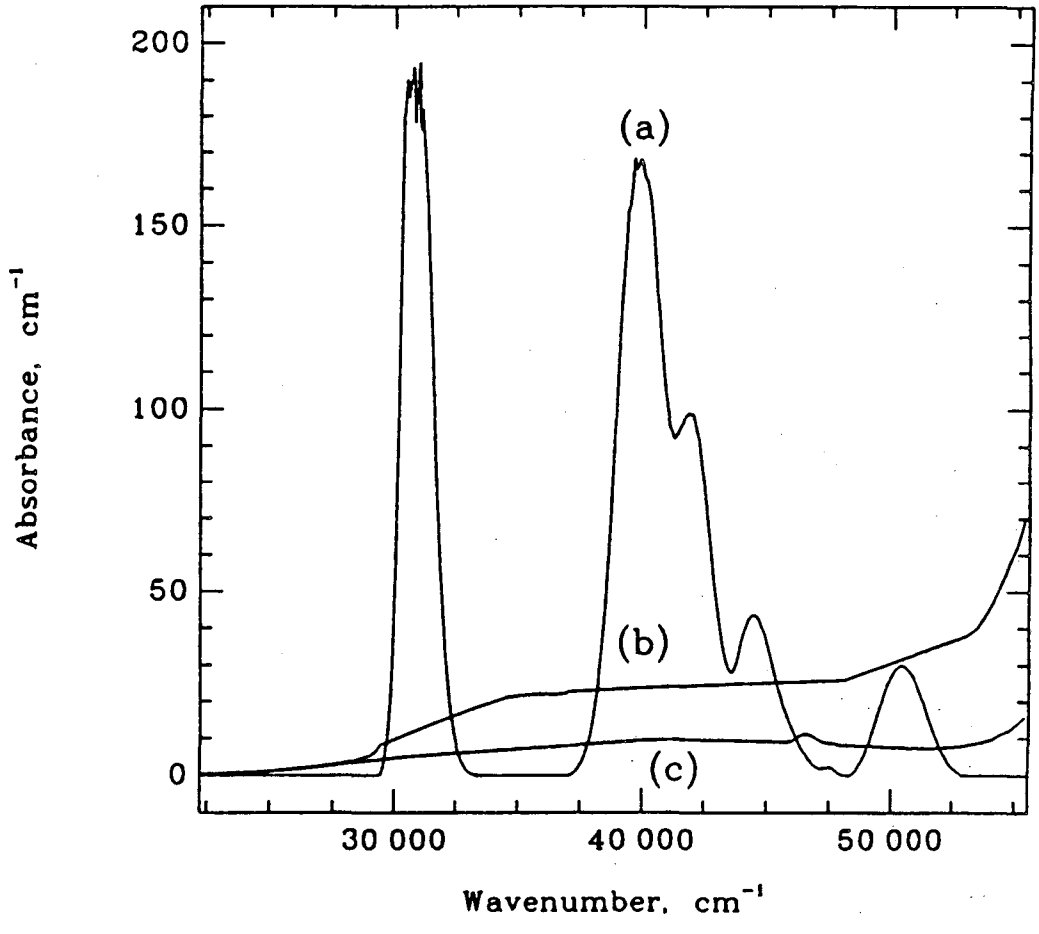

Figure 3.23: (a) Room temperature absorption spectrum for the nominally 20% Ce^{3+}:$LuPO_4$ crystal with background absorption subtracted. (b) Background absorption. (c) Room temperature absorption spectrum of $LuPO_4$.

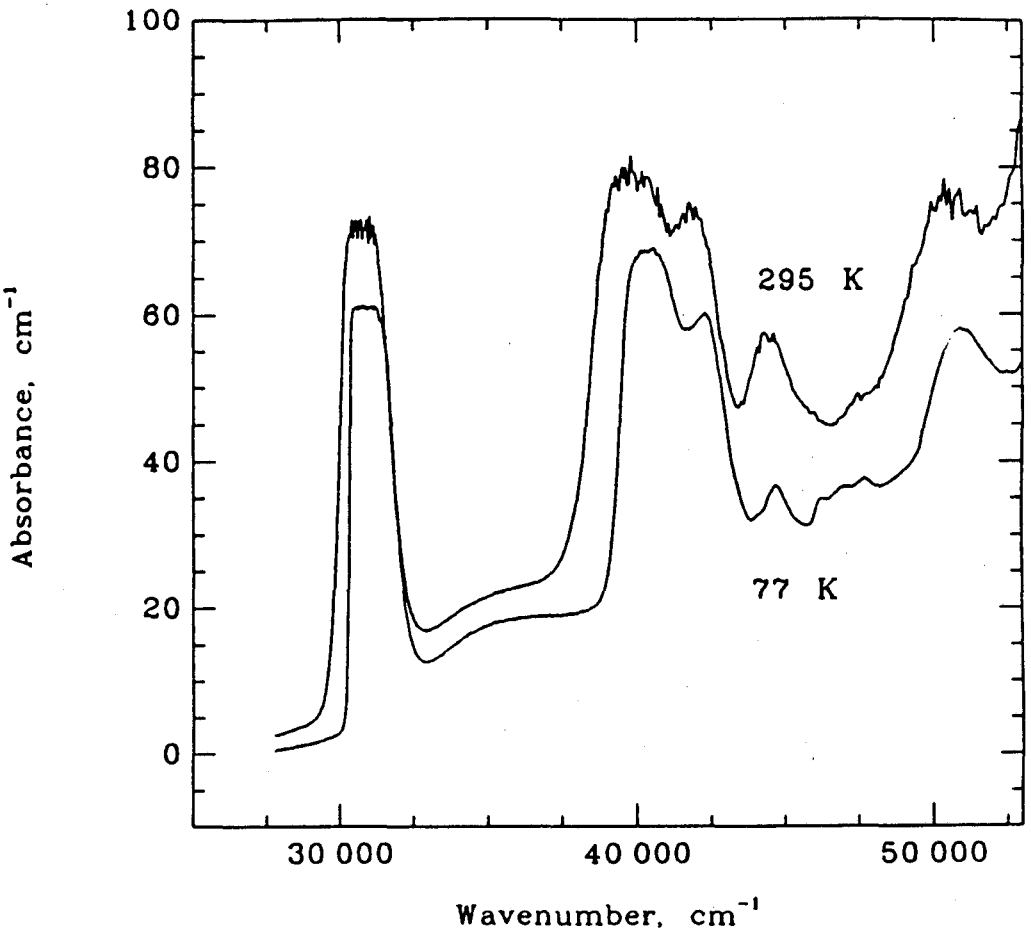

Figure 3.24: Comparison of room temperature and 77K absorption spectra of the nominally 10% Ce^{3+}:$LuPO_4$.

30,000-50,000 cm^{-1} including the background. Oscillator strengths are easily calculated from these values and will be listed in the following section.

Spectra were also taken at 4.2 K and 77 K. Figure 3.24 shows absorption spectra of a nominally 10% Ce^{3+}:$LuPO_4$ crystal taken at room temperature and at 77 K. The differences between the two spectra are not dramatic. The most notable difference is the shift in the room temperature spectrum toward lower energies. This is probably due to absorption from thermally populated excited states which are of either vibrational or electronic origin.

Comparison Between Calculated and Observed Oscillator Strengths

For an ion embedded in a crystal the oscillator strength associated with a polarized electric dipole transition between a state $|i\rangle$ and a state $|f\rangle$ is given by

$$P_{fi\hat{\mathbf{e}}} = \frac{L^2}{n}\left(\frac{4\pi\alpha_{fs}}{r_o}\right)k|\langle f|\hat{\mathbf{e}}\cdot\vec{D}|i\rangle|^2 \tag{3.36}$$

where $\alpha_{fs} = \frac{e^2}{\hbar c} \approx \frac{1}{137.04}$ is the fine-structure constant, k is the wavenumber of the light absorbed in the transition, $\hat{\mathbf{e}}$ is a unit vector describing the polarization direction of that light, $\vec{D}$ is the electric dipole operator, n is the index of refraction of the host crystal, and L is the local field correction factor. L is related to the index of refraction of the host crystal and is given by the expression [85],

$$L = \frac{n^2+2}{3}. \tag{3.37}$$

$LuPO_4$ is birefringent so that the value of L is anisotropic. The values of the indices of refraction of $LuPO_4$ are assumed to be equal to the known values for the very similar crystal, YPO_4 for which $n_X = n_Y = 1.721$ and $n_Z = 1.816$ at $\lambda = 589.3$ nm.

As a result of the difference in the coupling to the crystal lattice for a 4f electron (very weak) and a 5d electron (weak to moderate), it is likely that the vibrational state of the crystal will change during a 4f$\longrightarrow$ 5d transition. Thus, in order to accurately describe such a transition the vibrational state of the crystal is included in the initial and final state descriptions. In the Born-Oppenheimer approximation which is valid as long as the rare earth electron-crystal coupling is not too strong, the wavefunctions are written as the product of a part describing the electronic state of the rare earth ion and a part describing the vibrational state of the crystal,

$$|f\rangle = |f_e\rangle|\chi^m_{f_e}\rangle. \tag{3.38}$$

$|\chi^m_{f_e}\rangle$ represents one particular vibrational mode of the crystal with the superscript m representing the occupation number of that mode. However, in the following discussion what holds for one mode holds for all.

Using these wavefunctions the expression for the oscillator strength is written as

$$P_{fi\hat{\mathbf{e}}} = \frac{L^2}{n}\left(\frac{4\pi\alpha_{fs}}{r_o}\right)k|\langle f_e|\hat{\mathbf{e}}\cdot\vec{D}|i_e\rangle|^2|\langle\chi^m_{f_e}|\chi^n_{i_e}\rangle|^2 \tag{3.39}$$

where the vibrational parts of the wavefunctions have been separated out since they do not depend explicitly on the electronic coordinates of the rare earth ion. The oscillator strengths measured in the previous section are sums over many such oscillator strengths described in the above equation. In the absorption measurements the areas under the observed broad peaks included all the transitions to a particular final electronic state. Equation 3.39 should be summed over all possible final vibrational states associated with the final electronic state and in addition, summed over all possible initial electronic states and their associated vibrational states with each of these terms weighted by their respective populations at the temperature of the measurement;

$$P_{f\hat{e}} = \frac{L^2}{n}\left(\frac{4\pi\alpha_{fs}}{r_o}\right)k \times \frac{\sum_p e^{-\beta E_{ip}}|\langle f_e|\hat{e}\cdot\vec{D}|i_{ep}\rangle|^2 \sum_n e^{-\beta E_{pn}} \sum_m |\langle\chi_f^m|\chi_{ip}^n\rangle|^2}{\sum_p e^{-\beta E_{ip}} \sum_n e^{-\beta E_{pn}}}, \tag{3.40}$$

where β is $\frac{1}{k_B T}$, E_{ip} is the energy of the p^{th} initial electronic state, E_{ipn} is the energy of the n^{th} excitation of the vibrational mode under consideration, and k has been treated as a constant over all the summations. With the assumption that the vibrational properties of the lattice are independent of the rare earth ion electronic state for all states of the 4f configuration, it can be shown that the double summation over the vibrational quantum numbers reduces to the value of unity [86]. Thus, the oscillator strength associated with the observed unresolved peaks can be written as

$$P_{f\hat{e}} = \frac{L^2}{n}\left(\frac{4\pi\alpha_{fs}}{r_o}\right)k\frac{\sum_p e^{-\beta E_{ip}}\langle f_e|\hat{e}\cdot\vec{D}|i_{ep}\rangle|^2}{\sum_p e^{-\beta E_{ip}}}, \tag{3.41}$$

independent of the details of the vibrational wavefunctions. This remains true when all the vibrational modes are explicitly considered.

The expression for the oscillator strength, or more accurately summed oscillator strengths, depends solely on the dipole matrix elements between wavefunctions describing the electronic state of the rare earth ion. These matrix elements are most easily evaluated by expressing the operator $\hat{e}\cdot\vec{D}$ as linear combinations of the spherical electric dipole operators [14], D_q^1. The values of the matrix elements for the circularly polarized dipole operators are given by

$$\langle f_e|D_q^1|i_e\rangle = \langle 5d|r|4f\rangle\langle 2||C^{(1)}||3\rangle$$

$$\times \sum_{JM_J} \sum_{J'M'_J} a_{i_e JM_J} a^*_{f_e J'M'_J}$$
$$\times (-1)^{J'-M_J} \begin{pmatrix} J' & 1 & J \\ -M'_J & q & M_J \end{pmatrix}$$
$$\times (-1)^{L'+S'+J+1} (2J+1)^{\frac{1}{2}} (2J'+1)^{\frac{1}{2}}$$
$$\times \begin{Bmatrix} J' & 1 & J \\ L & S & L' \end{Bmatrix} \langle L' || U^1 || L \rangle. \qquad (3.42)$$

The reduced matrix element of the spherical tensor operator, U^1, is unity for a one electron system. The value of the radial integral, $\langle 4f|r|5d\rangle$, is known from the Hartree-Fock calculations to be $0.441\mathring{A}$ for Ce^{3+}. The value of $\langle l' = 2||C^1|||l = 3\rangle$ is 1.73. In the experimental measurements no polarizers were used, so that for comparison purposes the calculated oscillator strengths are averaged over polarizations. In the experiments light was incident along the crystal $\hat{\mathbf{Y}}$ axis so that the measured oscillator strengths correspond to averages of the oscillator strengths calculated for the $\hat{\mathbf{X}}$ polarized and $\hat{\mathbf{Z}}$ polarized electric dipole operators. Finally note that all the electronic states are actually Kramers doublets. The final oscillator strengths are averaged over the oscillator strengths for the doublets of the initial states and summed over the oscillator strengths for the doublets of the final states.

The results of the oscillator strength calculations for T = 295 K are compared to the oscillator strengths measured for the nominally 20% Ce^{3+}:$LuPO_4$ crystal at room temperature in Table 3.16. The same comparison is made for the oscillator strengths at liquid helium temperatures in Table 3.17. There is little difference between the results for the two temperatures. For both temperatures the observed total 4f$\longrightarrow$5d oscillator strength is about 5.0 times smaller than the corresponding calculated value. The largest discrepancy occurs for the transition to the highest energy level of the 5d configuration while the smallest discrepancy occurs for the transition to the lowest energy level.

The smaller than expected oscillator strengths are in accord with what has been observed for Ce^{3+} in aqueous solution. For that system the 4f$\longrightarrow$ 5d oscillator strength [82] of .022 was approximately a factor of 2 times smaller than the expected value of .047 calculated using a partial sum rule for oscillator strengths derived by Judd, [73]

Peak cm^{-1}	$P/10^{-2}$ Calculated	Observed	Ratio $\frac{calc}{obs}$
30,468	.86	.368	2.3
39,931	2.21	.486	4.5
41,626	.63	.185	3.4
44,038	.44	.098	4.5
50,290	1.98	.081	24.4
Total	6.12	1.22	5.0

Table 3.16: Comparison of observed and calculated oscillator strengths for the nominally 20% Ce^{3+}:$LuPO_4$ crystal at room temperature.

Peak cm^{-1}	$P/10^{-2}$ Calculated	Observed	Ratio $\frac{calc}{obs}$
30,468	.88	.35	2.5
39,931	1.05	.36	2.9
41,626	.81	.20	4.1
44,038	.40	.05	8.0
50,290	2.7	.14	19.0
Total	5.8	1.1	5.3

Table 3.17: Comparison of observed and calculated oscillator strengths for the nominally 20% Ce^{3+}:$LuPO_4$ crystal at liquid helium temperature.

$$\sum_b P_{ab} = \left(\frac{2N}{7}\right) \frac{L^2}{n} \frac{\Delta E}{E_o} \langle 4f|\frac{r}{a_o}|5d\rangle^2 \tag{3.43}$$

where a represents a state of the $4f^N$ configuration and b labels the states of the $4f^{N-1}5d$ configuration. ΔE is the energy difference (in cm^{-1}) between a and b (assumed to be constant for all b), E_o=219,475 cm^{-1}, and a_o=0.5292Å. Evaluating Equation 3.43 for Ce^{3+} in $LuPO_4$ yielded a value for the 4f⟶5d oscillator strength of 0.055 in good agreement with the value of approximately 0.059 calculated in this paper.

A review of the literature shows that the 4f⟶5d oscillator strengths for Ce^{3+} in solid state systems are in general smaller than the values calculated using the Judd sum rule. Table 3.18 shows the comparison of calculated and observed oscillator strengths for Ce^{3+} in various crystals along with the values of the quantities used in evaluation

Host Crystal	coordination	M-L $\overline{R}(\AA)$	$\overline{\Delta E}(cm^{-1})$	lowest 5d(cm^{-1})	n	P_{calc} $/10^{-2}$	P_{obs} $/10^{-2}$
$LuPO_4$	8	2.309[a]	41,570	30,700	1.75[b]	5.5[c]	1.24[d]
YAG	8	2.368[e]	34,200	22,040	1.9[f]	5.7	0.57[g]
aquo	9	2.575[h]	44,000	39,000	1.3[i]	4.7	2.2[h]
$YAlO_3$	9	2.62[j]	37,940	32,920	2[k]	6.9	4.0[l]
YLF	8	2.269[m]	43,690	34,270	1.5[n]	5.3	0.48[o]
CaF_2	8	2.364[p]	44,500	32,400	1.434[q]	5.1	1.7[r]
SrF_2	8	2.511[p]	45,730	33,600	1.442[q]	5.3	2.5[r]
LaF_3	9	2.52[s]	44,380	40,600	1.6[t]	5.8	2.1[u]
BaF_2	8	2.685[p]	45,940	34,200	1.475[q]	5.5	4.4[r]

a:[6], b:[87], c:calculated using Equation 3.43, d:this work, e:[88], f:[89], g:[35], h:[90], i:[87], j:[91], k:[92], l:[33], m:[93], n:[94], o:[36], p:[95], q:[28], r:[87], s:[96], t:[97], u:[37],

Table 3.18: Comparison between calculated and observed 4f⟶5d oscillator strength for Ce^{3+} in various host crystals. M-L are the average metal ion-ligand distances. $\overline{\Delta E}$ are the average $5d^1$ energies. n are the refractive indices used in Equation 3.43.

of Equation 3.43. The observed oscillator strengths were derived by us from spectra published in the cited references. This approach is at best very approximate. The values of the quantities that might be useful in attempts to explain the variations in 4f⟶5d oscillator strengths are also listed in Table 3.18. The quantity that is most obviously correlated to the oscillator strengths is the average Ce^{3+}-ligand distance. The values given in the table are actually averages over the metal ion-neighboring ligand distances for the pure crystal. In general, the smaller this distance the greater the reduction of the 4f⟶ 5d oscillator strength relative to the expected free ion value. This is true whether the surrounding ligands are oxygen ions or fluorine ions. The correlation is shown graphically in Figure 3.25.

It is possible the correlation shown in Figure 3.25 only reflects the different solubilities of Ce^{3+} in the various crystal hosts. In many of the earlier studies the exact concentrations of Ce^{3+} were not of crucial importance so that only starting material concentrations were reported. We have shown that the actual concentration of Ce^{3+} in a crystal can be substantially smaller than the concentration in the starting materials. Too large a value for the Ce^{3+} concentration in Equation 3.35 will lead to a reduced value for the calculated oscillator strength. Thus, the correlation will follow directly if

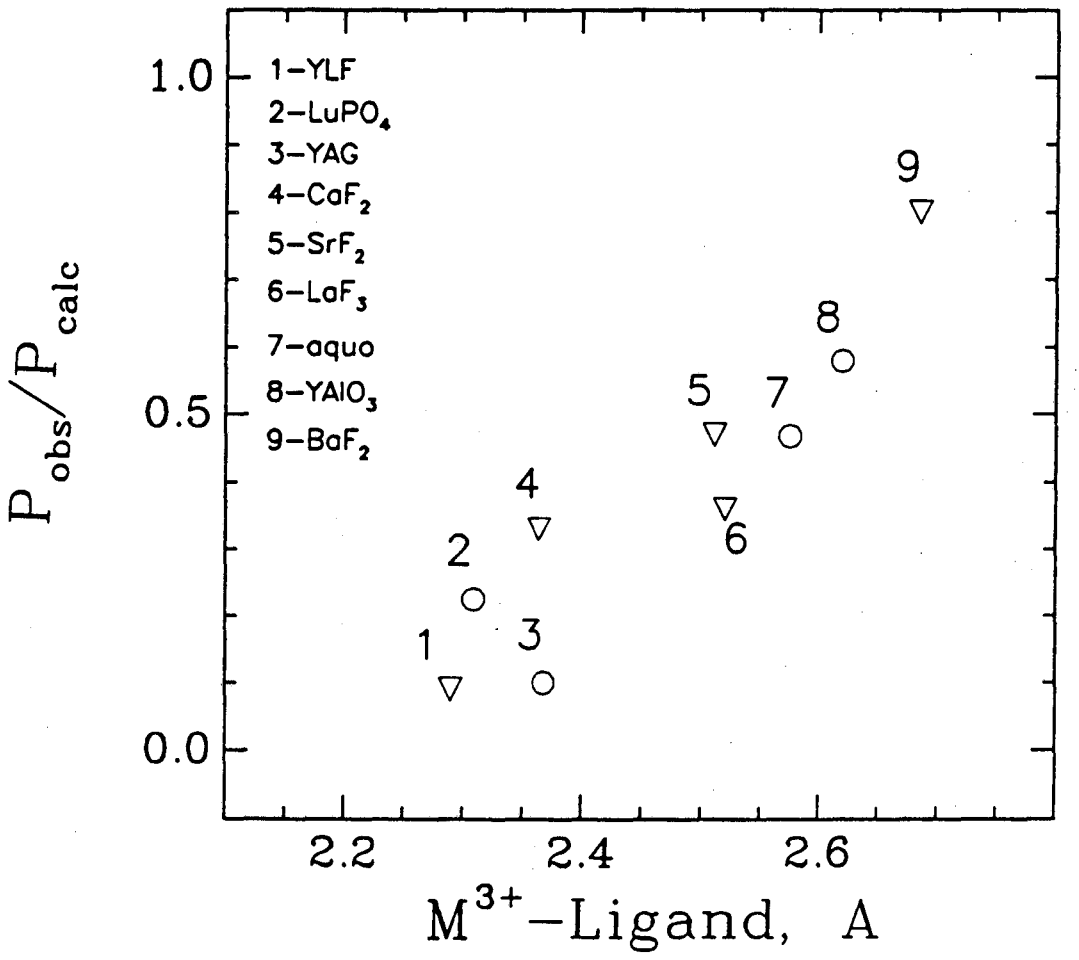

Figure 3.25: Ratio of observed over calculated oscillator strength vs. the average M^{3+}-ligand distance. Oxide crystals are marked by circles, fluoride crystals are marked by inverted triangles. The oscillator strengths were calculated using the Judd sum rule.

the solubilty of Ce^{3+} into a crystal is related to the metal ion-ligand distance. Such a relationship might be expected for cases in which the replaced metal ion is smaller than the cerium ion (*i.e.*Y^{3+} and Lu^{3+}). However, such a relationship does not follow as readily for the crystals CaF_2, SrF_2, BaF_2, and LaF_3 in which the metal ion is the same size or larger than Ce^{3+} . In addition, the Ce^{3+} concentrations for $LuPO_4$ and $YAlO_3$ are known to be accurate from analysis. Thus, for a number of the crystals the correlation can not be explained by inaccuracies in the Ce^{3+} concentration.

One possible explanation is based on the neuphelauxetic effect [26]. It is generally accepted that upon introduction of a rare earth ion into a solid state system the rare earth ion orbitals expand radially as a result of overlap with the ligand orbitals. This interaction of the ligand and rare earth ion orbitals may be viewed as a first step toward covalent bonding. The effect is expected to be much greater for the 5d orbitals than the shielded 4f orbitals. Krupke [98] has noted that a differential expansion of the 5d orbitals relative to the 4f orbitals could lead to a substantially reduced dipole matrix element $\langle 4f|r|5d\rangle$. This possibility becomes evident when one notes that $|4f\rangle$ and $|5d\rangle$ have opposite signs in some regions of space, as shown in Figure 3.26. A simple calculation may be performed following Morrison and Leavitt[99], which involves the rescaling of the radial 5d wavefunction by replacing r by r/τ, where τ is some number less than unity. It is seen that smaller values of τ (greater expansion) lead to decreases in the dipole matrix element, and that for example a value of $\tau = 0.7$ results in a reduction in the dipole matrix element by a factor of approximately 2. The correlation with the Ce^{3+}-ligand distance thus can be seen as a consequence of the greater expansion of the 5d wavefunction (smaller τ) as the 5d orbital-ligand orbital overlap increases.

4f-4f Electronic Raman Scattering

Observed Absolute Cross-Sections

In this section we describe how the absolute differential electronic Raman scattering

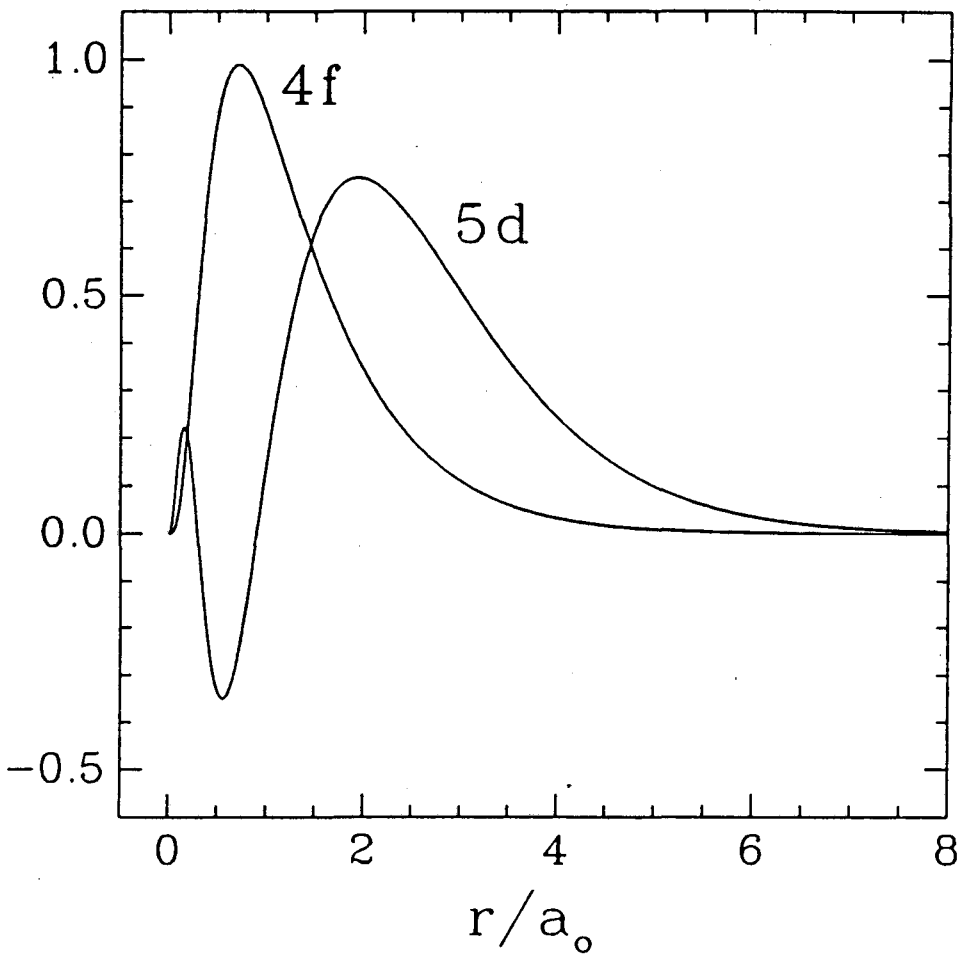

Figure 3.26: Hartree-Fock calculated radial wavefunctions for the 4f and 5d orbitals of Ce^{3+}. The functions plotted are actually $r|4f\rangle$ and $r|5d\rangle$.

cross-sections for Ce^{3+} in $LuPO_4$ were determined from the scattering spectra. The differential scattering cross-section per unit solid angle per ion is defined by the relation

$$N_s = n_o l N_o \left(\frac{d\sigma}{d\Omega}\right), \tag{3.44}$$

where N_s is the number of photons scattered per unit time per unit solid angle, N_o is the number of photons incident on the sample per unit time, l is the sample thickness, and n_o is the number density of ions. This expression is valid in cases in which the scattering does not severely deplete the incident beam ($n_o l \frac{d\sigma}{d\Omega} \ll 1$).

If the value of N_s is known for a given transition the differential scattering cross-section for that transition can be determined directly from Equation 3.44. However, absolute values of N_s cannot be measured directly from the scattering spectra because the efficiency of the experimental light collection system is unknown. All that can be determined directly from the spectra are the relative values of the differential scattering cross-sections between different transitions.

In order to overcome this difficulty we compared the scattering from crystal of $LuPO_4$ (specifically the $\hat{\mathbf{X}}\hat{\mathbf{Z}}$ 1034 cm^{-1} vibrational transition) to the scattering from a sample with a known scattering cross-section, the 992 cm^{-1} vibrational Raman transition in benzene. The 992 cm^{-1} transition in benzene has a differential scattering cross-section of 2.57×10^{-29} cm^2 per steradian of solid angle [100]. The benzene was contained in a quartz cuvette with the side facing the collection lens masked such as to approximate the shape and size of the $LuPO_4$ crystals. If S_c and S_b are the scattering signals measured from the spectra of $LuPO_4$ and benzene, respectively, then the differential scattering cross-section for the $\hat{\mathbf{X}}\hat{\mathbf{Z}}$ 1034 cm^{-1} transition in $LuPO_4$ is given by

$$\left(\frac{d\sigma}{d\Omega}\right)_c = \left(\frac{S_c n_{ob} l_b}{S_b n_{oc} l_c}\right)\left(\frac{\epsilon_b}{\epsilon_c}\right)\left(\frac{d\sigma}{d\Omega}\right)_b \tag{3.45}$$

where all quantities are defined as in Equation 3.44. The term $\frac{\epsilon_b}{\epsilon_c}$ is a correction to account for the fact that the indices of refraction are different for $LuPO_4$ and benzene. Benzene has an index of refraction of approximately 1.5 [87] (and is contained in a quartz cuvette with an index of refraction of approximately 1.55 [87] while $LuPO_4$ has a refractive index of approximately 1.75. Thus reflection losses are larger and the solid angle

Transition Δcm^{-1}	$\frac{d\sigma}{d\Omega}(\theta = \frac{\pi}{2})$ /10^{-30}, cm^2				
	$\hat{X}\hat{Y}$	$\hat{Z}\hat{Z}$	$\hat{X}\hat{Z}$	$\hat{Z}\hat{Y}$	all pol.
240	.587	0	0	0	.294
429	1.62	1.20	9.51	2.46	7.40
2,179	.545	1.76	1.05	3.08	3.22
2,221	1.68	0	1.86	.171	1.86
2,620	.685	0	1.80	.190	1.34
2,676	.643	0	.467	0	.555

Table 3.19: Measured differential scattering cross-sections for electronic Raman scattering in Ce^{3+}:$LuPO_4$. Differential cross-sections are given in units of 10^{-30} cm^2.

of collection is smaller for $LuPO_4$ relative to the benzene sample. With a collection lens with an f-number of 1.2 the correction factor is calculated to be approximately 1.4. Given this factor and the measurements from the two scattering spectra the differential scattering cross-section for the $\hat{X}\hat{Z}$ 1034 cm^{-1} transition of $LuPO_4$ is found to be 1.28×10^{-30} cm^2 $ster^{-1}$.

In our earlier work on electronic Raman scattering in Ce^{3+}:$LuPO_4$ all the scattering intensities were scaled relative to the $\hat{X}\hat{Z}$ 1034 cm^{-1} Raman transition. Thus, the absolute electronic Raman differential scattering cross-sections are easily computed by using these earlier results and the value for absolute differential scattering cross-section for the $\hat{X}\hat{Z}$ 1034 cm^{-1} Raman transition (and also taking into account that the Ce^{3+}:$LuPO_4$ crystal contain 0.638 mol% Ce^{3+}). The resulting differential scattering cross-sections are listed in Table 3.19. We estimate that these values are accurate to within a factor of 2.

Comparison Between Calculated and Observed Cross-Sections

The differential scattering cross-section for a Raman transition from an initial state $|i\rangle$ to a final state $|f\rangle$ is given by,

$$\frac{d\sigma}{d\Omega} = (2\pi\alpha_{fs})^2 \Lambda k k_s^3 \times \left| \sum_r \frac{\langle f|\hat{e_s}\cdot\vec{D}|r\rangle\langle r|\hat{e}\cdot\vec{D}|i\rangle}{k_{ri}-k} + \frac{[\hat{e_s}\leftrightarrow\hat{e}]}{k_{rf}+k_s} \right|^2 \tag{3.46}$$

where $\hat{\mathbf{e}}$ and $\hat{\mathbf{e}}_s$ describe the polarizations of the incident and scattered light, respectively, hck and hck_s are the energies of the incident and scattered photons, respectively, and hck_{ri} is the energy difference between the states $|r\rangle$ and $|i\rangle$. The term Λ accounts for the refractive index of the host crystal. Following Dexter [85] an expression for Λ may be derived as is given by

$$\Lambda = \frac{n_{\hat{e}_s}}{n_{\hat{e}}} L_{\hat{e}}^2 L_{\hat{e}_s}^2. \tag{3.47}$$

where n is the index of refraction, L is the field correction factor given in Equation 3.37, and the subscripts $\hat{e}$ and $\hat{e}_s$ refer to the polarizations of the incident and scattered light.

The states $|r\rangle$ are the virtual intermediate states of the Raman process. In order for the electric dipole matrix elements to be nonzero the states $|r\rangle$ must have parity opposite that of the states $|i\rangle$ and $|f\rangle$. For electronic Raman scattering from rare earth crystals, the initial and final states are both associated with the rare earth ion $4f^N$ electronic configuration so that the opposite parity states closest in energy are from the $4f^{N-1}5d$ configuration. As a first approximation one assumes these states to be the dominant virtual intermediate states in the electronic Raman process. This assumption directly connects the electronic Raman scattering differential cross-sections and the 4f$\longrightarrow$5d oscillator strengths.

In our earlier work on electronic Raman scattering in Ce^{3+}:$LuPO_4$ the relative electronic Raman scattering intensities between different transitions were computed in two ways. The first method followed Axe's standard calculation for two-photon processes in rare earth ions [14]. Following the Judd-Ofelt one photon calculation [15,16], this calculation assumes average values may be given to the denominators in Equation 3.48 for all the states in a given configuration. Closure is then performed over the states of each configuration separately. The result is an expression containing matrix elements of the spherical unit tensors $\mathbf{U}^1$ and $\mathbf{U}^2$, between the angular parts of the initial and final state wavefunctions and two associated parameters labelled F_1 and F_2. These parameters are dependent on the radial parts of the initial, final, and intermediate state wavefunctions and the average energies of the excited configurations. Explicitly

$$F_t(k) = (-1)^t \sum_{4f^{N-1}n'l'} \left[\frac{1}{\bar{k}_{n'l'} - k} + \frac{(-1)^t}{\bar{k}_{n'l'} + k} \right]$$

Transition	$\frac{d\sigma}{d\Omega}/10^{-30}$,cm^2		
	Observed	Calculated Judd-Ofelt,5d	Calculated 5d Wavefunctions
$^2F_{5/2} \longrightarrow {}^2F_{5/2}$	7.69	76.8	104.3
$^2F_{5/2} \longrightarrow {}^2F_{7/2}$	6.98	9.04	35.5

Table 3.20: Multiplet averaged electronic Raman differential scattering cross-sections.

$$\times \langle 4f||C^{(1)}||l'\rangle^2 \langle 4f|r|n'l'\rangle^2 (2t+1)^{\frac{1}{2}} \left\{ \begin{array}{ccc} 1 & 3 & l' \\ 3 & 1 & t \end{array} \right\} \qquad (3.48)$$

where the sum over $4f^{N-1}n'l'$ is a sum over excited configurations with parity opposite that of the ground configuration. The relative electronic Raman scattering intensities can be written in terms of $\frac{F_1}{F_2}$ which may then be treated as a parameter. Here Hartree-Fock radial wavefunctions are used to explicitly evaluate F_1 and F_2 so that absolute differential scattering cross-sections can be obtained. Assuming only a contribution from the $5d^1$ configuration and using a value of $\overline{k}_{5d} = 40{,}000$ cm^{-1} along with the angular terms evaluated previously yields the differential scattering cross-sections.

The second calculation employed in the earlier work was an explicit evaluation of the sum over intermediate states using the angular parts of the $4f^1$ and $5d^1$ wavefunctions obtained from crystal field fits. The absolute differential scattering cross-sections are obtained simply by scaling these results by $|\langle 4f|r|5d\rangle|^4 |\langle 2||C^{(1)}||3\rangle|^4$.

A comparison between the observed and calculated differential scattering cross-section is given in Table 3.20. In this table the cross-sections have been averaged over polarizations and summed over the crystal field levels of each Russell-Saunders multiplet. The comparison shows that the observed differential cross-sections are smaller than both sets of calculated values. However, the calculation using the closure approximation is closer to the observed values then the calculation in which the $5d^1$ wavefunctions and energies are explicitly used. This is surprising in that it has been shown that the explicit calculation predicts the relative electronic Raman differential scattering cross-sections much more accurately.

To understand these results, one has to look at the previous discussion of 4f⟶5d oscillator strengths. The 4f⟶5d oscillator strengths for Ce^{3+} in $LuPO_4$ are, on the average 5.3 times smaller than calculated. For the lowest energy 5d level, the observed oscillator strength is 2.5 times smaller than the calculated value. We have suggested that this reduction results from a decrease in the value of the radial integral $\langle 4f|r|5d\rangle$ in the solid state relative to the free or gaseous state. It follows that the electronic Raman differential scattering cross-sections should be reduced by factors on the order of $(2.5)^2 \approx 6.3$ to $(5.3)^2 \approx 28$. From Table 3.20 it can be seen that the results of the explicit calculation fall into this range.

A more detailed calculation may be performed if an assumption is made regarding the nature of the supposed reduction in the radial integral $\langle 4f|r|5d\rangle$. The measured oscillator strengths are smaller than their respective calculated values by factors ranging from 2.5 to 19. In the above estimation we used the reduction factor for the lowest $5d^1$ level and the average reduction factor for the entire $5d^1$ configuration to calculate the expected reduction of the electronic Raman scattering cross-sections. A potentially more accurate description would include all the reduction factors. Accordingly a calculation is proposed in which each amplitude in the summation over the $5d^1$ states in Equation 3.46 is weighted by a factor given by the square root of the ratio of the measured oscillator strength to the calculated oscillator strength for that particular $5d^1$ state. The differential scattering cross-sections are then given by

$$\frac{d\sigma}{d\Omega} = (2\pi\alpha_{fs})^2 \Lambda k k_s^3 \left| \sum_r \zeta_r A_{ifr} \right|^2 , \tag{3.49}$$

where,

$$A_{ifr} = \frac{\langle f|\hat{e_s}\cdot\vec{D}|r\rangle\langle r|\hat{e}\cdot\vec{D}|i\rangle}{k_{ri}-k} + \frac{[\hat{e_s}\leftrightarrow\hat{e}]}{k_{rf}+k_s} , \tag{3.50}$$

and

$$\zeta_r = \sqrt{\frac{\text{meas. osc. strength}_r}{\text{calc. osc. strength}_r}}. \tag{3.51}$$

Such a calculation is justified as long as the reduction factor associated with a given 4f→5d transition ζ_r is independent of which particular 4f state is under consideration. This statement is correct under the plausible assumption that the reductions in the

Transition	$\frac{d\sigma}{d\Omega}/10^{-30}$,cm^2		
	Observed	Calculated 5d Wavefunctions	Calculated Weighted 5d Wavefunctions
$^2F_{5/2} \longrightarrow {}^2F_{5/2}$	7.69	104.3	10.6
$^2F_{5/2} \longrightarrow {}^2F_{7/2}$	6.98	35.5	7.2

Table 3.21: Multiplet averaged electronic Raman differential scattering cross-sections.

radial overlap integral result solely from the expansion of the 5d orbitals and that the 4f orbitals retain their free ion radial distributions.

In Tables 3.21 and 3.22, the results of the weigthed calculation are compared to the measured cross-sections and the earlier results of the explicit calculation without weighting. The comparison is somewhat startling in the degree to which the weighted calculation agrees with the measured values of the differential scattering cross-sections. The agreement may be somewhat fortuitous given the large uncertainty in the measurement of the cross-sections (we estimated earlier that the measured cross-sections might be off by as much as a factor of 2). Even given this, the results of the calculation with weighting are impressive. In addition, examination of Tables 3.21 and 3.22 shows that the the calculation with weighting offers a slight improvement over the calculation without weighting in describing the relative values of the cross-sections for the different transitions.

Transition	$\frac{d\sigma}{d\Omega}/10^{-30}$,cm^2		
	Observed	Calculated 5d Wavefunctions	Calculated Weighted 5d Wavefunctions
240	0.3	31	2.8
429	7.4	74	7.8
2,179	3.2	20	2.9
2,221	1.9	5.3	1.9
2,620	1.3	6.7	1.9
2,676	0.6	3.5	0.5

Table 3.22: Observed and calculated electronic Raman differential scattering cross-sections for Ce^{3+} in $LuPO_4$.

The above discussion is based on the assumption that states of the $5d^1$ configuration serve as the dominant intermediate channel in the electronic Raman scattering process. For Ce^{3+} in $LuPO_4$ the results of an experiment in which the electronic Raman scattering was enhanced by tuning the incident light near the onset of the $5d^1$ configuration indicated that the states of that configuration are indeed the dominant intermediate states. However, this may not be the case in general. The results of several one and two photon intensity experiments in rare earth solids are most readily explained by the inclusion of g-orbital effects. If all g-orbitals are considered to be degenerate in energy, it can be shown [15] by closure that their contribution to the electronic Raman scattering process is proportional to $|\langle 4f|r^2|4f\rangle|^2$. As pointed out most recently by Chase and Payne [66] and earlier by Krupke, [98] this radial integral does not vary significantly with the radial expansion of the rare earth ion orbitals. In addition, in the solid-state the energy of the g type orbitals may be substantially reduced from the free ion values. Thus, one can imagine situations in which these orbitals contribute significantly to the electronic Raman scattering process. In such cases, the 4f$\longrightarrow$ 5d oscillator strengths could be much smaller than expected with electronic Raman cross-sections not being proportionally reduced. It is interesting to note that Ce^{3+} in both YAG and YLF shows substantially reduced 4f$\longrightarrow$5d oscillator strengths. However, Chase and Payne [66] found that while Nd^{3+} in YLF showed smaller than expected two-photon absorption cross-sections, Nd^{3+} in YAG had cross-sections that were very near the calculated values. One explanation

offered for this was an increased g orbital contribution for the YAG crystal.[66]

Conclusions

For Ce^{3+} in $LuPO_4$ the intensities of the two parity allowed optical processes, 4f$\longrightarrow$5d absorption and 4f$\longrightarrow$4f electronic Raman scattering, are both smaller than expected from calculations based on free ion estimates of the radial wavefunctions. These results can be explained in terms of a reduction of the radial integral, $\langle 4f|r|5d\rangle$, in the solid state. Furthermore, a compilation of data on 4f$\longrightarrow$5d oscillator strengths for Ce^{3+} in other crystal hosts shows that the reduction in the value of the radial integral is correlated with the Ce^{3+}-ligand distance. The nearer the ligands are to the cerium ion, the greater the reduction. However, it is suggested that a reduction in the value of $\langle 4f|r|5d\rangle$ does not always result in a corresponding reduction in the electronic Raman cross-sections. This suggestion is based on the possibility of contributions from intermediate states other than those associated with $5d^1$ configuration.

Chapter 4

Resonant Electronic Raman Scattering from $ErPO_4$ Crystals: A Formally Parity Forbidden Resonance

4.1 Introduction

In the previous chapter, it was demonstrated that significant enhancement of electronic Raman scattering intensities occurs for excitation frequencies in near resonance with transitions between the ground and first excited configurations of the rare earth ion. However, possibilities for such resonances are limited to systems containing Ce^{3+} and, to lesser extent, Tb^{3+} and Pr^{3+}, as a result of the high energies of the first excited configurations for the other trivalent rare earth ions.

By far the greatest number of opportunities for resonance are of the type in which both states belong to the ground configuration ($4f^N \rightarrow 4f^N$). However, the strength of such intra-configurational resonances are expected to be small because they depend on $4f^N \rightarrow 4f^N$ electric dipole matrix elements which are formally parity forbidden. This is why such states are not included in the sum over virtual intermediate states in the expression describing non-resonant electronic Raman scattering intensities.

It is a simple matter to estimate the magnitudes of such intra-configurational resonances. The ratio of the resonant scattering intensity, I_R, to the non-resonant intensity,

I_{NR}, is approximated by

$$\frac{I_R}{I_{NR}} \approx \frac{\left|\frac{\langle 4f|D|4f\rangle\langle 4f|D|4f\rangle}{\omega_{4f}-\omega}\right|^2}{\left|\frac{\langle 4f|D|5d\rangle\langle 4f|D|5d\rangle}{\omega_{5d}-\omega}\right|^2} \tag{4.1}$$

where the terms such as $\langle 4f|D|4f\rangle$ are electric dipole matrix elements, $\hbar\omega_{5d}$ represents the average energy for the states of the first excited configuration, $\hbar\omega_{4f}$ is the energy of the resonant state, and $\hbar\omega$ is the energy of the incident laser photons. The size of the formally parity forbidden electric dipole matrix elements is dependent on the degree of the admixing of the opposite parity configurations into the $4f^N$ configuration by the crystal-field, H_{cf},

$$\frac{\langle 4f|D|4f\rangle}{\langle 4f|D|5d\rangle} \approx \frac{H_{cf}}{\hbar\omega_{5d}} \tag{4.2}$$

Substituting this result into Equation 4.1, we have

$$\frac{I_R}{I_{NR}} \approx \frac{\frac{H_{cf}^4}{\hbar^2\omega_{5d}^2}}{\hbar^2(\omega_{4f}-\omega)^2} \tag{4.3}$$

Values for H_{cf} range between 100 and 1,000 cm^{-1} while $\hbar\omega_{5d}$ may be anywhere on the order of 50,000 to 150,000 cm^{-1}. These values result in a large range of possible enhancements;

$$\frac{I_R}{I_{NR}} \approx \frac{0.005 \text{ to } 500}{\hbar^2(\omega_{4f}-\omega)^2}\ , \left(\hbar(\omega_{4f}-\omega) \text{ in } cm^{-1}\right) \tag{4.4}$$

For the high end of this range, enhancement will be observable for detunings from resonance, $\hbar(\omega_{4f}-\omega)$, no greater than approximately 20 cm^{-1}. For a more typical case the detuning would have to be quite small (< 1 cm^{-1}, in the range where the pump laser beam is absorbed by the resonant state. Thus, resonances of this type are not expected to be dramatic, if observable at all.

The few earlier studies on resonant electronic Raman scattering in rare earth systems [67,68,69,70,71] seem to bear this out. Grunberg and Koningstein [67] found a factor of 5 increase in the intensity of electronic Raman scattering from Nd^{3+} in $NdAlO_3$ when the excitation wavelength was changed from 488 nm to 476.5 nm. Wadsack and Chang [69] used the assortment of wavelengths available from argon and krypton ion lasers to excite Raman scattering between crystal field states of the ground $^6H_{15/2}$ multiplet of Dy^{3+} in DyAlG. They observed enhancements on the order of only 2 for excitation

energies in near coincidence with transitions between the $^6H_{15/2}$ and $^4F_{9/2}$ multiplets. Nicollin and Koningstein [68] used a tunable dye laser to examine the excitation profile of electronic Raman scattering between levels of the $^7F_6$ multiplet of Tb^{3+} in TbAlG. For resonance with the $^5D_4$ multiplet at approximately 20,500 cm^{-1} enhancements on the order of 5 were observed. In the same crystal Myslinski and Koningstein [70] have studied the excitation profile of Raman scattering between the $^7F_6$ and $^7F_5$ multiplets. For resonance with the $^5D_4$ multiplet no enhancement of the scattering was observed.

Recently, however, a large intra-configurational resonance has been observed for electronic Raman scattering in crystals of $ErPO_4$. While studying the intensities of Raman scattering between states of the $^4I_{15/2}$ multiplet of Er^{3+} in $ErPO_4$ Becker *et al.* [11,72] noticed that the scattering intensities increased by factors up to 100 when the excitation wavelength was changed from 514.5 nm to 488 nm. The 488 nm (20,486.7 cm^{-1} *vacuum*) line is in coincidence with the transitions between the ground multiplet, $^4I_{15/2}$ and the $^4F_{7/2}$ multiplet. This is an interesting result in that the observed enhancements are much greater than anything reported previously and at the upper limit of what was estimated (Equation 4.4).

In this chapter we will describe additional experiments studying this resonance using a tunable dye laser as the excitation source. The results of these experiments confirm that the observed light signals are indeed associated with Raman processes and are not just the result of fluorescence from the $^4F_{7/2}$ states to the $^4I_{15/2}$ states. In addition, we present excitation profiles for the scattering intensities. The shapes and magnitudes of these profiles are accurately modelled. The modelling allows us to draw conclusions on under what conditions large intra-configurational resonances of multi-photon processes in rare earth crystals might be expected.

An interesting feature of the excitation profiles is their asymmetric shape. While the absorption profiles for the resonant state are symmetric about the center frequency the Raman excitation profiles are markedly asymmetric. This is explained in terms of an interference between the resonant and non-resonant intermediate state amplitudes for the Raman scattering. Such interference effects have helped to make resonance Raman scattering a popular complementary tool to absorption measurements in the study of the

vibrational states of excited electronic states of molecular systems. Here we are presented with a much simpler situation in which to study these effects. In addition, details of the interference are of particular importance for the case of intra-configurational resonances in rare earth crystals because, as it will be shown, the interference term determines the *range* of the resonant effect.

4.2 $ErPO_4$: Background

In this section background information regarding the electronic structure and properties of Er^{3+} in $ErPO_4$ will be presented. This information is important in explaining the results of the resonance Raman experiments.

4.2.1 Electronic Structure

Er^{3+} has eleven 4f electrons, three short of a full shell. Free ion levels are determined by the coulombic repulsion between electrons and the spin-orbit coupling. Figure 4.1 shows the free ion energy levels to approximately 21,000 cm^{-1}. The free ion wavefunctions may be written as sums of Russell-Saunders terms, $^{2S+1}L_J$. The leading term(s) in the expansion for each level are shown in Figure 4.1. Most of the states are fairly accurately represented by one Russell-Saunders term. Also marked in Figure 4.1 are the energies of the 514.5 nm and 488 nm lines of the argon ion laser. The resonance of the 488 nm line with the $^4I_{15/2} \rightarrow ^4F_{7/2}$ transition may be clearly seen.

For more detail on this resonance it is necessary to look at the effects of the crystal field. As was discussed in the previous chapter introduction of the ion into a crystal breaks the spherical symmetry and splits the free ion levels into the crystal field levels. The symmetry of the Er^{3+} site in $ErPO_4$ is represented by the operations of the group D_{2d} so that the eigenstates of the system are properly labelled by the irreducible representations of this group. Since Er^{3+} is an odd-electron system the double group representations of D_{2d} are used, Γ_6 and Γ_7. The crystal field splitting for the $^4I_{15/2}$ and $^4F_{7/2}$ multiplets are shown in Figure 4.2. In addition, the energy of the 488 nm argon laser line is shown. Note that the laser line is not in direct resonance but very close to two of the crystal field levels.

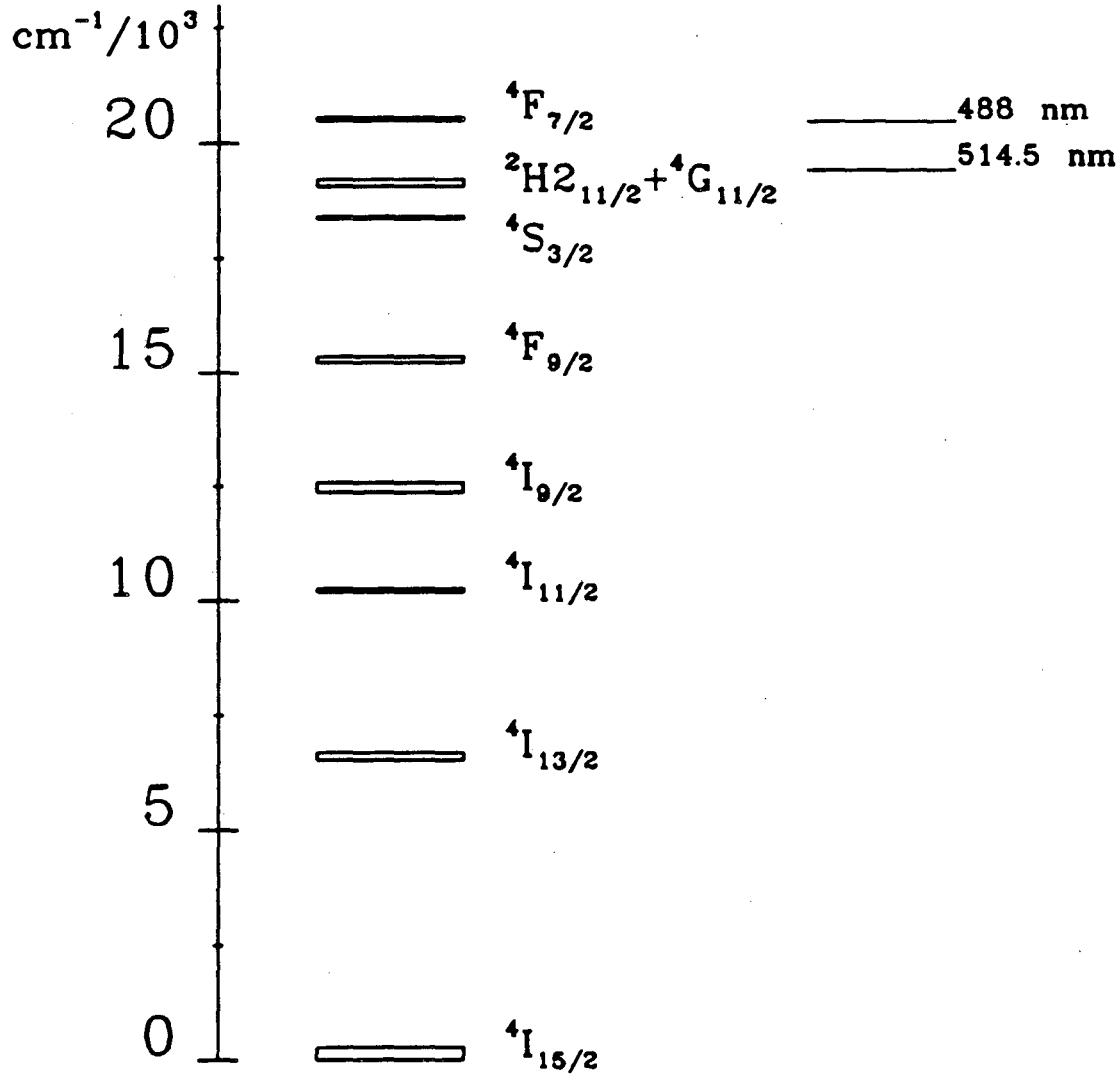

Figure 4.1: Free ion energy levels for Er^{3+}, $4f^{11}$

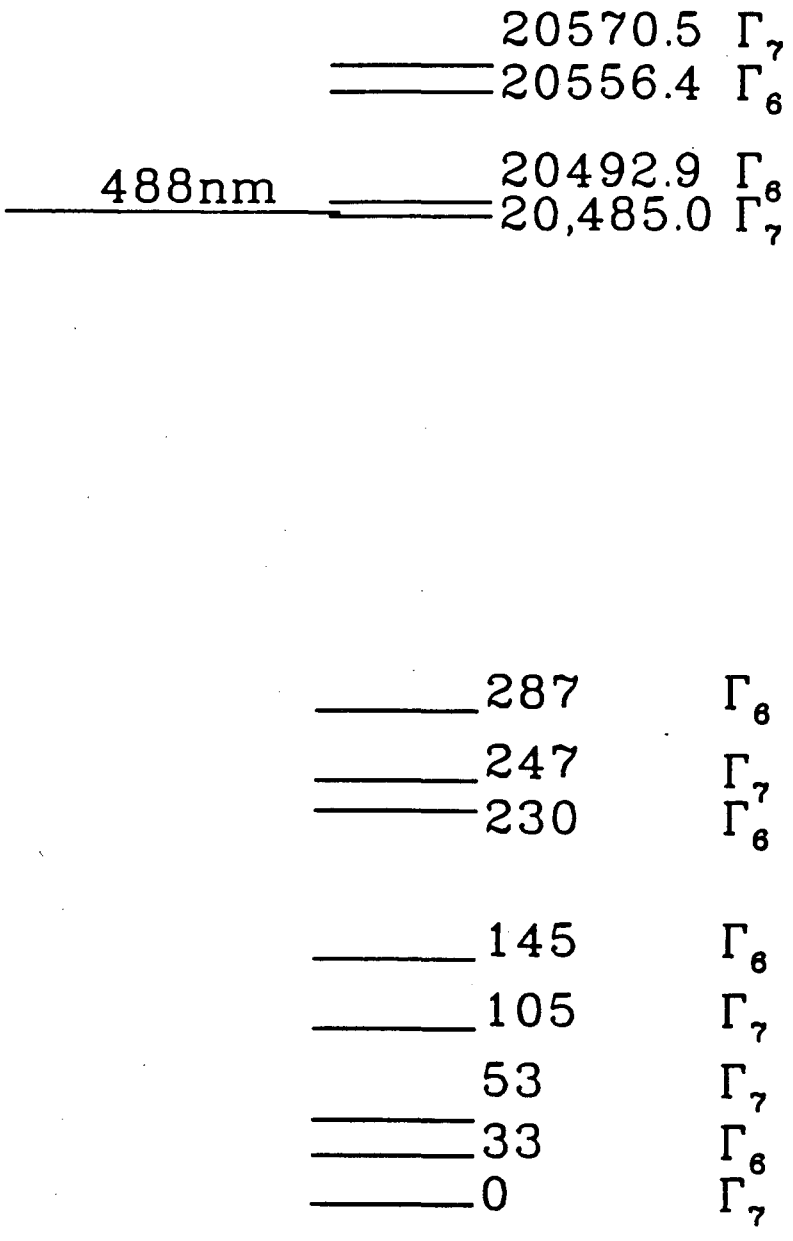

Figure 4.2: Crystal field levels for the multiplets $^4I_{15/2}$ and $^4F_{7/2}$ for Er^{3+} in crystals of $ErPO_4$. The level at 287 cm^{-1} has not been observed but is predicted by calculation.

The crystal field levels were located using absorption and non-resonant (514.5 nm) electronic Raman spectroscopy [11,64]. Group labels for the levels were determined using the polarization selection rules for these two spectroscopies. The selection rules are the same as those listed in sections 3.2.2 and 3.2.3 for Ce^{3+} in $LuPO_4$. Hayhurst *et al.* [25] have fit a parameterized Hamiltonian to the observed spectrum of Er^{3+} in $LuPO_4$ (a system nearly identical to Er^{3+} in $ErPO_4$) obtaining expressions for the angular parts of the wavefunctions for each level.

The levels of the first excited electronic configuration of Er^{3+} ($4f^{10}5d^1$) are also of interest because they are the states that are expected to contribute as virtual intermediate states in the non-resonant amplitude for electronic Raman scattering. Unfortunately, data are not available on these states for either the system Er^{3+} in $ErPO_4$ or for the similar systems Er^{3+}:$LuPO_4$ and Er^{3+}:YPO_4. However, spectra taken for Er^{3+} in crystals of CaF_2 indicate that the $4f^{10}5d^1$ band starts at approximately 62,000 cm^{-1} [101]. The overall width of the $4f^{10}5d^1$ band may be estimated to be approximately 100,000 cm^{-1} from the width of the $4f^{10}$ ground configuration of Tm^{3+} ($\approx$80,000 cm^{-1}) and the crystal field splitting of the $5d^1$ configuration of Ce^{3+} in $LuPO_4$ ($\approx$30,000 cm^{-1}). This width places most of the states of the $4f^{10}5d^1$ configuration above the band gap of $LuPO_4$ which hase been measured to be approximately 70,000 cm^{-1} [20].

4.2.2 Fluorescence Dynamics

For electronic Raman scattering experiments in rare earth crystals, fluorescence from transitions between $4f^N$ levels can be a troublesome source of background signal. Fluorescence can be on the order of 10^6 times more intense than the weak electronic Raman scattering signals. In general, for scattering experiments the excitation source is carefully chosen so as not to populate excited states. However, for a resonant scattering experiment, by definition, excitation is in an energy region in which population is likely. Fortunately, as we shall see population does not always lead to strong fluorescence.

Because the electric dipole transition moments between states associated with the $4f^N$ configuration are small, one would expect the fluorescence lifetimes of such transitions to be quite long (on the order of 10μs to 1 ms). In practice, however, much shorter lifetimes

for many transitions are observed. The reason for this is that the excited electronic states of rare earth ions may decay through non-radiative mechanisms (giving up energy to the crystal host in the form of phonons). Thus, the rate of decay of an excited state is the sum of two decay rates a radiative one and a non-radiative one

$$A = A_R + A_{NR} \tag{4.5}$$

Even though the coupling between the shielded 4f electrons and the phonons of the crystal is known to be small, the non-radiative decay rates, A_{NR}, can be very large compared to A_R. Values of A_{NR} on the order of 0.1 $(\text{ns})^{-1}$ or larger are not uncommon. The relative strength of non-radiative processes over radiative processes can be understood in general terms as a result of the much higher density of states of phonons relative to photons.

The fraction of excited state population that de-excites through fluorescence is given by

$$\frac{A_R}{A_R + A_{NR}} \tag{4.6}$$

Thus, we see that very little fluorescence will be emitted from states with large non-radiative decay rates.

In determining which excited states will have large non-radiative decay rates, an important consideration is the size of the energy gap between the state under consideration and the levels below it compared to the energies of the phonons of the host crystal. Two energy regimes may be discussed.

The crystal field splitting of the free ion multiplets results in energy gaps between states on the order of 10-100 cm^{-1}. In this energy regime there are usually ample acoustic phonon modes of the crystal which may interact with the 4f electrons in a variety of ways [102]. Whether these interactions on balance lead to excitation or de-excitation is a function of the population of the phonon modes which is directly related to the temperature. Qualitatively, one can say at temperatures T such that k_BT is less than the crystal field splitting most of the fluorescence from a multiplet will originate from its lowest crystal field level. At higher temperatures fluorescence will originate from higher crystal field levels with the relative intensities being distributed in a Boltzmann

type fashion.

The second energy regime of interest is on the order of the gaps between free ion multiplets. These gaps are typically in the range of 500-10,000 cm^{-1}. For such large energy gaps the non-radiative decay occurs through emission of one or more optical phonons of the crystal. Optical phonons in crystals typically have energies in the range 100-1,000 cm^{-1}. Thus, for gaps on the order of 1,000 cm^{-1} or less only one phonon need be emitted, while for a gap of say 3,000 cm^{-1} three phonons would have to be emitted. The probability of such a multi-phonon emission is proportional to the electron-phonon coupling constant (a small number) raised to the power of the number of phonons emitted. Generally, multiplets with large gaps will have smaller non-radiative decay rates resulting in greater fluorescence with a longer lifetime while the converse will be true for smaller gaps.

For Er^{3+} in $ErPO_4$ excitation at 476.5 nm (20,981 cm^{-1}) results in visibly strong fluorescence from the transitions $^4S_{3/2} \rightarrow ^4 I_{15/2}$ (yellow) and $^4F_{9/2} \rightarrow ^4 I_{15/2}$ (red). Only very weak fluorescence is observed from the transitions $^4F_{7/2} \rightarrow ^4 I_{15/2}$ and $^2H2_{11/2} \rightarrow ^4 I_{15/2}$. The same holds true for excitation directly into the upper crystal field levels of the $^4F_{7/2}$ multiplet. The gaps associated with the multiplets $^4F_{7/2}$, $^2H2_{11/2}$, $^4S_{3/2}$, and $^4F_{9/2}$ are approximately 1250, 675, 3000, and 2650 cm^{-1}, respectively. Examination of the phonon energies for $ErPO_4$ listed in Table 2.2 shows that non-radiative decay from $^4F_{7/2}$ and $^2H2_{11/2}$ involves emission of one or possibly two phonons while at least three phonons are necessary for the decay of $^4S_{3/2}$ and $^4F_{9/2}$. Figure 4.3 from Reference [11] shows proposed decay routes for excited state population in $^4F_{7/2}$.

The fact that there is almost no fluorescence from the $^4F_{7/2}$ multiplet is crucial in allowing the observation of the resonance with this multiplet for electronic Raman scattering.

4.2.3 Oscillator Strengths and Line Widths of One-Photon Transitions

The strength of the 4f→4f resonance enhancement of the electronic Raman scattering intensities depends directly upon the of size of the electric dipole matrix elements between

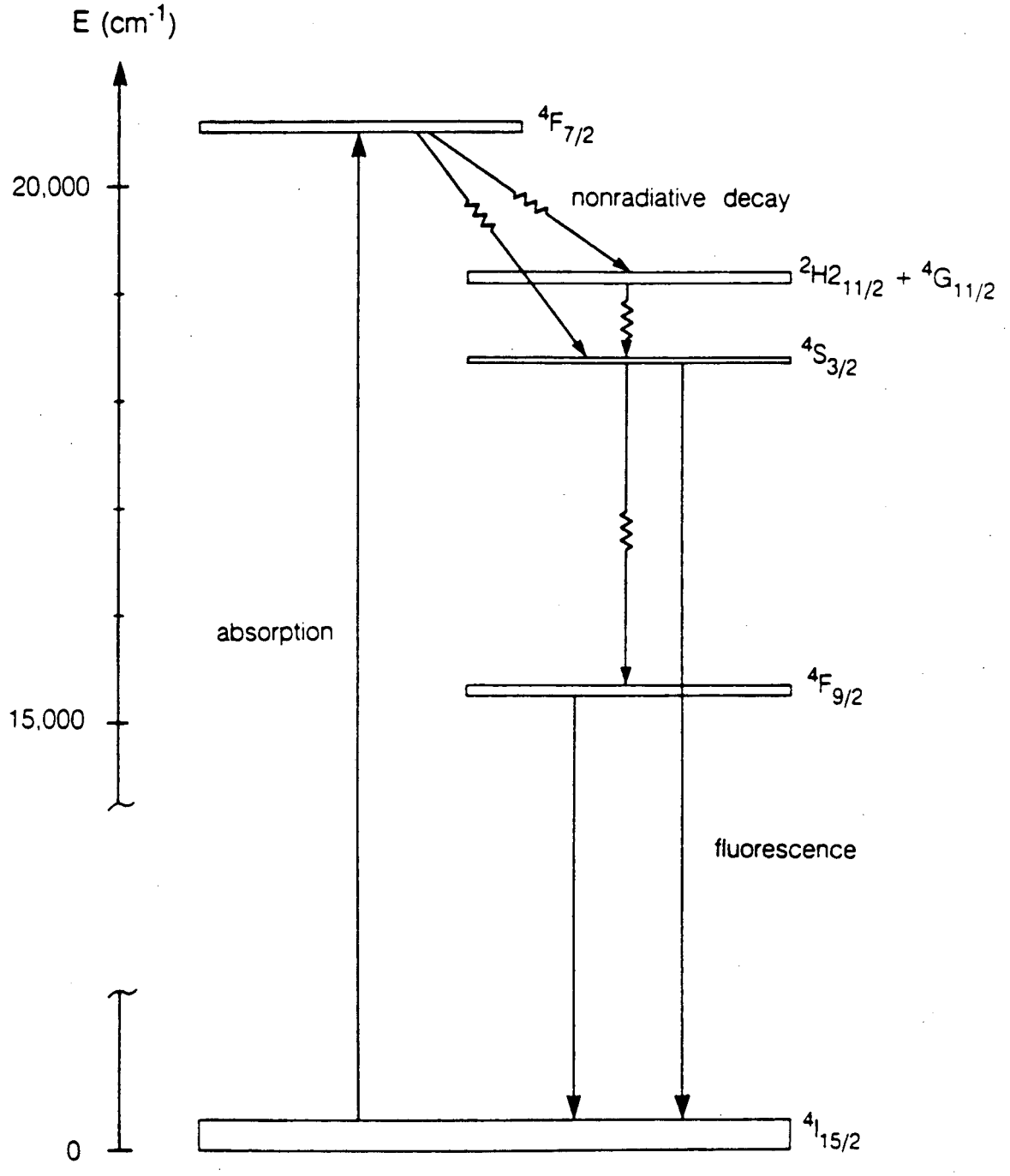

Figure 4.3: Decay routes for excited state population in $^4F_{7/2}$ of Er^{3+} in $ErPO_4$. Drawing is from Reference [11].

the intial state and the resonant state and between the final state and the resonant state . The values of the squared magnitudes of these electric dipole matrix elements may be attained directly from one photon absorption measurements.

In this section we present the results of one photon absorption measurements on crystals of $ErPO_4$. The strengths of the observed absorptions are given in terms of oscillator strengths. The oscillator strength (P) of a transition is proportional to squared magnitude of the electric dipole matrix element for that transition. Values for P are obtained from the absorption spectrum by use of the relation

$$P = \left(\frac{1}{\pi r_o}\right) \frac{1}{n_o l} \int \alpha(k) dk \tag{4.7}$$

where $r_o = (e^2/m_e c^2) \approx 2.813 \times 10^{-13}$cm is the classical radius of the electron, n_o is the number density of absorbers, l is the thickness of the sample, and the integral is over the absorption coefficient α as as function of wavenumber $k = 1/\lambda$. The absorption coefficient is given in the usual way by $\ln(I_o/I)$.

In addition to the information regarding the size of the dipole matrix elements, the absorption spectrum yields information on the spectral widths of the resonant transitions and the physical mechanisms which lead to these widths. As will be shown, the spectral widths and their form are important considerations in determining the properties of the Raman resonance.

Figure 4.4 shows the room temperature absorption spectrum of an $ErPO_4$ crystal over the range 5,000-50,000 cm^{-1}. Each absorption feature (up to 31,000 cm^{-1}) is labelled by the leading Russell-Saunders terms in the expansion of the wavefunction associated with it. Listed in Table 4.2.3 are the oscillator strengths of each feature. It is interesting to note that the oscillator strength for the transition $^4I_{15/2} \rightarrow ^4F_{7/2}$ is only moderate in size while the enhancements in electronic Raman scattering intensities, as a result of resonance with this transition, are quite large. However, it must be remembered that the multiplet to multiplet oscillator strengths include contributions from many different crystal field transitions. To understand fully the observed enhancements in $ErPO_4$ it will be necessary to look at oscillator strengths associated with transitions between individual crystal field levels of the multiplets.

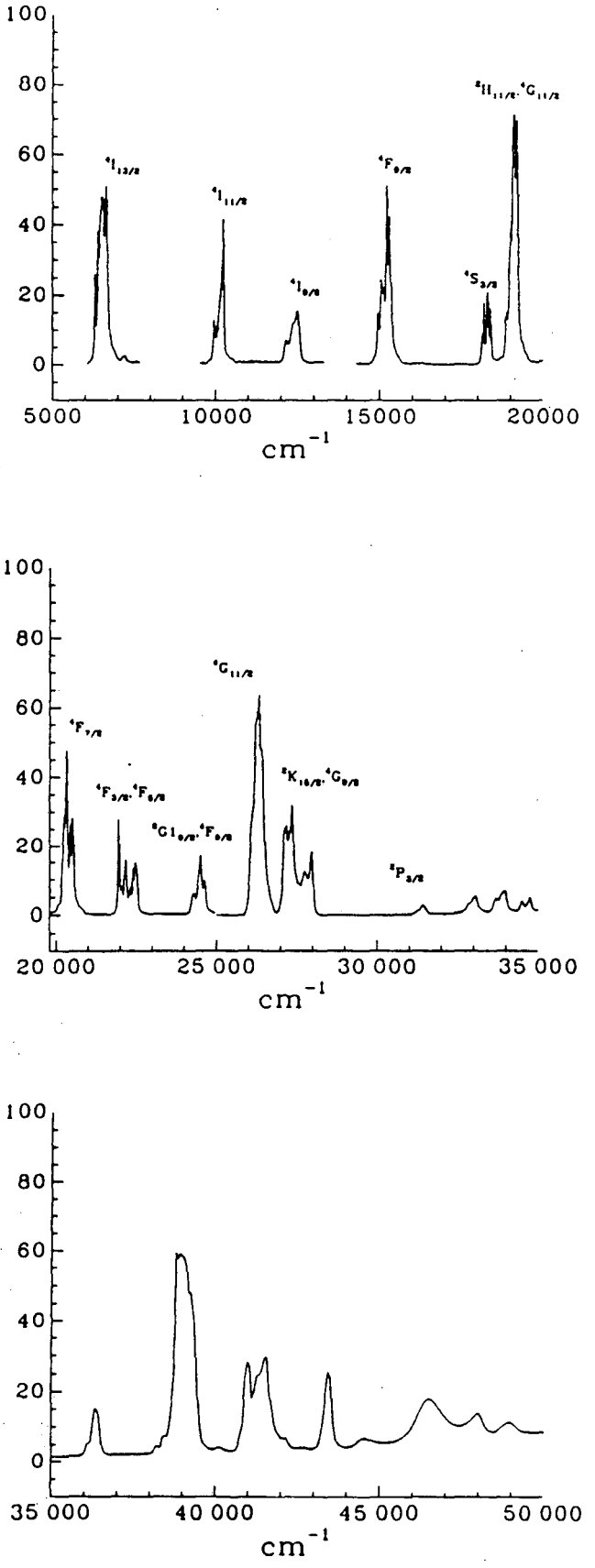

Figure 4.4: Room temperature absorption spectrum of $ErPO_4$.

Multiplet $^4I_{15/2} \rightarrow$	Energy (cm^{-1})	Oscillator Strgth. $\times 10^6$
$^4I_{13/2}$	6,550	1.31
$^4I_{11/2}$	10,150	0.53
$^4I_{9/2}$	12,400	0.37
$^4F_{9/2}$	15,200	1.20
$^4S_{3/2}$	18,250	0.37
$^2H_{11/2}, ^4G_{11/2}$	19,050	1.82
$^4F_{7/2}$	20,400	1.06
$^4F_{3/2}, ^4F_{5/2}$	22,250	0.68
$^2G1_{9/2}, ^2H2_{9/2}, ^4F_{9/2}$	24,500	0.41
$^4G_{11/2}$	26550	2.12
$^2K_{15/2}, ^4G_{7/2}, ^4G_{9/2}$	28,000	1.52
$^2P_{3/2}$	31,400	0.06
$^2K_{3/2}, ^4P_{1/2}$	33,000	0.14
$^4G_{7/2}$	33,900	0.19
$^2D1_{5/2}$	34,650	0.09
$^2G1_{9/2}, ^2H2_{9/2}$	36,350	0.39
$^2D1_{5/2}, ^2I_{11/2}, ^4D_{5/2}, ^4D_{7/2}$	39,050	3.67
$^2D1_{3/2}, ^2L_{17/2}, ^4D_{3/2}$	41,350	2.00
$^2D2_{3/2}, ^2I_{3/2}, ^4D_{3/2}$	43,450	0.60

Table 4.1: Oscillator Strengths for transitions from the ground $^4I_{15/2}$ multiplet of $ErPO_4$ to excited multiplets.

In Becker's work [11,72] much of the focus was on the scattering transitions between the ground state and the crystal field levels at 33 cm^{-1} and 53 cm^{-1}, all associated with the multiplet $^4I_{15/2}$. The resonance was with the lower two crystal field levels of the $^4F_{7/2}$ multiplet located at 20,485 cm^{-1} and 20,492.9 cm^{-1} (see Figure 4.2). In this work the focus will involve the same crystal field levels. Thus, we present here values of the oscillator strengths associated with all the transitions between these levels. In addition, qualitative estimates are given for the oscillator strengths for the transitions to the upper two crystal field levels of the $^4F_{7/2}$ at 20,556.4 cm^{-1} and 20,570.5 cm^{-1}.

The absorption spectrum resolving individual crystal field transitions were obtained by measuring the transmission of a pulsed dye laser as its frequency was scanned. The spectral resolution of the resulting spectra was limited by the line width of the laser to about 0.25 to 0.5 cm^{-1}. Complete details of the experimental setup are given in Section 2.2. An example of an absorption spectrum resolving individual crystal field transitions in $ErPO_4$ is shown in Figure 4.5.

The oscillator strength associated with a transition is given as before by Equation 4.7 but with the addition of a Boltzmann correction factor,

$$\left(\frac{e^{-\frac{E}{k_B T}}}{\sum_r e^{-\frac{E_r}{k_B T}}} \right)^{-1}, \tag{4.8}$$

to account for the different thermal populations of the initial states. T is the temperature of the sample, E is the energy of the initial state of the particular transition under consideration, and the sum is over all states that could be populated at temperature T. There are two major difficulties encountered in these measurements.

The first difficulty concerns inaccuracies associated with strong absorption by the samples. If through some combination of large oscillator strength, high absorber number density, or large sample thickness the transmission of the sample is almost nil the result is a large error in the value $\alpha = \ln(I_o/I)$. The second problem is associated with the determination of the sample temperature and the consequent determination of initial state populations. As discussed in Chapter 2 the samples are mounted on a copper cold-finger. The temperature of the copper cold-finger is monitored by a Si diode. However, the temperature could be slightly higher than measured by the detector as a result of

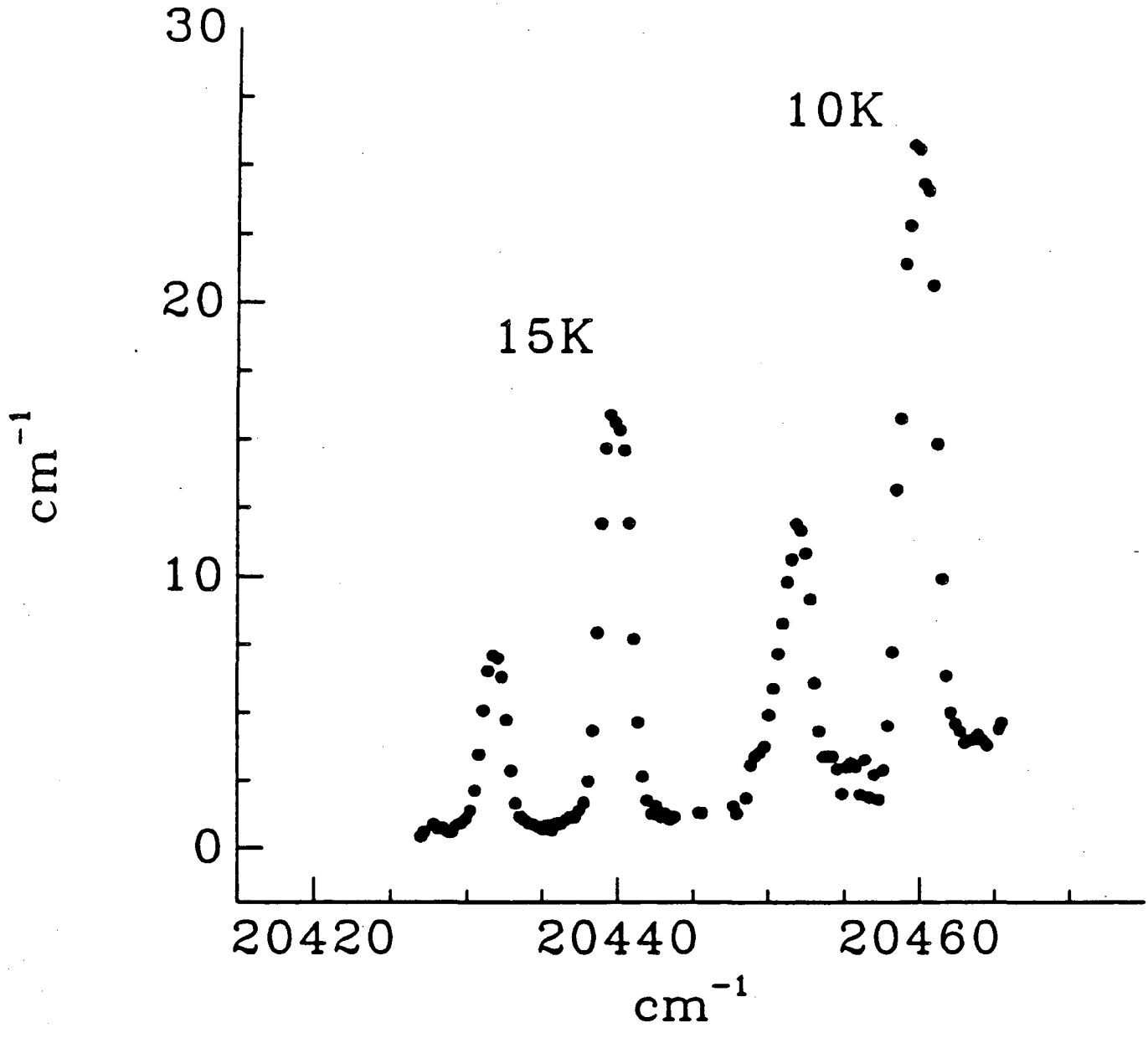

Figure 4.5: Example of the low temperature absorption spectrum of the $^4I_{15/2} \rightarrow ^4F_{7/2}$ transition resolving individual crystal field levels.

the finite thermal conductivity of the sample and the mount.

The solution to the first problem is to use the thinnest crystals available and to keep temperatures (and thus populations) as low as possible for the excited state absorptions. The solution to the second problem is to operate in temperature regions in which errors of a few degrees in temperature determination would result in only small errors in population determination. Of course, it is always necessary to stay at temperatures low enough so that thermal broadening of the line widths does not blend the spectral features of interest.

However, for the case of several transitions originating from the 33 cm^{-1} level the solutions to the two problems were in conflict. Figure 4.6 shows the fractional populations for the levels at 0, 33, and 53 cm^{-1} as a function of temperature. Clearly as far as population certainty is concerned the best operating temperatures are above 25K where the population curve begins to flatten out. However, the transitions from the 33 cm^{-1} level have large enough oscillator strengths that with the thinnest crystals available the transmission of the sample was nearly zero at temperatures above 10K.

To overcome this difficulty absorption measurements were made on samples of $Er_{.01}Y_{.99}PO_4$. The energy level structure of this crystal [103] nearly duplicates that of $ErPO_4$, and it is assumed that the oscillator strengths of the two systems are comparable. Direct comparison of the measured oscillator strengths in both crystals proved this assumption to be valid.

Table 4.2.3 lists the final results of the oscillator strength measurements. Although the absolute values of these measurements might be off by factors as high as two, the relative values are correct to within 25%. In addition it should be mentioned that through use of these "high confidence" relative values, the true sample temperature is estimate to be approximately 3 ± 1K higher than indicated by the detector.

Rough estimates of the oscillator strengths associated with transitions to the upper two crystal field levels of the $^4F_{7/2}$ multiplet can be made from absorption spectra taken by Becker [11]. These spectra are shown in Figures 4.7 and 4.8. Table 4.3 lists the estimated oscillator strengths.

In addition to oscillator strengths, the absorption spectra yield information on the

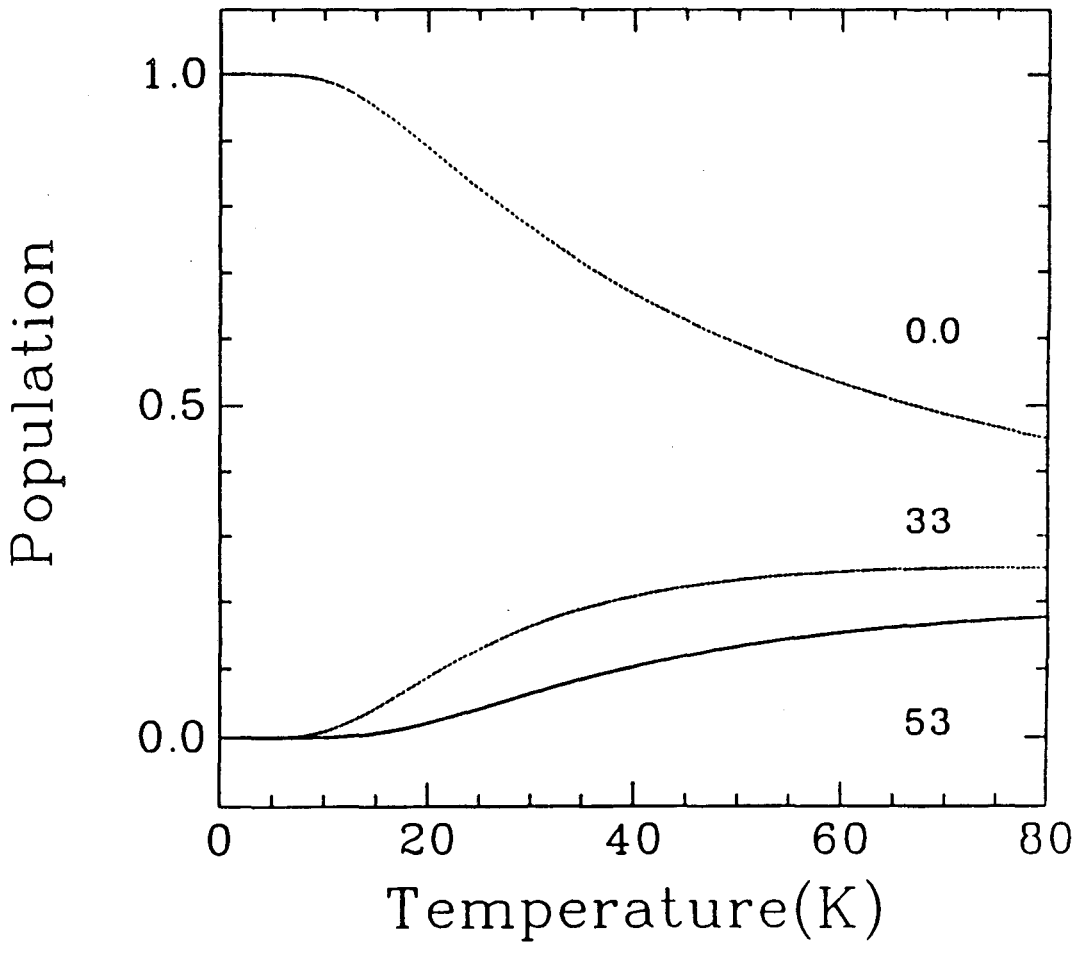

Figure 4.6: Fractional populations of the levels at 0, 33, and 53 cm^{-1}

Transition	Energy (cm^{-1})	Polarization	Oscillator Strgth. $\times 10^6$
$0 \rightarrow 20,492.9$	20,492.9	$\hat{X} = \hat{Y}$	0.092
		$\hat{Z}$	0.069
$0 \rightarrow 20,485.0$	20,485.0	$\hat{X} = \hat{Y}$	0.003
		$\hat{Z}$	na
$33 \rightarrow 20,492.9$	20,459.9	$\hat{X} = \hat{Y}$	0.760
		$\hat{Z}$	na
$33 \rightarrow 20,485.0$	20,452.0	$\hat{X} = \hat{Y}$	0.187
		$\hat{Z}$	0.020
$53 \rightarrow 20,492.9$	20,439.9	$\hat{X} = \hat{Y}$	0.671
		$\hat{Z}$	0.011
$53 \rightarrow 20,485.0$	20,432.0	$\hat{X} = \hat{Y}$	0.148
		$\hat{Z}$	na

Table 4.2: Oscillator strengths for transitions between the crystal field levels of the $^4I_{15/2}$ and $^4F_{7/2}$ multiplets in $ErPO_4$. na= not allowed.

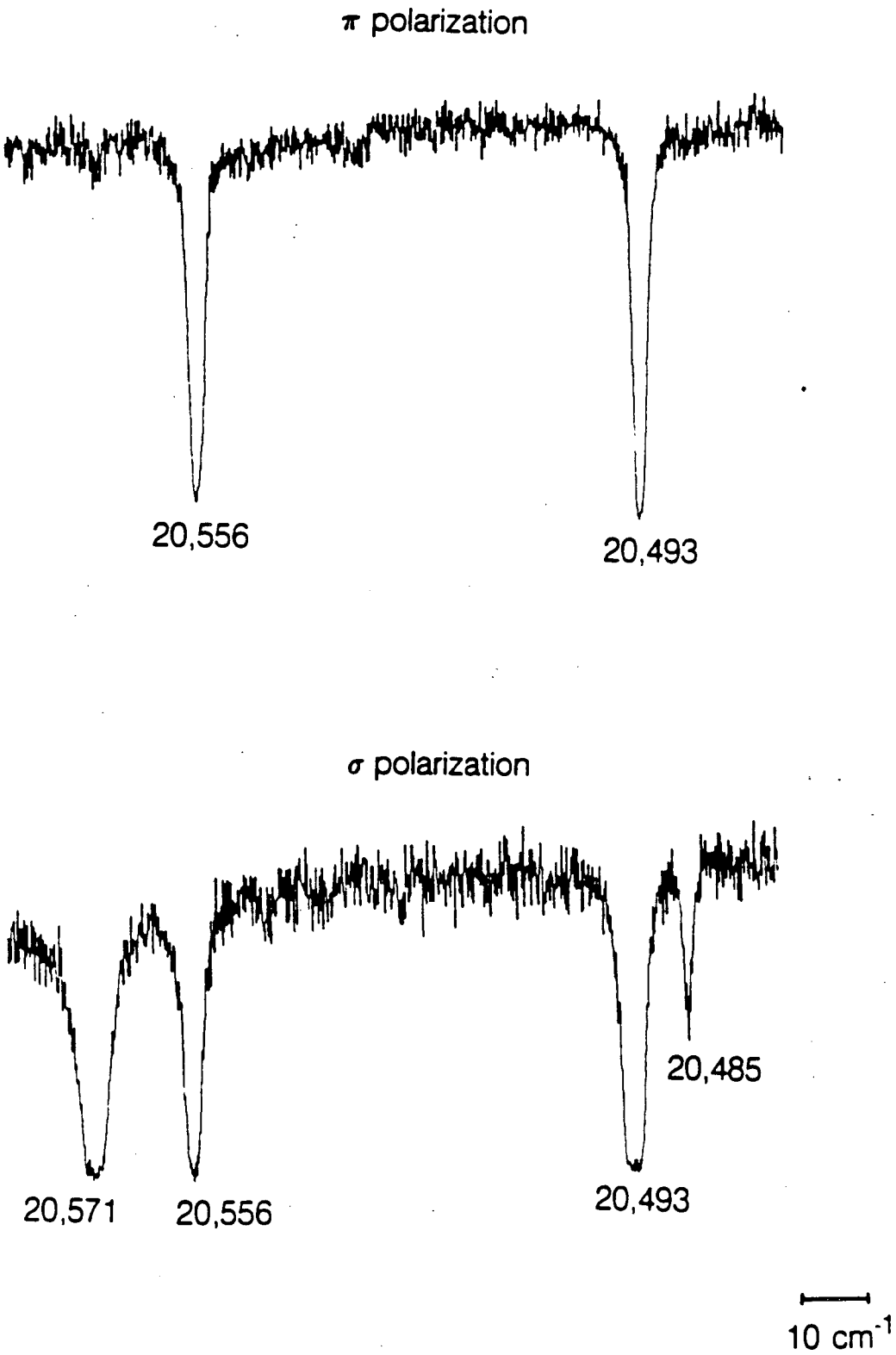

Figure 4.7: Absorption spectra for transitions between the $^4I_{15/2}$ and $^4F_{7/2}$ multiplets of $ErPO_4$. The temperature was nominally 4.2 K.

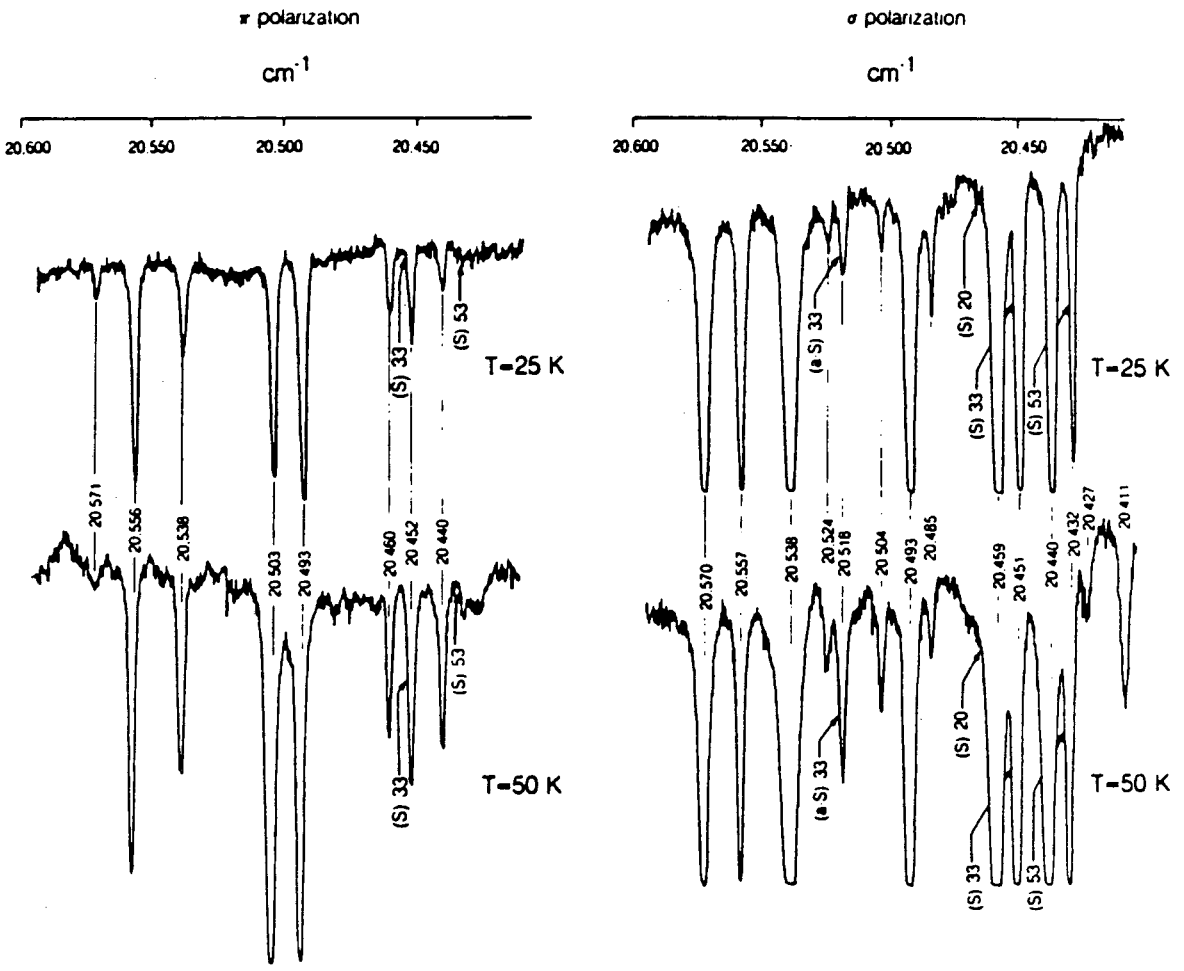

Figure 4.8: Elevated temperature absorption spectra for transitions between the $^4I_{15/2}$ and $^4F_{7/2}$ multiplets of $ErPO_4$.

Transition	Energy (cm^{-1})	Polarization	Oscillator Strgth.
$0 \rightarrow 20,571.0$	20,571.0	$\hat{X} = \hat{Y}$	m
		$\hat{Z}$	na
$0 \rightarrow 20,556.0$	20,556.0	$\hat{X} = \hat{Y}$	m
		$\hat{Z}$	m
$33 \rightarrow 20,571.0$	20,538.0	$\hat{X} = \hat{Y}$	vl
		$\hat{Z}$	s
$33 \rightarrow 20,556.0$	20,523.0	$\hat{X} = \hat{Y}$	vs
		$\hat{Z}$	na
$53 \rightarrow 20,571.0$	20,518.0	$\hat{X} = \hat{Y}$	s
		$\hat{Z}$	na
$53 \rightarrow 20,556.0$	20,503.0	$\hat{X} = \hat{Y}$	vs
		$\hat{Z}$	vl

vs=$(0.0 \rightarrow 0.01) \times 10^{-6}$
s =$(0.01 \rightarrow 0.05) \times 10^{-6}$
m = $(0.05 \rightarrow 0.1) \times 10^{-6}$
l = $(0.1 \rightarrow 0.5) \times 10^{-6}$
vl=$(0.5 \rightarrow 1.0) \times 10^{-6}$

Table 4.3: Oscillator strengths for transitions between the crystal field levels of the $^4I_{15/2}$ and $^4F_{7/2}$ multiplets in $ErPO_4$. na= not allowed.

line widths of various transitions. The broadening of line widths of optical transitions in rare earth crystals may be explained in terms of two different types of mechanisms, characterized by two different line shapes.

One type of broadening is a result of the fact that the crystals are not perfect and different sites in the crystal have slightly different crystal fields. Thus, for a crystal as a whole there will be a statistical distribution of energies associated with any optical transition. The distribution of energies can be, in general, quite complicated. However, using simple statistical arguments one expects the distribution of energies to be close to Gaussian in form.

$$g(k) = \frac{2}{\Delta}\sqrt{\frac{\ln 2}{\pi}} \exp\left[-4\ln 2\left(\frac{k-k_o}{\Delta^2}\right)^2\right] \tag{4.9}$$

where k_o is the center of the resonance and Δ is the full width of the line at half its maximum value. This type of broadening is commonly referred to as *inhomogeneous* in that it is a result of different ions in the crystal having different energy levels. The Doppler broadening of optical transitions in gases is another example of inhomogeneous broadening.

The second type of broadening is the same for every ion in the crystal and is thus referred to as *homogeneous* broadening. It is essentially the energy broadening associated with the finite lifetime of excited states. Homogeneous width is inversely proportional to lifetime. However, one must be careful in terms of what is meant by lifetime. We must not only consider the lifetime that would be measured by monitoring the fluorescence from an excited state but also the so-called *dephasing* time which is not associated with the depopulation of an excited state but with the dephasing of coherent excitation amongst an ensemble of ions. A more in-depth discussion of the nature of these two types of lifetimes and their significance in resonance Raman scattering will be offered in a later section. However, whatever the cause of the lifetime, the shape associated with lifetime broadening is a Lorentzian in form.

$$g(k) = \frac{\frac{\Gamma}{2\pi}}{(k_o-k)^2 + (\frac{\Gamma}{2})^2} \tag{4.10}$$

where k_o is center of the resonance and Γ is the FWHM.

Most lines in rare earth spectra are a convolution of the inhomogeneous (Gaussian)

Transition	Energy (cm^{-1})	Line Width (FWHM), cm^{-1}
$0 \rightarrow 20,492.9$	20,492.9	2.8*
$0 \rightarrow 20,485.0$	20,485.0	not measured
$33 \rightarrow 20,492.9$	20,459.9	2.2
$33 \rightarrow 20,485.0$	20,452.0	2.0
$53 \rightarrow 20,492.9$	20,439.9	1.9
$53 \rightarrow 20,485.0$	20,432.0	2.0

Table 4.4: Line widths (FWHM) of absorption lines in $ErPO_4$. All measurements were taken at approximately 8-12K. * indicates that value could be larger than the actual value as a result of inaccuracies in measurement due to strong absorption.

and homogeneous (Lorentzian) shapes. The inhomogeneous broadening is nearly independent of temperature while the homogeneous broadening generally increases strongly with temperature (many of the lifetime shortening mechanisms are mediated by phonons). Thus, while low temperature line shapes tend to be Gaussian, high temperature line shapes tend to be more Lorentzian.

Table 4.2.3 shows the measured line widths (FWHM) for transitions to the lower two crystal field levels of the $^4F_{7/2}$ in $ErPO_4$. The line widths were measured from spectra taken at temperatures below 12K. All line widths with the exception of the ground state transitions are on the order of 2 cm^{-1}. The values for the ground state transitions are probably overestimated as a result of the measuring problems associated with strong absorption mentioned earlier. However, it is possible to estimate these line widths by extrapolation from the line widths measured for $Er_{.01}Y_{.99}PO_4$.

In Table 4.2.3 the line widths for transitions in $Er_{.01}Y_{.99}PO_4$ are shown. Some of these values were measured at elevated temperatures as indicated in the table caption. With the exception of the ground state transitions, the line widths are all on the order of one-half the corresponding values in $ErPO_4$. From this we deduce that the true line width values for the ground state transitions in $ErPO_4$ are on the order of twice the values measured in $Er_{.01}Y_{.99}PO_4$ or 2×0.9 $cm^{-1} \approx 2$ cm^{-1}.

A few observations can be made with regard to broadening mechanisms. The line shapes for $ErPO_4$ are all Gaussian in shape indicating the line widths are dominated

Transition	Energy (cm^{-1})	Line Width (FWHM), cm^{-1}
$0 \rightarrow 20,496.4$	20,496.4	0.9
$0 \rightarrow 20,484.7$	20,484.7	0.9
$33 \rightarrow 20,496.4$	20,463.4	1.2
$33 \rightarrow 20,484.7$	20,451.7	0.9
$53 \rightarrow 20,496.4$	20,443.4	0.8
$53 \rightarrow 20,484.7$	20,431.7	0.8

Table 4.5: Line widths (FWHM) of absorption lines in $Er_{.01}Y_{.99}PO_4$. Line widths of transitions originating in the ground state were measured at approximately 8K, while line widths of transitions originating from the 33 cm^{-1} and 53 cm^{-1} levels were measured at 21K and 35K, respectively.

by inhomogeneous broadening. However, the line shapes of the $Er_{.01}Y_{.99}PO_4$ peaks all appear to have some component of Lorentzian broadening. The difference between the $ErPO_4$ and $Er_{.01}Y_{.99}PO_4$ line shapes is shown in Figure 4.9. The more Lorentzian shape for the $Er_{.01}Y_{.99}PO_4$ could be the result of the elevated temperatures at which some of these spectra were taken. However, this explanation can not be used for the line shapes of the ground state transitions which are taken from 8K spectra. A second possibility is that both $ErPO_4$ and $Er_{.01}Y_{.99}PO_4$ have Lorentzian components on the order of 0.5 cm^{-1} (FWHM), however, for the case of $ErPO_4$ it is obscured by a fairly large inhomogeneous component. The other item of note is that the Lorentzian width of 0.5 cm^{-1} quoted above is approximately equal to the line width of the laser used in the absorption experiments indicating that the observed Lorentzian width may be for the most part resulting from the laser line width.

4.2.4 Previous Electronic Raman Scattering Experiments: Non-resonant and Resonant Excitation

Becker has studied the relative intensities of electronic Raman scattering from $ErPO_4$[11,64]. Table 4.2.4 shows the observed relative intensities for scattering from the ground state to all the crystal field levels of the $^4I_{15/2}$ multiplet excited non-resonantly by the 514.5 nm argon ion laser line. The same relative intensities (within experimental error) were obtained from spectra excited with the 457.9 nm line. Also shown are values for the

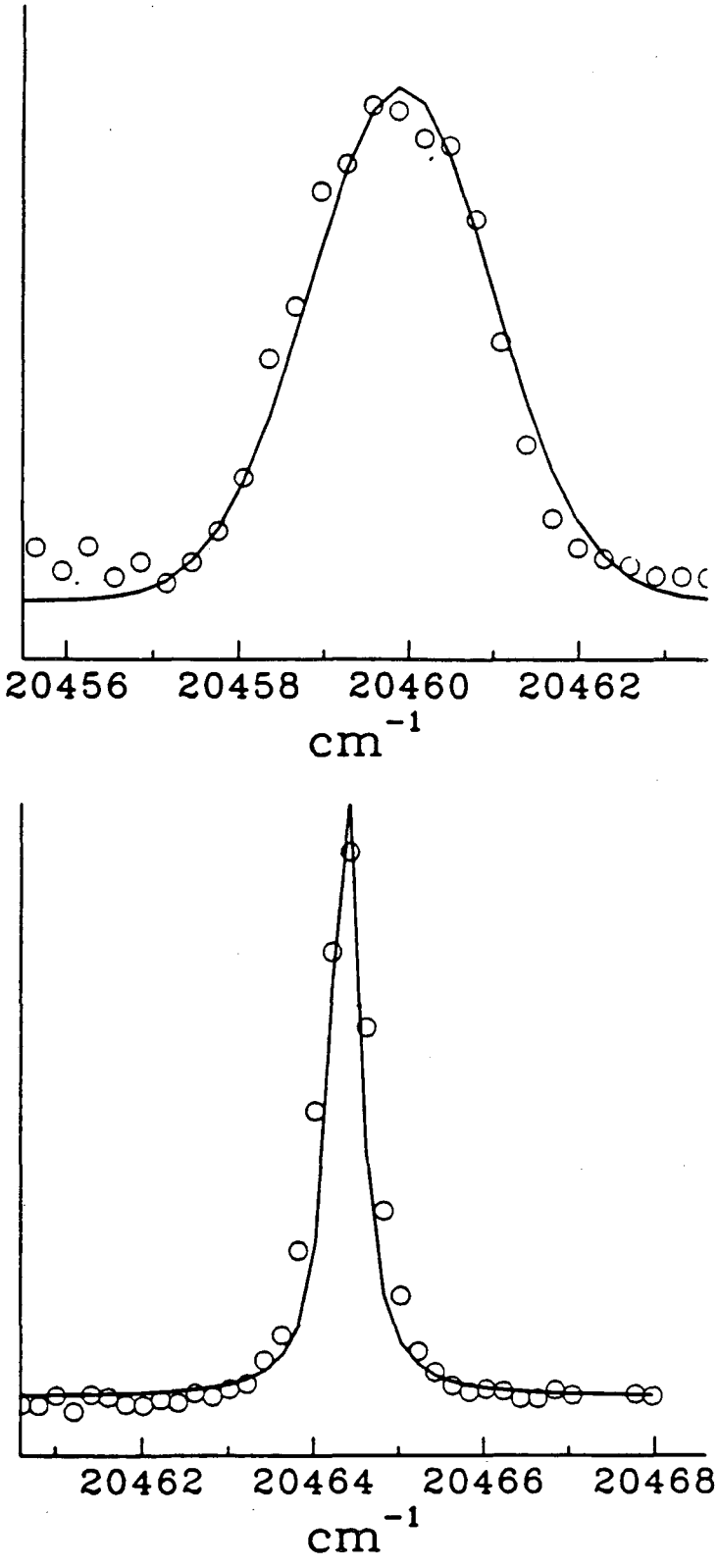

Figure 4.9: Absorption peaks for the transition between the first excited crystal field level of $^4I_{15/2}$ and the first excited crystal field level of $^4F_{7/2}$ in crystals of $ErPO_4$ (above) and $Er_{.01}Y_{.99}PO_4$(below).

relative intensities calculated from the standard theory using two different values for the parameter $\frac{F_1}{F_2}$ (see section 3.4). The value $\frac{F_1}{F_2} = 0.25$ corresponds to dominant virtual intermediate state contributions from the states of the $4f^{10}5d^1$ configuration. The fit to the experimentally observed values is adequate. However, the best fit was obtained for $\frac{F_1}{F_2} = -0.03$ which was interpreted as indicating equal virtual intermediate state contributions from d and g type orbitals.

Becker also used the 488 nm line of the argon ion laser to excite electronic Raman scattering from $ErPO_4$. As stated previously, large enhancements in the scattering intensities were observed. Becker interpreted this as being the result of resonant enhancement due to the near coincidence in energy between the laser excitation and the transitions $^4I_{15/2} \rightarrow ^4F_{7/2}$. Listed in Table 4.2.4 are the observed enhancements in the scattering intensities for transitions between the ground state and the states at 33 and 53 cm^{-1} when the laser excitation was switched from 514.5 nm (19,429.7 cm^{-1}) to 488 nm (20,486.7 cm^{-1}).

4.3 Resonant Electronic Raman Scattering in $ErPO_4$: Scope of the Present Experiment

The following sections describe the results of electronic Raman scattering experiments on $ErPO_4$ using a tunable dye laser as the excitation source. Details of the experimental setup are given in Section 2.4.2.

The resonance associated with the lower two crystal field levels of the $^4F_{7/2}$ multiplet for the scattering transitions from the ground state to the crystal field levels at 33 and 53 cm^{-1} was the focus of this work. In addition, the experiments were limited to one particular combination of scattered and incident polarizations, $\hat{X}\hat{Z}$. The choice of $\hat{X}\hat{Z}$ polarization is advantageous in terms of both performing the experiments and in modelling the results.

The experimental advantage is the large reduction in the amount of scattered laser light entering the detection system when the scattered light is polarization analyzed at 90° from the polarization of the incident laser light. However, in this respect a polarization combination of $\hat{Z}\hat{Y}$ would do just as well as $\hat{X}\hat{Z}$. The final choice of the

Transition	Polarization	Observed intensity	Predicted intensity $F_1/F_2 = 0.25$	Predicted intensity $F_1/F_2 = 0.03$
33 cm^{-1}	XX,YY	a	0.6	0.6
	XY,YX	15.2	15.2	15.2
	XZ,YZ	3.0	46.6	5.0
	ZX,ZY	0.6	13.1	0.9
53 cm^{-1}	XX,YY	a	0.04	0.04
	ZZ	a	0.2	0.2
	XY,YX	0.9	14.6	0.2
	XZ,YZ	0.9	1.8	4.5
	ZX,ZY	6.1	42.9	9.4
105 cm^{-1}	XX,YY	a	2.0	2.0
	ZZ	1.5	7.8	7.8
	XY,YX	a	1.7	0.02
	XZ,YZ	a	0.6	0.5
	ZX,ZY	a	0.4	0.5
145 cm^{-1}	XX,YY	a	0.2	0.2
	XY,YX	1.8	8.4	8.4
	XZ,YZ	0.6	4.9	3.8
	ZX,ZY	0.9	2.5	3.5
229[b] cm^{-1}	XX,YY	a	4.4	4.4
	XY,YX	a	0.2	0.2
	XZ,YZ	a	0.8	0.04
	ZX,ZY	a	0.5	5×10^{-5}
246[b] cm^{-1}	XX,YY	a	0.2	0.2
	ZZ	a	0.8	0.8
	XY,YX	a	0.6	0.6
	XZ,YZ	a	0.3	0.3
	ZX,ZY	a	0.2	0.2
286[b] cm^{-1}	XX,YY	a	0.5	0.5
	XY,YX	a	0.3	0.3
	XZ,YZ	a	0.2	0.1
	ZX,ZY	a	0.03	0.1

a: not observed.

b: from the crystal field fit, Table 4.4.

Table 4.6: Non-resonantly excited electronic Raman scattering in $ErPO_4$(from Reference [11]. Predicted and observed intensities are for the transitions from the ground state to the crystal field levels of the $^4I_{15/2}$ multiplet of Er^{3+}. The XX and YY intensities could not be accurately measured.

	Polarization			
	$\hat{X}\hat{Y}$	$\hat{Z}\hat{Y}$	$\hat{X}\hat{Z}$	$\hat{Z}\hat{Z}$
33 cm^{-1} transition	1.8	80.0	18.1	a
53 cm^{-1} transition	124.8	1.9	29.1	a

a: ZZ transitions are absent or weak.

Table 4.7: Ratio of the resonant to non-resonant excited Raman scattering intensities. Resonant excitation was at 20,486.7 cm^{-1}. The Δ1026 cm^{-1} phonon was used as an internal standard to normalize the spectra to a common scattering efficiency.

$\hat{X}\hat{Z}$ polarization combination was predicated on the resulting large simplification in the analysis of the experimental results for this polarization combination.

Figure 4.10 shows the important crystal field levels and their respective symmetry labels. Because only states with different group labels are connected by the $\hat{Z}$ electric dipole operator, we see that for scattering originating in the ground state, Γ_6 symmetry, that resonance is only possible with one of the two states in the energy range of interest. The only resonant level is the Γ_7 at 20,492.9 cm^{-1}. Thus the choice of $\hat{Z}$ polarization for the incident laser light effectively reduces the system to three levels with the final state being either the 33 or 53 cm^{-1} states.

4.4 Discrimination between electronic Raman scattering and fluorescence

The first task was to guarantee that the observed signals were indeed the result of Raman scattering and not just fluorescence. The possibility of making such a determination depends greatly on how close the exciting radiation is to exact resonance.

4.4.1 Frequency Discrimination: The case of near-resonant excitation

For excitation energies not directly resonant with any transition the simplest way to differentiate between fluorescence and Raman signals is through frequency (spectral) discrimination .

Figure 4.11 shows a system with three levels labelled $i, r,$ and, f with energies $E_i, E_r,$ andE_f, respectively. For laser excitation at E_l the Raman signal will be at energy $E_l - (E_f - E_i)$,

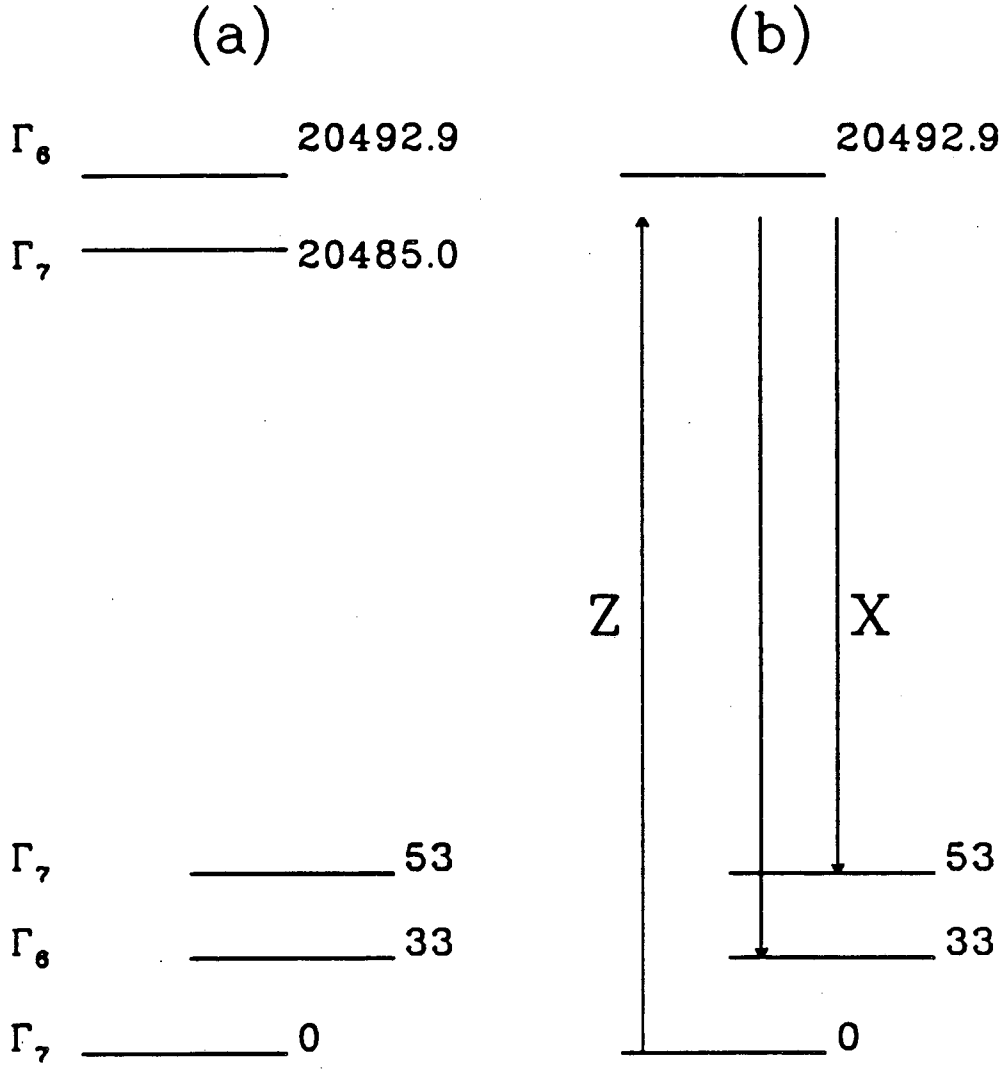

Figure 4.10: (A) $ErPO_4$ crystal field levels of importance in the resonance electronic Raman experiments and (B) the important levels when only polarization combination $\hat{X}\hat{Z}$ is studied.

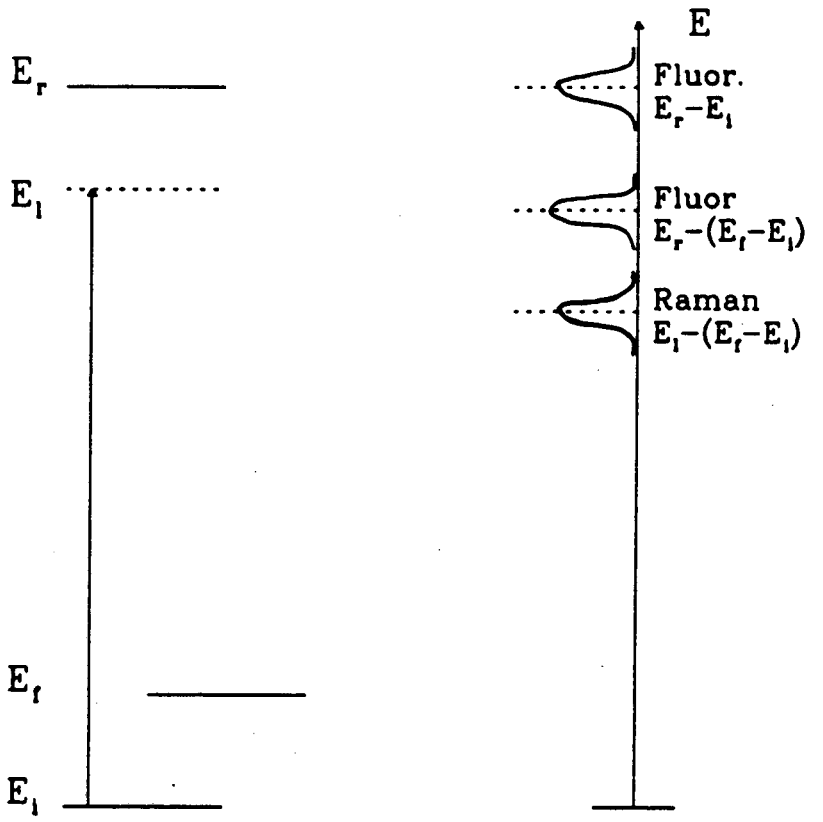

Figure 4.11: Excitation of a three level system and resulting Raman and fluorescence signals. The Raman signal and the fluorescence to the state f are spectrally distinguishable as long as $E_l \neq E_r - E_i$.

while any fluorescence will be at energies $E_r - E_i$ or $E_r - E_f$. It can be seen that for E_l approaching resonance at $E_r - E_i$ the Raman signal and the fluorescence $E_r - E_f$ will coincide spectrally. However, as long as E_l is removed from direct resonance ($E_r - E_i$) the Raman scattering and fluorescence signals should be distinguishable spectrally.

Figure 4.12 shows a series of $\hat{\mathbf{X}}\hat{\mathbf{Z}}$ spectra from $ErPO_4$ excited by several different frequencies of the dye laser all about or near the resonance $0 \rightarrow 20,492.9$ cm^{-1}. The spectra are plotted as a function of energy shift in cm^{-1} from their respective excitation energies. In such a plot Raman signals maintain a fixed value (representing a fixed shift from the excitation energy) while fluorescence signals move about (representing a fixed absolute energy location). Clearly , the observed signals in these plots represent Raman scattering to the 33 and 53 cm^{-1} levels.

Figures 4.13 and 4.14 show the compilation of the measured shifts for all the spectra taken in this work. The vertical axis gives the shift of the spectral peaks from the exci-

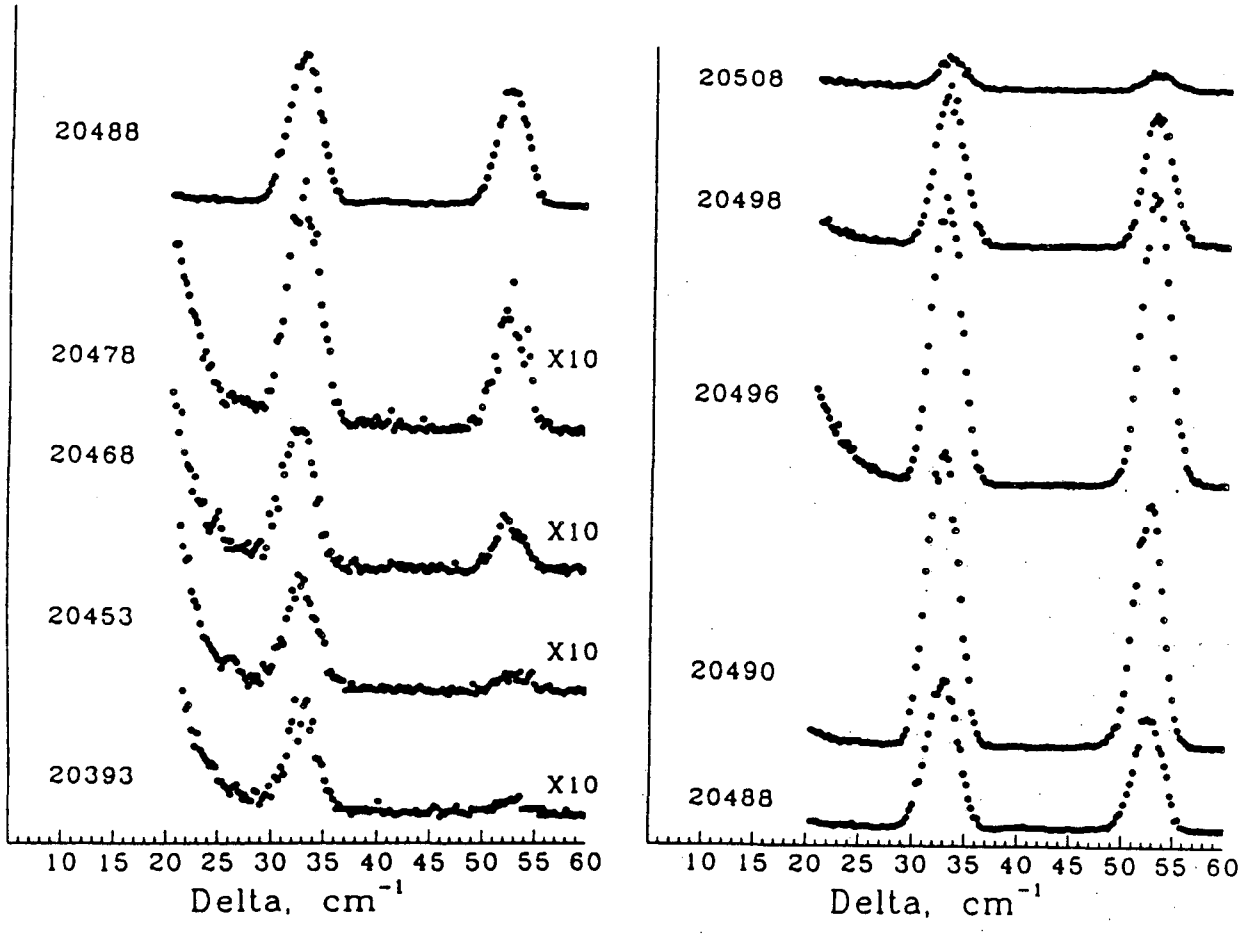

Figure 4.12: $\hat{X}\hat{Z}$ polarized spectra of $ErPO_4$ excited using different photon energies. The horizontal axis represents the shift from the labelled excitation energies.

tation energy while the horizontal axis gives the excitation energy. For each point both values are accurate to about $\pm 0.5 cm^{-1}$. The horizontal lines shows the expected positions of peaks resulting from Raman scattering while the skewed lines show the expected positions of the fluorescence peaks, $20,492.9 \rightarrow 53\ cm^{-1}$ and $20,492.9 \rightarrow 33\ cm^{-1}$. Again, except for the case of direct resonance (at which no determination can be made) the spectra are consistent with Raman scattering to the 33 and 53 cm^{-1} levels.

However, care must be taken in describing what is meant by direct resonance. To this point the discussion has assumed a resonance with a single well defined energy. However, as we have seen, the resonances in rare earth crystals, although relatively narrow, have some width. The resonance in this case has a FWHM of approximately 2 cm^{-1} believed to be mostly attributable to inhomogeneous broadening. Thus, we actually have a collection of ions with slightly different resonant energies distributed about some mean energy, which we have up to now referred to as the "resonant energy". The question arises if it is possible to distinguish spectrally Raman scattering from fluorescence for excitation energies anywhere within the linewidth of the resonance. It is clear at what energies Raman scattering appear. However, what is the spectral distribution of the fluorescence resulting from a selective excitation of a certain group of ions ?

The answer to this question depends on the relative rates of two processes. An ion in an excited state may relax either by decaying internally or by transferring its energy to a neighboring ion. The first process will result in *site selective fluorescence* (if the decay has some radiative component) at an energy which is specific to that particular ion. The second process tends to re-distribute the excitation energy across the entire linewidth resulting in a fluorescence spectra like that which would result from non-selective excitation. In general, one expects a selectively excited fluorescence to have the spectral attributes of both processes with the partitioning dependent on the relative rates of the two processes (see Reference[18] and references therein).

Figure 4.15 shows spectra of $ErPO_4$ excited at energies inside the resonant linewidth. In this case there is no re-distribution of fluorescence to the line center. Not even a slight skewing of the peaks toward the center of the resonance is apparent. The conclusion drawn is that the observed spectra are either the result of Raman scattering

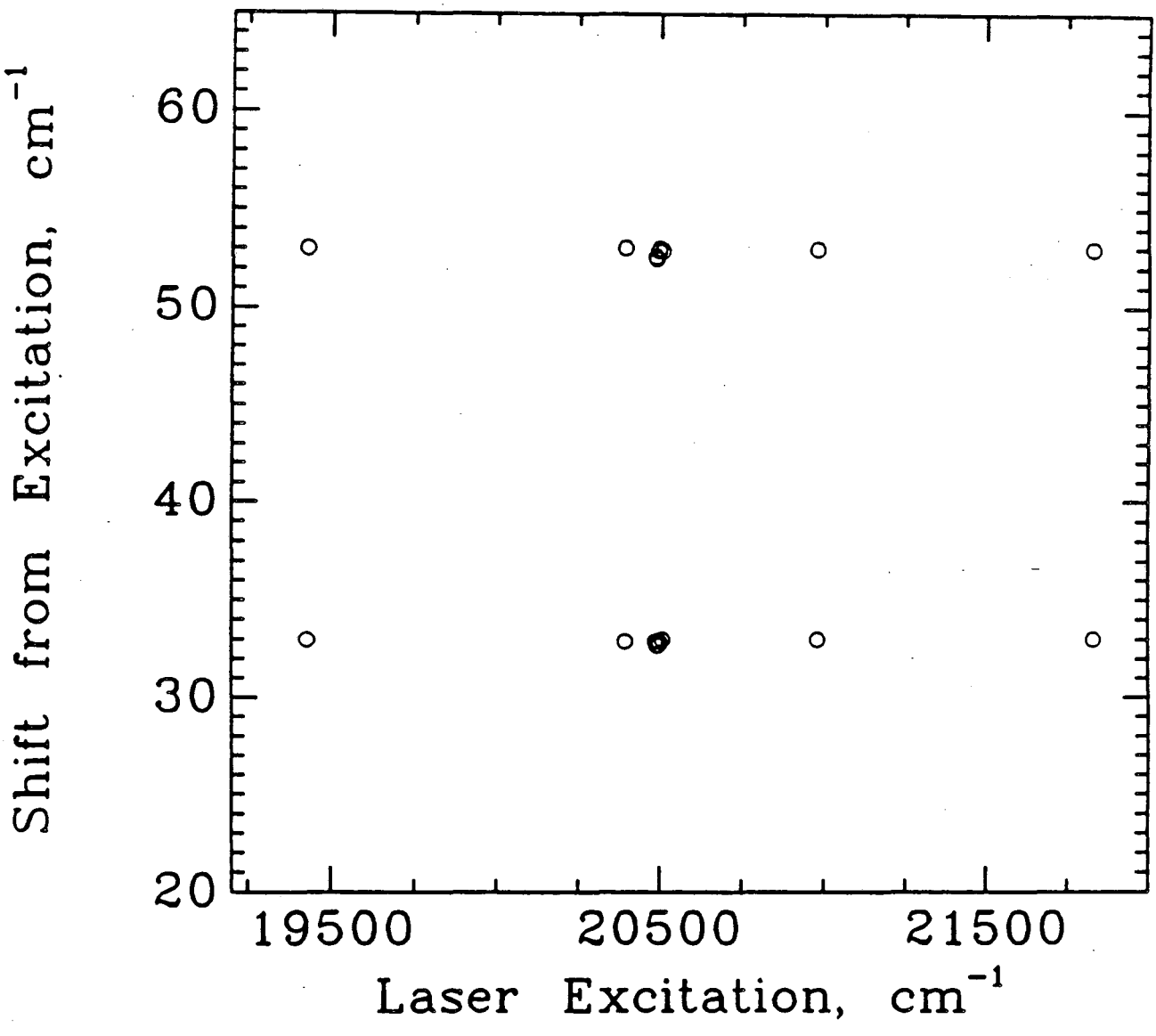

Figure 4.13: Energy shifts of the peaks in the $\hat{X}\hat{Z}$ spectra of $ErPO_4$ as a function of excitation energy.

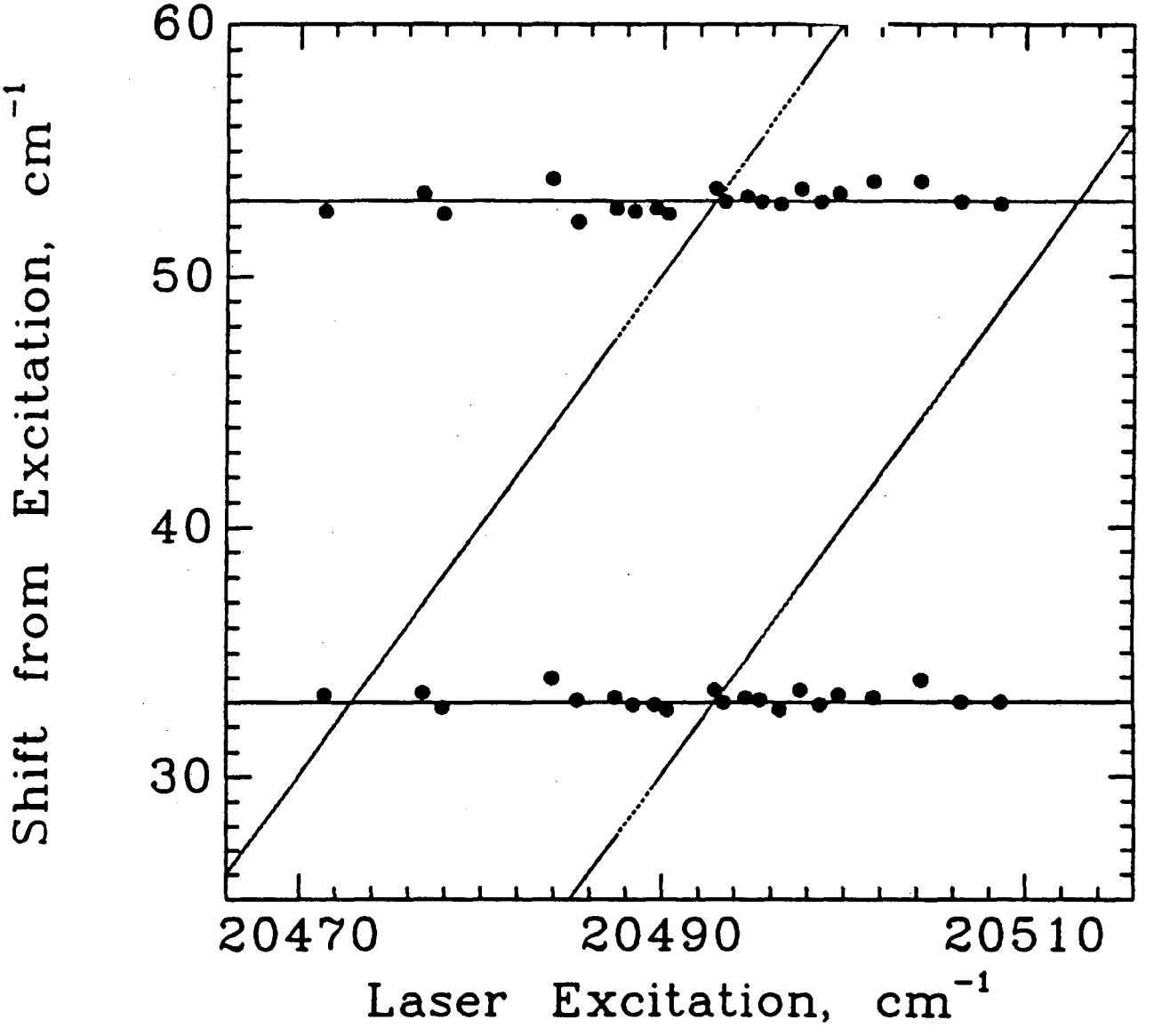

Figure 4.14: Energy shifts of the peaks in the $\hat{X}\hat{Z}$ spectra of $ErPO_4$ as a function of excitation energy. Dashed lines are the expected location of Raman peaks. Solid lines are expected locations of fluorescence peaks.

or *site selective fluorescence* with no re-distribution. *Site selective fluorescence* with no re-distribution requires ion de-excitation times that are much shorter than the ion-ion transfer times. This seems plausible for $ErPO_4$ because the lifetime of the resonant state is measured to be less than 10 ns (due to strong non-radiative decay). However, we should look more closely at the energies expected from *site selective fluorescence* in a three level system.

Figure 4.16 shows a three level system with the mean energies of the states at $\overline{E}_i$, $\overline{E}_r$, and $\overline{E}_f$. The inhomogeneous broadening of each state is represented in terms of a variation of the energy of a level as a linear function of some parameter κ (κ representing some property of the ion environment which varies from site to site). This linear variation is no doubt an oversimplification but will serve to illustrate a point.

Exciting with a laser with photon energy E_l somewhere in the linewidth of the transition $i \rightarrow r$ will excite ions characterized by the value of $\kappa = \kappa_o$ given by

$$\kappa_o = \frac{E_l - (\overline{E}_r - \overline{E}_i)}{\zeta_r - \zeta_i}. \tag{4.11}$$

The *site selective fluorescence* from $r \rightarrow f$ will be at an energy

$$E_r(\kappa_o) - E_f(\kappa_o) = (\overline{E}_r - \overline{E}_f) + (\zeta_r - \zeta_f)\kappa_o \tag{4.12}$$

$$= (\overline{E}_r - \overline{E}_f) + \left(\frac{\zeta_r - \zeta_f}{\zeta_r - \zeta_i}\right)\left[E_l - (\overline{E}_r - \overline{E}_i)\right]. \tag{4.13}$$

Now Raman scattering from excitation at E_l will be at energy

$$E_l - (\overline{E}_f - \overline{E}_i). \tag{4.14}$$

We see that *site selective fluorescence* and Raman scattering will only exactly coincide for $\zeta_f = \zeta_i$ or $E_l = \overline{E}_r - \overline{E}_i$(direct resonance). $\zeta_i = \zeta_f$ implies the not very likely condition of zero inhomogeneous broadening for the $i \rightarrow f$ transition. So, in general, we expect *site selective fluorescence* to be spectrally distinguishable from Raman scattering for excitation energies not in direct resonance. Thus, we have high confidence that for excitation energies removed by more than 0.5 cm^{-1} from direct resonance in $ErPO_4$ the observed spectral peaks are the result of Raman transitions from the ground state to the 33 and 53 cm^{-1} levels. For excitation at direct resonance other methods of discrimination between Raman scattering and fluorescence are needed.

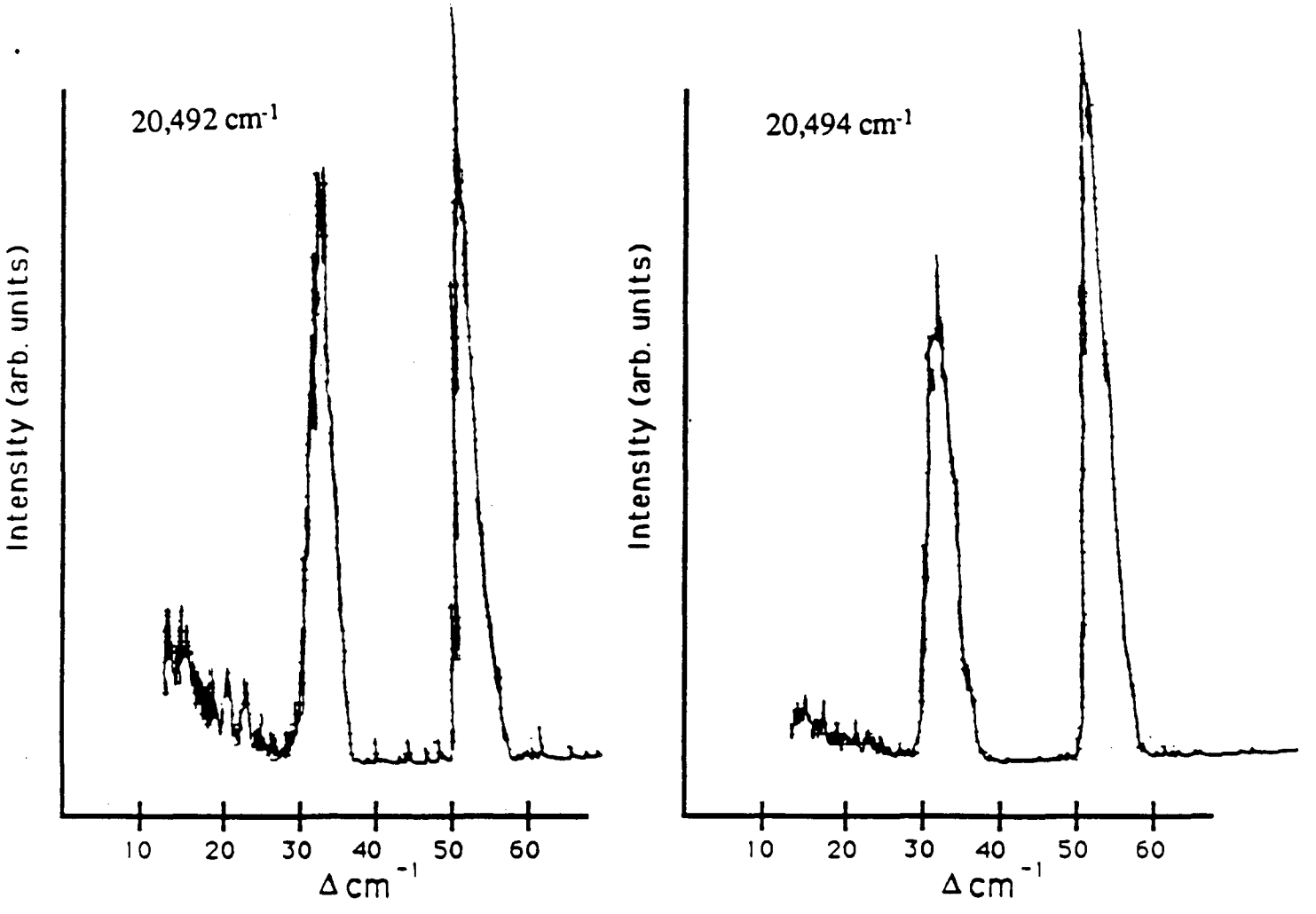

Figure 4.15: $\hat{X}\hat{Z}$ spectrum of $ErPO_4$ excited at 20,492 and 20,494 cm^{-1}.

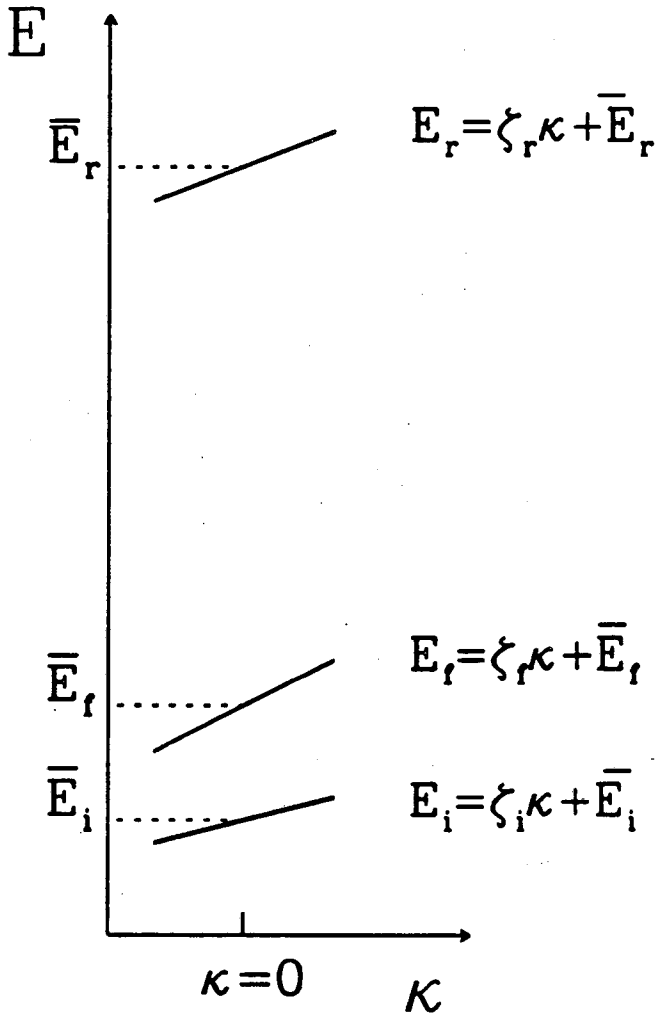

Figure 4.16: Graphical representation of an inhomogeneously broadened three level system. The vertical axis is energy. The horizontal axis κ represents a parameter that varies from site to site in the crystal.

4.4.2 Temporal Discrimination: The case of resonant excitation

There has been a great deal of discussion in the literature concerning the differences between resonance Raman scattering (in this section resonance is always used to refer to direct resonance) and the process of absorption followed by fluorescence to an excited state (other terminology commonly used to refer to the latter process or related processes are hot luminescence or resonant fluorescence) [104,105,106,107], [108,109,110], [111,112,113,114,115,116], [117,118,119,120]. Most of the discussion concerned whether there existed any difference between the two processes and if so what experimental determinations could be made to distinguish the two. A great deal of confusion over the issue has resulted from varying terminology and definitions. It is now generally agreed that there are fundamental physical differences between resonance Raman scattering and absorption followed by fluorescence which are most clearly displayed in the temporal decay of the respective signals after pulsed excitation.

Resonance Raman scattering is viewed as a one-step coherent process. The Raman signal results from radiation emitted by a polarization of the material system oscillating at the frequency ω_s. The polarization is generated by the beating of the incident laser field with other resonant polarizations of the material system. The persistence of such a radiation after the exciting field is turned off will depend on the persistence of the phase coherence of the contributing polarizations. The relevant time is denoted by T_2, the phase relaxation time or transverse lifetime. On the other hand, resonance fluorescence is a two-step process with loss of coherence in between. The resonant state becomes populated and then decays with the lifetime T_1, commonly referred to as the population or longitudinal lifetime.

Phase relaxation can occur through a multitude of processes most of which just involve pure dephasing of the polarization and not necessarily decay of the polarization. As a result, T_2 is often much shorter than the population lifetime. Thus, in general, one might expect for pulsed excitation two signals with two distinctly different lifetimes; a fast signal, Raman scattering with lifetime T_2, and a longer lived fluorescence signal with lifetime T_1. The partitioning of the energy between the two, Raman/fluorescence,

should be proportional to the ratio $\frac{T_2}{T_1}$ [121].

Temporal discrimination of resonance Raman scattering and resonance fluorescence have been reported. Williams, Rousseau, and Dworetsky [122] observed scattering signals resulting form resonant excitation in I_2 gas that had a fast component (Raman) and a longer-lived component (fluorescence). Masumoto *et al.* [123] studied scattering from the semi-conductor CuCl with the exciting laser in resonance with an excitonic level. They observed an emitted light signal with two separate temporal components; a fast Raman part and a slower luminescence part. Weiner and Yu [124,125] used temporal discrimination to determine that scattered light from resonant excitation of an excitonic level in the semi-conductor CuO_2 was dominated not by Raman scattering but by hot luminescence. Nicollin and Koningstein [68] reported a scattering signal from resonant excitation of the $^5D_4$ multiplet in TbAlG that decayed with two different time constants.

In $ErPO_4$ an attempt was made to discriminate temporally between resonance Raman scattering and resonance fluorescence. Figure 4.17 shows the temporal response of two different signals excited by the pulsed laser. The circles give the time evolution of the non-resonantly excited Raman scattering of the 303 cm^{-1} phonon of $ErPO_4$. Such scattering should have approximately zero lifetime so that the curve in the figure is really displaying some convolution of the lifetime of the laser pulse ($\approx$ 7ns) and the temporal response of the detection system. The triangles give the time evolution of the signal at 20,459.9 cm^{-1} (corresponding to the transition $20,492.9 \rightarrow 33cm^{-1}$) excited by radiation at 20,492.9 cm^{-1}. This signal corresponds to either resonance Raman scattering or resonance fluorescence. As can be seen the signal follows the time evolution of the laser pulse and detection system (given by the 303 phonon time response). There is no indication of two signals with different time responses. However, it is difficult to draw any definite conclusion from this result. The single decay could just indicate that both T_2 and T_1 are much shorter than the laser pulse.

Figure 4.19 shows the temporal response of two different signals. Again the circles exhibit the time evolution of the Raman scattering to the 303 cm^{-1} phonon. The triangles give the time evolution of a signal at 20,459.9 cm^{-1} $(20,492.9 \rightarrow 33cm^{-1})$ excited by tuning the laser to 20,556 cm^{-1} corresponding to the transition between the ground

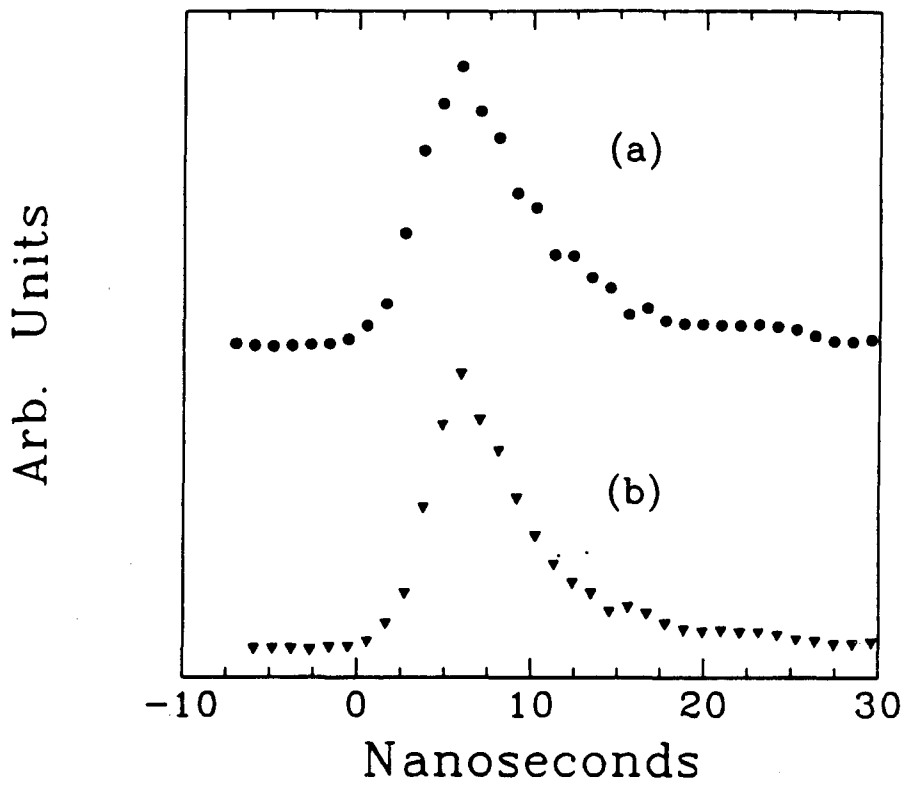

Figure 4.17: Temporal evolution of (a) non-resonantly excited Raman scattering to the 303 cm^{-1} phonon, (b) resonantly excited signal at $\Delta 33$ cm^{-1}.

state and the upper state of the $^4F_{7/2}$ multiplet. Figure 4.18 shows the excitation and proposed decay mechanism associated with this measurement. As shown in the figure the signal is believed to be due solely to the population decay of the level at 20,492.9 cm^{-1}. From 4.19 we see that there is no difference between the temporal evolution of the fluorescence and that of phonon Raman scattering indicating, indeed, that the population lifetime is shorter than the laser pulse.

In conclusion, we can not differentiate between absorption followed by fluorescence and resonance Raman scattering temporally since both T_2 and T_1 are markedly shorter than the laser pulse.

4.5 The Excitation Profiles

In this section the excitation profiles (Raman scattering intensity vs. excitation frequency) for scattering from the ground state to the levels at 33 and 53 cm^{-1} in $\hat{X}\hat{Z}$ polarization are given. We start by giving the excitation profile for the $\hat{X}\hat{Z}$ Raman

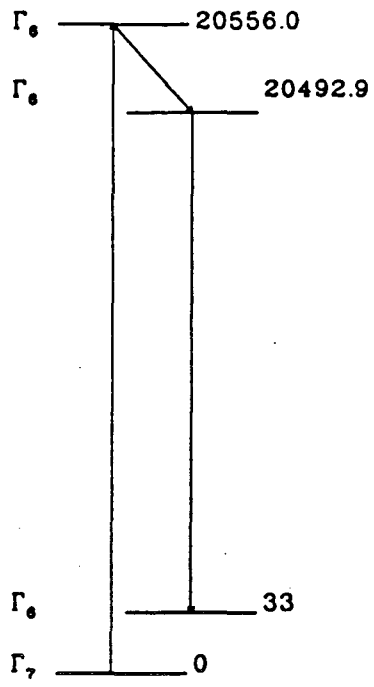

Figure 4.18: Excitation of the $20,492.9 \rightarrow 33\text{cm}^{-1}$ fluorescence for temporal study displayed in Figure [4.17].

scattering to the E_g phonon at 303 cm^{-1}.

4.5.1 The Δ303 Phonon

In rare earth crystals there is only a small interaction between the phonons of the crystal and the shielded 4f electrons of the rare earth ion. Thus, a resonance of the exciting laser light with a $4f^N \rightarrow 4f^N$ electronic transition of the rare earth ion should have very little effect on the phonon Raman scattering cross-sections. Therefore, the phonon Raman excitation profiles serve as good standards for comparison with the electronic Raman scattering profiles in attempts to elucidate the features in the electronic Raman scattering profiles that result from $4f^N \rightarrow 4f^N$ resonance.

Shown in Figure 4.20 is the excitation profile for the Raman scattering to the 303 cm^{-1} phonon. This profile was taken at a temperature of approximately 10K. It was obtained by scanning the exciting dye laser frequency and spectrometer analysis frequency simultaneously maintaining a constant difference of 303 cm^{-1} between the two

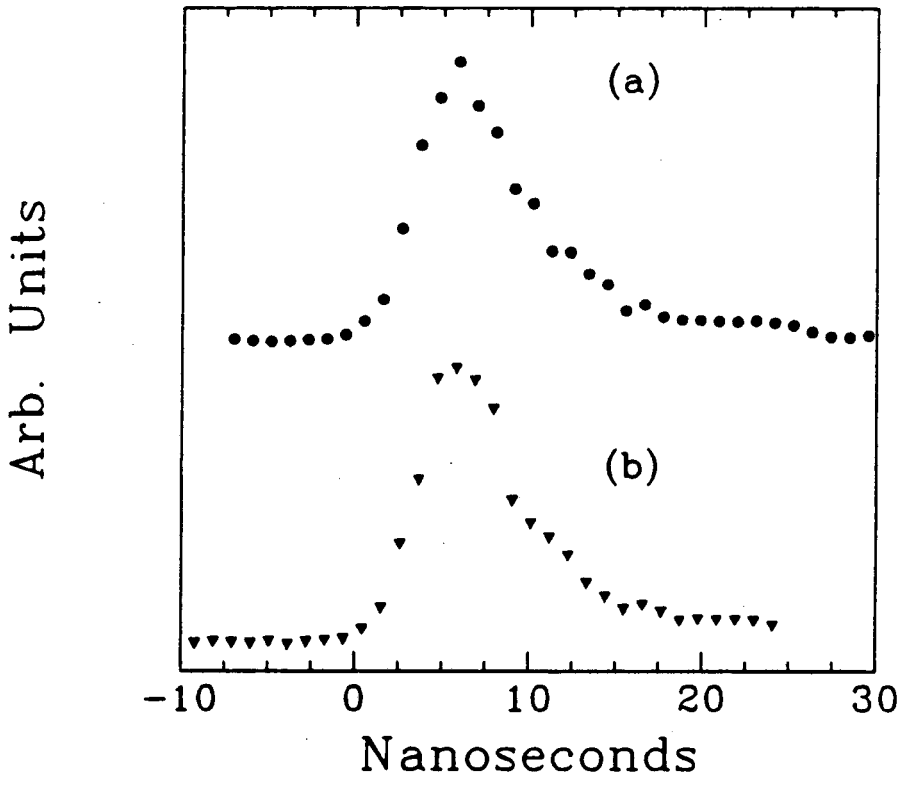

Figure 4.19: Temporal evolution of (a) non-resonantly excited Raman scattering to the 303 cm^{-1} phonon and (b) population decay of the 20,492.9 cm^{-1} level.

(see Section 2.4.2 for details). Thus, the peak intensity of the Raman scattering was monitored as a function of excitation frequency. The peak intensity is proportional to the intensity integrated over the entire line width so long as the the line shape does not change as a function of excitation frequency. Complete spectra taken at several excitation frequencies indicates the line shape is, indeed, constant.

The excitation profile is flat with exception of a large dip at approximately 20,493 cm^{-1} and a smaller one at 20,503 cm^{-1}. These dips are not the result of variation in the Raman scattering cross-section, but simply reflect the absorption of the incident laser light by the resonant transition $0 \rightarrow 20,492.9\ cm^{-1}$ at 20,492.9 cm^{-1} and the excited state absorption $53 \rightarrow 20,556 cm^{-1}$ at 20,503 cm^{-1} (this excited state absorption is effective at such low temperatures as a result of its very large oscillator strength, see Table 4.3). The absorptions reduce the amount of incident laser light available for Raman scattering thus resulting in the dips in the excitation profile. An item of note is that the dip (or absorption) at 20,492.9 cm^{-1} is symmetric in the excitation frequency about the mean value. This fact will be of importance in the following sections.

4.5.2 The $\Delta 33$ and $\Delta 53$ Electronic Raman Scattering

The excitation profiles for the electronic Raman scattering from the ground state to the levels at 33 and 53 cm^{-1} are dramatically different from the phonon Raman profile. Shown in Figure 4.21 is the excitation profile for the $\hat{X}\hat{Z}$ scattering to the 33 cm^{-1} level. The profile was taken by the method described earlier of scanning the dye laser and spectrometer in synchronization. The vertical axis gives the enhancement of the scattered intensity over the non-resonantly excited (19,429.7 cm^{-1}) value reported by Becker [11]. Becker reported the electronic Raman intensities relative to the intensity of Raman scattering to the 1026 cm^{-1} E_g phonon. In this work the same comparison was made (for excitation energies removed from any absorptions) thus allowing a direct comparison with Becker's values. However, it should be noted that this does not mean that the enhancements in Figure 4.21 have been normalized overall by the phonon Raman scattering intensity, thus correcting for the absorption of the incident laser beam. The profile shown in the figure is *raw* with no correction for the absorption of the incident

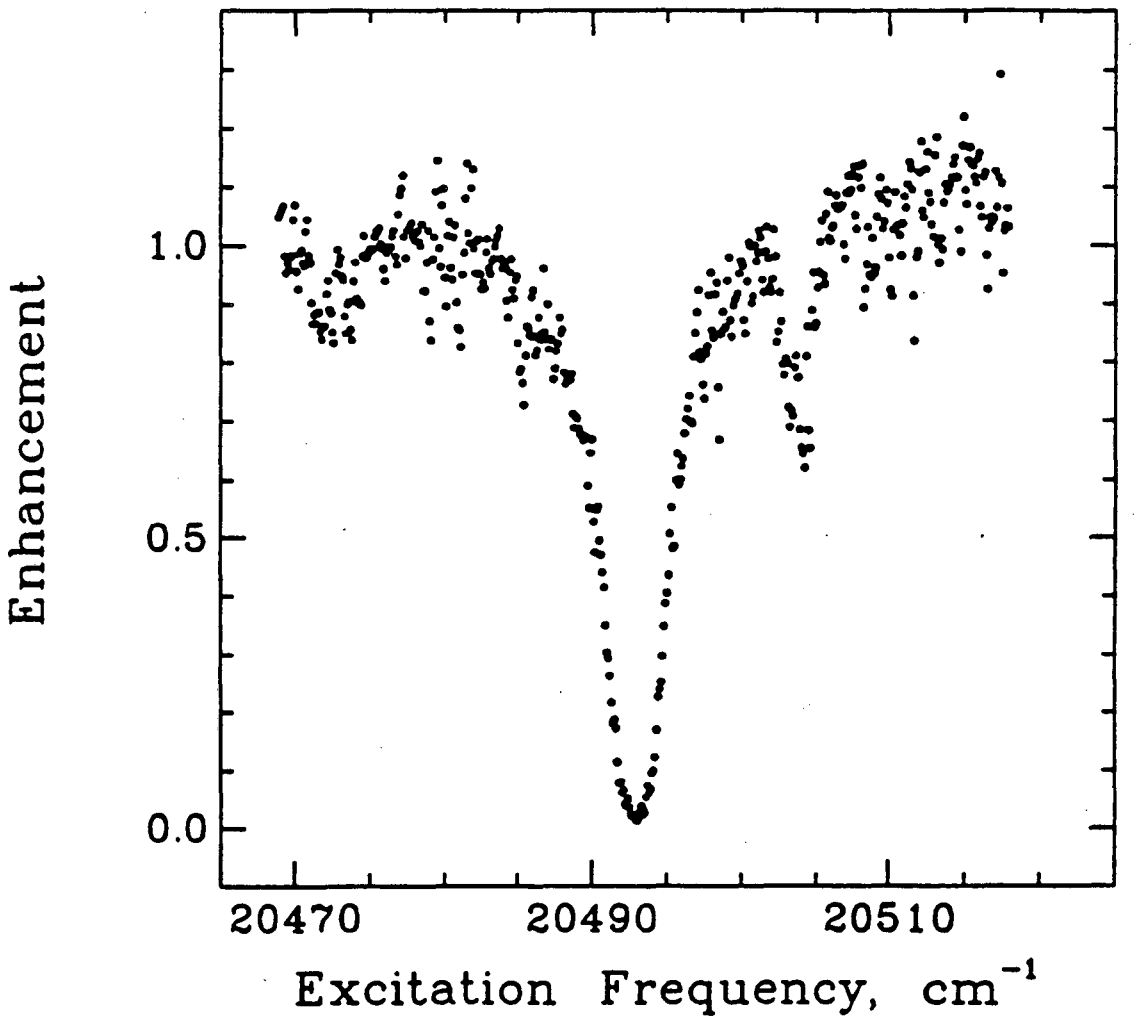

Figure 4.20: Excitation profile for $\hat{\mathbf{X}}\hat{\mathbf{Z}}$ Raman scattering to the 303 cm^{-1} E_g phonon in $ErPO_4$. Profile was taken at a temperature of approximately 10K.

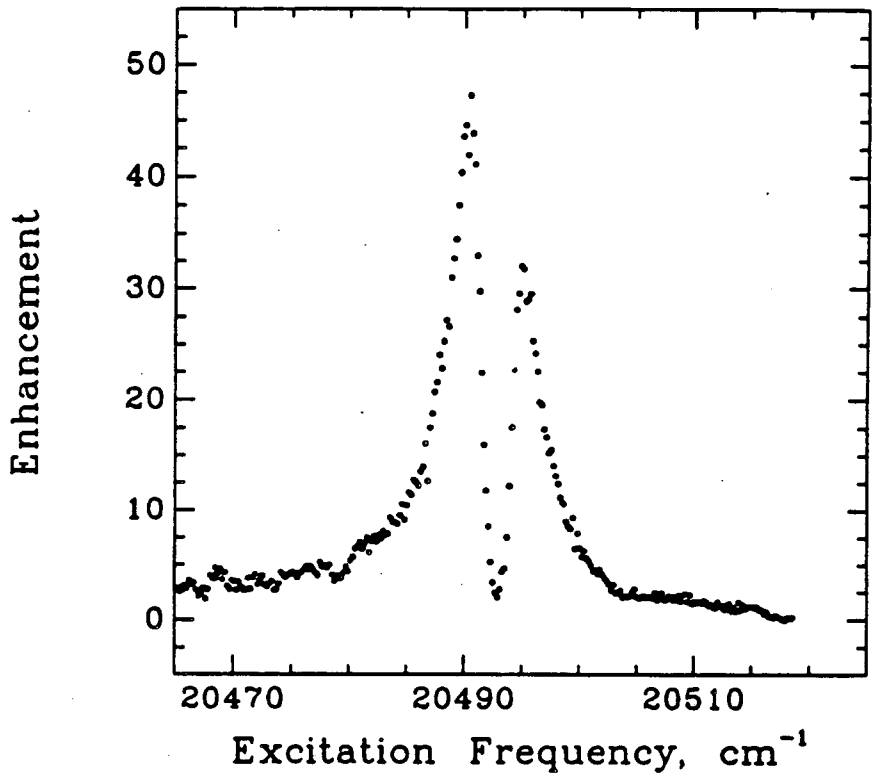

Figure 4.21: Enhancement of $\hat{\mathbf{X}}\hat{\mathbf{Z}}$ electronic Raman scattering to the 33 cm^{-1} level as a function of excitation frequency. Profile has not been corrected for absorption losses of the pump beam.

laser.

The most notable aspects of the excitation profile are:

- The unusual double-peak shape. The profile looks like one that would result from a double resonance. However, the shape actually represents a single resonance structure with a hole in the center. The hole is directly on resonance and is the result of either absorption of the incident laser beam or possibly absorption of the scattered light by population in the final state of the Raman process.

- The enhancements are very large. The peak enhancement is a factor of 47.1 at Δ3.0 cm^{-1} from the center of the resonance.

- The profile is asymmetric in the excitation frequency about the center of the resonance. This may be most markedly noted at the peaks on either side of the

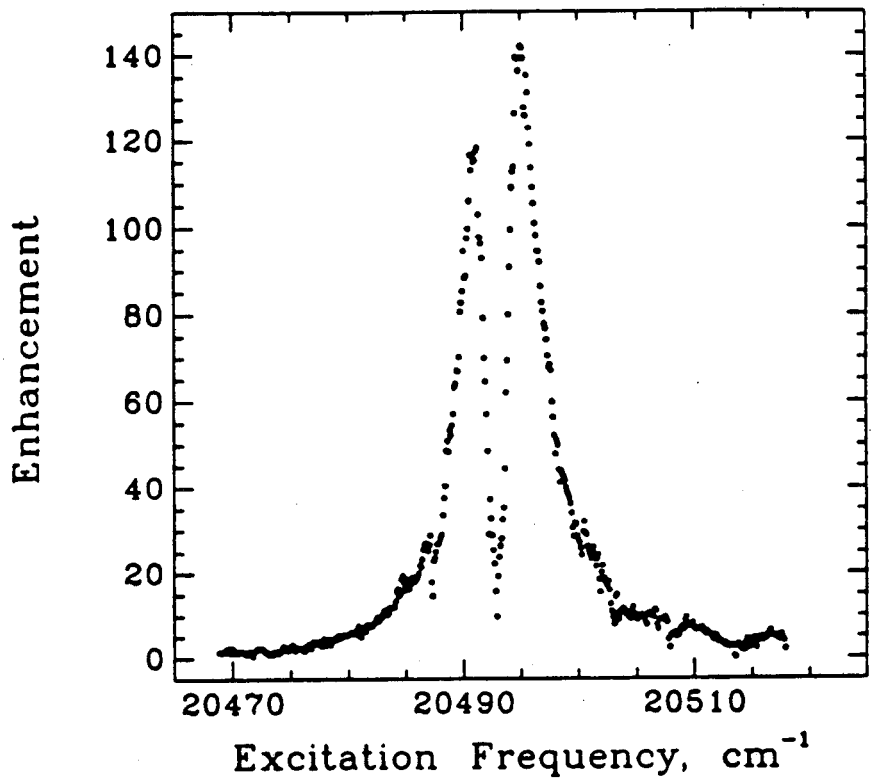

Figure 4.22: Enhancement of $\hat{X}\hat{Z}$ electronic Raman scattering to the 53 cm^{-1} level as a function of excitation frequency. Profile has not been corrected for absorption losses of the pump beam.

resonance. This asymmetry can not be explained by any corresponding asymmetry in the inhomogeneous profiles of any of the transitions associated with the Raman process. As will be seen in Section 4.6 it will be explained by an interference between non-resonant and resonant virtual intermediate state channels in the Raman process.

Figure 4.22 shows the excitation profile for $\hat{X}\hat{Z}$ scattering from the ground state to the state at 53 cm^{-1}. The profile has the same general shape as the 33 cm^{-1} profile with the interesting difference that the anti-symmetric part has a reversed sign. The enhancement is also larger for the 53 cm^{-1} scattering having a peak value of 141 at Δ2.1 cm^{-1} from the center of the resonance.

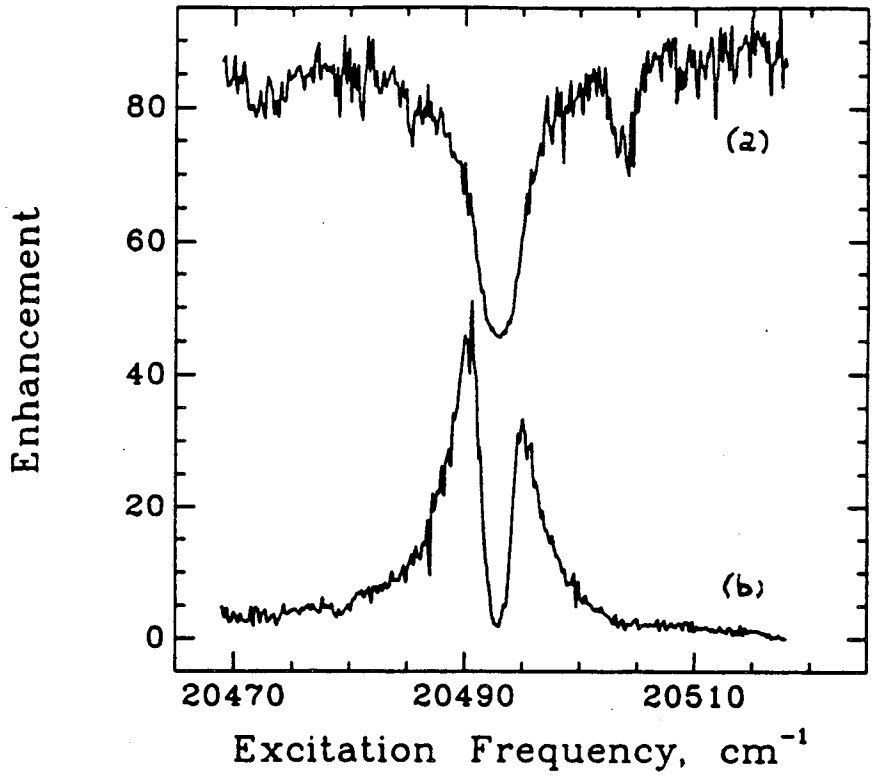

Figure 4.23: *Raw* excitation profiles for the (a) $\hat{\mathbf{X}}\hat{\mathbf{Z}}$ Raman scattering to the 303 cm^{-1} phonon and (b) $\hat{\mathbf{X}}\hat{\mathbf{Z}}$ electronic Raman scattering to the 33 cm^{-1} level.

4.5.3 The Normalized Profiles

To facilitate comparison with the computational models presented in the next section we would like to correct the *raw* excitation profiles for the absorption losses of the incident laser beam. In this section we present the absorption loss corrected excitation profiles. The simplest and most direct way of doing this is to divide the *raw* profiles of the previous section by the excitation profile of the 303 cm^{-1} phonon (Figure 4.20).

Figure 4.23 shows the raw excitation profile for 33 cm^{-1} level and the excitation profile for the 303 cm^{-1} phonon. Figure 4.24 shows the absorption loss corrected excitation profile for the 33 cm^{-1} level.

The points near direct resonance are not included because of the high uncertainty in their values resulting from the nearly complete zeroing of the 303 cm^{-1} phonon scattering in this region. Also shown in Figure 4.24 are absorption corrected enhancement values (circles) obtained from complete Raman spectra taken using a few selected excitation frequencies. In each case the area under the 33 cm^{-1} electronic Raman scattering

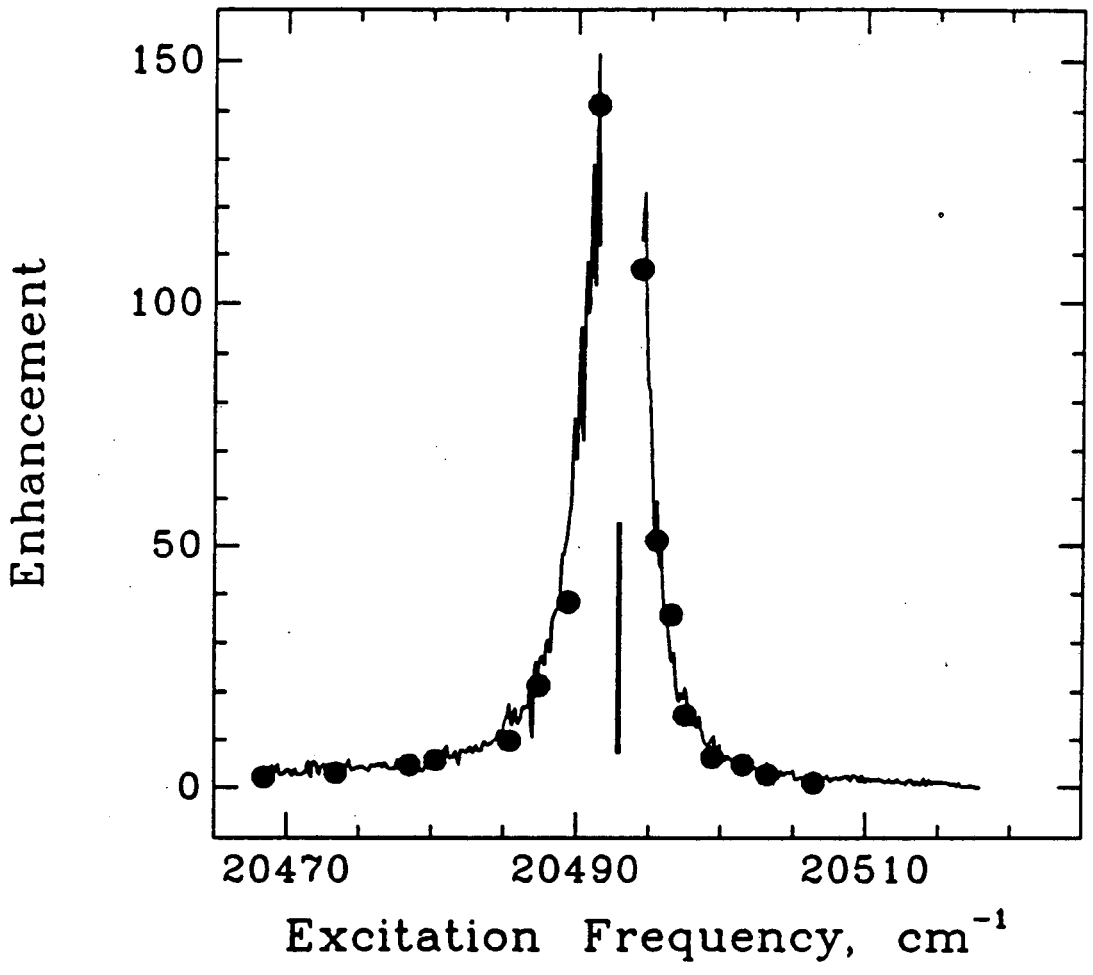

Figure 4.24: Absorption loss corrected excitation spectrum for the $\hat{X}\hat{Z}$ electronic Raman scattering to the 33 cm^{-1} level. See text for more details.

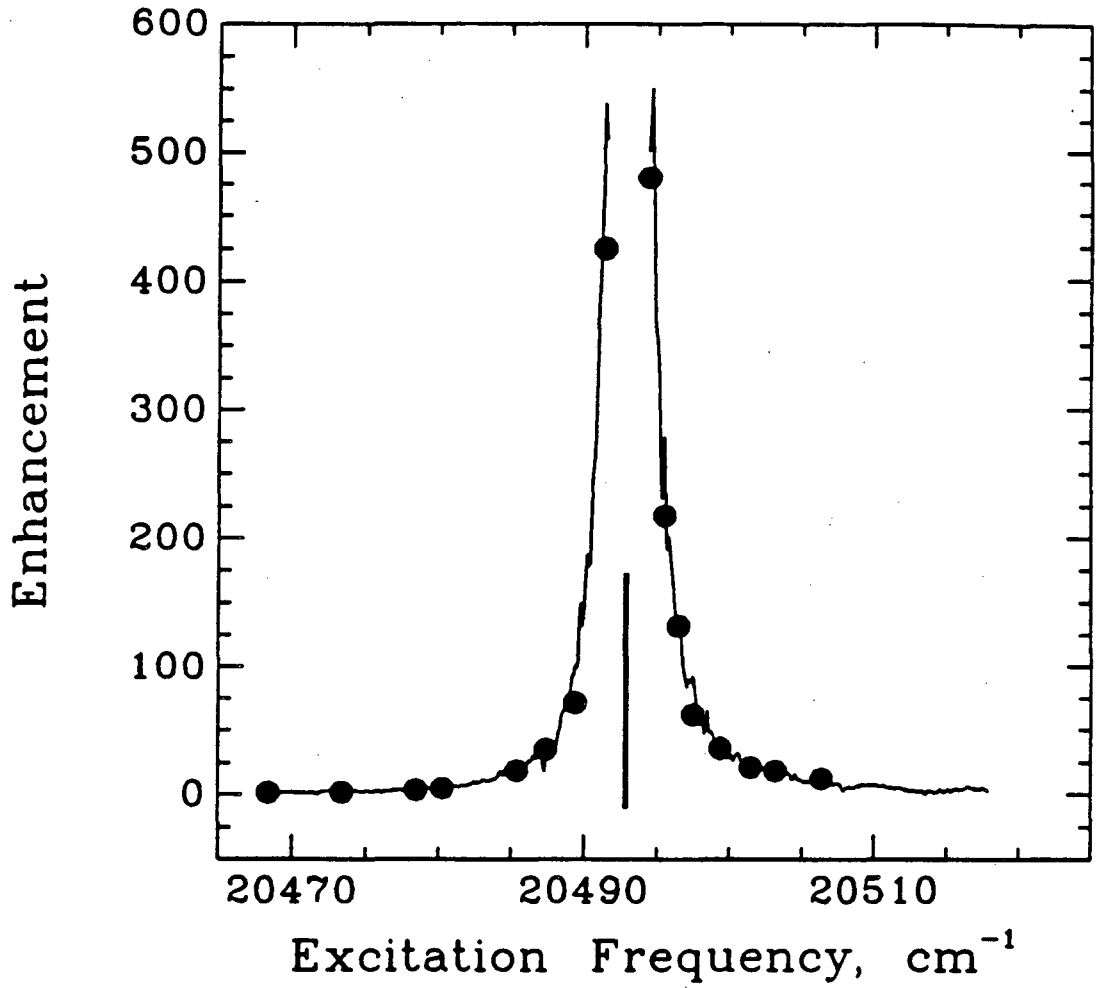

Figure 4.25: Absorption loss corrected excitation spectrum for the $\hat{X}\hat{Z}$ electronic Raman scattering to the 53 cm^{-1} level. See text for more details.

peak was normalized by the area under the 303 cm^{-1} phonon Raman peak. As can be seen there is good agreement with the values obtained by scanning the dye laser and spectrometer in synchronization.

Shown in Figure 4.25 is an identically prepared absorption loss corrected excitation profile for $\hat{X}\hat{Z}$ scattering to the 53 cm^{-1} level. Again, the circles in the plot are data points taken from integrating peaks in the complete spectra.

At this point a comparison can be made with Becker's [11] reported absorption loss corrected enhancements in $ErPO_4$. For excitation, Becker had only the discrete lines of an argon ion laser available. With an argon ion laser he would be able to obtain only one near resonant excitation frequency at 20,486.7 cm^{-1} = Δ6.2 cm^{-1}. However, Becker was able to obtain additional points by the ingenious trick of tuning the energy

Experiment	Excitation Shift, cm^{-1}	$\Delta 33 cm^{-1}$	$\Delta 53 cm^{-1}$
Becker, $ErPO_4$ Ar^+ laser	−6.2	18.1	29.1
Williams, $ErPO_4$ Dye laser	−6.2	18.5 ± 5	28.3 ± 5
Becker, $Er_{.10}Lu_{.90}PO_4$ Ar^+ laser	3.0	172	501
Williams, $ErPO_4$ Dye laser	3.0	43.2 ± 10	192 ± 50

Table 4.8: Comparison of $\hat{X}\hat{Z}$ electronic Raman scattering enhancements. Errors are estimated from noise in the excitation profiles. See text for additional details.

levels of the crystal instead of tuning the exciting laser. Electronic Raman scattering experiments were performed on crystals of $LuPO_4$ containing various doping levels of Er^{+3}. As the concentration of Er^{3+} in the crystal is varied the crystal field changes ever so slightly moving the resonant transition closer or farther from the laser excitation. Of course other parameters relevant to the scattering such as line width (homogeneous and inhomogeneous) could also vary with the doping level. However, for simplicity we will ignore these difficulties. The most accurate data is for $Er_xLu_{1-x}PO_4$, $x = 1.0$ and $x = 0.10$. For $x = 1.0$ the argon blue line is 6.2 cm^{-1} below the center of the resonance. For $x = 0.10$ the argon blue line is 3.0 cm^{-1} above the center of the resonance. Table 4.8 shows Becker's reported enhancements for these two shifts compared to those in the pulsed dye laser experiments in $ErPO_4$.

The agreement between the two sets of experiments is remarkably good for excitation at $\Delta 6.2$ cm^{-1} (both experiments done in $ErPO_4$). However, for excitation at $\Delta 3.0$ cm^{-1} the enhancement values observed in this work are considerably smaller than those observed by Becker. These differences most probably arise from the differences between $ErPO_4$ and $Er_{.10}Lu_{.90}PO_4$ alluded to previously.

Up to this point the enhancement data presented have been for excitation frequencies within ± 25 cm^{-1} from the resonance, in the region in which strong enhancements are observed. However, the enhancements observed at greater detunings, even though harder to measure because of their small size, will serve as an important test of the models of

resonant enhancement to be presented in the following section. They are particularly important in that they test the models in the *non-resonant* excitation region, yielding new insight into the intensity contributions of $4f^N$ virtual intermediate states in non-resonant electronic Raman scattering. Figure 4.26 shows the $\Delta 33$ cm^{-1} and $\Delta 53$ cm^{-1} Raman enhancement profiles (enhancements are relative to scattering excited by the argon ion 514.5 nm line) for excitation frequencies in the range 30-100 cm^{-1} removed from resonance on the low energy side. Data for excitation on the high energy side of the resonance are complicated by the numerous absorptions in this region and are not presented. The plot is somewhat surprising in that the electronic Raman intensities appear to be affected by the resonance even at excitation frequencies removed by nearly 100 cm^{-1}. The $\Delta 33$ cm^{-1} intensity is nearly 1.5 times its non-resonant value while the $\Delta 53$ cm^{-1} intensity is approximately one half its non-resonant value.

4.6 Modelling the Excitation Profiles

In this section we present a model which accurately describes the shapes and magnitudes of the resonance electronic Raman excitation profiles given in the previous Sections. The model helps one understand, in general, what conditions are important for generating large intermediate state resonances in multi-photon processes in rare earth crystals. The results of the modelling also raise some questions as to what extent $4f^N$ virtual intermediate states might contribute to the "non-resonant" intensities of multi-photon processes in these systems.

4.6.1 General Theory of Resonance Raman Scattering

The standard theory describing the intensities of the electronic Raman scattering process has been described in Chapter 3. The second-order term in the perturbative expansion of the electric dipole operator yields the well-known Kramer-Heisenberg [126,127] result for the intensity of Raman scattering between a state $|i\rangle$ and a state $|f\rangle$.

$$(I_s)_{\rho\sigma} \propto \left| \sum_j \left(\frac{\langle f|D_\rho|j\rangle\langle j|D_\sigma|i\rangle}{\omega_j - \omega} + \frac{[D_\rho \leftrightarrow D_\sigma]}{\omega_j + \omega_s} \right) \right|^2 \qquad (4.15)$$

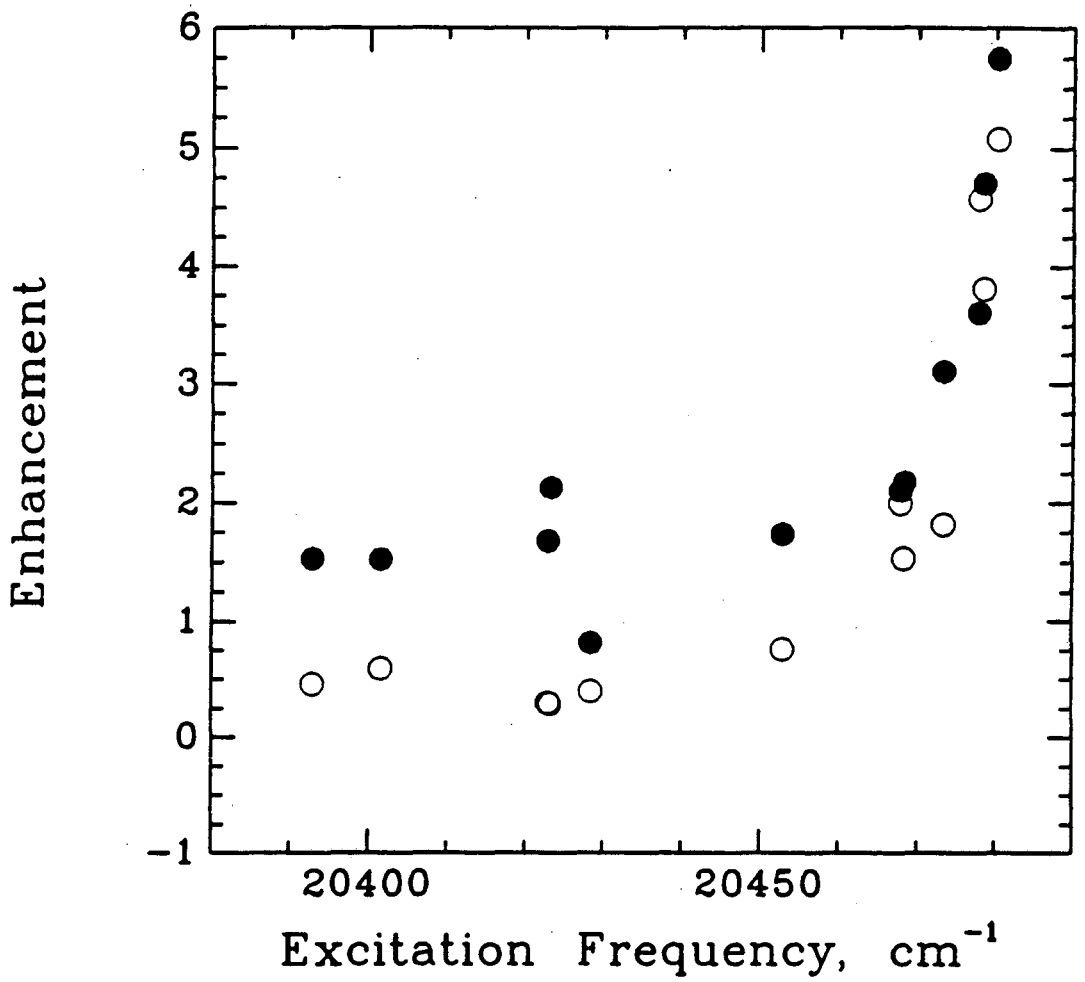

Figure 4.26: Excitation spectra for the $\Delta 33$ and $\Delta 53$ $\hat{X}\hat{Z}$ Raman scattering Closed circles are for the $\Delta 33$ cm^{-1} scattering. Open circles are for the $\Delta 53$ cm^{-1} scattering.

where the sum over j is a sum over virtual intermediate states, ω is the angular frequency of the laser radiation , ω_s is the angular frequency of the scattered light, and ω_j is the angular frequency associated with the energy difference, $E_j - E_i$.

For describing resonance conditions (ω equal to some ω_j) this expression has the obvious failing that the scattering intensity becomes infinite. Somehow the fact that the resonances are not infinite Q systems must be included in the expression. This is accomplished in a somewhat *ad hoc* manner simply by adding a phenomenological damping parameter. For the laser (ω) in near resonance with a single state $|r\rangle$ (ω_r) we write

$$(I_s)_{\rho\sigma} \propto \left| \sum_{j \neq r} \left(\frac{\langle f|D_\rho|j\rangle\langle j|D_\sigma|i\rangle}{\omega_j - \omega} + \frac{[D_\rho \leftrightarrow D_\sigma]}{\omega_j + \omega_s} \right) + \frac{\langle f|D_\rho|r\rangle\langle r|D_\sigma|i\rangle}{\omega_r - \omega + i\Gamma} \right|^2 \tag{4.16}$$

where Γ is the phenomenological damping parameter. We do not label Γ with the subscript r, as commonly done, for the following reasons.

A more exact treatment of the damping problem requires the use of the density matrix formalism. This treatment, unlike the Kramer-Heisenberg expression, includes in the description of the Raman process all the ions of the solid and statistical properties of this ensemble. Shen [105] first carried out the density matrix calculation for Raman scattering and Lee and Albrecht [119] have recently written an excellent review of subsequent work along these lines. The results of the calculation are somewhat complicated. However, it can be shown that the complicated results simplifies to the Kramer-Heisenberg expression (Equation 4.16 above) for the case in which the damping is solely the result of the finite lifetime (lifetime obtained by measuring the temporal decay of fluorescence) of the resonant state. Thus, the common labelling, Γ_r, for the dephasing parameter, since it's value is inversely proportional to the lifetime of the state $|r\rangle$. However, we have seen that in the damping associated with a Raman process a more important mechanism is the dephasing of excitation amongst the ensemble of ions. This so-called "pure dephasing" (not associated with population lifetime) can not be precisely described by the Kramer-Heisenberg result. However, for simplicity the Kramer-Heisenberg expression will be the starting point for our calculation.

4.6.2 Modelling of Resonance Electronic Raman Scattering in Rare Earth Crystals

Equation 4.16 includes two amplitudes; the amplitude associated with the non-resonant channels (the sum over states $|j\rangle$) and the amplitude associated with the resonant channel (state $|r\rangle$). Many times in modelling resonant enhancements the effects of the non-resonant amplitude may be ignored since it is negligibly small compared to the resonant amplitude. However, this is not the case here. The non-resonant channels (parity allowed) are of comparable size to the resonant channel (parity disallowed). Thus, to accurately model the excitation profiles both amplitudes must be included.

Because the states contributing to the non-resonant amplitude (states from opposite parity configurations) are at high enough energies relative to the laser frequency (and its variations during the experiments) such that variations in the energy denominator $1/(\omega_j - \omega)$ are small, the non-resonant amplitude may be considered independent of ω. The ω dependence appears only in the resonant amplitude (or amplitudes if there were more than one resonant channel). In this case we believe there is only one significantly contributing resonant state. The next nearest allowed resonant state is approximately 55 cm^{-1} higher (at 20,556 cm^{-1}) and should not contribute significantly in the tuning range of interest. Note that all states are Kramer doublets. However, it can be shown that this does not affect the analysis.

Let us define the following quantities,

$$A \equiv \sum_{j \neq r} \left(\frac{\langle f|D_\rho|j\rangle\langle j|D_\sigma|i\rangle}{\omega_j - \omega} + \frac{[D_\rho \leftrightarrow D_\sigma]}{\omega_j + \omega_s} \right) \tag{4.17}$$

$$B \equiv \langle f|D_\rho|r\rangle\langle r|D_\sigma|i\rangle \tag{4.18}$$

$$\Delta\omega \equiv \omega_r - \omega \tag{4.19}$$

Expanding Equation 4.16 we have,

$$\begin{aligned} I_s \propto\ & |A|^2 + \frac{|B|^2}{(\Delta\omega)^2 + \Gamma^2} + \frac{2(Re(B)Im(A) - Re(A)Im(B))\Gamma}{(\Delta\omega)^2 + \Gamma^2} \\ & + \frac{2(Re(A)Re(B) + Im(A)Im(B))\Delta\omega}{(\Delta\omega)^2 + \Gamma^2} \end{aligned} \tag{4.20}$$

where we have assumed for generality that A and B are complex, and $Re(A)$ refers to the real part of A and $Im(A)$ refers to the imaginary part of A.

The overall phase of the amplitudes in Equation 4.20 has no physical significance. Thus, we may pick this phase such that A is a real number. However, with such a choice B, in general , will remain complex and we write,

$$B \equiv Be^{i\delta} \tag{4.21}$$

Substituting into Equation 4.20 yields,

$$I_s \propto A^2 + \frac{B^2}{(\Delta\omega)^2 + \Gamma^2} + \frac{-2AB\sin\delta\Gamma}{(\Delta\omega)^2 + \Gamma^2} + \frac{2AB\cos\delta\Delta\omega}{(\Delta\omega)^2 + \Gamma^2} \tag{4.22}$$

The excitation profiles in Section 4.5.3 are presented in terms of the enhancement of the Raman scattering intensities relative to their respective non-resonant values. The enhancement E is given by,

$$E = \frac{I_s(\omega)}{I_s^{non-resonant}} \tag{4.23}$$

where $I_s(\omega)$ is given by Equation 4.22 and $I_s^{non-resonant}$ is proportional to A^2. Defining,

$$\eta \equiv \frac{B}{A} \tag{4.24}$$

we have for E,

$$E(\Delta\omega) = 1 + \frac{\eta^2}{(\Delta\omega)^2 + \Gamma^2} + \frac{-2\eta\sin\delta\Gamma}{(\Delta\omega)^2 + \Gamma^2} + \frac{2\eta\cos\delta\Delta\omega}{(\Delta\omega)^2 + \Gamma^2} \tag{4.25}$$

4.6.3 The Inhomogeneous Line Width

Equation 4.11 is derived for resonance between states with a single well defined energy difference. For rare earth ions in solids the energy of any given transition is known to vary slightly from ion to ion resulting in the inhomogeneous broadening discussed in Section 4.2.3. This variation results in a variation amongst the rare earth ions in $\Delta\omega$ for any given laser frequency ω. To account for this, Equation 4.25 for E is summed over the distribution of possible resonant energies in the crystal. We assume a Gaussian distribution (the absorption line shapes of Section 4.2.3 indicate this is an appropriate choice) of the form,

$$S(\Delta\omega') = \frac{1}{\sqrt{2\pi}\Delta} e^{-\left(4\ln 2\frac{(\Delta\omega')^2}{\Delta^2}\right)} \tag{4.26}$$

where Δ is the full width of the Gaussian at half of its maximum value, and $\Delta\omega'$ is the detuning from the mean frequency of the Gaussian. E is summed over the inhomogeneous profile by taking the integral,

$$E(\Delta\omega) = \int_{-\infty}^{\infty} E(\Delta\omega - \Delta\omega')S(\Delta\omega')d(\Delta\omega') \tag{4.27}$$

This integration is performed numerically.

4.6.4 Features of the Model and Fitting the Data

An enhancement profile may now be calculated using Equations 4.25, 4.26 and 4.27 once the quantities Δ, Γ, η, and δ are specified.

The inhomogeneous line-width Δ is estimated from the absorption line-widths reported in Section 4.2.3. The observed line-width for the resonance transition ($0 \rightarrow$ 20492.9 cm^{-1}) is estimated to be 2.0 cm^{-1} with most of the width attributed to inhomogeneous broadening. Thus, Δ is fixed at 2.0 cm^{-1}.

Limits may be set on the damping parameter Γ for both the 33 cm^{-1} and 53 cm^{-1} Raman processes. For each case the damping parameter is related to the homogeneous widths associated with the three pairs of states involved in the resonance Raman process. Because all the line-widths, $0 \rightarrow$ 20492.9 cm^{-1}, 33 or 53 $\rightarrow$ 20492.9 cm^{-1} (line-widths determined from absorption measurements) and $0 \rightarrow$ 33 or 53 cm^{-1} (line-widths determined form non-resonant electronic Raman spectra[11]) are on the order of 2.0 cm^{-1} or less, we may set this value as a rough upper limit on the value of Γ for both the 33 cm^{-1} and 53 cm^{-1} Raman processes. It is actually more likely that the damping parameters are considerably smaller than this upper limit. The observed line shapes are considerably more Gaussian (inhomogeneous broadening) than Lorentzian (homogeneous broadening). However, the smallness of Γ in our model is limited by the line-width of the exciting laser line which is somewhere on the order of 0.25-0.5 cm^{-1}. Thus, we may set a lower limit on Γ of approximately .25 cm^{-1} for both the 33 and 53 cm^{-1} scattering. For the Raman transitions Γ is confined to be between 0.25 and 2.0 cm^{-1}. As far as determining the actual value of Γ in this range, from Equation 4.25 it can be seen that the results of our modelling will be fairly insensitive (with the stipulation $\eta \gg \Gamma$) to the value of Γ so long as $\Delta\omega \gg \Gamma$. In other words the value of Γ only becomes

important when the laser is tuned into direct resonance. In this region the pump laser is strongly absorbed and the excitation profile data becomes very uncertain (as we have seen in Section 4.5.3). A comparison between the data and our model in this region is of questionable validity.

The values of η (the relative strength of the resonance) and δ (the phase difference between the non-resonant and resonant amplitudes) are determined by fitting the model to the experimental data. This fitting is facilitated by noting a few characteristics of the model.

For values of $\Delta\omega$ larger than the inhomogeneous width associated with the resonant transition the enhancement profile is accurately modelled by Equation 4.25 with no need for the integration described in Equation 4.27. Equation 4.25 can be divided into three terms. The value unity is the part of the enhancement contributed by the non-resonant intensity. The term,

$$\frac{\eta^2}{(\Delta\omega)^2 + \Gamma^2} \tag{4.28}$$

is the part of the enhancement contributed by the resonant intensity. The term,

$$\frac{-2\eta \sin\delta\Gamma}{(\Delta\omega)^2 + \Gamma^2} + \frac{2\eta \cos\delta\Delta\omega}{(\Delta\omega)^2 + \Gamma^2} \tag{4.29}$$

is the part of the enhancement resulting from the interference (or heterodyning) of the non-resonant and resonant amplitudes. It is this interference that results in the asymmetric shape of the excitation enhancement profiles. The term proportional to $\Delta\omega$ changes sign as the laser is tuned through the resonance. One can think of the 180° phase change of a driven harmonic oscillator as the driving frequency is tuned through resonance. On one side of the resonance the resonant amplitude interferes constructively with the non-resonant amplitude while on the other side they interfere destructively. Such an effect was first observed by Bjorkholm and Liao [128] in intermediate state resonantly enhanced two photon absorption in Na gas. Subsequently, interference effects have been observed in resonance vibrational Raman scattering by a number of researchers including Friedmann and Hochstrasser [129], Stein *et al.* [130], Rebane and Khaav [131], and Hirlimann *et al.* [132].

The question is how do we exploit these features to help us fit η and δ ?

- $E(\Delta\omega)$ may be divided into two parts; a totally symmetric part ($E_s(\Delta\omega) = E_s(-\Delta\omega)$) and a totally anti-symmetric part ($E_a(\Delta\omega) = -E_a(\Delta\omega)$). The ratio $E_a/(E_s - 1)$ with the assumption $\eta \gg \Gamma$ (a valid assumption for this case) yields

$$\frac{E_a}{E_s - 1} = \frac{2\cos\delta}{\eta}\Delta\omega \tag{4.30}$$

  a straight line in $\Delta\omega$ with a slope of $2\cos\delta/\eta$. Thus, the quantity $2\cos\delta/\eta$ can be easily determined from the values of $E_a/(E_s - 1)$ generated from the data.

- $E(\Delta\omega)$ has a local minimum (due to the destructive interference) at $\Delta\omega = -(\eta/\cos\delta)$ (again with the condition $\eta \gg \Gamma$). The value of this minimum is $1 - \cos^2\delta$. Thus, we have a second way of determining the value of $\eta/\cos\delta$. However, what is needed is a way of determining independently η or δ. The value of $\cos\delta$ can be determined independently by measuring the depression in the Raman signal at the local minimum. However, this turns out to be a difficult measurement, and we will start our fitting procedure by making some educated guesses regarding the values of δ based on the underlying physics.

4.6.5 Fit of the Enhancement Profiles, $\delta = 0$ or π

We are interested in knowing the relative phase between the non-resonant amplitude,

$$\sum_j \left(\frac{\langle f|D_\rho|j\rangle\langle j|D_\sigma|i\rangle}{\omega_j - \omega} + \frac{[D_\rho \leftrightarrow D_\sigma]}{\omega_j + \omega_s} \right) \tag{4.31}$$

and the matrix elements associated with the resonant amplitude,

$$\langle f|D_\rho|r\rangle\langle r|D_\sigma|i\rangle \tag{4.32}$$

Expansion of one of the matrix elements of Equation 4.32 in the Judd-Ofelt manner helps to elucidate the similarities between Equation 4.31 and 4.32.

$$\langle f|D_\rho|r\rangle = \sum_j \left(\frac{\langle f|D_\rho|j\rangle\langle j|H_{cf}|r\rangle}{\omega_j - \omega_r} + \frac{[D_\rho \leftrightarrow H_{cf}]}{\omega_j - \omega_f} \right) \tag{4.33}$$

where H_{cf} represents the odd parity components of the crystal field, and the sum is over the states of opposite parity configurations just as in Equation 4.31. The similarity between Expressions 4.31 and 4.32 is self-evident. The only source from which phase

differences between expressions 4.31 and 4.32 could be derivable are the components of the crystal field Hamiltonian. A complex crystal field could result in a phase difference between expressions 4.31 and 4.32. However, the crystal field components for the symmetry D_{2d} are known to be either purely real or purely imaginary [133]. Such components can only result in phase differences of 0 radians (0°) or π radians (180°). So as a starting point in our analysis we restrict δ to be 0 or π.

Figure 4.27 shows the observed enhancement profile ($E(\Delta\omega)$) for the Raman scattering to the 33 cm^{-1} level along with the totally symmetric part ($E_s(\Delta\omega)$) and the totally anti-symmetric part ($E_a(\Delta\omega)$) of the profile. Figure 4.28 shows the ratio $E_a/(E_s - 1)$ for the $\Delta 33$ cm^{-1} scattering and the best linear fit to this ratio. From the linear fit (and using Equation 4.30) a value of $\eta/\cos\delta = 44$ is obtained. Based on the observation that the non-resonant and resonant amplitudes interfere constructively for $\Delta\omega > 0$, $\delta = 0$ radians (instead of π radians) is selected for the phase difference, implying $\eta = 44$.

Figure 4.29 shows the enhancement data $E(\Delta\omega)$ for the 33 cm^{-1} scattering along with a model profile calculated using $\eta = 44$, $\delta = 0$, $\Delta = 2.0$ cm^{-1}, and $\Gamma = 0.4$ cm^{-1}. As can be seen the fit is very poor with the value $\eta = 44$ greatly exaggerating the magnitude of the resonance.

Through trial and error a much more suitable value of η is found. Figure 4.30 shows a fit with $\eta = 22$, $\delta = 0$, $\Delta = 2.0$ cm^{-1}, and $\delta = 0.4$ cm^{-1}. The fit models the overall magnitude and shape of the resonance profile quite satisfactorily. The only failings of the model can be seen under closer examinations of the wings of the profile. Shown in Figure 4.31 is an enlarged view of Figure 4.30 showing in greater detail the enhancement profile wings. The asymmetry of the model profile is noticeably greater than the asymmetry exhibited in the data. Figure 4.32 shows the model profile ($\eta = 22$, $\delta = 0$, $\Delta = 2.0$ cm^{-1}, and $\Gamma = 0.4$ cm^{-1}) and measured enhancements in the region $\Delta 20 - \Delta 100$ cm^{-1}. There is agreement in the region around $\Delta 100$ cm^{-1}, however, in the region $\Delta 20 - \Delta 60$ cm^{-1} the model generally overestimates the enhancements.

Similar analyses can be performed for the $\Delta 53$ cm^{-1} scattering. Figure 4.33 shows the observed enhancement profile ($E(\Delta\omega)$) for the Raman scattering to the 53 cm^{-1} level along with the totally symmetric part ($E_s(\Delta\omega)$) and the totally anti-symmetric

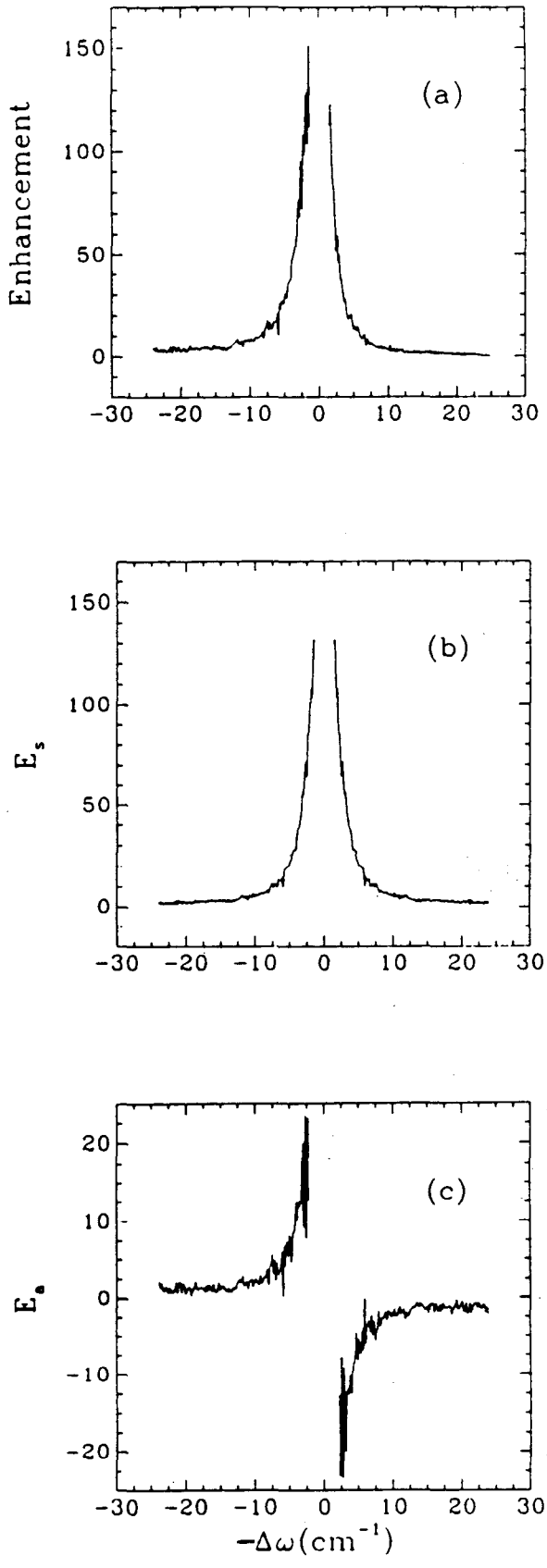

Figure 4.27: (a) Measured enhancements of $\hat{\mathbf{X}}\hat{\mathbf{Z}}$ electronic Raman scattering to the 33 cm^{-1} level. $\Delta\omega$ is measured for the resonance at 20492.9 cm^{-1}. (b) Symmetric part of (a). (c) Anti-symmetric part of (a).

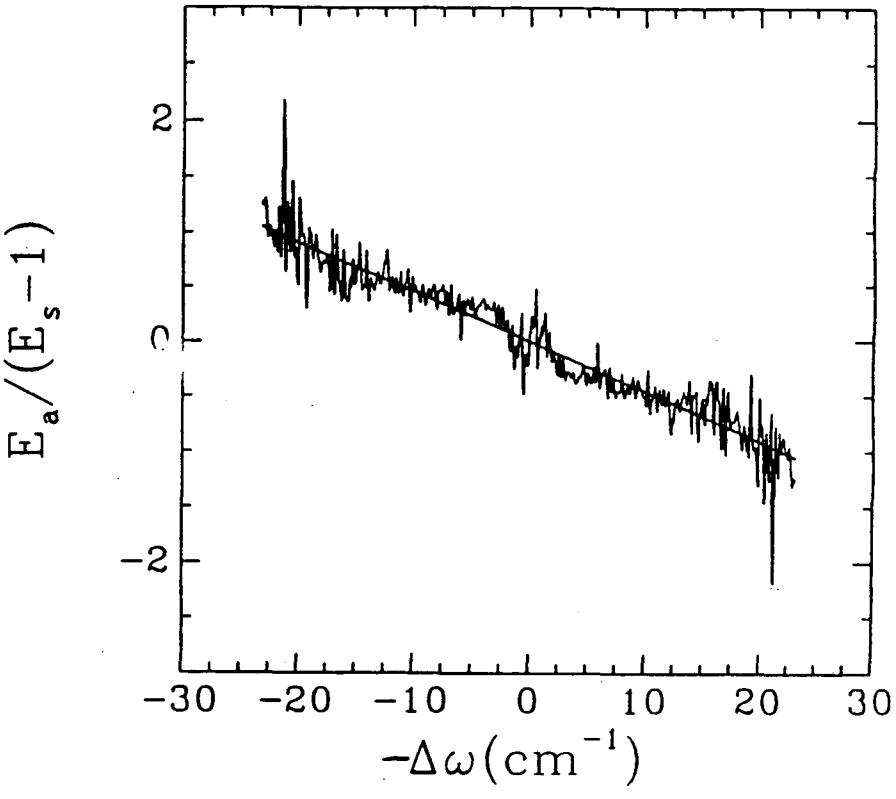

Figure 4.28: Measured ratio $E_a/(E_s-1)$ for $\hat{\mathbf{X}}\hat{\mathbf{Z}}$ scattering to the 33 cm^{-1} level. Straight line is the best linear fit to the ratio.

part ($E_a(\Delta\omega)$) of the profile. Figure 4.34 shows the ratio $E_a/(E_s-1)$ for the $\Delta 53$ cm^{-1} scattering and the best linear fit to this ratio. From the linear fit (and using Equation 4.16) a value of $\eta/\cos\delta = 71$ is obtained. Based on the observation that the non-resonant and resonant amplitudes interfere constructively for $\Delta\omega > 0$, $\delta = \pi$ radians is selected for the phase difference, implying $\eta = 71$.

Figure 4.35 shows the enhancement data $E(\Delta\omega)$ for the 53 cm^{-1} scattering along with a model profile calculated using $\eta = 71$, $\delta = 0$, $\Delta = 2.0$ cm^{-1}, and $\Gamma = 0.4$ cm^{-1}. As can be seen the fit is very poor with the value $\eta = 71$ greatly exaggerating the magnitude of the resonance.

As with the fitting of the 33 cm−1 enhancement profile we find that a smaller value of η fits the data much more accurately. Figure 4.36 shows a fit with $\eta = 35.5$, $\delta = 0$, $\Delta = 2.0$ cm^{-1}, and $\delta = 0.4$ cm^{-1}. The fit is very good. However, close examination of the wings of the profile (Figure 4.37) shows the degree of asymmetry is overestimated by the model. Figure 4.38 shows the model profile and the measured enhancements in

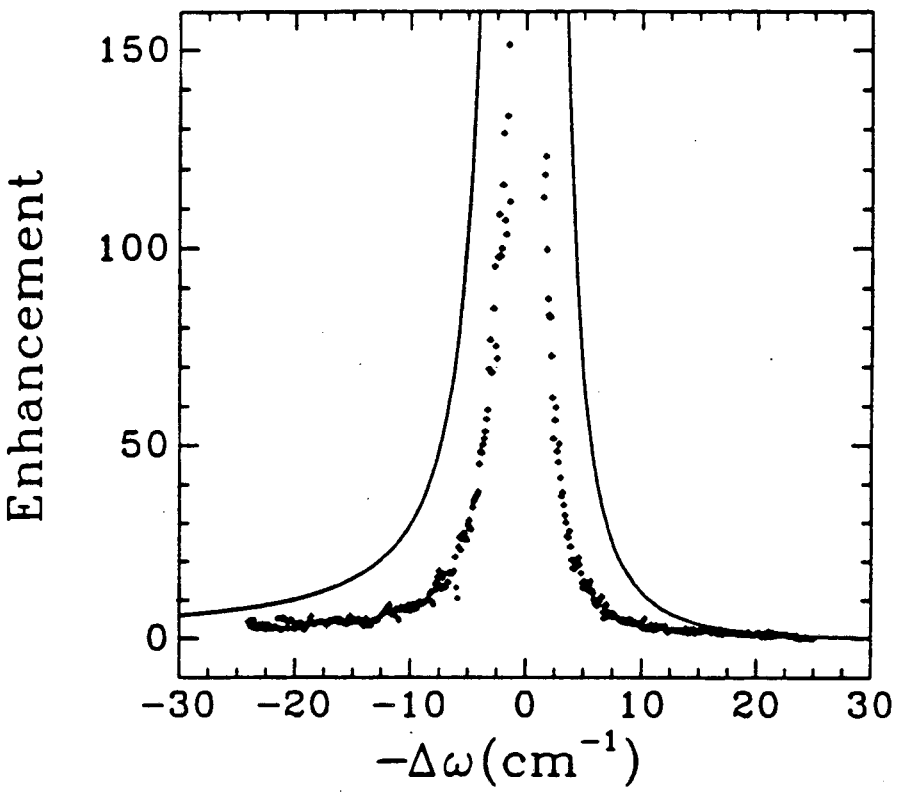

Figure 4.29: Measured enhancement profile (symbols) for the $\hat{\mathbf{X}}\hat{\mathbf{Z}}$ $\Delta 33$ cm^{-1} Raman scattering. Modelled profile using $\eta = 44$, $\delta = 0$, $\Delta = 2.0$ cm^{-1}, and $\Gamma = 0.4$ cm^{-1}.

the region $\Delta 20 - \Delta 100$ cm^{-1}. The model profile predicts complete nulling of the Raman signal at $\Delta\omega = 35.5$ cm^{-1} (complete destructive interference), a fact not borne out by the data.

4.6.6 Fit of the Enhancement Profiles, Arbitrary δ

Because of the inadequacies in the fits to the Raman enhancement profiles with modelled profiles confined to have $\delta = 0$ or π we fitted the enhancement profiles allowing δ to vary.

For the $\Delta 33$ cm^{-1} profile the value $\eta = 22$ predicts the overall magnitude of the enhancement fairly well. However, the degree of asymmetry in the profile (indexed by $E_a/(E_s - 1)$) points to a value $\eta/\cos\delta$ of 44. With $\eta = 22$ we are led to a value of $\delta = \pi/3$. For the $\Delta 53$ cm^{-1} line the overall magnitude of the enhancement is best fit by $\eta = 35.5$ with the asymmetry index ($E_a/(E_s - 1) = \eta/\cos\delta$) equivalent to -71 yielding a phase of $\delta = 2\pi/3$.

Figure 4.39 shows the fit for the $\Delta 33$ cm^{-1} scattering with $\eta = 20$, $\delta = \pi/3$, $\Delta =$

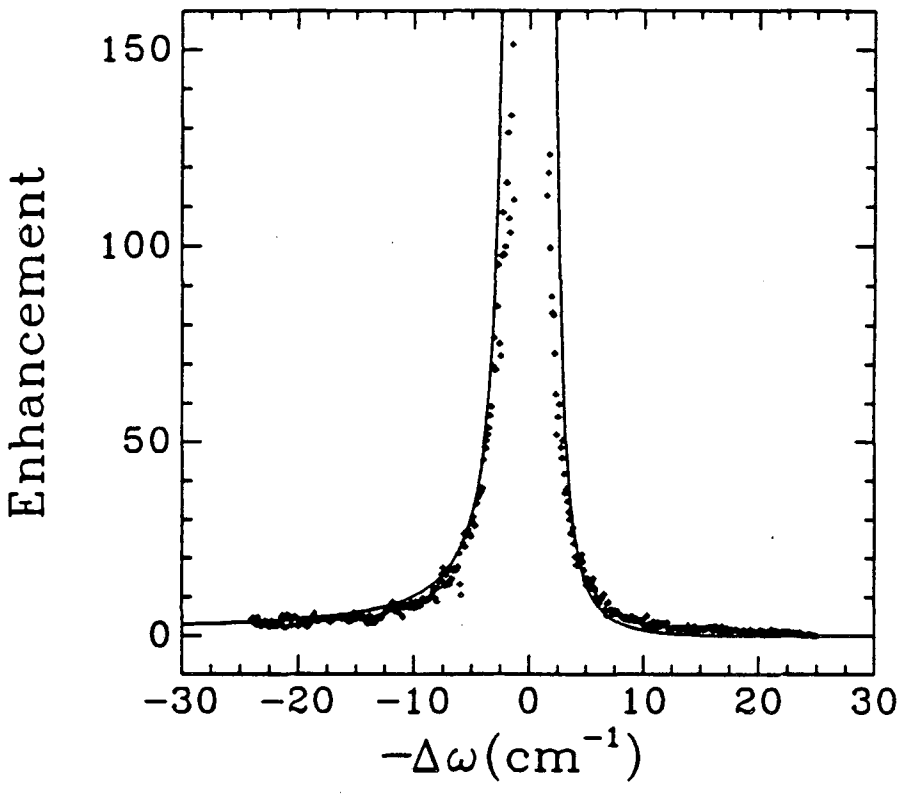

Figure 4.30: Measured enhancement profile (symbols) for the $\hat{\mathbf{X}}\hat{\mathbf{Z}}$ $\Delta 33$ cm^{-1} Raman scattering. Modelled profile using $\eta = 22$, $\delta = 0$, $\Delta = 2.0$ cm^{-1}, and $\Gamma = 0.4$ cm^{-1}.

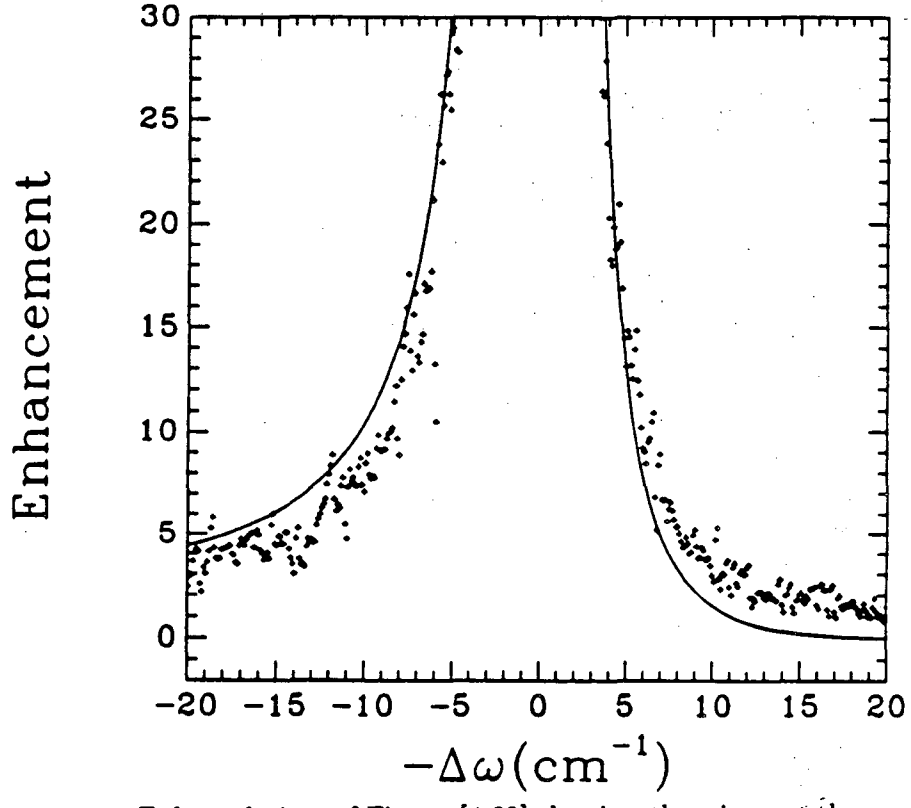

Figure 4.31: Enlarged view of Figure [4.30] showing the wings of the resonance.

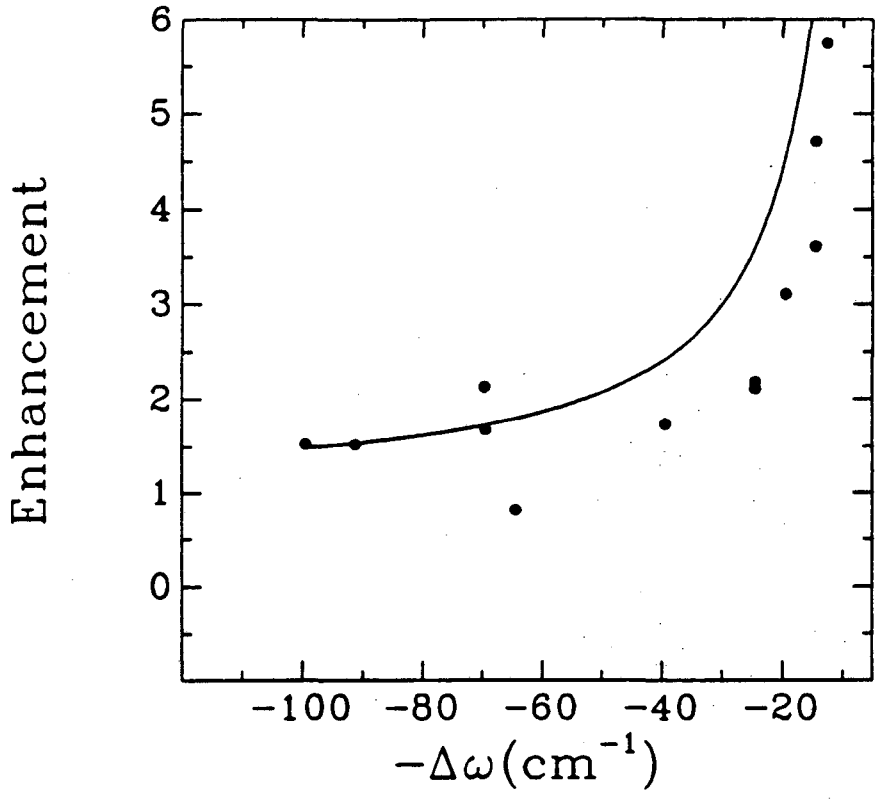

Figure 4.32: Enhancements of $\hat{\mathbf{X}}\hat{\mathbf{Z}}$ $\Delta 33\ \mathrm{cm}^{-1}$ Raman scattering in the region $\Delta 20$ – $\Delta 100\ \mathrm{cm}^{-1}$. Circles are measured values and the solid line gives the modelled results.

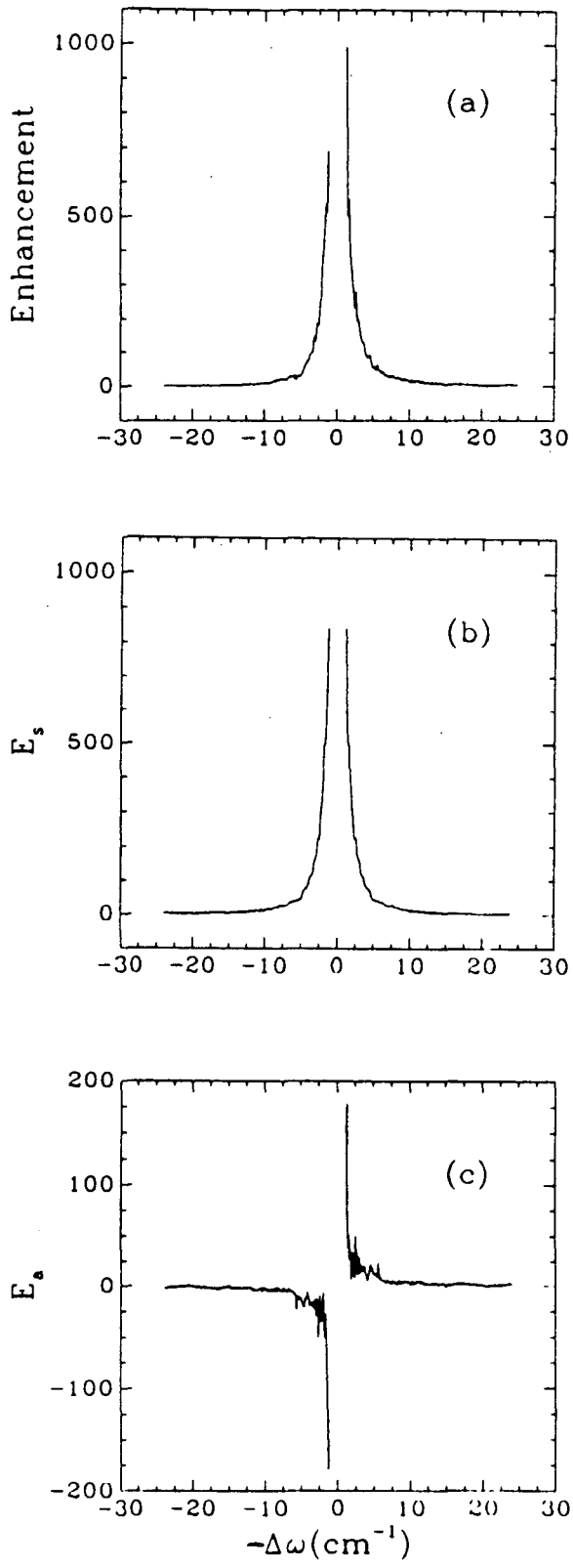

Figure 4.33: (a) Measured enhancements of $\hat{\mathbf{X}}\hat{\mathbf{Z}}$ electronic Raman scattering to the 53 cm^{-1} level. $\Delta\omega$ is measured for the resonance at 20492.9 cm^{-1}. (b) Symmetric part of (a). (c) Anti-symmetric part of (a).

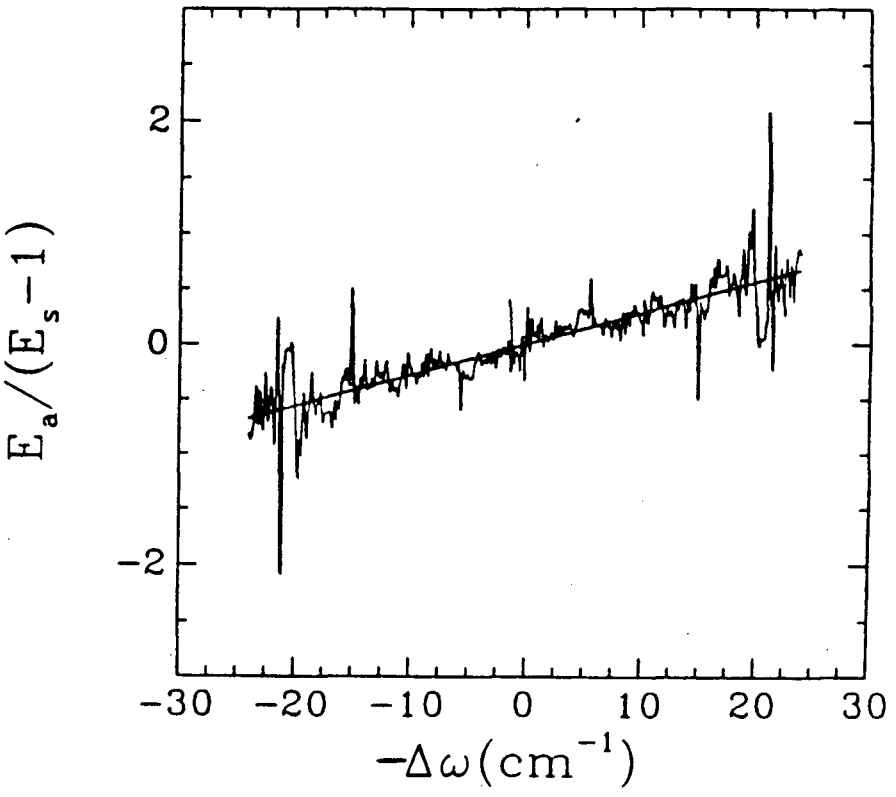

Figure 4.34: Measured ratio $E_a/(E_s-1)$ for $\hat{\mathbf{X}}\hat{\mathbf{Z}}$ scattering to the 53 cm^{-1} level. Straight line is the best linear fit to the ratio.

2., 0 cm^{-1}, and Γ = 0.4 cm^{-1}. Figure 4.40 shows the wings in detail and Figure 4.41 displays the region $\Delta 20 - \Delta 100$ cm^{-1}. Figures 4.42, 4.43, and 4.44 are the corresponding figures for the $\Delta 53$ cm^{-1} scattering with η = 35.5, $\delta = 2\pi/3$, Δ = 2.0 cm^{-1}, and Γ = 0.4cm^{-1}.

For both the $\Delta 33$ and $\Delta 53$ cm^{-1} scattering the fits with δ allowed to vary show noticeable improvement in the profile wings and in the region $\Delta 20 = \Delta 100$ cm^{-1} over the fits with δ confined to be either 0 or π. In the region $\pm\Delta 3$ cm^{-1} (near line center) the fixed phase fits seem to fit the data somewhat better than the arbitrary phase fits. However, this is not considered a serious failing of the arbitrary phase fits for the following reasons. In the line center region (a) we have low confidence in the data (because of the strong absorption of the pump laser beam) and (b) we expect the model to be inadequate. To elaborate on the second point we offer two problems that have not been considered to this point.

- Trapping of the Raman scattered radiation. When the pump laser is in resonance

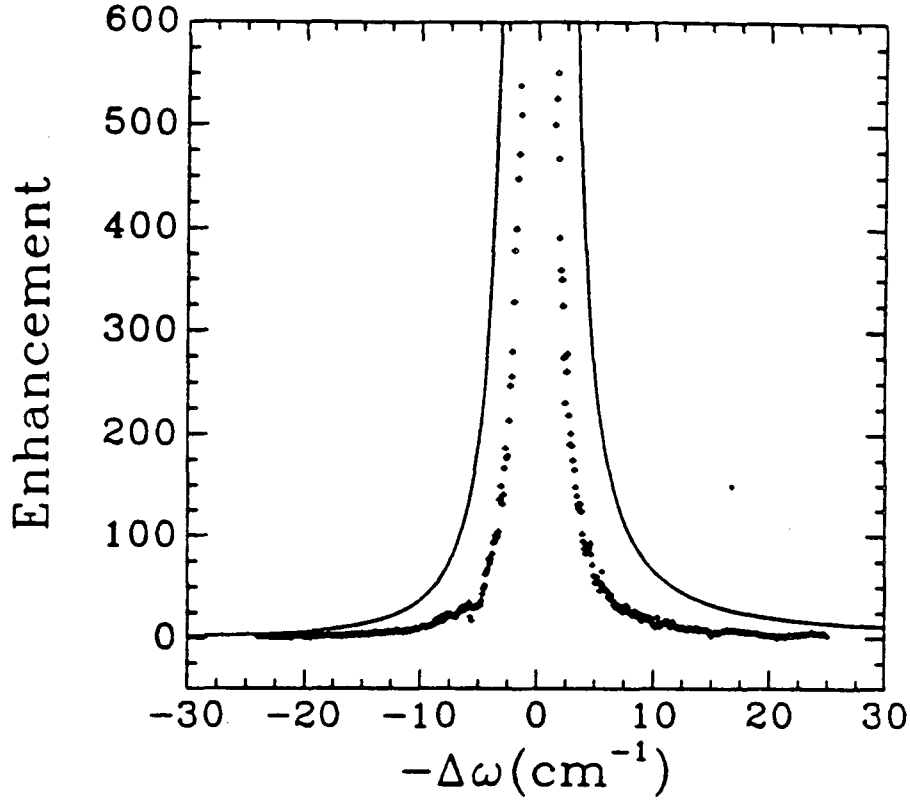

Figure 4.35: Measured enhancement profile (symbols) for the $\hat{X}\hat{Z}$ $\Delta 53$ cm^{-1} Raman scattering. Modelled profile using $\eta = 71$, $\delta = 0$, $\Delta = 2.0$ cm^{-1}, and $\Gamma = 0.4$ cm^{-1}.

the scattered Raman light is in resonance with an excited state absorption. If the excited state is sufficiently populated (a condition facilitated by the heating of the crystal by the pump laser), a significant portion of the Raman scattered light could be trapped.

- Temperature induced variation of the damping parameter Γ. Heating of the crystal by the resonant pump laser could lead to significant variation in the damping parameter Γ.

Given the improvements introduced by the introduction of the arbitrary phase in the model the question arises as to the physical explanation of this phase. Unfortunately, we can offer no explanation here. A broader question might be whether it is correct at all to interpret the results of the modelling in terms of a phase difference between the non-resonant and resonant amplitudes. In actuality all we have done by introduction of the arbitrary phase is allow the magnitudes of the resonant term (Equation 4.28) and

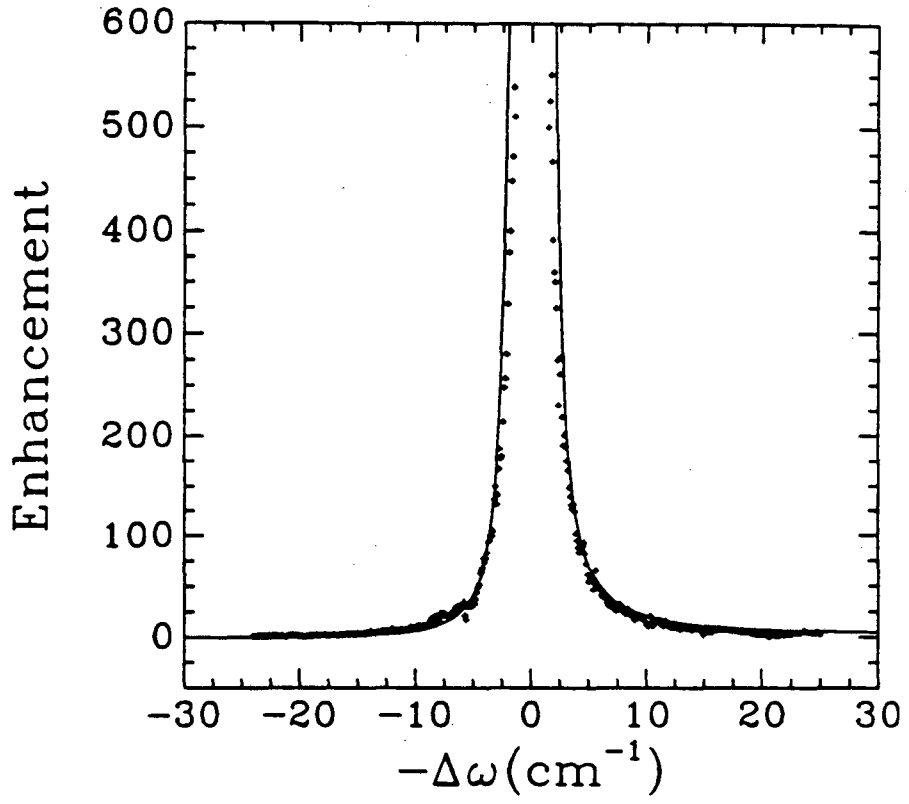

Figure 4.36: Measured enhancement profile (symbols) for the $\hat{\mathbf{X}}\hat{\mathbf{Z}}$ $\Delta 53$ cm^{-1} Raman scattering. Modelled profile using $\eta = 35.5$, $\delta = 0$, $\Delta = 2.0$ cm^{-1}, and $\Gamma = 0.4$ cm^{-1}.

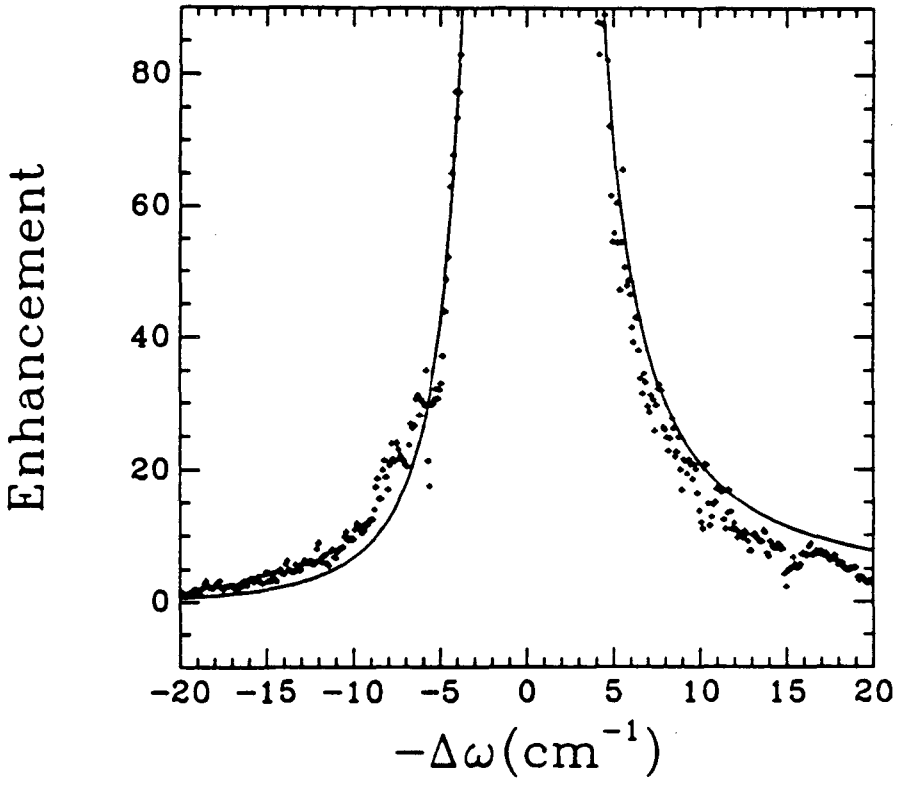

Figure 4.37: Enlarged view of Figure [4.36] showing the wings of the resonance.

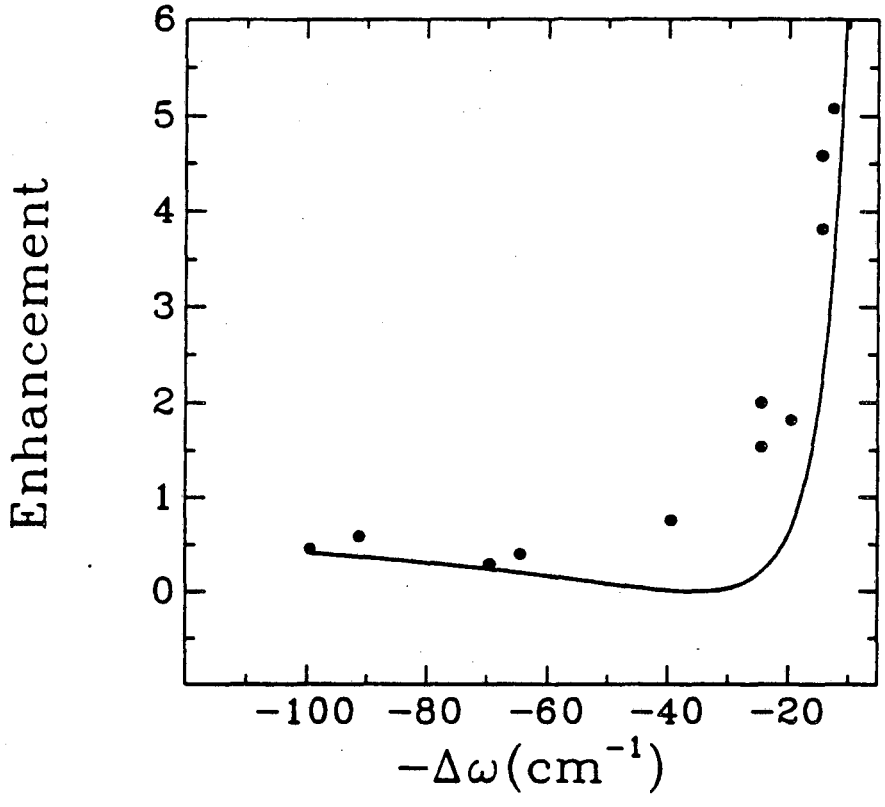

Figure 4.38: Enhancement values for the $\hat{\mathbf{X}}\hat{\mathbf{Z}}$ $\Delta 53$ cm^{-1} Raman scattering (circles) with modelled values (solid line), $\eta = 35.5$, $\delta = \pi$, $\Delta = 2.0$ cm^{-1}, and $\Gamma = 0.4$ cm^{-1}.

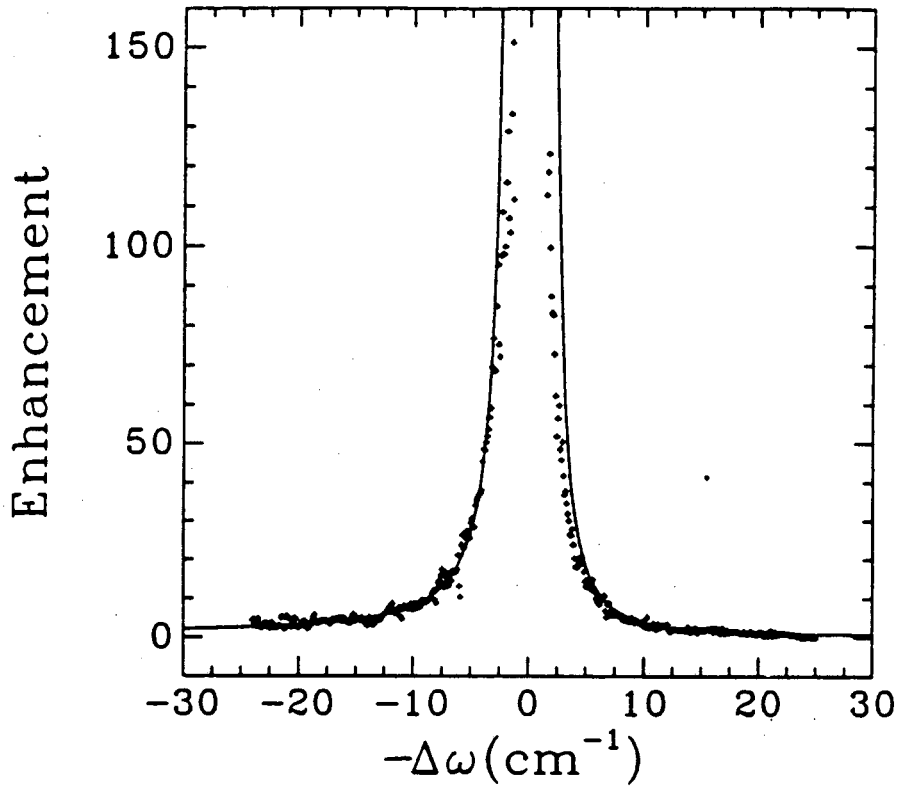

Figure 4.39: Measured and modelled (arbitrary phase) Raman enhancement profiles for the $\Delta 33$ cm^{-1} scattering ($\Delta 33$ cm^{-1} $\eta = 22, \delta = \pi/3, \Delta = 2.0$ cm^{-1}, and $\Gamma = 0.4$ cm^{-1}).

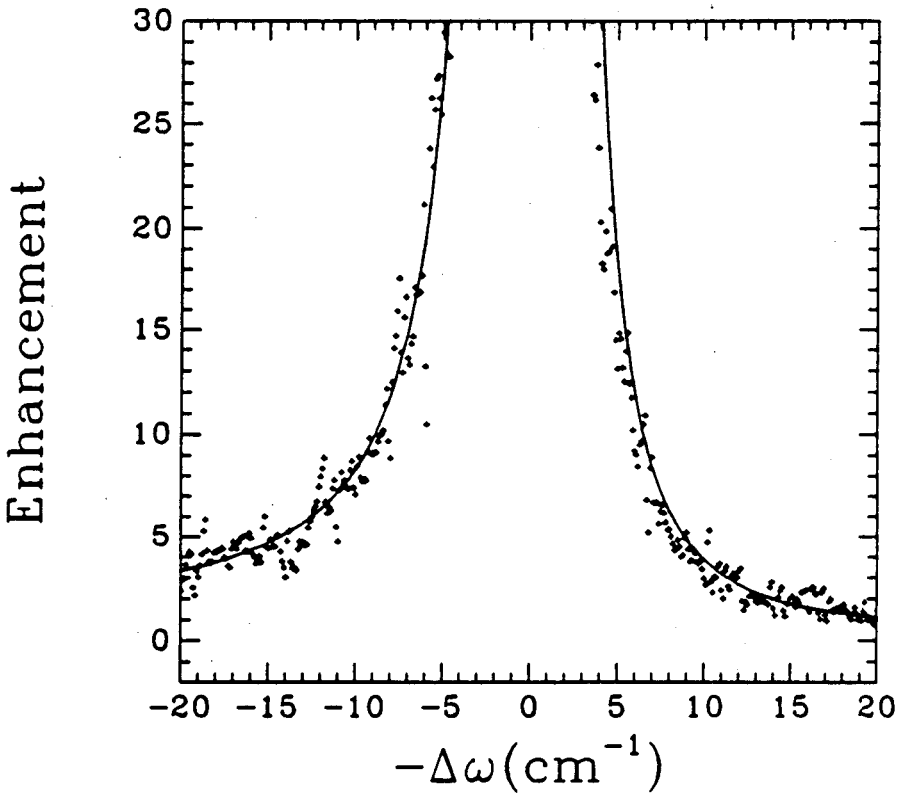

Figure 4.40: Wings of enhancement profile shown in Figure [4.40].

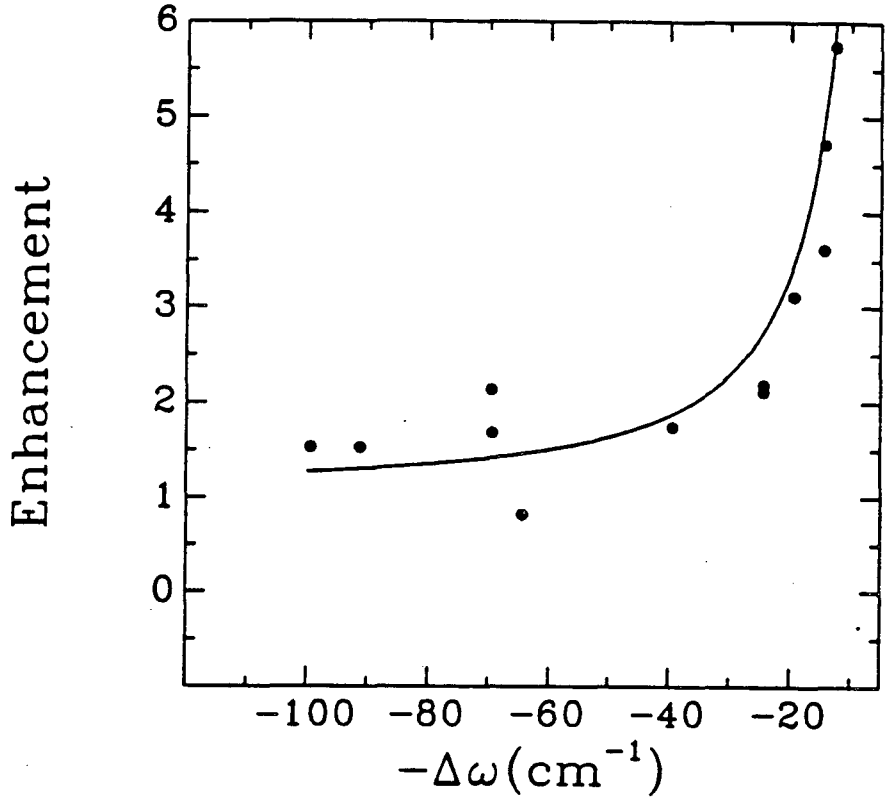

Figure 4.41: Enhancements of the $\Delta 33$ cm^{-1} scattering in the region $\Delta 20 - \Delta 100$ cm^{-1}. Model profile (solid line) has $\eta = 22$, $\delta = \pi/3$, $\Delta = 2.0$ cm^{-1}, and $\Gamma = 0.4$ cm^{-1}.

interference term (Equation 4.29) in the expression describing Raman enhancements to vary independently . The true physical justification for this is still unclear.

4.6.7 The Arbitrary Phase and the Range of the Resonance

Whatever the reason for it, the unlinking of the resonant and interference terms could have important implications in the understanding of "non-resonant" Raman intensities. In general it has been assumed that the states of the rare earth ion $4f^N$ configuration do not contribute significantly as virtual intermediate states in electronic Raman scattering (or any other multi-photon process). However, we have seen that the effects of a $4f^N$ intermediate state can be detected for detunings as great as 100 cm^{-1}. It is interesting to note that the range of influence of the $4f^N$ resonance is controlled by the interference term (Equation 4.29). The interference term (Equation 4.29) drops off with detuning only as $1/\Delta\omega$ while the resonance term (Equation 4.28) drops off as $(1/\Delta\omega)^2$. It can be seen that the unlinking of the magnitudes of these two terms allows for a large sharp

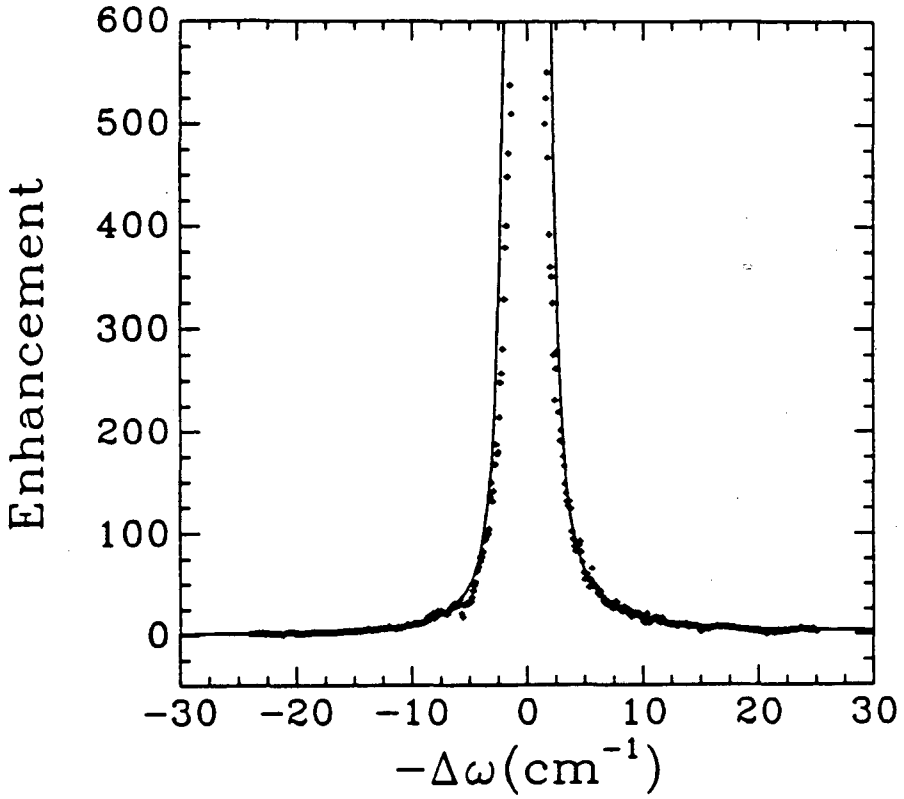

Figure 4.42: Measured and modelled (arbitrary phase) Raman enhancement profiles for the $\Delta 53$ cm^{-1} scattering ($\eta = 35.5$, $\delta = 2\pi/3$, $\Delta = 2.0$ cm^{-1}, and $\Gamma = 0.4$ cm^{-1}).

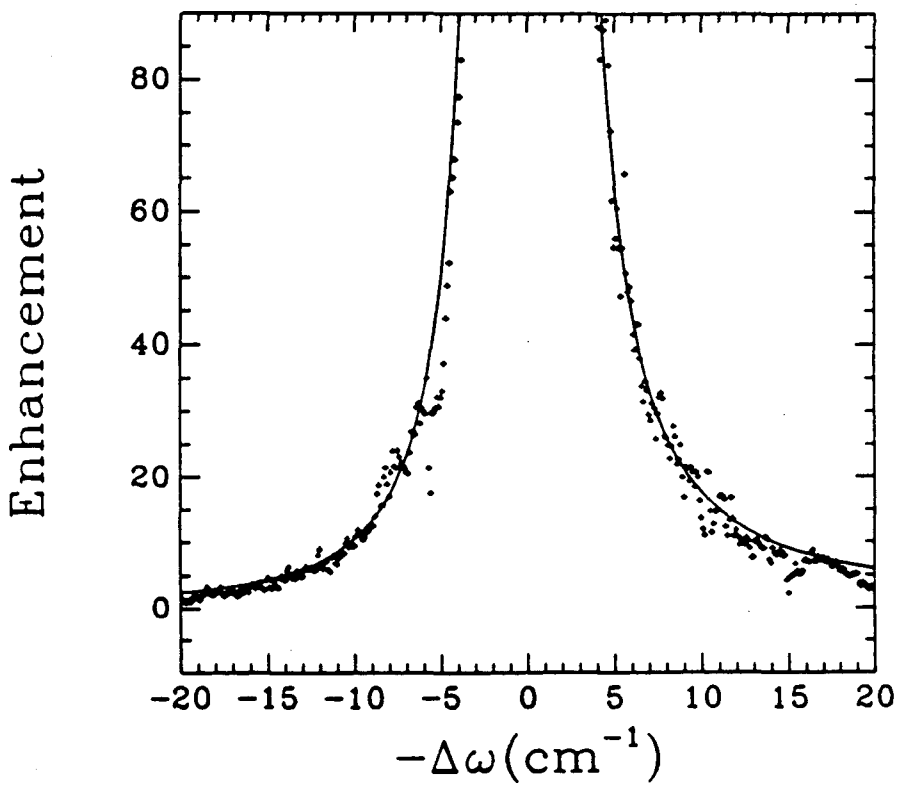

Figure 4.43: Wings of enhancement profile shown in Figure [4.42].

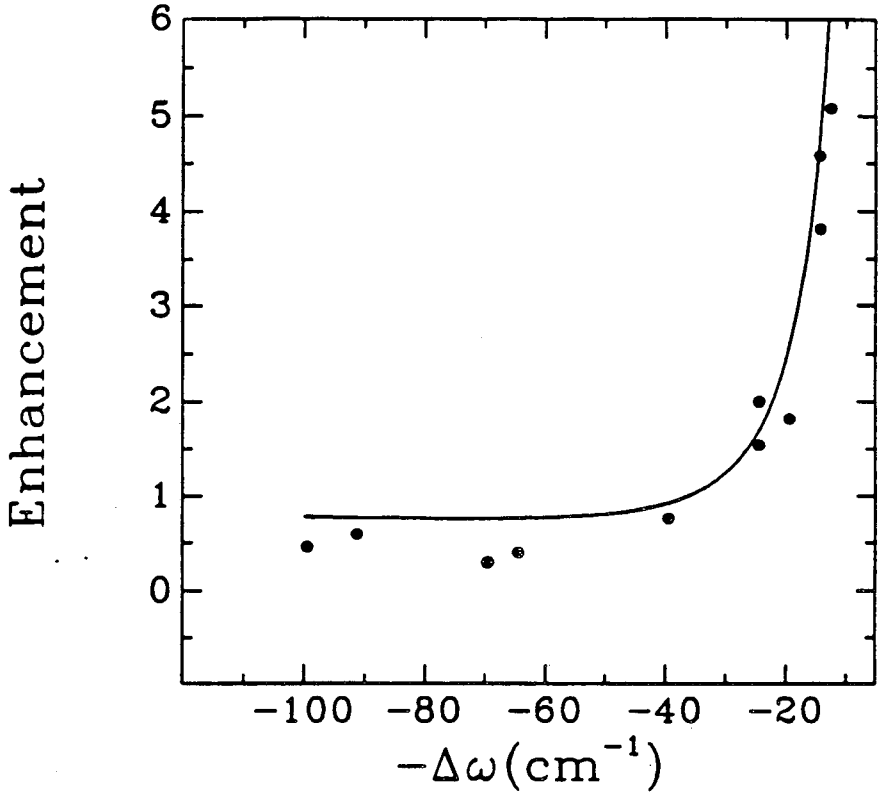

Figure 4.44: Enhancements of the $\Delta 53$ cm^{-1} scattering in the region $\Delta 20 - \Delta 100$ cm^{-1}. Model profile (solid line) has $\eta = 35.5$, $\delta = 2\pi/3$, $\Delta = 2.0$ cm^{-1}, and $\Gamma = 0.4$ cm^{-1}.

$4f^N$ resonance with either limited range ($|\cos\delta| \ll 1$) or large range ($|\cos\delta| \approx 1$).

The relative signs of the resonance and interference terms can also be of great importance in determining the range of influence of resonances. Consider a situation in which there are a number of resonant states contributing, for example where the laser is tuned outside a $^{2S+1}L_J$ multiplet in the range in which the interference terms dominate. If all the interference terms have the same sign the results will be very much different than a case in which the signs of the interference terms are in general different. In the former case one would observe a large range for the resonances while in the latter case the range of influence would be greatly lessened by cancellation among terms.

4.6.8 Comparison of Enhancements with Expectations from Measured Oscillator Strengths

In this section we compare the fitted values of η for the $\Delta 33$ and $\Delta 53$ cm^{-1} scattering with the values calculated using one photon transition oscillator strengths.

The ratio of the fitted values for η for the $\Delta 33$ and $\Delta 53$ cm^{-1} scattering is given by,

$$\left(\frac{\eta_{33}}{\eta_{53}}\right)_{fitted} = \frac{22}{35.5} = 0.62 \tag{4.34}$$

To calculate this ratio from one photon transition oscillator strengths we use the definition for η found in Equations 4.17, 4.18, and 4.24. Using these Equations we have,

$$\left(\frac{\eta_{33}}{\eta_{53}}\right)_{calc.} = \left| \frac{\frac{\langle 33|X|r\rangle\langle r|Z|0\rangle}{A_{33}}}{\frac{\langle 53|X|r\rangle\langle r|Z|0\rangle}{A_{53}}} \right| \tag{4.35}$$

where $|r\rangle$ is the resonant state at 20,492.9 cm^{-1}, and A_{33} and A_{53} are the non-resonant Raman amplitudes for the $\Delta 33$ and $\Delta 53$ cm^{-1} scattering. The matrix elements are related to one photon transition oscillator strengths. For example, $\langle 33|X|r\rangle$ is proportional to the square root of the oscillator strength associated with the $\hat{\mathbf{X}}$ polarized transition between the 33 cm^{-1} state and the 20492.9 cm^{-1} state. Thus, the magnitudes of the matrix elements may be obtained directly from Table 4.2. The magnitudes of the non-resonant Raman amplitudes are proportional to the square roots of the non-resonant Raman intensities listed in Table 4.6. Using all of this information, we have,

$$\left(\frac{\eta_{33}}{\eta_{53}}\right)_{calc.} = \frac{\frac{\sqrt{.760}}{\sqrt{3.0}}}{\frac{\sqrt{.671}}{\sqrt{.9}}} = 0.58 \tag{4.36}$$

As one can see, the calculated and fitted values are in excellent agreement.

4.6.9 Why are the Enhancements so LARGE ?

Given the success of the above calculation, it seems as though by using the oscillator strengths of one photon transitions one should be able to predict for which intermediate state resonances electronic Raman scattering (or any other multi-photon process) large enhancements will be observed. However, the determination of the strength of intermediate state resonances is somewhat more complicated than just multiplying two oscillator strengths together. In this section we describe the important features associated with a resonance that contribute to a strong and observable enhancement of signal. In doing so a scheme is developed for predicting resonance enhancement of electronic Raman scattering (and other multi-photon processes) in rare earth crystals.

One important factor contributing to the observability of the Raman signal is the amount of fluorescence coming from the resonant level. As pointed out earlier (Section

4.2.2), fluorescence can easily obscure any Raman signal. In this study the population in the resonant level decayed mostly through non-radiative processes with virtually no fluorescence, thus contributing greatly to the observabilty of the Raman signal.

A second consideration is the question of partitioning between absorption followed by fluorescence and resonance Raman scattering when the excitation is in direct resonance. Recently Koningstein [134] has addressed this issue in discussing the small $4f^N$ intermediate state resonance enhancements for electronic Raman scattering from Tb^{3+} in TbAlG. In direct resonance the partitioning of the two process is governed by the relative sizes of the dephasing time (T_2) and the population lifetime (T_1) of the resonant state. As stated in previously, the ratio of Raman scattering to absorption followed by fluorescence is given by the ratio T_2/T_1. Unfortunately, for our system very little is known at this time about the ratio T_2/T_1. In any event, such a discussion is relevant only for direct resonance excitation for which in our case we have limited information as a result of the strong linear absorption of the pump radiation.

The most important consideration in the determination of resonance enhancement strengths is the strengths of the one photon oscillator strengths (but in a somewhat less than straight-forward way). In this study we have observed large resonance enhancements of electronic Raman scattering. We look back to our early estimate of the expected resonance enhancement of electronic Raman scattering in rare earth crystals (Section 4.1). Enhancements given by the expression

$$\frac{I_R}{I_{NR}} \approx \frac{.005 \text{ to } 500}{\hbar^2(\omega_{4f} - \omega)^2} \tag{4.37}$$

were expected. In this expression the numerator (.005 to 500) corresponds roughly to the value of η^2 in our model. For this work we have found values of η^2 of 484 (22^2) and 1260 (35.5^2), definitely on the high side of what was expected. Examination of the oscillator strengths that are associated with the resonance,

$$\begin{array}{ll} 0 \rightarrow 20492.9, \hat{Z} & 0.069\times10^{-6} \\ 33 \rightarrow 20492.9\ , \hat{X} & 0.760\times10^{-6} \\ 53 \rightarrow 20492.9\ , \hat{X} & 0.671\times10^{-6} \end{array}$$

shows that they range from moderately small (for rare earths) to strong. It is interesting to note that in earlier electronic Raman scattering resonance enhancement experiments (for which only small enhancements were observed) the resonance transitions were approximately spin forbidden (see Section 4.1) which could result in smaller than average oscillator strengths.

We believe the most important aspect of the oscillator strengths in this case leading to the large enhancements is that the oscillator strength for the ground state to resonant state transition is small while the oscillator strength for the resonant state back to the final state is large. In the resonance electronic Raman scattering process there is a trade-off between absorption of the pump beam and enhancement of the Raman scattering. A large product of the two contributing oscillator strengths leads to the large enhancements but a large oscillator strength associated with the transition from the ground state to the resonant state results in strong absorption of the exciting laser. Thus, for large observable enhancement the optimum situation is a large oscillator strength for the transition from the resonant to final state and a small oscillator strength for the transition from the ground to the resonant state.

We offer a simple calculation in order to demonstrate this behavior. The calculation is simple in that it assumes a temperature of 0 K (no population of the excited states) and ignores the possibility of non-linear effects (such as saturated absorption). In the calculation we combine the effects of the resonance enhancements of the electronic Raman scattering (something we have already modelled) and the absorption of the pump laser. Let us start by modelling the effects of the absorption of the pump beam.

Let us write down as expression for the amount of light scattered ($d\mathrm{I}_s$) from a volume element of thickness dx located at a depth x in the crystal sample (see Figure 4.45.

$$d\mathrm{I}_s(x) = \mathrm{I}(x)\sigma n_o dx \tag{4.38}$$

where $\mathrm{I}(x)$ is the intensity of light incident on the volume element, n_o is the number density of Raman scatterers, and σ is the Raman scattering cross-section. Now if the sample is absorbing, $\mathrm{I}(x)$ will not be a constant function of x but will decay as x increases.

$$\mathrm{I}(x) = \mathrm{I}_o e^{-\alpha x} \tag{4.39}$$

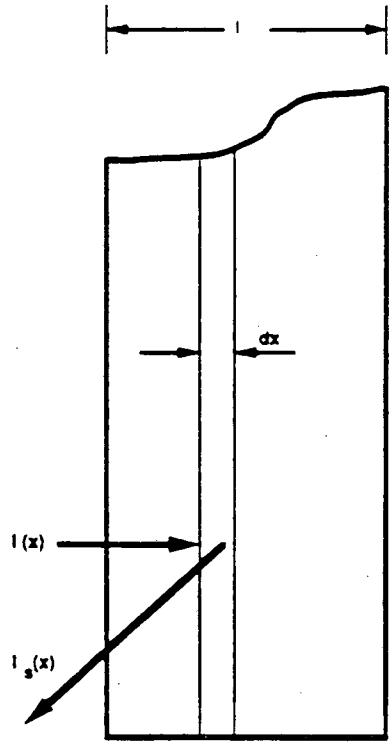

Figure 4.45: Raman scattering from an absorbing sample (see text for details).

where I_o is the intensity of the light incident on the sample (at $x = 0$) and α is the absorption coefficient of the sample. The absorption coefficient is a function of frequency and may be written in terms of a constant times a normalized line shape.

$$\alpha(\omega) = \alpha_o g(\omega) \tag{4.40}$$

where $g(\omega)$ is the normalized line shape. To obtain an expression for the total amount of scattered light we need to integrate Equation 4.38 over the entire width of the crystal (l). The integration gives

$$I_s = I_o n_o \sigma l \left(\frac{1 - e^{-(\alpha_o g(\omega) l)}}{\alpha_o g(\omega) l} \right) \tag{4.41}$$

To check the validity of our model we try to duplicate the Raman excitation profile for the $\Delta 303$ cm^{-1} scattering (Figure 4.21). For the line shape of the absorption we use the convolution of a Gaussian with a FWHM of 2.0 cm^{-1} and a Lorentzian with a FWHM of 0.4 cm^{-1}. The value of α_o is easily obtained from the oscillator strength (0.069×10^6) and Equation 4.7 and found to be approximately 863 cm^{-1}. Figure 4.46 shows the observed Raman excitation profile and the modelled one. The agreement is fairly good.

We are now ready to model the enhancement profiles (with absorption of the pump

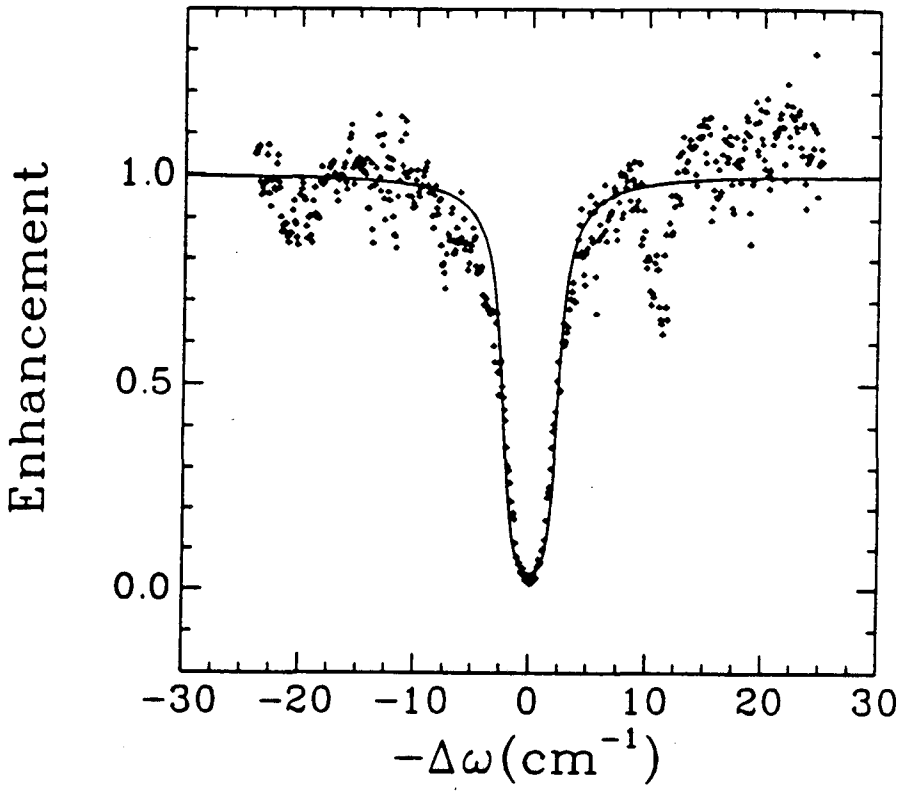

Figure 4.46: Raman scattering to the 303 cm^{-1} phonon in $ErPO_4$ showing the effects of the absorption at 20492.9 cm^{-1}. Symbols are data and solid line is the modelled result.

laser) for the electronic Raman scattering to the 33 cm^{-1} and 53 cm^{-1} levels. The enhancement profiles including absorption of the pump beam are simply given by the product of an enhancement part ($E(\Delta\omega)$), as given in Equation 4.25 and an absorptive part, as given by Equation 4.41.

$$E'(\Delta\omega) = E(\Delta\omega)\left(\frac{1-e^{-(\alpha_o g(\Delta\omega)l)}}{\alpha_o g(\Delta\omega)l}\right) \tag{4.42}$$

Shown in Figure 4.47 are the observed and modelled Raman excitation profiles for the $\Delta 33$ cm^{-1} scattering. For the absorptive part of the model we use $\alpha_o = 863$ cm^{-1}, with $g(\omega)$ being the convolution of a Gaussian (2.0 cm^{-1} FWHM) and Lorentzian (0.4 cm^{-1} FWHM), $l = 0.08$ cm, and $l = 0.08$ cm. For the enhancement part we use $\eta = 22$, $\delta = \pi/3$, $\Delta = 2.0$ cm^{-1}, and $\Gamma = 0.4$ cm^{-1}. Shown in Figure 4.48 are the observed and modelled Raman excitation profiles for the $\Delta 53$ cm^{-1} scattering. For the model $\alpha_o = 863$ cm^{-1}, $g(\omega)$ is the convolution of a Gaussian (2.0 cm^{-1} FWHM) and Lorentzian (0.4 cm^{-1} FWHM), $l = 0.08$ cm, $\eta = 35.5$, $\delta = 2\pi/3$, $\Delta = 2.0$ cm^{-1}, and $\Gamma = 0.4$ cm^{-1}.

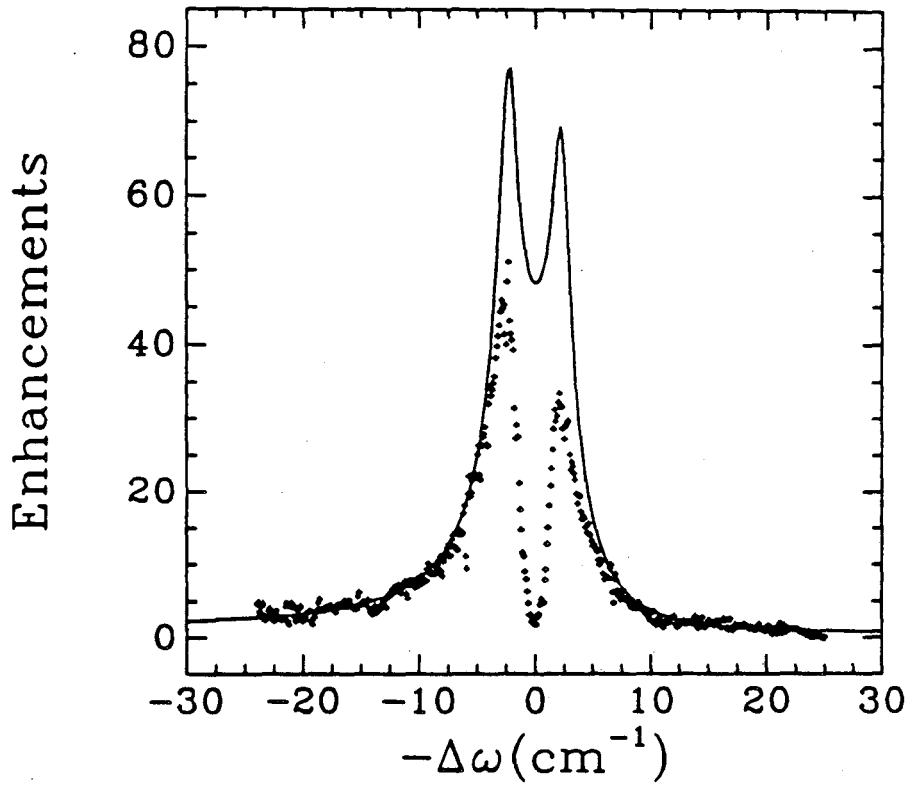

Figure 4.47: Observed(symbols) and modelled(solid-line) Raman excitation profiles for the $\Delta 33$ cm^{-1} scattering. See the text for details.

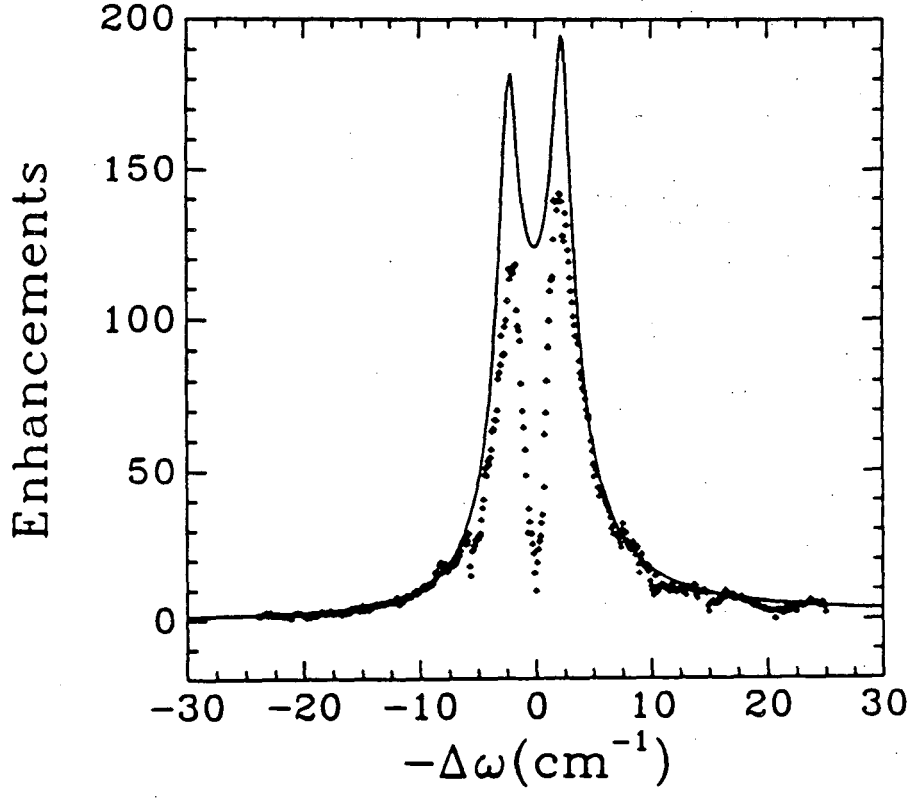

Figure 4.48: Observed(symbols) and modelled(solid-line) Raman excitation profiles for the $\Delta 53$ cm^{-1} scattering. See the text for details.

For both cases the model overestimates the actual enhancement, but the results are surprisingly good given the complexity of the problem and the simplicity of our model. The discrepancies could be the result of a number of things. Either excited state absorption of the Raman scattered light or increases in the damping parameters due to resonance heating of the crystal could both explain the reduction in signal. However, for now we will not concern ourselves with the small difference between model and data and use the model to demonstrate our point regarding the importance of the relative sizes of the oscillator strengths in determining the strength of electronic Raman resonances.

Let M_{ri} represent the electric dipole matrix element between state $|r\rangle$ (resonant state in the Raman process) and state $|i\rangle$ (initial state). M_{fr} represents the electric dipole matrix element between state $|f\rangle$ (final state) and the state $|r\rangle$. We have the following relationships,

$$\begin{aligned} P_{ir} &\propto |M_{ri}|^2 \\ P_{fr} &\propto |M_{fr}|^2 \\ \alpha_o &\propto |M_{ri}|^2 \\ \eta &\propto |M_{fr}M_{ri}| \end{aligned} \tag{4.43}$$

(4.44)

where P refers to an oscillator strength.

Using our model we would like to show what happens to the Raman excitation profile when η is held fixed but the relative sizes of M_{ri} and M_{fr} are allowed to vary. Figure 4.49 shows the results of such a calculation for the $\Delta 33$ cm^{-1} scattering. Basically we have started with all the parameters fixed at the values used previously in modelling the $\Delta 33$ cm^{-1} scattering and then allowed M_{ri} to vary, varying M_{fr} to keep η constant, and scaling α_o appropriately. The plot shows the peak enhancement as a function of the ratio P_{ir}/P_{fr}. As can be seen the peak enhancement increases as the ratio P_{ir}/P_{fr} becomes smaller. A similar behavior is observed for the $\Delta 53$ cm^{-1} scattering as shown in Figure 4.50.

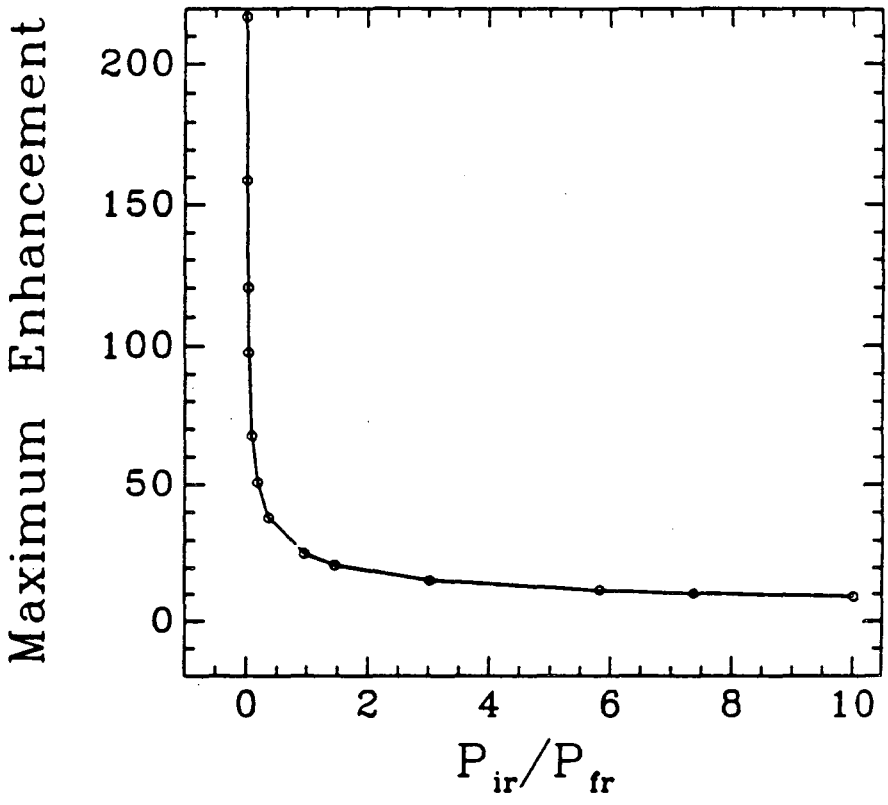

Figure 4.49: Calculated peak enhancement (including the effects of absorption of the pump laser) for the $\Delta 33$ cm^{-1} Raman scattering as a function of P_{ir}/P_{fr}.

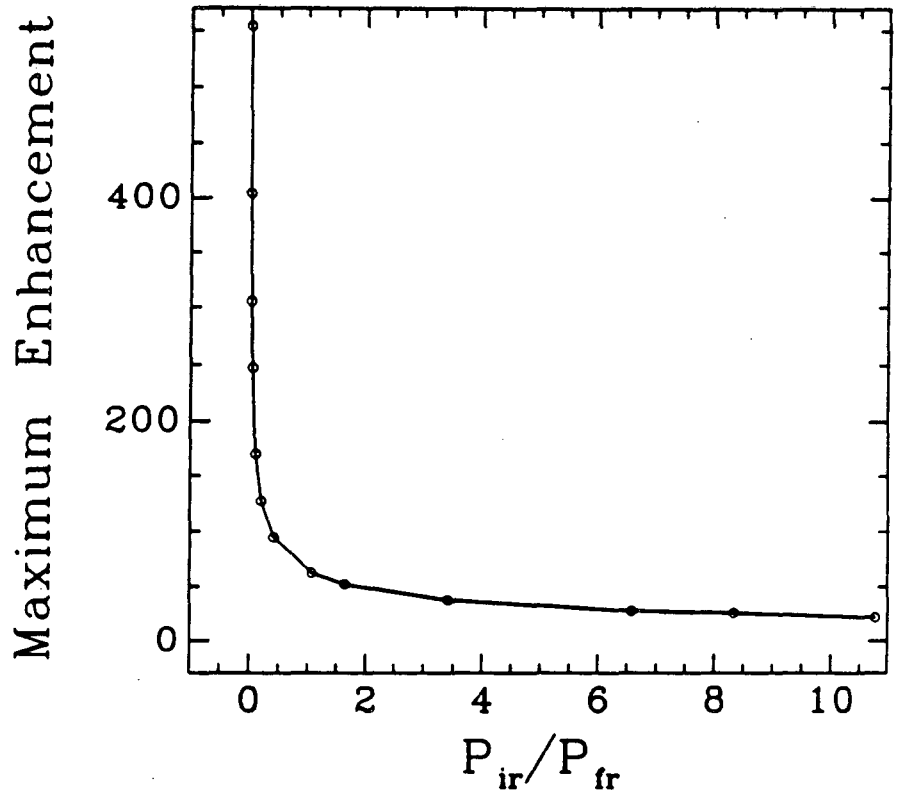

Figure 4.50: Calculated peak enhancement (including the effects of absorption of the pump laser) for the $\Delta 53$ cm^{-1} Raman scattering as a function of P_{ir}/P_{fr}.

Bibliography

[1] L.A. Boatner and M.M. Abraham. Solid State Div., Oak Ridge National Laboratory.

[2] M. Petek, M.M. Abraham, L.A. Boatner. *Scientific Basis for Nuclear Waste Management, vol.4*. Elsevier-North Holland, New York, 1982.

[3] R.S. Feigelson. *J. Am. Ceram. Soc.* **47**, 257 (1964).

[4] M. Rappaz, L.A. Boatner, and M.M. Abraham. *J. Chem. Phys.* **73**, 1095 (1980).

[5] W.O. Milligan, D.F. Mullica, G.W. Beall, and L.A. Boatner. *Inorg. Chim. Acta* **70**, 133 (1983).

[6] W.O. Milligan, D.F. Mullica, G.W. Beall, and L.A. Boatner. *Inorg. Chim. Acta* **60**, 39 (1982).

[7] W.O. Milligan, D.F. Mullica, G.W. Beall, and L.A. Boatner. *Acta Cryst.* **C39**, 23 (1983).

[8] C. Linares, A. Louat, and M. Blanchard. *Structure and Bonding* **33**, 179 (1977).

[9] E. Nakazawa and F. Shaiga. *J. Luminescence* **15**, 255 (1977).

[10] R.D. Giauque, R.B. Garett, and L.Y. Goda. *Anal. Chem.* **49**, 1012 (1977).

[11] Philippe C. Becker. *Electronic Raman Scattering in Rare Earth Phosphate Crystals.* PhD thesis, University of California, Berkeley, November 1986. LBL-22634.

[12] R.J. Elliott, R.F. Harley, W. Hayes, and S.R.P. Smith. *Proc. R. Soc. Lond. A* **328**, 217 (1972).

[13] S.A. Miller, H.H. Caspers, and H.E. Rast. *Phys. Rev.* **168**, 964 (1968).

[14] J.D. Axe. *Phys. Rev.* **136A**, 42 (1964).

[15] B.R. Judd. *Phys. Rev.* **127**, 750 (1962).

[16] G.S. Ofelt. *J. Chem. Phys.* **37**, 511 (1962).

[17] Brian G. Wybourne. *Spectroscopic Properties of Rare Earths.* John Wiley and Sons, 1965.

[18] W.M. Yen and P.M. Seltzer. *Topics in Applied Physics, vol.49: Laser Spectrscopy of Solids.* Springer-Verlag, 1981.

[19] T. Hoshina and S. Kuboniwa. *J. Phys. Soc. Japan* **31**, 828 (1971).

[20] E. Nakazawa and S. Shionoya. *J. Phys. Soc. Japan* **36**, 504 (1974).

[21] M.M. Abraham, L.A. Boatner, J.O. Ramey, and M. Rappaz. *J. Chem. Phys.* **78**, 3 (1983).

[22] T. Hayhurst, G. Shalimoff, J.G. Conway, N. Edelstein , L.A. Boatner, and M.M. Abraham . *J. Chem. Phys.* **76**, 3960 (1982).

[23] P.C. Becker, T. Hayhurst, G. Shalimoff, J.G. Conway, N. Edelstein, L.A. Boatner, and M.M. Abraham. *J. Chem. Phys.* **81**, 2872 (1984).

[24] D.Piehler and D.S. Kim, private communication. Preliminary crystal field fit for Eu^{3+}:$LuPO_4$.

[25] T. Hayhurst, G. Shalimoff, N. Edelstein, L.A. Boatner, and M.M. Abraham. *J. Chem. Phys.* **74**, 5449 (1981).

[26] R. Reisfeld and C.K. Jørgensen. *Lasers and Excited States of Rare Earths. Inorganic Chemistry Concepts vol. 1*, Springer-Verlag, Berlin, 1977.

[27] G. Blasse and A. Bril. *J. Chem. Phys.* **47**, 5139 (1967).

[28] E. Loh. *Phys. Rev.* **154**, 270 (1967).

[29] W.J. Manthley. *Phys. Rev. B* **8**, 4086 (1973).

[30] T. Szcurek, G.W.F. Drake, and M. Schlesinger. *Phys. Rev. B* **8**, 4910 (1973).

[31] L.R. Elias, Wm. S. Heaps, and W.M. Yen. *Phys. Rev. B* **8**, 4989 (1973).

[32] W. Hayes, M.C.K. Wiltshire, W.J. Manthley, and D.S. McClure. *J. Phys. C: Solid State Phys.* **6**, L273 (1973).

[33] M.J. Weber. *J. Appl. Phys.* **44**, 3205 (1973).

[34] R.R. Jacobs, W.F. Krupke, and M.J. Weber. *Appl. Phys. Lett.* **33**, 410 (1978).

[35] W.J. Miniscalco and W.M. Yen. *J. Appl. Phys.* **49**, 6109 (1978).

[36] D.J. Ehrlich, P.F. Moulton, and R.M. Osgood,Jr. *Opt. Lett.* **4**, 184 (1979).

[37] D.J. Ehrlich, P.F. Moulton, and R.M. Osgood,Jr. *Opt. Lett.* **5**, 339 (1980).

[38] L. Brewer. *J. Opt. Soc. Am.* **61**, 1666 (1971).

[39] E. Loh . *Phys. Rev.* **147**, 332 (1966).

[40] R.C. Ropp. *J. Electrochem. Soc.* **115**, 841 (1968).

[41] J.P. Briffaut and J.P. Denis. *Phys. Stat. Sol.* **41**, 781 (1970).

[42] G. Balasubramanian and D.J. Newman. *J. Phys. Chem. Solids* **36**, 57 (1975).

[43] R.C. Naik and N.P. Karanjikar. *'Luminescence from Higher 5d Levels of* Ce^{3+} *in* YPO_4*'*. Technical Report, Bhabha Atomic Research Center, Bombay, India, 1982.

[44] Norman Edelstein, private communication.

[45] J. Becquerel. *C.R. Acad. Sci.* **142**, 775 (1906).

[46] J. Becquerel. *Le Radium* **4**, 328 (1906).

[47] J. Becquerel and H. Kammerlingh Onnes. *Proc. Acad. Amsterdam* **10**, 592 (1908).

[48] J.H. Van Vleck. *J. Phys. Chem.* **41**, 67 (1937).

[49] M. Dagenais, M. Downer, R. Neumann, and N. Bloembergen. *Phys. Rev. Lett.* **46**, 561 (1981).

[50] M.C. Downer, A. Bivas, and N. Bloembergen. *Opt. Comm.* **41**, 355 (1982).

[51] M.C. Downer and A. Bivas. *Phys. Rev. B* **28**, 3677 (1983).

[52] B.R. Judd and D.R. Pooler. *J. Phys. C: Solid State Phys.* **15**, 591 (1982).

[53] R.J. Elliott and R. Loudon. *Phys. Lett.* **3**, 189 (1963).

[54] J.T. Hougen and S. Singh. *Phys. Rev. Lett.* **10**, 406 (1963).

[55] J.A. Koningstein. *J. Opt. Soc. Am.* **56**, 1405 (1966).

[56] J.A. Koningstein. *J. Chem. Phys.* **46**, 2811 (1967).

[57] J.A. Koningstein and O.S. Mortensen. *Phys. Rev. Lett.* **18**, 831 (1967).

[58] J.A. Koningstein and O.S. Mortensen. *Chem. Phys. Lett.* **56**, 1405 (1966).

[59] J.A. Koningstein and O.S. Mortensen. *Nature* **217**, 445 (1968).

[60] O.S. Mortensen and J.A. Koningstein. *J. Chem. Phys.* **48**, 3971 (1968).

[61] G. Placzek. *Handbuch der Radiologie, Vol. 6, part 2.* Akademische Verlaggesellschaft, Leipzog, 1934.

[62] A. Kiel, T.C. Damen, S.P.S. Porto, S. Singh, and F. Varsanyi. *IEEE J. Quant. Elec.* **QE-4**, 318 (1968).

[63] A. Kiel, T. Damen, S.P.S. Porto, S. Singh, and F. Varsanyi. *Phys. Rev.* **178**, 1518 (1969).

[64] P.C. Becker, N. Edelstein, G.M. Williams, J.J. Bucher, R.E. Russo, J.A. Koningstein, L.A. Boatner, and M.M. Abraham. *Phys. Rev. B* **31**, 8102 (1985).

[65] P.C. Becker, N. Edelstein, B.R. Judd, R.C. Leavitt, and G.M.S. Lister. *J. Phys. C* **18**, L1063 (1985).

[66] L.L. Chase and S.A Payne. *Phys. Rev. B* **34**, 8883 (1986).

[67] P. Grünberg and J.A. Koningstein. *J. Chem. Phys.* **53**, 4584 (1970).

[68] D. Nicollin and J.A. Koningstein. *Chem. Phys.* **49**, 377 (1980).

[69] R.L. Wadsack and R.K. Chang. *Solid State Comm.* **10**, 45 (1972).

[70] P. Myslynski and J.A. Koningstein. *Chem. Phys.* **114**, 137 (1987).

[71] A. Kiel and J.F. Scott. *Phys. Rev. B* **2**, 2033 (1970).

[72] P.C. Becker, G.M. Williams, R.E. Russo, N. Edelstein, J.A. Koningstein, L.A. Boatner, and M.M. Abraham. *Opt. Lett.* **11**, 282 (1986).

[73] B.R. Judd. *Inorg. Chim. Acta* **139**, 341 (1987).

[74] C.K. Jørgensen and B.R. Judd. *Mol. Phys.* **8**, 281 (1964).

[75] S.F. Mason and R.D. Peacock. *Mol. Phys.* **30**, 1829 (1975).

[76] R.D. Peacock. *Structure and Bonding* **22**, 88 (1975).

[77] Michael Coffin Downer. *Two-Photon Spectroscopy of Rare Earth Ions in In Condensed Matter Enviroments.* PhD thesis, Harvard University, February 1983.

[78] J. Sztucki and W. Stręk. *Phys. Rev. B* **B34**, 3120 (1986).

[79] J. Sztucki and W. Stręk. *Chem. Phys. Letters* **125**, 520 (1986).

[80] J. Sztucki and W. Stręk. *Chem. Phys. Letters* **138**, 410 (1987).

[81] M.F. Reid and F.S. Richardson. *Phys. Rev. B* **B29**, 2830 (1984).

[82] W.T. Carnall. *Handbook on the Physics and Chemistry of Rare Earth Ions in Solution.* North-Holland, Amsterdam, 1979.

[83] W.T. Carnall, J.V. Beitz, and H. Crosswhite. *J. Chem. Phys.* **80**, 2301 (1984).

[84] R.D. Cowan. *The Theory of Atomic Structure and Spectra.* University of California Press, Berkeley, 1981.

[85] D.L. Dexter. Optical properties of imperfections. In F.Seitz and D.Turnbull, editors, *Solid State Physics no. 6, Advances in Research and Application*, page 353, Academic Press Inc., New York, 1958.

[86] C. J. Ballhausen. *Molecular Electronic Structures of Transition Metal Complexes.* McGraw-Hill, Inc., Great Britain, 1979.

[87] R.C. Weast. *CRC Handbook of Physics and Chemistry, 59th Edition.* CRC Press Inc., West Palm Beach, Florida, 1978-1979.

[88] R.W.G. Wyckoff. *Crystal Structures.* Volume 3, John Wiley and Sons, 1965.

[89] T.S. Lomheim and L.G. Deshazer. *Phys. Rev. B* **20**, 4343 (1979).

[90] K. Okada, Y. Kaizu, H. Kobayashi, K. Tanaka , and F. Marumo. *Mol. Phys.* **54**, 1293 (1985).

[91] S. Geller and E.A. Wood. *Acta Cryst.* **9**, 563 (1956).

[92] M.J. Weber, B.H. Matsinger, V.L. Donlan and G.T. Stuart. *J. Chem. Phys.* **57**, 562 (1972).

[93] P. Blanchfield and G.A. Saunders. *J. Phys. C: Solid State Phys.* **12**, 4673 (1979).

[94] D.E. Castleberry and A. Linz. *Appl. Opt.* **14**, 2506 (1975).

[95] R.W.G Wyckoff. *Crystal Structures.* Volume 1, John Wiley and Sons, 1965.

[96] A. Zalkin and D.H. Templeton. *Acta Cryst. B* **41**, 91 (1985).

[97] M.P. Wirich. *Appl. Opt.* **5**, 1966 (1966).

[98] W.F. Krupke. *Phys. Rev.* **145**, 325 (1966).

[99] C.A. Morrison and R.P. Leavitt. *Handbook on the Physics and Chemistry of Rare Earths, vol. 5.* North Holland Press, Amsterdam, 1982.

[100] A.Yariv. *Quantum Electronics.* John Wiley and Sons, New York, 1975.

[101] T. Sczurek and M. Schesinger. *Rare Earth Spectroscopy.* World Scientific Pub. Co., Singapore, 1984.

[102] S. Hüfner. *Optical Spectra of Transparent Rare Earth Compounds.* Academic Press, 1978.

[103] D. Kuse. *Z. Phys.* **203**, 49 (1967).

[104] M.V. Klein. *Phys. Rev. B* **8**, 919 (1973).

[105] Y.R. Shen. *Phys. Rev. B* **9**, 622 (1974).

[106] Y.R. Shen. *Phys. Rev. B* **14**, 1772 (1976).

[107] J.R. Solin and H. Merkelo. *Phys. Rev. B* **14**, 1775 (1976).

[108] J.M. Friedmann and R.M. Hochstrasser. *Chem. Phys.* **6**, 155 (1974).

[109] J.O. Berg, C.A. Langhoff, and G.W. Robinson. *Chem. Phys. Lett.* **29**, 305 (1974).

[110] D.L. Rousseau and G.D. Patterson. *Phys. Rev. Lett.* **34**, 1306 (1975).

[111] D.L. Rousseau and P.F. Williams. *J. Chem. Phys.* **64**, 3519 (1976).

[112] Y. Toyozawa. *J. Phys. Soc. Jap.* **41**, 400 (1976).

[113] E. Courtens and A. Szöke. *Phys. Rev. A* **15**, 1588 (1977).

[114] T. Takagahara, E. Hanamura, R. Kubo. *J. Phys. Soc. Jap.* **43**, 1522 (1977).

[115] T. Takagahara, E. Hanamura, R. Kubo. *J. Phys. Soc. Jap.* **43**, 802 (1977).

[116] T. Takagahara, E. Hanamura, R. Kubo. *J. Phys. Soc. Jap.* **43**, 811 (1977).

[117] J.M. Friedmann. *Solid State Comm.* **32**, 39 (1979).

[118] J.M. Friedmann. *J. Chem. Phys.* **71**, 3147 (1979).

[119] R.J.H. Clark and R.E. Hester. *Advances in Infrared and Raman Spectroscopy , Vol. 12.* John Wiley and Sons, 1985.

[120] R.A. Harris, R.A. Mathies, and W.T. Pollard. *J. Chem. Phys.* **85**, 3744 (1986).

[121] T. Kushida. *Solid State Comm.* **32**, 33 (1979).

[122] P.F. Williams, D.L. Rousseau, and S.H. Dworetsky. *Phys. Rev. Lett.* **32**, 196 (1974).

[123] Y. Masumoto, S. Shionoya, and Y. Tanaka. *Solid State Comm.* **27**, 1117 (1978).

[124] J.S. Weiner and P.Y. Yu. *Solid State Comm.* **50**, 493 (1984).

[125] J.S. Weiner. *A Subnanosecond Time Resolved Emmission Study of Cu_2O and GaAs.* PhD thesis, University of California, Berkeley, August 1984. LBL-18276.

[126] W. Heitler. *The Quantum Theory of Radiation.* Clarendon Press, Oxford, 1958.

[127] R. Loudon. *The Quantum Theory of Light.* Clarendon Press, Oxford, 1983.

[128] J.E. Bjorkholm and P.F. Liao. *Phys. Rev. Lett.* **33**, 128 (1974).

[129] J. Friedmann and R.M. Hochstrasser. *Chem. Phys. Lett.* **32**, 414 (1975).

[130] P. Stein, V. Miskowski, W.H. Woddruff , J.P. Griffin, K.G. Werner, B.P. Gaber, and T.G. Spiro. *J. Chem Phys.* **64**, 2159 (1976).

[131] L.A. Rebane and A.A. Khaav. *Sov. Phys. Solid State* **24**, 1452 (1982).

[132] C. Hirlimann, M.P. dos Santos, and M. Balkanski. *J. Phys. C: Solid State Phys.* **18**, 6297 (1985).

[133] J.L. Prather. *Atomic Energy Levels in Crystals, NBS Monograph 19.* Dept. of Commerce, 1961.

[134] J.A.. Koningstein. *Chem. Phys. Lett.* **146**, 576 (1988).

LAWRENCE BERKELEY LABORATORY
TECHNICAL INFORMATION DEPARTMENT
1 CYCLOTRON ROAD
BERKELEY, CALIFORNIA 94720